TECHNISCHE UNIVERSITÄT
BERGAKADEMIE FREIBERG
The University of Resources. Since 1765.

Modeling of realistic microstructures on the basis of quantitative mineralogical analyses

By the Faculty of Mechanical, Process and Energy Engineering
of the Technische Universität Bergakademie Freiberg

approved

Thesis

to attain the academic degree of

Doktor-Ingenieur
(Dr.-Ing.)

submitted by **M. Sc. Michael Klichowicz**

born on the 06.10.1988 in Dresden

Assessor: Prof. Dr.-Ing. Holger Lieberwirth
Prof. Malcolm Powell

Date of the award: Freiberg, 21.07.2020

Acknowledgement

I would like to thank my PhD advisor, Professor Holger Lieberwirth for his encouraging trust in me and my visions. He guaranteed me sheer unlimited freedom to develop and implement the various ideas and concepts, which, in summary, are the essence of this thesis. This, however, would not be possible without the funding of the Deutsche Forschungsgemeinschaft (DFG, German Research Foundation) – Project No.: 320596194. Of course, I would like to thank Professor Malcolm Powell for being the second advisor for this thesis. He is definitely one of the most outstanding scientists in the world of comminution.

I also have to thank Thomas Frühwirt and his team from the Rock Mechanics Laboratory for the helpful discussions and support in the time-consuming indenter tests.

Furthermore, I am indebted to all my colleagues at the Institute of Mineral Processing Machines. I would have never been landed at this institute without Klaus Meltke, who, with his indescribably warm-hearted and honest nature, convinced half of the mechanical engineering class of 2008 to specialize in mineral processing machines. He is definitely one of the best lecturers I have ever met. Just as much I thank Mathis Reichert, who accompanied my first steps in scientific writing and Max Hesse for the many debates on comminution and mineral processing principles. Not to forget, I thank all the other people of our breakfast circle. This was definitely a not to be underestimated hoard of knowledge and exhilaration, which pushed me a lot.

Of course I also thank all the people behind the scenes, which are the mandatory gearbox for any movement of the institute. Among those are Sylvia Richter (a secretary like none other), Rudolf Müller and his workshop team (what would traditional mechanical engineering without manufacturing?), Marius Ehrig and the team of the measurement and test engineering lab (what would modern mechanical engineering do without sensors and control systems?) and Andreas Peukert (a walking encyclopedia of both the people of Freiberg and the inventory of the institute).

In addition, I thank all the students, which I was allowed to accompany during the different phases ranging from the first undergraduate practical training with screening machines to numerous interesting master theses. It is an amazing experience to work with such different talented engineer candidates.

Last but not least, I would like to express my deepest gratitude to my family, especially my wife Anja and my sons Theodor and Emil. Coming home to you is always like a second start in the day.

Versicherung

Hiermit versichere ich, dass ich die vorliegende Arbeit ohne unzulässige Hilfe Dritter und ohne Benutzung anderer als der angegebenen Hilfsmittel angefertigt habe; die aus fremden Quellen direkt oder indirekt übernommenen Gedanken sind als solche kenntlich gemacht.

Bei der Auswahl und Auswertung des Materials sowie bei der Herstellung des Manuskripts habe ich Unterstützungsleistungen von folgenden Personen erhalten:

- Professor Dr.-Ing. Holger Lieberwirth

Weitere Personen waren an der Abfassung der vorliegenden Arbeit nicht beteiligt.

Die Hilfe eines Promotionsberaters habe ich nicht in Anspruch genommen. Weitere Personen haben von mir keine geldwerten Leistungen für Arbeiten erhalten, die nicht als solche kenntlich gemacht worden sind. Die Arbeit wurde bisher weder im Inland noch im Ausland in gleicher oder ähnlicher Form einer anderen Prüfungsbehörde vorgelegt.

21.07.2020 M. Sc. Michael Klichowicz

Declaration

I hereby declare that I completed this work without any improper help from a third party and without using any aids other than those cited. All ideas derived directly or indirectly from other sources are identified as such.

In the selection and use of materials and in the writing of the manuscript I received support from the following persons:

- ○ Professor Dr.-Ing. Holger Lieberwirth

Persons other than those above did not contribute to the writing of this thesis.

I did not seek the help of a professional doctorate-consultant. Only those persons identified as having done so received any financial payment from me for any work done for me. This thesis has not previously been published in the same or a similar form in Germany or abroad.

21.07.2020 M. Sc. Michael Klichowicz

List of Acronyms

BPM Bonded Particle Model

CFD Computational Fluid Dynamics

CPU Central Processing Unit

DEM Discrete Element Method

DoE Design of Experiments

EDM Event-Driven Methods

FBM Fast-Breakage Model

FEM Finite Element Method

GPU Graphics Processing Unit

GUI Graphical User Interface

HPGR High Pressure Grinding Rolls

IPA Imaging Particle Analysis

MD Molecular Dynamics

MLA Mineral Liberation Analysis

NDP Non-Differentiated Phase

PFC Particle Flow Code

PIL Python Imaging Library

PRM Particle Replacement Model

PyQt Python library for creating graphical user interfaces on the basis of Qt

QMA Quantitative Microstructural Analysis

SAG Semi Autogenous Grinding

SPH Smoothed Particle Hydrodynamics

TDM Time-Driven Methods

UCS Unconfined Compressive Strength

UV Ultraviolet

YADE Yet Another Dynamic Engine

List of Latin Symbols

Sign	Description	Unit
A	Area of an object	mm^2
a	Longest principal semi-axis of the unit microbody	mm
A_{canvas}	Area of the canvas used for drawing a synthetic microstructure	mm^2
A_{crack}	Area of the fracture surface	mm^2
a_0	Area of the measuring field of the line analysis	mm^2
A_A	Area of objects per test area	mm/mm^2
A_i	Area of the ith grain of a give cut surface distribution	mm^2
AM	Arithmetic Mean - *unit depends on analyzed set	*
b	Median principal semi-axis of the unit microbody	mm
C	Circumference of an object	mm
c	Shortest principal semi-axis of the unit microbody	mm
C_A	Specific boundary line length	mm/mm^2
$C_{A,(\alpha,\beta)}$	Specific boundary line length between neighboring grains of phase α and grains of phase β	mm/mm^2
$C_{A,all}$	Specific boundary line length of the whole mineral microstructure	mm/mm^2
$C_{A,(\alpha,\alpha)}$	Specific boundary line length between neighboring grains of phase α	mm/mm^2
$C_{A,I}$	Ideal specific boundary line length	mm/mm^2
$C_{A,I,actual}$	Ideal specific boundary line length of the actual grain size distribution referring to the area of the phase of interest	mm/mm^2
$C^*_{A,I,actual}$	Ideal specific boundary line length of the actual grain size distribution referring to the total area of the field of measuring	mm/mm^2
$C_{A,I,approx}$	Ideal specific boundary line length of the approximated grain size distribution referring to the area of the phase of interest	mm/mm^2
$C^*_{A,I,approx}$	Ideal specific boundary line length of the approximated grain size distribution referring to the total area of the field of measuring	mm/mm^2
C_α	Degree of clustering of phase α	%

Sign	Description	Unit
$C_{A,R}$	Real specific boundary line length referring to the area of the phase of interest	mm/mm^2
$C^*_{A,R}$	Real specific boundary line length referring to the total area of the field of measuring	mm/mm^2
$C_{Ellipsis}$	Estimated circumference of an ellipsis	mm
CV	Coefficient of variation	%
d	Distance between two parallel lines of the line analysis	mm
$d_{specimen}$	Thickness of the specimen	mm
$d_{p,max}$	Maximum particle size inside the particle filling	mm
d_{pot}	Diameter of the pot of the piston die press	mm
E	Young's modulus	GPa
W_{crack}	Energy absorbed by the crack creation	J
El	Elongation of the unit microbody	%
F	Force	N
F_{crack}	Fracture force	N
$\vec{F}_I$	Force on body I	N
$\vec{F}_{II}$	Force on body II	N
F_{end}	Final load at the end of a fracture test	N
Fl	Flatness of the unit microbody	%
F_N	Normal force	N
h	Stroke of the piston	mm
h_0	Initial height of the particle filling inside the pot of the piston die press	mm
h_{rel}	Relative stroke of the die	%
$K_{I,(\alpha,\beta)}$	Degree of intergrowth between grains of phase α and grains of phase β	%
K_{iso}	Degree of isotropic orientation	%
K_{lin}	Degree of linear orientation	%
k_n	Normal stiffness constant	N/m
K_{pla}	Degree of planar orientation	%
K_R	Degree of roughness	%
$K_{R,actual}$	Degree of actual roughness	%
$K_{R,estimated}$	Degree of estimated roughness	%
l_{crack}	Total length of the crack	mm
$l_{crack,boundary}$	Length of the crack along the grain boundaries	mm

Sign	Description	Unit
L_L	Length of objects per unit test line	mm/mm
m_I	Mass of the particle I	kg
m_{II}	Mass of the particle II	kg
m_i	Mass of the particle i	kg
$M_{k,r}$	Complete r$^{\text{th}}$ moment of the q_r distribution	*
n	Number of intersections between the objects of interest and the lines of the line analysis in relation to the total length of the analysis lines	–
N_{all}	Number of intersection points on all lines of the line analysis	–
$N_{(\alpha,\beta)}$	Number of intersection points between grains of phase α and grains of phase β on a line of the line analysis	–
n_{iso}	Radius of the spatial rose of intersection of an ideal isotropic orientated microstructure	1/mm
n_{lin}	Radius of the spatial rose of intersection of an ideal linear orientated microstructure	1/mm
n_{pla}	Radius of the spatial rose of intersection of an ideal planar orientated microstructure	1/mm
$p_{boundary}$	Proportion of the length of grain boundary cracks of the total crack length	%
p_{grain}	Proportion of the length of the non-boundary cracks of the total crack length	%
$P_{L,(\alpha\alpha)}$	Number of intersection points between grain boundaries of neighboring grains of phase α per unit test line (single-counted)	–
$P_{L,(\alpha\beta)}$	Number of intersection points between grain boundaries of neighboring grains of phase α and phase β per unit test line (double-counted)	–
$P_{L,all}$	Number of all intersection points per unit test line	–
$poly_A$	Internal synthesis parameter for the estimated average size of a polygon or grain of phase i	pixel^2
$poly_{angle}$	Internal synthesis parameter for the orientation angle of the polygons or grains of phase i	°
$poly_{angular}$	Internal synthesis parameter for the angularity of the polygons or grains of phase i	%
$poly_{color}$	Internal synthesis parameter for the color of the polygons or grains of phase i	–
$poly_{\Delta angle}$	Internal synthesis parameter for the deviation of the orientation angle of the polygons or grains of phase i	°

Sign	Description	Unit
$poly_{desity}$	Internal synthesis parameter for the polygon or grain density of phase i	%
$poly_{\Delta size}$	Internal synthesis parameter for the deviation of the size of the polygons or grains of phase i	%
$poly_{Pr}$	Internal synthesis parameter for the probability for setting a seed point for drawing a polygon or grain of phase i	%
$poly_{ratio}$	Internal synthesis parameter for length ratio of the polygons or grains of phase i	%
$poly_{rough}$	Internal synthesis parameter for the roughness of the polygons or grains of phase i	%
$poly_{seeds}$	Internal synthesis parameter for the number of seeds for drawing polygons or grains of phase i	–
$poly_{size}$	Internal synthesis parameter for the average size of the polygons or grains of phase i	pixel
$poly_{vert}$	Internal synthesis parameter for relative number of vertices of the polygons or grains of phase i	%
P_P	Number of points per test points	–
P_{seed}	Seed point	–
$p - value$	Observed significance level for a test hypothesis	–
$P_{vert,j}$	Coordinates of the the j^{th} vertex of a polygon	–
$q_0(x)$	Frequency number distribution of the grain size	–
$Q_2(x)$	Cumulative area distribution of the grain size	–
$q_2(x)$	Frequency area distribution of the grain size	–
$q_3(x)$	Frequency volume distribution of the grain size	–
r	Coefficient of restitution	–
r_j	Radius for drawing the j^{th} vertex of a polygon	–
s	Displacement of the indenter	mm
s_0	Displacement of the indenter at the beginning of the crack propagation	mm
s_{crack}	Displacement of the indenter after the crack propagation has finished	mm
SD	Standard deviation - *unit depends on analyzed set	*
S_L	Length scale	Pixel/mm
S_V	Specific surface	mm^2/mm^3
$S_{V,all}$	Specific surface of all interfaces in a mineral microstructure	mm^2/mm^3
$S_{V,(\alpha\alpha)}$	Specific surface of the interfaces between neighboring grains of phase α	mm^2/mm^3

Sign	Description	Unit
$S_{V,(\alpha\beta)}$	Specific surface of the interfaces between neighboring grains of phase α and grains of phase β	mm^2/mm^3
$S_{V,I}$	Ideal specific surface	mm^2/mm^3
$S_{V,iso}$	Specific surface of the ideal isometric orientated component of a given system	mm^2/mm^3
$S_{V,lin}$	Specific surface of the ideal linear orientated component of a given system	mm^2/mm^3
$S_{V,pla}$	Specific surface of the ideal planar orientated component of a given system	mm^2/mm^3
$S_{V,R}$	Real specific surface	mm^2/mm^3
U	Overlapping of two discrete elements	m
$\vec{u}_I$	Velocity of body I after collision	m/s
$\vec{u}_{II}$	Velocity of body II after collision	m/s
UCS	Unconfined Compressive Strength	MPa
$\vec{u}_i$	Velocity of body i after collision	m/s
v_{crack}	Speed of the crack propagation	mm/s
$\vec{v}_I$	Velocity of body I before collision	m/s
$\vec{v}_{I,1^{st}}$	Suggested velocity of body I in the first substep of an implicit collision model	m/s
$\vec{v}_{I,2^{nd}}$	Suggested velocity of body I in the second substep of an implicit collision model	m/s
$\vec{v}_{II}$	Velocity of body II before collision	m/s
$\vec{v}_i$	Velocity of body i before collision	m/s
V_V	Volume of objects per unit test volume	mm^3/mm^3
W	Mechanical work	J
W_{crack}	Deformation work done by the indenter	J
x	Grain size	mm
$x_{50,0}$	Median grain size of the approximated log-normal frequency distribution	mm
$x_{50,2}$	Median grain size of the approximated log-normal area distribution	mm
$x_{50,3}$	Median grain size of the approximated log-normal volume distribution	mm
$z_{boundary}$	Factor for adjusting the strength of the grain boundary	–

List of Greek Symbols

Sign	Description	Unit
α	A specific type or group of mineral constituents	–
β	A specific type or group of mineral constituents	–
Δt_{crack}	Time that elapses during crack propagation	s
ϵ_A	Areal proportion	%
$\epsilon_{A,crystalline\,phases}$	Areal proportion of all crystalline phases	%
ϵ_{AF}	Areal degree of space filling of a microstructure	%
$\epsilon_{A,\,pores}$	Areal proportion of a pores	%
ϵ_V	Volumetric proportion	%
$\epsilon_{V,crystalline\,phases}$	Volumetric proportion of all crystalline phases	%
ϵ_{VF}	Volumetric degree of space filling of a microstructure	%
$\epsilon_{V,\,pores}$	Volumetric proportion of the pores	%
γ	A specific type or group of mineral constituents	–
κ	Factor for the grain shape	–
Ω	Set of all grains of a given distribution	–
φ	Factor for the grain shape	–
ϕ	Porosity of a mineral microstructure	%
ψ_j	Drawing angle for the i^{th} vertex of a polygon	°
$\rho_{spearman}$	Spearman's rank correlation coefficient	–
σ_{ln}	Dispersion parameter of the approximated log-normal grain size distribution	–
σ_n	Normal strength	MPa
σ_{tB}	Brazilian tensile strength	MPa

Contents

1 Introduction

1.1 Motivation for using realistic microstructures in Discrete Element Method (DEM)

Sustainability and its relation to mineral processing. We live in a world, which is shaped by the dichotomy of growth and sustainability. Due to an increasing understanding of the complex relations between the human way of living and the changes in our environment we can see a slight but inexorable change in the way of thinking about sustainability. A good indicator for this change is the ongoing debate about negative long-term consequences of the economic growth like the greenhouse effect and possible ways out. The occurrence of agreements like the Paris Agreement [140] was unthinkable 50 years ago. But even now the inner strife of many signatory nations is obvious. The best example is the withdrawal of the USA in the year 2017, only half year after it entered into force. On the one side, the governments are anxious to guarantee the best conditions for economic growth and welfare of their own nations today. On the other side, they have to act with more respect to nature than previous governments to secure safe and well-balanced environmental conditions for the following generations.

A substantial point in the struggle for sustainable growth is the reduction of greenhouse gas emissions like CO_2. It is estimated that about 70 % of the energy consumption in mineral processing refers to crushing and grinding processes [39, 134]. Based on this number it can be extrapolated that only the existing mineral crushing and grinding processes require about 5080 PJ/y, which is about 3 % of the world energy consumption [57, 134]. Obviously, those relations underline that well-balanced and efficient comminution technology is not only a major factor for economic efficiency. The energy consumption of these processes also has an effect on the global energy demand.

Hence, there is a wide variety of research that focuses on this topic. The studies range from analyzing and improving existing circuits via the development of new technologies to basic research of comminution and processing principles. What these efforts have in common is that they are increasingly using computer technology.

A good example for this trend are the changes in the way of modeling of mineral processes in the past years. Whereas empirical formulas and laboratory tests in combination with the expert knowledge of process engineers dominated the design of processing plants for a very long time, there are new trends identifiable. Due to increasing computing capacities as well as potential economic advantages, simulation and modeling software finds use in an increasing number of branches of mineral processing.

The conventional methods of mineral processing design and research. In the past, the used models were mostly empirical. Furthermore, due to the complexity of the relevant parameters and their interactions, such approaches were often only suitable for very limited fields of application. Exemplary for this are the numerous tests, which were and are used to determine the grindability of minerals. Depending on the kind of comminution machine that should be used, very different tests are available. Indeed, there are sometimes diverse tests, even for one machine, which do not necessarily offer the same results at comparable conditions.

For instance, a Semi Autogenous Grinding (SAG) mill may be designed with the support of at least eight different comminution tests [46, 169, 196, 197]. The tests are mostly realized with different machines and do have differing requirements for the feed material. Moreover, these tests do not necessarily give the same results at all [7]. Although, the tendencies are the same in principle, the expertise of an experienced process engineer is always needed to interpret the outcome of these mostly empiric models. Significantly, the outlined problem is symptomatic for many areas of mineral processing.

Simulation and modeling in mineral processing. Consequently, different research groups try to overcome these shortcomings. As already mentioned, one attempt is to use simulation and modeling software. The general aim is to allow faster, cheaper, and more reliable predictions of the processes. The fundamental idea behind the use of computer simulations is the theoretical ability to map every real process to a virtual twin on a computer. In the end, this results in the idea of a virtual processing plant. With this technology, it would be possible to comprehensively plan the plant structure and customize the machines as well as the processes at the computer.

If this concept becomes real, one could save the time-consuming and cost intensive laboratory and pilot plant tests. Furthermore, it would allow to optimize the plant and its components. The process designer could run case studies on a computer and quickly determine plant performance and potential bottlenecks without having to consider the limitations and conditions of existing equipment.

There is indeed a range of specific commercial software like MODSIM [94, 202], USIM PAC [18, 19, 193], JKSimMet [59, 178, 203] or JKSimFloat [179, 180] available that already can simulate different aspects of mineral processing and help at the flow sheet design. Furthermore, there are different research groups that use more general software solutions like MATLAB/Simulink to simulate mineral processing circuits on their own [5, 93, 106].

So far, none of this software packages can be seen as incontrovertible. Until now, there is no real mechanistic model for all the different processes in mineral processing. They all rely on semi empiric tests and mostly historically grown data bases, which are often opaque to the end user. Therefore, plant design calculations are typically done within distinct modeling environments [8].

Discrete Element Method (DEM) in mineral processing. Further improvements of the plant design models mostly depend on the development of the underlying understanding of the relations between the different macro and micro processes. An interesting approach to tackle this problem is to simulate comminution systems using the Discrete Element Method (DEM) [220]. The DEM provides the ability to build up mechanistic models, which describe the interactions between distinct bodies. DEM is used to simulate systems ranging from complete processing machines to micro processes. Theoretically, it is even conceivable to go down to the level of the primitive cells of the crystals within minerals or even to the underlying atomic structure.

However, simulations at such detailed levels are not very practicable by now, as firstly, the structure of the mineral constituents has to be incorporated. For this, here and below, the term "mineral microstructure" is used as an umbrella term for the mode and the fabric of a rock like material. According to this definition, the mode describes the type and the volume fractions of the phases of the material. In contrast, the fabric includes the texture, that is, the formation of the individual constituents and the structure, that is, the arrangement of the constituents in space [146]. Since these definitions are not restricted to natural rock, but can also be used to describe other materials such as artificial stone, concrete or ceramics, which consist of minerals and mineraloid matter as well, the term "mineral" is used. However, it has to be noted, that the term mineral microstructure is only used for structures made up of several grains or equivalent objects such as pores or Non-Differentiated Phase (NDP). Hence, intracrystalline microstructures or equivalents are not considered here.

So far, most DEM simulations of mineral processes neglect the influence of the intrinsic complexity of the minerals and the resulting influence on the process. Of course, the influence of those parameters depends on the topic and the scale of the research field, where the DEM is used. As long as the structure of the material itself is not changed or the material is homogeneous and isotropic, the characteristics of the minerals may be described sufficiently accurate by a few integral parameters like average density or the average Young's modulus.

For instance, selected transport and storage processes can already be simulated satisfactorily with the existing models as the mineral microstructure is insignificant for the processes.

In contrast, the effect of the mineral microstructure on comminution itself and possible subsequent processes like flotation and magnetic separation is significant. The characteristics of crack propagation is often predestined by the mineral microstructure to a certain degree. Hence, material and process characteristics like cleavage, brittleness, selective comminution, and mineral liberation, which, among other things, depend on the way the cracks propagate, can hardly be simulated with DEM without taking the mineral microstructure into account.

1.2 Possibilities for using realistic mineral microstructures in DEM simulations

Given the importance of the above mentioned characteristics for mineral processing operations in general, it may be surprising why the actual mineral microstructure is so rarely considered for DEM simulations. The main reason for this seems to be the question of how the real mineral microstructures can be realistically digitized if such processes or parts of them shall be simulated with DEM. For that reason, it is the aim of this work to develop a technique that allows to incorporate the structure and texture of mineral microstructures into DEM as realistic as possible. The basis for this has to be a suitable procedure to describe the characteristics of the mineral microstructure. That is because the structure and texture of the real microstructure has to be measured and described by suitable quantitative parameters first, before the same can be incorporated into a simulation environment.

Approaches for making mineral microstructures accessible for DEM If one is interested in how realistic mineral microstructures can be integrated into simulation environments, the non-exhaustive schema in Figure 1.1 can be used as reference. It shows two basic ways that are possible to generate a model of a real structure, which is later integrated into a simulation environment.

The first solution for finding a suitable model is to generate an image of the real structure. This image has to contain the characteristics of the real structure, which are important for the simulation. Furthermore, it has to be available in a format that is suitable for the simulation. The other principle way to generate a model is to derive the characteristics of the real structure, for example by measure or estimation, and generate an analogous model. This model has to have characteristics that are comparable to those of the real structure, and it has to be available in a format suitable for the simulation.

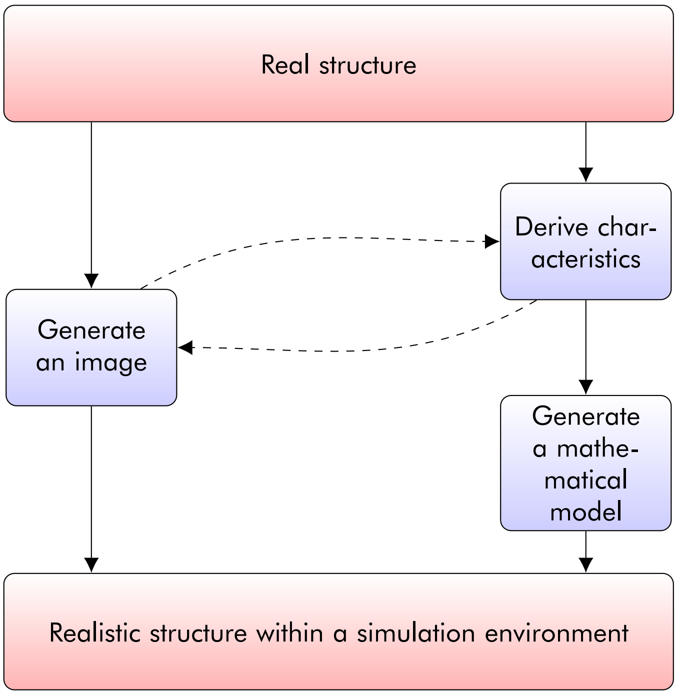

Fig. 1.1: Schema for importing a realistic microstructure into a simulation environment

Irrespective of these two separate straight forward approaches, it is also possible to connect them in order to improve the modeling process. In schema in Figure 1.1 two possibilities of these connections are shown by the dotted arrows.

The first one is the connection between the generation of an image and deriving characteristics of a given structure. This procedure can for example be used if it is not possible to directly access the characteristics of the real structure so that the detour using an image can be necessary. The contrary procedure is possible as well. For example, if it is not feasible to create an image directly, it may be possible to first measure the characteristics of the structure and then try to create an image of the real structure based on the measured characteristics.

Direct image based approaches for microstructure modeling. If this schema is applied for the model generation of mineral microstructures, the existing approaches can easily be characterized. The generation of images of mineral microstructures is principally possible with tomography for three-dimensional structures and photography for two-dimensional structures.

An example for three-dimensional imaging approaches is computed tomography. This is a proven technique for the analysis of mineral material. There are various possible fields of application, ranging from the analysis of the composition of particle beds, [122, 212, 213] to the analysis of the composition of single particles [131, 205]. For two-dimensional imaging, it is, for example, possible to use X-ray spectroscopy, which is successfully applied for Mineral Liberation Analysis (MLA) [51, 92, 108]. As both approaches are based on X-ray technology, they create density images in principle. Hence, these approaches have problems to resolve structures with similar densities like neighboring grains of the same phase. This is a significant disadvantage, as grain boundaries between grains of the same phase are often an important part of the mineral microstructure.

But also optical photography is a possible approach for creating a suitable image of the mineral microstructure. This technique has recently been applied by LI; KONIETZKY, and FRÜHWIRT [107] and TAN; KONIETZKY, and CHEN [200] who used photos taken under normal lighting of thin sections of mineral microstructure as basis for their DEM studies. But this approach has the same disadvantage of detecting boundaries between grains of the same phase as those are hardly recognizable under normal lighting as well.

Furthermore, the direct generation of an image of the real mineral microstructure is relatively inflexible in the sense of modeling. Even if it was possible to resolve the mineral microstructure accurately, including structures having no differences in density or visual appearance, it would still be a disadvantage that such an image is an unchangeable object for simulations. Given the example, that one would like to analyze how a specific material would behave if the grains of the microstructure would be rougher or bigger than in the analyzed image, this would be a problem. Based on this technique it is sheer not possible to change the characteristics of such a microstructure that is used in the simulation as it is only an image. For changing the roughness or grain size, further processing is needed. This circumstance is of great significance as the variability of the characteristics of the material is one of the most important aspects in the design and operation of mineral processes. Therefore, it is in many cases of particular interest to analyze the influence of this variability on the process. Methods, which exclude the possibility to study these effects can therefore not be the right choice for incorporating realistic mineral microstructures into DEM simulations.

Quantitative Microstructural Analysis (QMA) as option for a more flexible indirect approach for microstructure modeling. In order to overcome the explained limitations, it is necessary to firstly derive the characteristics that are important to describe all relevant parameters and subsequently generate a realistic model of the mineral microstructure. These characteristics have to be evaluated and processed in order to be able to generate a mathematical model that represents the mineral microstructure statistically. Having such an approach, it would be possible to adjust the properties of the model so that variations of the material can easily be considered in the simulation. A powerful method that is suitable for this task can be found in the QMA [147, 148]. The QMA is a method that describes microstructures in detail with quantitative values, relevant, among others, for mineral processing. Therefore, it is a promising basis for generating mathematical models of mineral microstructures, which can then be imported into diverse DEM simulation environments.

1.3 Objective and disposition of the thesis

Based on the above explained boundary conditions, the focus of this thesis is set on finding a method for incorporating the QMA as basis for using realistic mineral microstructures in DEM simulations. Therefore, first the background of DEM and QMA are explained (Chapter 2), in order to allow the reader a sufficient understanding of both methods.

Subsequently, in Chapter 3, it is analyzed how it is possible to generate a realistic model of a given mineral microstructure that can be used as basis for DEM simulations. These considerations are the basis for the formulation of the so-called synthetic microstructure approach.

In the following, this new approach is subjected to a proof of concept study in Chapter 4, in order to evaluate the proposed method. This is done on the basis of comparative crushing tests with selected material. By doing so, the real tests are compared to DEM simulations using realistic microstructural models at grain size level.

Finally, Chapter 5 summarizes the main findings of this study. Besides the conclusions from the proof of concept experiments, the presented research is finished with an outlook on possible further developments and a classification of the proposed approach in the context of existing simulation tools for mineral process design and optimization.

2 Background

In the first part, the following chapter summarizes the background of the DEM (Section 2.1.1) and the way in which the DEM is used in comminution science (Section 2.1.2). In accordance with the limitations of the DEM in this area (Section 2.1.3), requirements for the proper incorporation of realistic microstructures to the DEM are derived.

The second part is dedicated to the QMA. Firstly, the background of this stereological method is explained in detail, as well (Section 2.2.1). This is followed by a brief summary of the application of the QMA in mineral processing in Section 2.2.2.

2.1 Discrete Element Method (DEM)

2.1.1 Fundamentals of the Discrete Element Method (DEM)

The use of computer-based simulations has nearly become a standard in many aspects of mineral processing research. They are widely used for design, evaluation, and improvement in the whole range between basic research and lab scale experiments up to full size plant technology. Thus, the quality of the simulations has to cover a big spectrum. On the one hand, there are exemplary simple simulations, which represent long time existing and continuously used models, just integrated into computer simulations. On the other hand, also very complex simulations exist that often depend on extensive computing capacities. An example for the latter category is the so-called DEM.

The DEM, which is also known as distinct element method, is an approach to compute the motion and interaction within particle systems. For this, it uses the Lagrangian approach to calculate the motion of each particle. Due to that, the particles can be referred to as discrete or distinct elements. Advantageously, this general approach makes it possible to calculate parameters of particle systems, which are impossible to measure in real systems. Hence, this approach is an interesting tool for the characterization and examination of granular systems.

Generally, DEM simulations have in common that they always use some kind of calculation cycle as core for any computation. This cycle consists at least of a model for the particle motion and a model for the particle contact, as shown in Figure 2.1. However, the nature of this cycle can be very different and is always tailored to the specific requirements of the various fields of application. Thus, it is possible to modify the two main models almost indefinitely and to insert further models into the cycle.

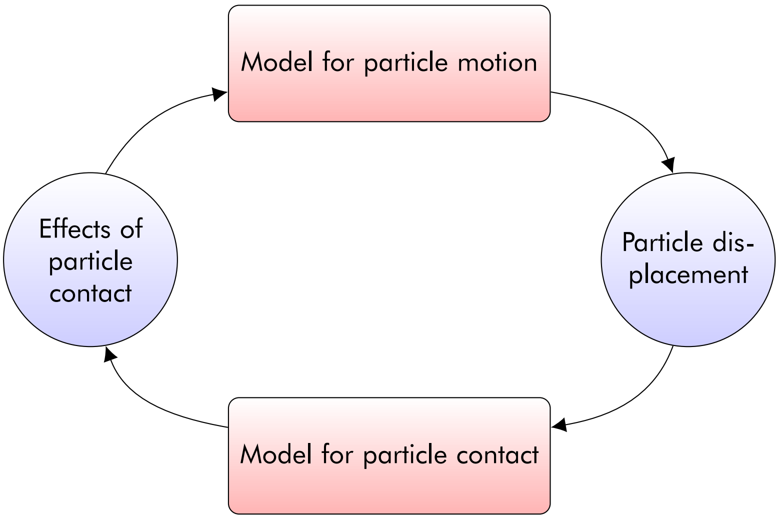

Fig. 2.1: General calculation cycle of for a DEM simulation

The universality of the DEM approach makes it a suitable tool for many other fields of research as well, spanning from molecule dynamics to the fracturing processes of discontinuous rock masses. Therefore, the general approach is implemented into specific simulations, which can vary to the same extend as the applications do. In order to put the DEM simulations of the present investigations into the right general context, it is helpful to categorize the models used in DEM simulations based on the different criteria [47, 80, 114]. The categories used in the following explanations try to cover the main differences in the used models:

- The dimension of the problem tackled
- The shape of the particles
- The models to describe the particle collision
- The models to describe the particle motion
- The software implementation
- Couplings to other simulation approaches

Nevertheless, it is noted that due to the diversity of the DEM approach, finding an exact category for every single DEM application is not expedient for this work.

The dimension of the problem

The dimensionality of DEM simulations is an important differentiating characteristic. Typically, DEM simulations are used to face planar and spatial problems. Furthermore, two-dimensional simulations are often the means of choice to test new models, as they are easier in both, implementation and plausibility check. In addition, the required computing power is usually significantly lower than for three-dimensional simulations.

If the model approaches are validated, and if there is a need for a spatial simulation of the problem, they can be extended with moderate effort to three-dimensional models. Due to the universality of the Lagrangian approach, the DEM can of course be used for one-dimensional or higher-dimensional problems as well, although publicized studies are not known to the author.

Shape of the particles

A key differentiator is the shape of the particles in the model. This parameter affects DEM simulations in two ways. On the one hand, the geometric complexity of the particles is a main factor for the computational complexity of the collision detection. Because of this, simple shapes are preferred. On the other hand, many tasks require particle shapes, which are close to reality as the particle shape itself is a main influencing parameter in certain processes. For this reason, the shapes of the particles are usually subclassified into the following categories:

Spherical particles. Spherical particles are used in many DEM models, since the collision detection is fairly easy and the computational complexity is limited to a minimum. As a matter of fact, spheres (Figure 2.2b) are the most popular shapes for three-dimensional DEM simulations [98, 112]. The same applies for circular disks (Figure 2.2a), which are the equivalent for spheres in two-dimensional DEM simulations [78, 99, 111, 113, 168].


(a) (b)

Fig. 2.2: Spherical Particles: (a) Circular disk for two-dimensional models; (b) Sphere for three-dimensional models

Using those two- or three dimensional spherical shapes has the advantage that only the distance between the centers of two involved particles has to be compared with the radii of the particles. If the distance is bigger than the sum of the radii, there is no contact between the particles. If the distance is equal to the sum of the radii, the particles touch each other, and if the distance is smaller the particles overlap each other.

Unfortunately, the limitation to spherical particles is a very strong restriction for many applications. The real systems that are to be investigated with DEM often consist of particles with more complex geometries. Since the influence of the particle shape is often not negligible for the investigated process, this can lead to significant discrepancies between a DEM simulation with spherical particles and reality.

Elliptical particles. An attempt to combine the good practicability of spherical particles with more complex shapes [109, 110, 207] are elliptical particles. The use of these within DEM shall enable more realistic results with still acceptable computational effort. For this, forms derived from ellipses (Figure 2.3a) are very well suited in two-dimensional simulations. In the three-dimensional case it is possible to create nearly arbitrary spherical, elongated, and platy shaped particles, only by the variation of the principal semi-axes of the ellipsoid (Figure 2.3b).

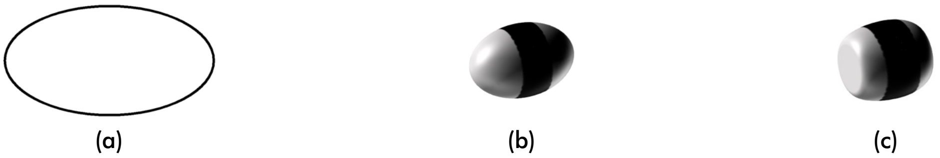

Fig. 2.3: Elliptical particles: (a) Ellipse for two-dimensional models; (b) Ellipsoid for three-dimensional models; (c) Superquadric for three-dimensional models

This approach can be further expanded, for example by the use of superquadrics (Figure 2.3c) instead [28, 32, 41, 145, 189, 194, 195, 221]. Although these are still well describable geometric bodies, the cost of collision detection increases significantly compared to models with spherical particles. This is due to the fact that not only the distance and the size of the involved particles is relevant for the collision detection, but also the spatial orientation.

Polygonal particles. Using polygonal particles can be mandatory if the DEM simulation must necessarily reflect the shape of the real particles [79, 125, 130, 142, 172]. If this is inevitable, the real particles are mostly simulated with polygons in two-dimensional simulations (Figure 2.4a) and polyhedra in three-dimensional simulations (Figure 2.4b). Since the collision detection is not trivial and computational extensive, this procedure is only used under special circumstances.

An exception are particles in the form of special geometric basic forms such as the equilateral triangle and the square for two-dimensional or the tetrahedron and the cube for three-dimensional simulations [55, 227]. Due to their strict mathematical formation rules, these are in principle less computationally intensive than more general polygonal particles. How-


(a) (b)

Fig. 2.4: Polygonal particles: (a) Polygon for two-dimensional models; (b) Polyhedron for three-dimensional models

ever, the cost of collision detection is still significantly higher for those special particle shapes than for spherical or elliptical particles although both have a comparable level of abstraction. Therefore, their use for DEM is limited to mostly niche applications.

Composite particles. Complex particles or structures that are bonded assemblies of basic elements like spherical particles (Figure 2.5) are called composite particles. The basic idea is to model the behavior of arbitrarily complex shaped particles without being obliged to handle the non-trivial problems of collision detection as those that are accompanied with polygonal approaches [45, 52, 183]. In most of the cases, spherical particles are "glued" together forming so-called clusters or clumps. Depending on the purpose of the specific DEM simulation, those bonded particles can be implemented with either fragile or unbreakable compounds.


(a) (b)

Fig. 2.5: Composite particles: (a) Clump made of bonded circular disks for two-dimensional models; (b) Clump made of bonded spheres for three-dimensional models

Models for the particle contact

Regardless of the particle shape, a DEM simulation has to evaluate what happens in the event of a particle contact. As the DEM has historically developed from Molecular Dynamics (MD) simulations, a particle contact is usually referred to as a particle collision. Although the manner of collision evaluation depends on the type of the motion model, it is beneficial to consider both separately, since also hybrid models for the particle motion exist.

Collision ignoring models. The first group are models that simply neglect the physical effects that should logically occur if two particles collide. This results in unhindered overlapping U of the involved particles, as it is shown in Figure 2.6. Although the two particles penetrate each other with their velocities $\vec{v}_I$ and $\vec{v}_{II}$, this contact model does not create repulsive forces or similar. For the chosen example, this results in unhindered movement of the particles through one another.

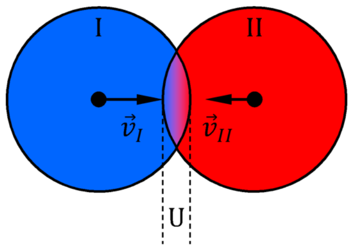

Fig. 2.6: Example for a collision ignoring model: The two particles I and II, which collide with their velocities $\vec{v}_I$ and $\vec{v}_{II}$ are not influenced by each other.

Of course, the scope of application for these models is very limited, since the interactions between the particles are in many cases the main reason for investigations by DEM. However, such a model may be advantageous for special applications.

For example, such a collision ignoring model can be used in combination with a soft sphere model to simulate the behavior of jointed rock masses within a so called Smooth-Joint contact model [82–84]. In this case, the collision ignoring model is applied only to specific particle contacts along an interface. These particles that are jointed by this contact model can overlap and slide past each other, simulating the mechanical behavior of jointed rock masses.

Implicit collision models. The second group of models for the particle collision is the group of implicit ones. These are usually predominant for statistical mechanics models [143, 144]. This type of collision model rejects every particle displacement, which would cause particle overlapping. Instead, only those movements are allowed, which result in a particle distance greater than or equal to zero. As this procedure requires the information of possible particle displacement, the way such an implicit collision model works in a simulation highly depends on the implemented model for the particle motion.

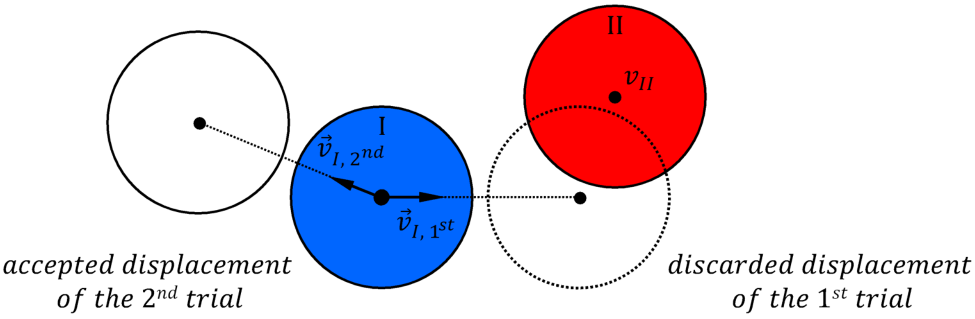

Fig. 2.7: Example for an implicit collision model: The motion model within the DEM simulation suggests a displacement for particle I, which would cause a collision with particle II and is therefore discarded by the collision model. The second trial for a displacement is then accepted as no collision is detected. One possible interpretation of this behavior is that particle I has bounced of particle II. In that way the model would have implicitly taken collisions into account without doing so in real.

In the example of Figure 2.7 the model for the particle motion suggests a movement of particle I in the first trial according to $\vec{v}_{I,1^{st}}$. However, this would result in a collision with particle II. Hence, the implicit collision model rejects this first trial and the model for particle motion suggests another movement along $\vec{v}_{I,2^{nd}}$ in a second trial. As there is no further collision detected, this displacement for particle II is accepted by the collision model. Although the actual collision event is physically ignored, this approach can be interpreted as an implicit way to model the result of particle collision in the sense of particle motion.

Exemplarily for this are the simulations of the segregation behavior of different sized particles of a granular media by shaking [44, 165]. By allowing a particle to move to unoccupied areas only, this model imitates the result of possible collisions with jostling neighbor particles that push the considered particle in a specific direction with less mechanic resistance like a void.

Hard sphere models. In contrast to the implicit simulation of particle collision, it is also possible to use models that describe the effects of particle collision explicitly. The so-called hard sphere model assumes that the colliding particles are perfectly rigid. Thus, the resulting collision duration is zero, which means that the velocities of the particles are changed instantaneously. This approach describes the post-collisional velocities of the involved particles as function of their pre-collisional states using the model of inelastic collision [2, 3, 111, 117, 162]. Figure 2.8 gives a one-dimensional example of the straight and central collision of two particles I and II: $\vec{v}_i$ and $\vec{u}_i$ are the pre- and post-collisional velocities of the particles with the masses m_i. Since the particles are assumed to be perfectly rigid, there is no overlapping but only a point contact between both of them.

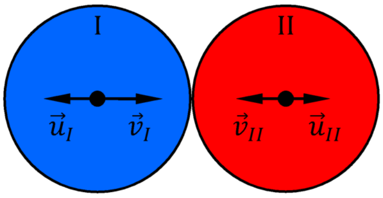

Fig. 2.8: Example for a hard sphere model: The particles I and II are in point contact. Their post-collisional velocities $\vec{u}_i$ are instantaneously calculated according to the pre-collisional velocities $\vec{v}_i$, the particle masses m_i, and the coefficient of restitution r.

The post-collisional velocities are calculated using the coefficient or restitution r [160]:

$$\vec{u}_I = \vec{v}_I + \left(\frac{1+r}{1+m_I/m_{II}} \right) (\vec{v}_I - \vec{v}_{II}) \tag{2.1}$$

For the calculation of $\vec{u}_{II}$ one has to exchange the indices I and II in Equation 2.1.

The hard sphere model is the usual approach for collision handling in Event-Driven Methods (EDM) simulations. Hence, the terms hard sphere model and Event-Driven Methods are often used as synonyms. In combination, both models are used for many MD simulations. Such systems typically have a relatively low system density, which guarantees that only binary collisions occur.

For systems with higher densities and more energy dissipation per contact the so-called inelastic collapse of the model becomes more likely [115, 120]. During such a singularity, infinite collisions can occur in an infinitesimal amount of time.

As typical mineral processing systems often have a relatively high system density with not just binary particle contacts, the hard sphere model is only used for certain applications like granular gases [123, 124] or gas-fluidized beds [78].

Soft sphere models. Another group of models that describe the effects of particle collision explicitly are the soft sphere models. In contrast to the hard sphere models, the collisions occur over a finite time. However, this type of model interprets the overlapping U of two particles as a degree of elastic deformation that, for example, causes repulsive normal forces F_N [36–38]. The interrelation between U and F_N is characterized by the so-called "contact law" or "force-displacement law" of the soft sphere model. The collision induced parameters are then used to calculate the particle displacement within the corresponding model for the particle motion.

The interpretation of the elastic deformable particle behavior led to the interpretation of "soft" particles. Due to the fact that the first simulations with this kind of model used spherical particles, this approach is referred to as the "soft sphere model". Since such overlapping usually occurs in Time-Driven Methods (TDM) simulations, these terms are sometimes used as synonyms.

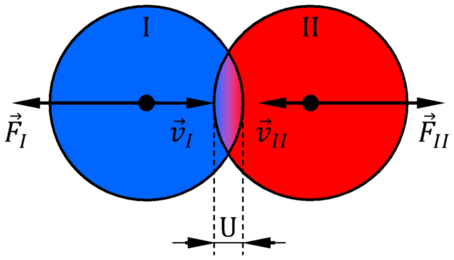

Fig. 2.9: Example for a soft sphere model: The particles I and II are overlapping each other. The overlapping U causes repulsive normal forces $\vec{F}_I$ and $\vec{F}_{II}$ according to the stiffness of the particles.

Figure 2.9 shows the basic idea exemplarily, for the simplest case of two particles I and II colliding straight and central with their velocities $\vec{v}_I$ and $\vec{v}_{II}$. According to the "soft sphere" approach the collision event itself is characterized by the overlapping U of the two particles. In order to calculate the forces $\vec{F}_I$ and $\vec{F}_{II}$ resulting of the overlapping, a force-displacement law has to be used. The simplest example may be that one of a linear spring that causes a general normal repulsive force F_N. Following, F_N is a simple function of the overlapping U and the stiffness of the involved elements k_n (Equation 2.2). As this model is purely elastic and neglects any friction, no tangential forces occur and the velocities are irrelevant for this calculation. Applying this model to the example of Figure 2.9 results in the trivial solution shown in Equation 2.3.

$$F_N = k_n \cdot U \tag{2.2}$$

$$F_N = |\vec{F}_I| = |\vec{F}_{II}| \tag{2.3}$$

After the calculation of the repulsive forces for all involved elements, the further processing is done within in the model for the particle motion.

Models for the particle motion

An essential feature of the DEM is the Lagrangian approach to calculate the motion of each particle in the system. However, the displacement of particles itself can be described by various different models. Therefore, it is mandatory to differentiate between three main groups of these motion models as they are highly correlated to specific fields of application.

Statistical mechanics models. The first group are statistical mechanics models. These use primary stochastic approaches for the determination of the particle displacement. For example, models using the Monte Carlo method [21, 44, 143, 144, 165], the cellular automate method [11], or the random walk approach [22], belong to this category. This model class is especially important for simulations of systems that behave like fluids, as the calculation of the particle movement is subjected to random processes. Hence, the application of these approaches, as in the cited publications, can mostly be assigned to processes with fluid like free particle movement. Exemplary for this are the granular flows that occurs at the discharge of particles from a hopper [11, 22] or the spatial orientation of rod and plate like crystal particles in a liquid [21].

Such a statistical mechanics model for the particle motion is typically coupled to an implicit collision model, which is exemplarily shown in Figure 2.10. In this example, particle I is statistically moved by the motion model. Particle II, which is nearby particle I, is assumed to have no kinetic energy and is thereby stationary. Within the first calculation cycle, the motion model suggests a displacement for particle I, which would cause a collision. Hence, this displacement is rejected by the implicit collision model. Thereupon follows a newly proposed displacement for particle I, which is then accepted by the collision model, as there is no collision detectable. Because particle II is assumed to have no kinetic energy and no other particle is considered in this example, the first calculation cycle is then finished and the second is started right away. Within this second cycle, the motion model suggests a random displacement for particle I that does not cause a collision at the first try. Hence, this is accepted right away by the collision model. The third calculation cycle proceeds analogously to the first one. Again, two attempts are needed to find a suitable displacement for particle I.

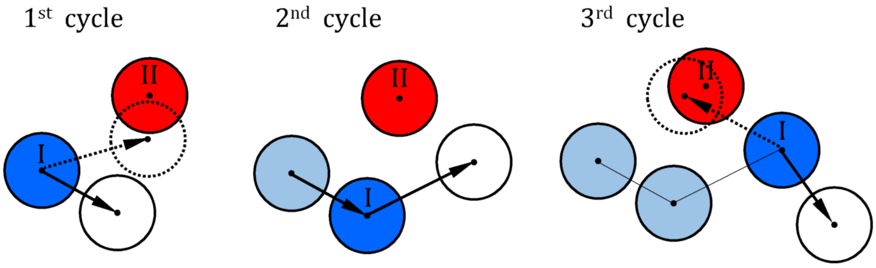

Fig. 2.10: Example of a statistical mechanics model for the particle motion in combination with an implicit collision model: 1st cycle - The initially suggested random displacement of particle I is rejected by the implicit collision model (dashed white circle). The second, subsequently suggested random displacement is accepted (continuous white circle). 2nd cycle - The initially suggested random displacement is accepted right away. 3rd cycle - Procedure is analogous to the 1st cycle

Classical Newtonian dynamics models. In contrast to the rather abstract statistical models, it is also possible to use Newton's laws of motion as basis for the calculation of the particle displacement. Although the interpretation of the classical Newtonian mechanics is nearly unambiguous, the models may differ in the type of conditions under which they are evaluated. Hence, two major subclassifications into Time-Driven Methods (TDM) and Event-Driven Methods (EDM) can be made.

EDM use variable time steps for their internal calculations [3, 78, 111, 115, 117, 120, 123, 124, 162]. Those models assume that velocities and accelerations of the particles are constant until a collision occurs. Hence, simulations using EDM update the state of the particles only at collision events. After each iteration it is necessary to calculate a new time step, which has to correspond to the time that elapses until the next collision event happens. The collisions itself are considered to be instantaneous. These models are often used for classical MD and fluid simulations, as they are suitable for simulations of low density systems, where asynchronous collision between two particles are the main contact type [47].

Typically, simulations that use EDM models for the particle motion are used in combination with hard sphere models for the particle collision. Exemplarily, Figure 2.11 shows such a simulation with three particles. In this example only particle I has kinetic energy in the initial state. In the first calculation cycle the motion model calculates that the first collision occurs between particle I and particle II. The collision event is then handled by the hard sphere model, which calculates the post collisional velocities for both particles. Those are in return handed to the particle motion model, which now again calculates the time step till the next particles collide. At this point, the next time step is again determined by the motion of particle I.

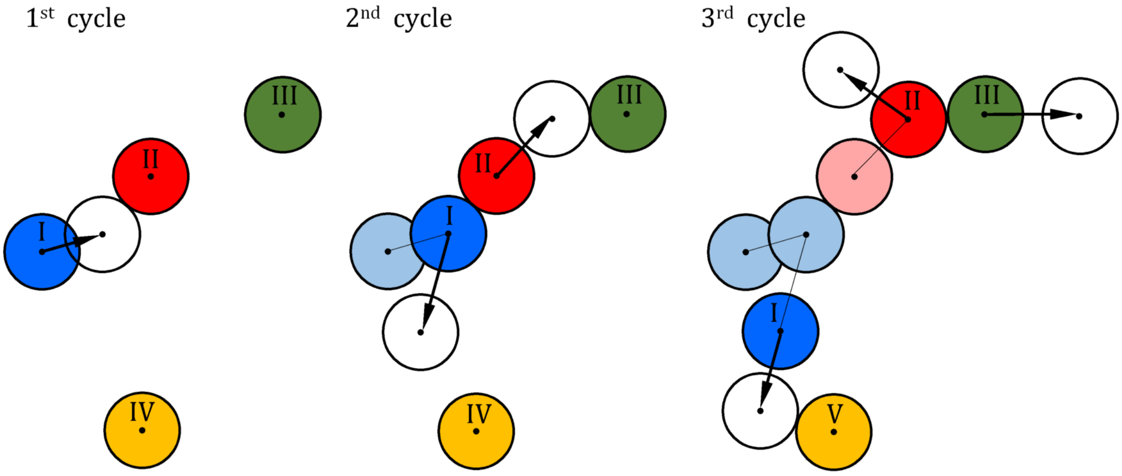

Fig. 2.11: Example of an Event-Driven Methods model for the particle motion in combination with a hard sphere model for particle collision: 1st cycle - Within the first calculation cycle the EDM predicts that the next upcoming collision will be between the only moving particle I and the initially motionless particle II. Hence, the length of the time step is adjusted so that two particles touch each other after the time step and the collision can be handled by a hard sphere model. 2nd cycle - Due to the primary collision, both particles I and II are now in motion. The EDM predicts that the next collision will occur between the now moving particle II and the motionless particle III. Again, the time step is adjusted in a way that the two particles II and III touch each other and the collision can be handled. The post-collisional motion of particle I is unaffected by this. 3rd cycle - Again particle I is responsible for the next time step evaluation as it is the first to collide with another particle. Comparable to the previous calculation cycles, the time step is set so that particles I and IV are in touch with each other and the collision is again handled by the hard sphere model.

TDM, by contrast, evaluate Newton's laws of motion always after a fixed time step [36–38]. In order to guarantee that no particle collision can be missed, this time step has to be smaller than the smallest possible impact duration. It is assumed that the velocities and accelerations are constant during a time step. TDM simulations are more suitable for denser systems where the collision time of the real particles is typically larger than the time between two particle contact events [47]. DEM simulations that are based on such a time- driven approaches for the particle motion calculation often use the soft sphere approach for the particle collision handling. A corresponding example for this combination is shown in Figure 2.12.

Hybrid motion models. It is also possible to combine the statistical approaches and Newtonian dynamics models to hybrid motion models. The aim of such composite simulations is mostly to increase the computation efficiency while maintaining specific physical correlations that cannot be realized with pure statistical models [77].

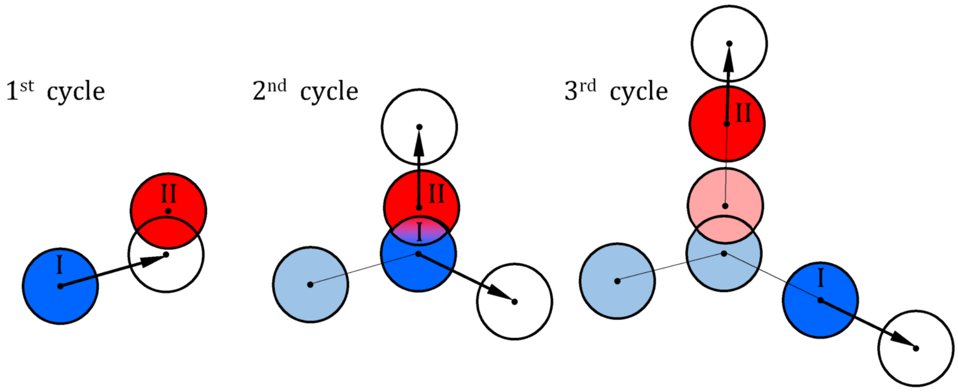

Fig. 2.12: Example of a Time-Driven Methods model for the particle motion in combination with a soft sphere model for particle collision: 1st cycle - The constant time step of the TDM model causes an overlapping of the moving particle I and the initially motionless particle II. This overlapping is handled as a collision by the subsequent following soft sphere model, which in turn calculates the collisional forces. 2nd cycle - The calculated collisional forces are used to update the velocities of the particles in the second calculation cycle. Hence, particle I changes the direction of motion and the initially motionless particle II now moves upward. As no overlapping occurs after the second constant time step, the soft sphere model is not needed to handle any collisions. 3rd cycle - The particles I and II continue to move as they were not involved in collision events during the previous time step. After the ongoing time step there is again no overlapping, so the soft sphere model does not need to handle any collision.

Couplings to other simulation approaches

As granular media and other comparable systems interact with other objects and phases in many cases, their interactions are a point of interest for many technical applications as well. In that case, a purely DEM based simulation is often not satisfactory. Hence, couplings to other simulation approaches, which are typically used to describe the interacting system, can be used. Such couplings can allow the simulation of effects, which originate in the interactions between these different systems. The most popular couplings of DEM exist to the Finite Element Method (FEM) and the Computational Fluid Dynamics (CFD) methods.

Finite Element Method (FEM) coupled models. In order to evaluate the interaction between a system of granular media and involved solid bodies, couplings to FEM are an interesting option. In this case the coupling can be used to simulate the deformation of a solid body due to the contact with the granular media [68, 199, 229]. But also other applications exist. Exemplary for this can be the simulation of the underground blast in rock masses by WANG; KONIETZKY, and SHEN [217]. This study uses such a coupled approach to simulate the blast loadings with FEM, while the induced dynamic effects in the surrounding rock are simulated with DEM.

Computational Fluid Dynamics (CFD) coupled models. Another possible coupling can be made to CFD environments. These CFD couplings are simulations where the Lagrangian approach to calculate the motion of particles is combined with fluid dynamics simulations.

This can be required if the interaction between a granular media and the surrounding fluid is not negligible. Furthermore, there are many technical processes whose basic component is the interaction of a granular medium and a fluid. The coupling to CFD can then be used to simulate the effect of the fluid stream onto the particle motion and vice versa [56, 85, 209, 211].

Smoothed Particle Hydrodynamics (SPH) coupled models. Besides the coupling to CFD, it is also possible to simulate fluids with Smoothed Particle Hydrodynamics (SPH). However, in contrast to CFD, Smoothed Particle Hydrodynamics (SPH) is a Lagrangian particle based method, where the particles represent small, discretized amounts of fluids or fluid like materials. These "blobs" are moved around as response to the fluid or solid stresses produced by the interaction with other particles. Advantageously, this method is a mesh and grid free approach, which for example makes simulation of free surfaces and material interfacial behavior significantly easier [33, 126, 164]. Hence, SPH coupled models combine the advantages of DEM for granular material with smoothed particle hydraulics for fluid simulation. Such coupled models are often used to simulate fluid-particle systems like slurries in a tower mill [188] or the process behavior in tumbling mills [31, 32, 186].

The software implementation

The available software solutions that can be used to perform DEM simulations are as numerous as their possible fields of applications. They may generally be subdivided into open-source projects such as YADE [191], LIGGGHTS [97] and ESyS-Particle [1, 49, 218] as well as commercial software packages such as EDEM [43], PFC [81], and Pasimodo [53]. While open-source projects allow for free customization of the source code and the use of self-developed models, commercial projects seek to ensure a reliable software development, service, and training courses for the users. The selection of the appropriate DEM software is therefore not only based on the scope and the supported models or couplings, but also on the user requirements such as freedom of modeling or user support.

2.1.2 Applications of DEM in comminution science

Due to its universality the DEM approach has become an often used tool in comminution science. As shown in the previous section, there are many different ways to implement DEM. These can be used to solve different problems of comminution processes and machines. In general, DEM approaches in comminution science can be divided into two main categories.

- Simulations focused on the motion of particles inside comminution processes

- Simulations focused explicitly on the particle breakage

Simulations focused on the motion of particles inside comminution processes

As DEM models work very well for simulations of particle motion, this technique is often used to characterize the working conditions of comminution technology with freely movable grinding media. The working conditions of such machines usually correlate with the effectiveness of the motion of the grinding media, as this is the key parameter for these comminution processes. Hence, it is not necessary to simulate the actual breakage process itself but to use DEM for optimization of the grinding media and grinding material motion. For example, an effective process design may ensure a high stress level for the feed material which in turn can results in more breakage events per time and therefore increases the throughput.

On the other side, the focus on particle motion can be used for wear optimization. In order to do so, there are different procedures possible. For example, this approach can be used to balance a given process in a way that the direct contact between the grinding media and the liners in a tumbling mill may be minimized, as this usually causes wear without comminuting the grinding material. The DEM can also be used to design the process so that the individual stresses on the different liners are equal in order to guaranty evenly distributed wear. This could allow to bundle the maintenance and decrease the down time. Another strategy could be to use the design of the liners to focus the wear on specific areas and design those so that their wear does not negatively affect the actual process in the machine.

Motion effects in SAG and ball mills. SAG and ball mills are of special interest for such simulations, since this is a robust method to evaluate the influence of the mill design on the grinding media motion. POWELL [154] demonstrated comprehensively the influence of the liner shape and material on the grinding process and wear in a rotary mill [151–153, 155]. Hence, especially, the influence of the design of the liners and lifters, charge and discharge openings on radial motion processes are a common research subject [65, 119, 139, 206]. Consequently, it is possible to predict wear due to the particle-liner interaction intensity [223] and estimate the influence of worn liners on the process and improve the liner design [15].

On the other side, the simulations can be used to estimate the strain of the dynamic mill charge on the mill body in order to improve the dimensioning process from the manufacturers point of view [116]. Other publications, however, concentrate on energy consumption estimations [29, 128, 219]. For ball mill operations, axial transport phenomena are of additional interest as they are determinant for segregation effects of grinding media and material along the mill [27].

Motion effects in stirred media mills. Stirred media mills are comparable to the tumbling mills with regard to the difficulty to measure grinding media dynamics inside the process room. Hence, DEM simulations focused on grinding media motion are an important tool to improve the understanding of the process dynamics [86–89, 188, 225]. But also the energy consumption [128, 187], the influence of the media shape on the grinding performance [190], and the prediction of wear are points of interest [30, 90].

Motion effects in other comminution machines. Although the majority of these studies focus on the analysis of motion processes in machines with freely movable grinding media, this approach can also be used to analyze other comminution processes. An example may be GLADKY [61]. There, this approach is used to examine the diverse parameters that can influence the process in a real High Pressure Grinding Rolls (HPGR). Due to the complexity of the particle bed comminution in this process, only the particle motion is simulated. However, as this is a serious limitation for such processes, this is usually only done for niche applications. BARRIOS and TAVARES [10] trie to overcome this by adding particle breakage to an otherwise comparable HPGR model. Despite this improvement, the also focus on motion processes, throughput, energy demand and roller forces.

Simulations focused explicitly on the particle breakage

The DEM is also a suitable tool if the real breakage of material and particles in grinding processes is in the focus. Contrary to the approach to characterize the comminution process indirectly by using the stress rates obtained by evaluating the dynamics of grinding media, it is possible to directly model interparticle breakage within DEM simulations. Therefore, the grinding material itself has to be simulated. The basis for such simulations is in many cases a Bonded Particle Model (BPM).

Bonded Particle Models. Bonded Particle Models are an approach, the basic idea of which was formed by MEGURO and HAKUNO [121]. They modified existing models by introducing additional springs, which simulate bondings between the elements (Figure 2.13a). Supported by the rapidly growing computer capabilities, this approach was picked up by POTYONDY; CUNDALL, and LEE [150] and POTYONDY and CUNDALL [149], who formed the presently used idea of a BPM.

Using such BPM based simulations allows modeling the behavior of real rock as a compound of cemented discrete elements, as shown exemplary in Figure 2.14. In general, this compound can be both deformable and breakable, but it has to be at least breakable in order to use it for explicit breakage modeling. Due to the universal character of this method, many other physical characteristics like viscous behavior, agglomeration, or plastic deformation can

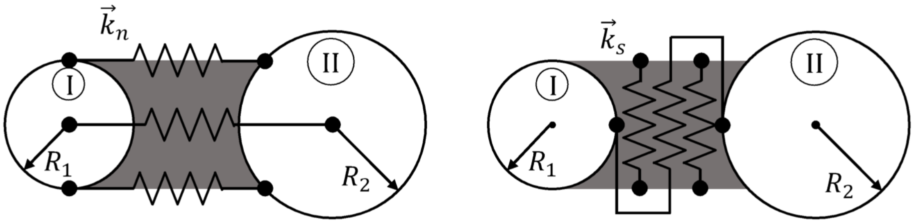

(**a**) normal bonding (**b**) tangential bonding

Fig. 2.13: Simple normal and tangential bonding of two discrete elements via springs. Modified from [24].

be modeled as well. This diversity is achieved by the adaptability of the specific bonding and interaction models. Hence, BPM is a popular way to simulate comminution processes of minerals.

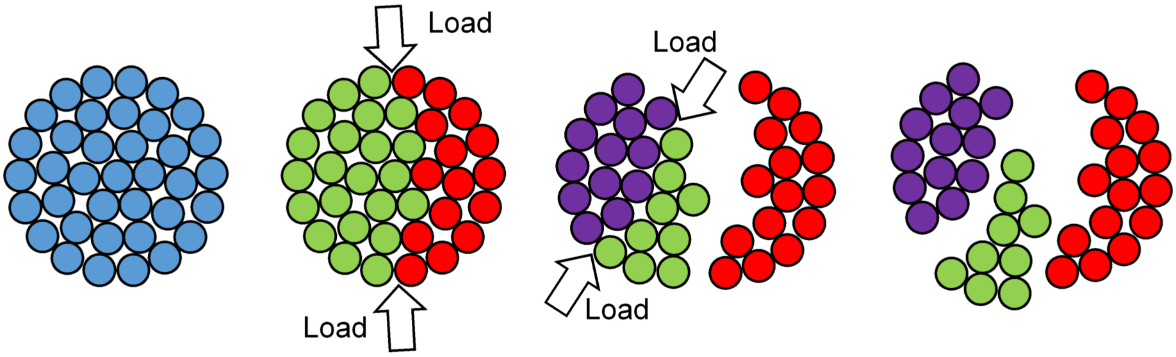

Fig. 2.14: Schematic example of a BPM model: The intact parent particle consisting of bonded sub-particles (left); The parent particle breaks into two fragments due an arbitrary external load (middle-left); The left progeny particle breaks due a second arbitrary external load (middle-right); Three progeny particles resulting from the two breakage events (right)

Tan; Yang, and Sheng [201] published a noticeable study on machining processes of polycrystalline ceramic SiC using BPM. In this case modeling is simplified, as the structure of SiC is comparatively homogeneous. The simulation of natural rock – usually an aggregate of several minerals with different size, shape and spatial distribution – is more challenging. In order to take the influence of structure and texture of mineral microstructures into account, more sophisticated approaches are required [24, 149, 157]. There are different ways to implement the actual grain structure. Possible solutions are the definition of clustered or clumped particles, which mimic the microstructure by merging closely spaced discrete elements to groups with specific properties. Other authors like Groh et al. [67] use non-spherical discrete elements in order to further improve the model significance.

The advantage of BPM simulations, which are used to simulate breakage behavior of mineral particles, is the ability to model fracture propagation and stress-strain behavior explicitly. Furthermore, it is possible to control the physical behavior of the fracturing process only via the physics of the bonding model. Hence, it is possible to achieve a realistic fracture behavior by using a realistic bonding model with appropriate parameters. This is an important point for the ability to use a model for the purpose of prediction. However, this approach presupposes that all particles that are potential breakage candidates do consist of enough bonded sub-particles, which can form the progeny particles after breakage. The resolution of the sub-particles has to be high enough to allow the formation of realistically shaped breakage fragments.

Unfortunately, the computational complexity of such DEM simulations correlates linearly with the number of particles involved. However, despite this, the particle contacts are also important for the computation. In contrast to the handling of the actual particles, the calculation complexity for handling contacts is in the worst case quadratic [160, 171, 191]. For this reason, the overall complexity of a DEM] calculation cycle depends mainly on how often particle contacts occur and how disordered they are. For this reason, under unfavorable conditions, such as dense packings with high dynamics, it is possible that algorithms with non-linear complexities dominate the computation time. Therefore, there must always be a trade-off between a sufficiently high resolution for the sub-particles and economic computational costs for simulating the process of interest. For the simulation of comminution processes on industrial scales this often leads to impractically high computation times, which usually makes this approach unusable for these cases. In order to overcome this limitation, other simulation strategies such as the Particle Replacement Model (PRM) have been developed.

Particle Replacement Models. The interesting point about PRM based simulations is that they work without the need to model every particle that is a potential breakage candidate as a composite of sub-particles. This approach was introduced by CLEARY [26], who wanted to overcome the problem of enormous computation time for BPM based industrial scale simulations of comminution problems.

In contrast to BPM, PRM based simulations handle all particles with their initial size and shape until the conditions are reached, where particles should fracture (Figure 2.15). If this happens, the fracturing parent particle is replaced with an appropriate assembly of progeny particles, which represent the fragments that should be formed by the fracture process. These are placed in the space that was originally occupied by the breaking particle. Consequentially, this approach does not waste computation power for sub-particles that are not involved in breakage processes.

The generation of sub-particles on demand significantly decreases the computation cost, making it attractive for simulations of industrial scale processes. Therefore, it is necessary to predefine what the breaking conditions are and how the parent particle should break. This includes at least the size distribution and the packing of the progeny particles, as well as the kinetic energy applied to them after the replacement. It is obvious that the physics and mineral microstructure, which are causal for the actual crack propagation and thereby for the fracturing process, have to be abstracted into those predefined fracture conditions. Hence, this approach can be suitable to analyze breakage processes at particle level where the process behavior of whole comminution machinery like tumbling mills [26, 76] or crushers [32,

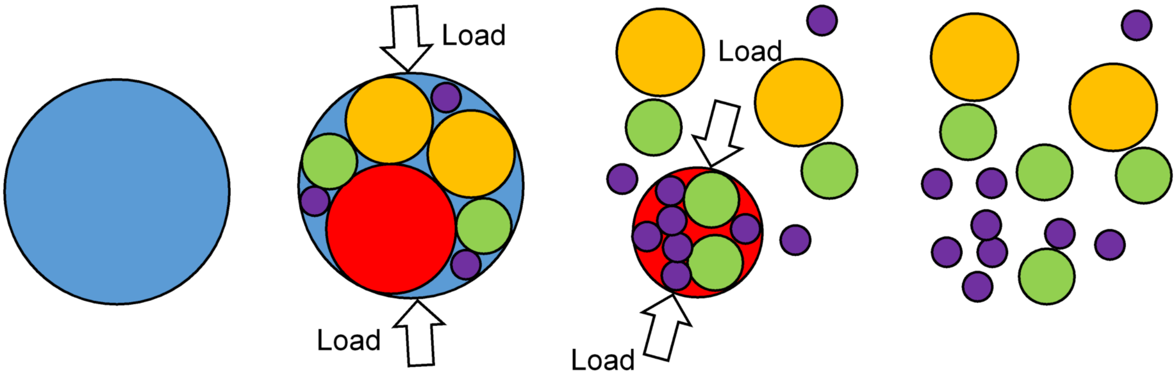

Fig. 2.15: Schematic example of a PRM model: The intact parent particle (left); The parent particle breaks due to external load and is replaced by a packing of progeny particles (middle-left); A progeny particle breaks due to external load and is replaced by a packing of progeny particles (middle-right); The progeny particles resulting the two breakage events (right)

41, 42, 157, 175, 189] is in focus. On the other side, PRM based simulations are not suitable if the actual crack propagation and fracturing itself is in focus.

A further problem of this approach lies the replacement process itself. As only the space formerly occupied by the broken parent particle can be used for the replacement process, there has to be an efficient packing strategy in use for the instantaneously created progeny particles. This packing algorithm has to fill the volume with a packing that fits the predefined size distribution of the progeny particles. In order to ensure the volume consistency, the replacement process theoretically has to fill every void with a progeny particle or allow overlapping of progeny particles. For spherical particles without overlapping this results in Apollonian packings. As the fractal character of those packings would cause a generation of an infinite number of infinite small progeny particles, the practical realization with DEM always includes that the packing is scalped at a predefined progeny size. In conclusion, this results in volume loss during the replacement process. A deduced approach that does not have the problem of volume losses during the replacement process of spherical parent particles is the Fast-Breakage Model (FBM) [91].

2.1.3 Limitations of DEM in comminution science

Despite those notable improvements, the use of DEM and BPM still presents some challenges that need to be considered. The most evident four have already been summarized in short by KLICHOWICZ and LIEBERWIRTH [96]. Since they are of particular interest to this study, they will first be briefly listed again and then explained in more detail below.

- Very detailed models with high numbers of discrete elements need extensive calculation capacities. Hence, the computing time may be out of scale.

- Due to the early stage of research at this area, the physical parameters of the models like the spring and damper constants are often not reliably predictable. For this reason, the physical relations have to be adjusted manually in order to fit the simulative fracturing behavior to the behavior observed in experiments.

- The predictive capability of DEM for mineral processing is strictly dependent on the correctness of the models and assumptions used. The validation of the underlying laws, the DEM code and interrelationships is sometimes difficult but crucial for every application [220, 224].

- In order to improve the simulation results of models with typical minerals, their microstructure has to be incorporated realistically. Mapping those structures into the models is challenging because of the diversity of possible mineral structures and the problems in the recognition and quantitative description of these spatial structures.

Limitations due to computing power. The limitation of model complexity due to limited computational capacities is a restriction for nearly every application of computer simulations. Nevertheless, the steady evolution of computing systems successively allows the handling of more calculation intensive models. This development is correlated to Moore's Law, which seems still to be valid [127]. The impact of mineral processing engineers on this development is quite limited, though. However, the programming code of proven models can be optimized for fast or parallel computing or ported to faster programming languages.

Furthermore, currently there are efforts to use the Graphics Processing Unit (GPU) of desktop computers to carry out the computing of DEM simulations. Due to the architecture of the GPU, it can handle simple, similar tasks much faster than a Central Processing Unit (CPU), since it is optimized for parallel computation of millions of pixels simultaneously [62–66]. However, GPU based DEM simulations are still in the prototype stage, as they are limited to specific hardware settings and current software is neither commercially available nor distributed under open access licenses. Furthermore, to the authors' knowledge it is not yet possible to simulate breakage processes.

Challenging parametrization and validation of the models. Both, the problem of finding adequate physical parameters for the models and validating the same may be treated in combination. Many efforts are focused on providing better internal parameters for the DEM to improve the model accuracy. In order to evaluate the quality of the resulting improvements, the same have to be validated in comparison with reality. It follows that this interplay should be seen as automatism. The quality of model validation has to match the intended model precision.

This may be illustrated with the help of an example: Let us suppose, that we want to describe a random problem with a simple empirical model. This model consists essentially of an equation with several independent variables. The goal is, that our model works accurately to three decimal places. In order to be able to guarantee this, we must also validate our equation with this precision. Hence, all input variables have to be of this resolution for the validation.

Although this demand sounds self-evident, this criterion is very often hard to reach. At this stage, open source DEM projects probably have an advantage, because everyone can check improvements and the correctness of the underlying DEM code.

Missing realism of the microstructure models. Compared to the progress of the models, DEM codes, and validation procedures, little work was spent on the implementation of grain structures, which are close to reality. Existing approaches are often based on one-to-one reproductions of example structures as done by TAN; KONIETZKY, and CHEN [200]. Irrespective of the type of example, which can be a photo of a thin section or tomography image, this approach is relatively inflexible as it is impossible to create randomized synthetic microstructures for simulations. Furthermore, these approaches have problems with the recognition of boundaries between grains of the same phase. This results in semi-realistic models as it is extremely challenging to map clusters of grains of the same mineral constituent to the simulation.

A possibility to overcome these problems is to use a stochastic equivalent approach as used by LI; KONIETZKY, and FRÜHWIRT [107]. In order to generate complex grain shapes the so-called clumped particle logic is used. Based on thin sections or tomography analysis of real mineral microstructures, first an appropriate microstructure based on spheres is created. Following, this is transferred to the Voronoi-body-based DEM environment, with remarkable results.

However, it seems hard to use this technique for more complex mineral microstructures. This is because the way of generating the statistical data and creating the resulting synthetic microstructure seems to be customized for the isotropic, mono-mineral microstructures like the sand stone analyzed by LI; KONIETZKY, and FRÜHWIRT [107].

Nevertheless, the missing realism of the microstructure models for DEM poses an interesting field of application for the so-called Quantitative Microstructural Analysis (QMA). With the help of this method it seems possible to overcome the explained shortcomings of mineral microstructure modeling. Therefore, the QMA is explained in detail in the following section.

2.2 Quantitative Microstructural Analysis

As discussed in Section 1.2, different approaches are possible to make realistic mineral microstructures usable in simulations. Based on these preliminary considerations, the modeling of mathematical models on the basis of a mineralogical analysis is considered to be the most promising. However, contrary to the typical engineering approach, traditional mineralogical analyzing methods describe the texture and structure of rock material mainly verbal. This classical approach is subjected to a certain subjectivity, because of the diversity and variety of ways to describe something verbally. The big range of possible descriptions in combination with floating boundaries between the used gradations makes it difficult to further use this information in an abstract way for numerical methods like DEM. To counteract this problem, the so-called Quantitative Microstructural Analysis was developed at the Institute of Mineral Processing Machines.

2.2.1 Fundamentals of the Quantitative Microstructural Analysis

The Quantitative Microstructural Analysis is an approach for characterizing the microstructure of minerals using mathematical petrographic methods. This method was developed by UNLAND and RAAZ [210] and validated by POPOV [146] in order to overcome the problems of classical mineralogical petrographic rock characterization. Particularly, the restriction to mostly verbal descriptions of microstructures possesses problems when it comes to mineral processing. In order to be useful for mineral processing and mechanical engineering, the rock properties deduced from mineral microstructure analysis have to be available in a quantitative and statistically reliable format instead. The QMA overcomes the shortages of previous attempts [4, 16, 138, 222], which are either found to be insufficient for characterizing an anisotropic spatial fabric, or which are too abstract for deducing reliable correlations for the properties of the fabric.

The potential of such a method, with which mineral structures can be characterized at grain size level, can be assessed from the tendency towards "grain engineering" in processing technology. Especially the last comminution step is often the crucial one. This step, however, normally requires the highest specific energy to grind the material, whereby the actual particle size reduction has usually to be accurate to a few micrometers. This is because, on the one hand, the setting of the final grinding step must ensure the maximum degree of mineral liberation, and on the other hand, overgrinding of the material must be prevented as well. Both can significantly reduce the process efficiency and material recovery. In order to allow such a detailed setup and the assessment on its effects on the subsequent processes to extract the actual ore minerals, it is mandatory to have a detailed understanding of the mineral microstructure. At this point, the quantitative microstructure analysis at grain size level can be a powerful tool.

The basis for the mathematical analysis are the methods of quantitative fabric analysis, which were in most cases developed as a tool for material science and applied there successfully for several decades. The theoretical principles of the so called stereology were first densely summarized in the textbook for metallography by SALTYKOV [170]. In general, quantitative fabric analysis is a collective term for a large number of different methods, used for the investigation of the geometry of structural constituents.

For petrographic applications the aim of these techniques is to find correlations between the structural composition and the properties of the rock or the conditions for the origin of the rock in most of the cases. By now, the quantitative fabric analysis is already seen as an independent scientific field [146]. That can be explained by the increasing importance of these methods for different fields of application like petrography, mineralogy, metallography, building material science etc., as well as the development of theoretical and practical basics like stochastic geometry and digital image analysis.

In detail, the QMA is based on the microscopic analysis of thin and polished sections of mineral rock samples. It uses the findings and methods of the stereology in order to capture the complexity of a given mineral fabric. This approach shall allow the assessment of the influence of the mineral microstructure on mineral processing. In order to do so for a spatial mineral microstructure, three orthogonal thin or polished sections of a representative rock sample have to be prepared as shown in Figure 2.16.

The Measuring methods

In general, performing a QMA is independent from the method, which is used to access the microstructure. However, due to the different limitations and side conditions of other methods (see Section 1.2), the polarization microscopy is still the most used measuring method.

Polarization microscopy. Using polarization microscopy is the quasi-standard for doing a QMA on mineral microstructures [54, 73, 146–148, 210]. It is done with a polarized light microscope, which is well established for mineralogical purposes [104, 141]. The reason for the ongoing usage of this relatively old method has two major aspects.

On one side, there is the historical reason. As the microscopy is an important and often used part of stereology and mineralogy, it is obvious that the QMA uses microscopy as basis, since it is the combination of both fields of research. On the other side, there is also a practical reason. Until now polarized light microscopy is a method that allows a very high degree of detail at distinguishing between the different microstructural components with a comparably easy to handle instrument and moderate effort for sample preparation.

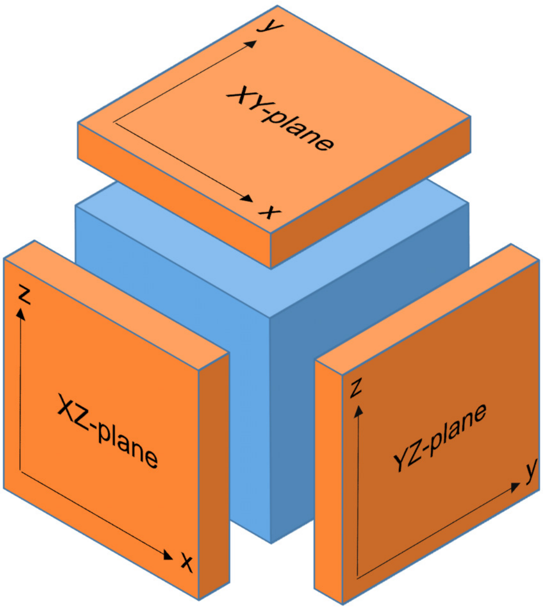

Fig. 2.16: Schematic representation of a representative rock sample (blue) and its three orthogonal slices (orange) as prepared for the QMA - Modified from [146].

There are of course numerous other comparable methods, which, however, have not been established for QMA yet. An example for this are the methods of automated mineralogy, which are indeed able to identify different microstructural constituents. Probably the most popular example for this is the so-called Mineral Liberation Analysis, which is based on X-ray spectroscopy [51, 92, 108] and the analysis of the back-scattered electrons. As explained in Section 1.2, the main disadvantage of this method is that it is not possible to distinguish neighboring grains of the same phase. Furthermore, the investment and operational costs of these analysis technique are significantly higher than for polarized light microscopy.

This can be overcome, for example, by more advanced measuring setups, where the measured diffraction of X-ray fluorescence mapping is used to distinguish between different grains [132, 133]. Another example of overcoming this limitation may be the use of electron backscatter diffraction [9, 74, 161]. However, all these approaches have not prevailed, because they are much more elaborative than microscopy for comparable results.

The measuring procedure

At first, the three orthogonal sections are analyzed separately using polarization microscopy. The size of the area that is used for evaluation basically depends on the size of the grains. On the one hand, the evaluated area has to contain as many grains as possible to ensure the statistical reliability of the analysis. On the other hand, the amount of grains per image section and the total number of image sections to be analyzed has to be manageable for the operator.

In consequence, the magnification is usually set to a value that ensures that the image sections of the microscope contain about 10 to 20 grains, which is the optimum for the operator. For reasons of representativeness this is repeated with about 25 uniformly distributed image sections using a raster plan of the thin or polished section (Figure 2.17). The results of the analyzed 25 independent image sections are summed up and used in combination for further evaluation [146].

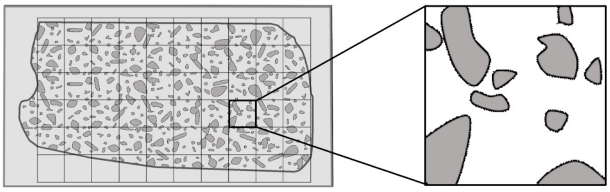

Fig. 2.17: Schema of a rasterized thin section with a corresponding image section for the point, line and area analysis

In detail, the analytic process of the QMA consists of measurements conducted in areal measurement fields, line and point grids (Figure 2.18). This is done with every image section for all three orthogonal thin or polished sections.

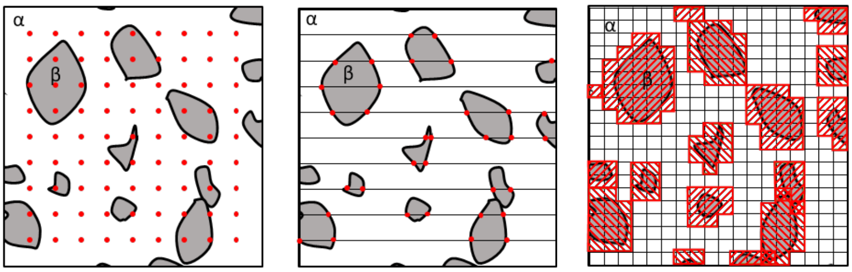

(a) Point analysis **(b)** Line analysis **(c)** Area analysis

Fig. 2.18: Schematic representation of the three analysis methods of the QMA. The exemplary microstructure consists of NDP (α) and a crystalline phase (β) (Modified from [146])

Point analysis is used to determine the volume percentage of the microstructure components. Therefore, a point grid is evaluated and the points belonging to the different components P_P are counted. Usually, QMA differentiates individual minerals as well as flaws (e.g. pores and cracks), which are filled with gases or liquids. Besides, glasses, micro-, and cryptocrystalline masses are consolidated into a Non-Differentiated Phase.

In contrast, a grid of parallel lines is needed to measure chord lengths of mineral grains as well as to count intersection points between the different phases. Eventually, the area of the cut faces of the single minerals of different phases is measured in order to calculate the area distributions. Due to the multiplicity of possible shapes of the grains, the single areas are measured by planimetry.

The evaluation of point, line, and area analysis

Although the results of all analysis methods are used in combination to calculate the characteristic numbers for the mineral microstructure, the point, line, and area analysis are evaluated separately in the first instance.

The evaluation of the point analysis. In case of the point analysis, the evaluation basically forms a counting process. Thereby, it is counted how many points of the raster belong to the different phases, pores and NDP. This results in histograms with the proportion of points belonging to the different microstructural components as shown in Figure 2.19.

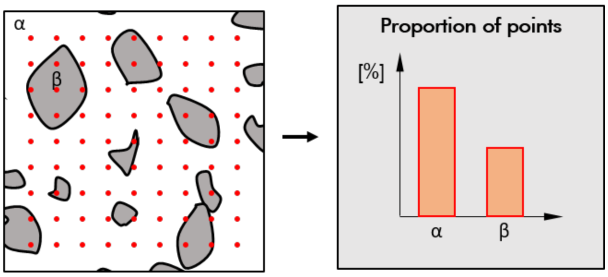

Fig. 2.19: Schematic representation of the point analysis and the corresponding histogram with the proportion of points belonging to phase α and phase β

The evaluation of the line analysis. In order to quantify the directionality of the microstructure within a plane, the line analysis is conducted under different angles. In the example in Figure 2.20 the analysis lines for 0°, 45°, 90°, and 135° are shown. The number of intersections per line is subsequently plotted in a polar plot. As this type of analysis is point symmetric, the results for the 3rd and 4th quadrant can be copied from the corresponding values of the 1st and 2nd quadrant.

Following, these results are approximated by a two-dimensional rose of intersections. Additionally, the number of intersections between grains of different phases is calculated for further evaluation. This data can be visualized with a matrix of interfaces. This matrix then shows the frequency with which grains of specific phases adjoin each other.

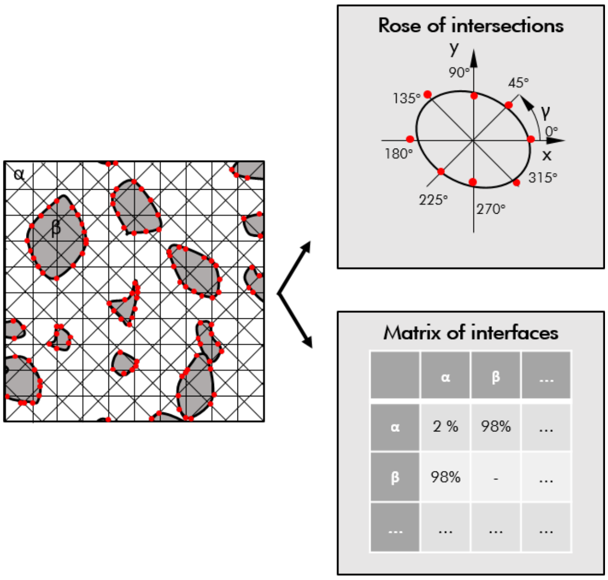

	α	β	...
α	2 %	98%	...
β	98%	-	...
...	...	...	...

Fig. 2.20: Schematic representation of the line analysis and the corresponding polar plot with the rose of intersections and the matrix of interfaces

The evaluation of the area analysis. The planimetry process of the area analysis is exemplarily shown in Figure 2.21. As the area occupied by every grain is measured, the distribution of the cut surfaces of the grains can be calculated. For the manual processing it has proven to be useful to use statistical data binning for further processing.

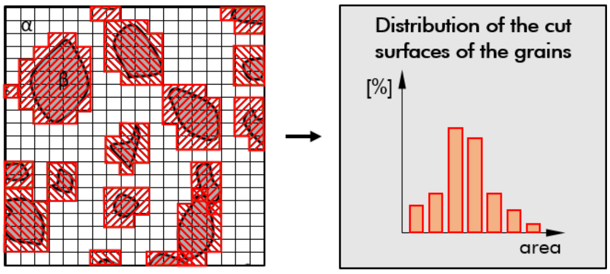

Fig. 2.21: Schematic representation of the area analysis and the corresponding histogram with the distribution of the cut surfaces of the grains

Since the grain size distribution can be approximated by a log-normal distribution in many cases [50, 146, 170], the distribution and size of the bins is often based on log-normal distributions as well. In contrast to a linear division, this approach has the advantage that the filling of the bins is more evenly distributed. Hence, an under or over occupation of the bins for the small or big grains can be avoided.

Combination of the planar measurement results to spatial models

Subsequently, the measured parameters of the three orthogonal sections are combined, which is an important step for the evaluation. The combination of the data of the three orthogonal slices allows to derive spatial information from the otherwise two-dimensional measuring fields. In a first step this data is used to calculate a three-dimensional model, and in a second step the model acts as basis for calculating the characteristic numbers for the mineral microstructure (Figure 2.26).

Spatial combination of the results of the orthogonal point analyzes. The combination of the data of the point analysis is a straightforward averaging process. Since the three orthogonal slices have to be made of a representative sample of the material of interest, it can be assumed that the combined proportion of the points of the orthogonal planes is representative for the starting material as well. Hence, the proportion of points in the volume is calculated as arithmetic mean from proportions of the three slices as shown in Figure 2.22.

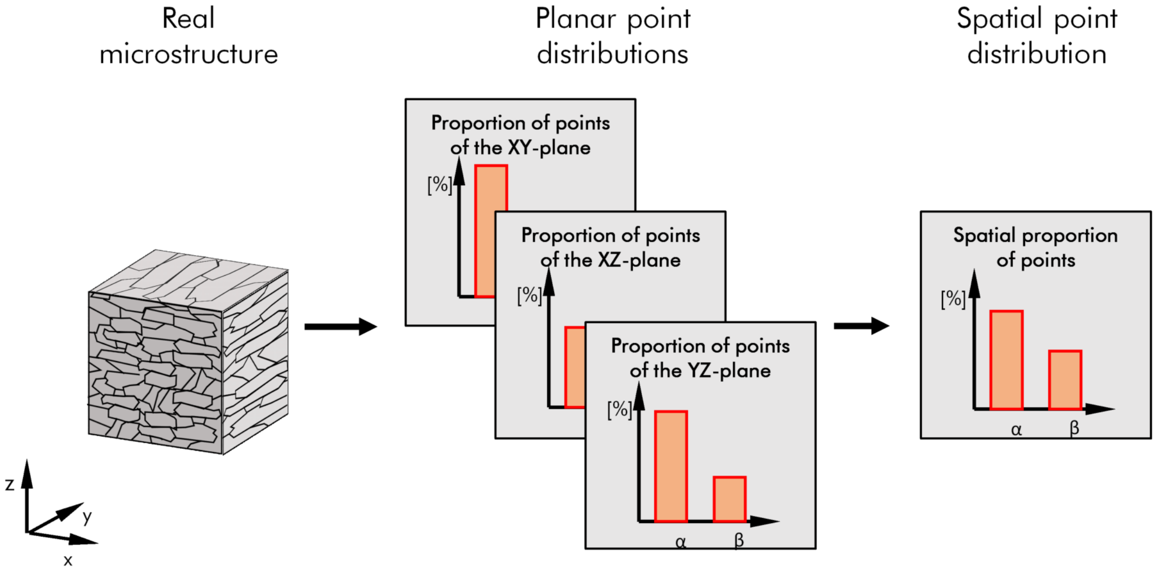

Fig. 2.22: Schematic representation of the spatial combination of the results of the point analyzes

Spatial combination of the results of the orthogonal line analyzes. The generation of a spatial matrix of interfaces is comparable to the above explained generation of the spatial point distribution. Again, the spatial results are calculated as average from the planar matrices, as it is assumed that the three orthogonal planes are representative for the whole real microstructure.

In contrast to this, combining the planar roses of intersections is rather different. As the line analysis does not provide one integral result for directionality of the intersections, but different results for the different analysis angles, generating a spatial model cannot be done by averaging. Instead, the three two-dimensional roses of intersections are combined to a spatial rose of intersections (Figure 2.23).

This three-dimensional rose of intersections serves as basis for further evaluation and can be calculated for every individual phase as well as for all microbodies together. Therefore,

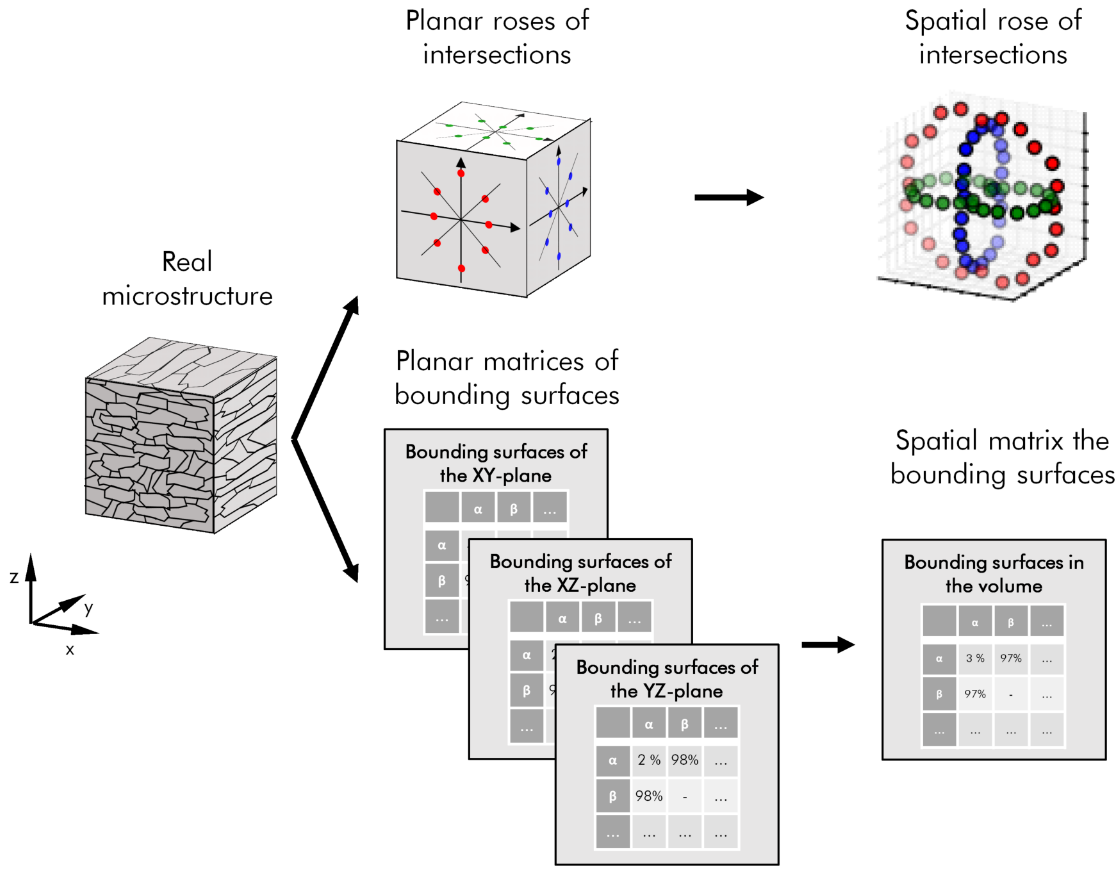

Bounding surfaces of the YZ-plane

	α	β	...
α	2 %	98%	...
β	98%	-	...
...	...	...	...

Bounding surfaces in the volume

	α	β	...
α	3 %	97%	...
β	97%	-	...
...	...	...	...

Fig. 2.23: Schematic representation of the spatial combination of the results of the line analysis

it is assumed that this spatial figure can be approximated by a superposition of the three elementary boundary systems.

Exemplarily, Figure 2.24 shows the elementary surface boundary systems, as well as their corresponding planar and spatial roses of intersection. Additionally, an example for a superposition of the three elementary boundaries is shown as well.

Ideal orientated spatial microstructures. For isotropic orientated systems the line analysis shows no preferred direction. In consequence, this type of microstructure is characterized by a circular rose of intersections in the polar plot, which results in a spherical spatial rose of intersections (Equation 2.4).

In contrast, ideally linear orientated microstructures do have only one plane in which the structure shows no preferred orientation. The two other orthogonal planes do have a very high directionality, which is indicated by the double circle in the polar plot with a point of tangency in the origin. The superposition of these three planar roses of intersections is a torus shaped spatial rose of intersections (Equation 2.5).

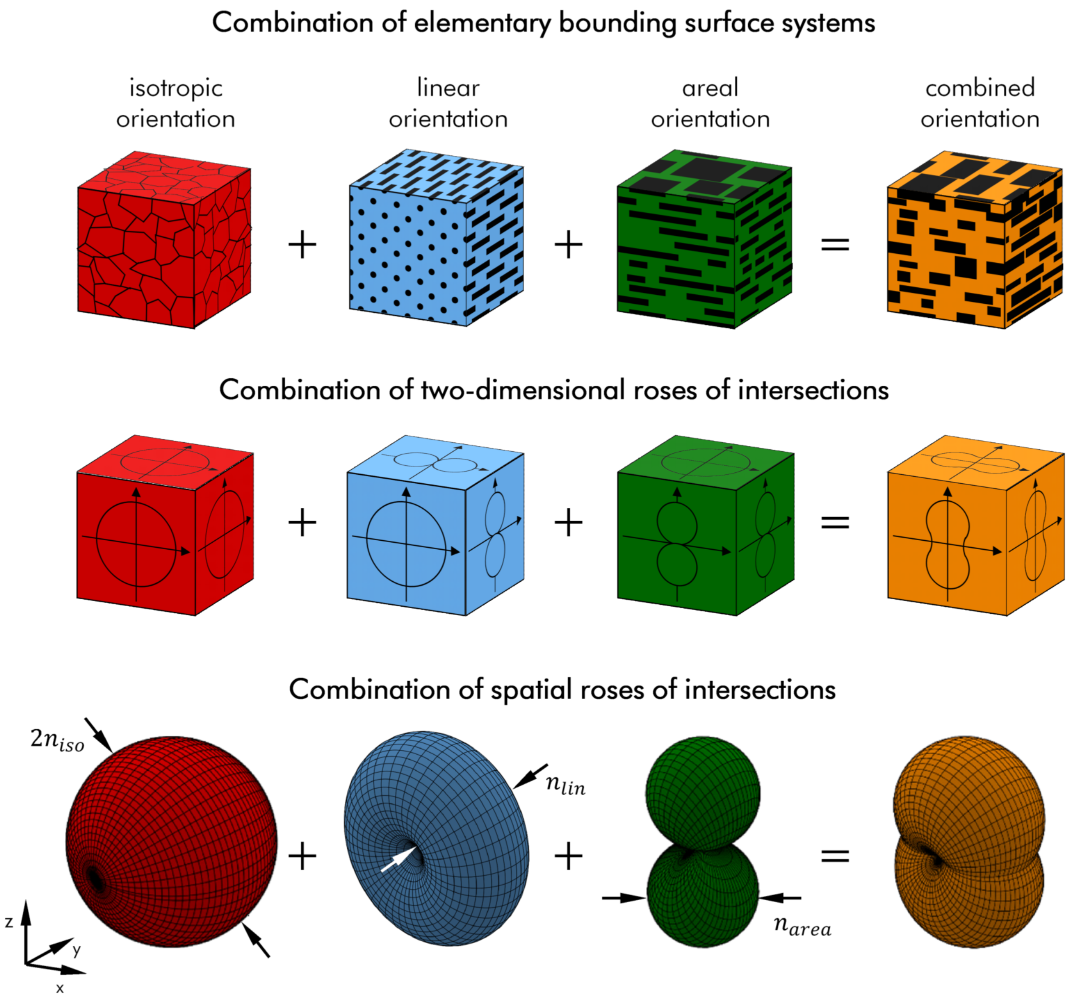

Fig. 2.24: Superposition of elementary surface boundary systems, the measured two-dimensional roses of intersections and the spatial roses of intersections (Modified from [146])

Areal orientated systems do have comparable results in the line analysis. The difference lies in the orientation of the directional, double circled roses of intersections. These are rotated 90 degrees in contrast to the polar plots of a linear orientated microstructure. The resulting spatial rose of intersections is a double spherical object, which again has its point of tangency at the origin (Equation 2.6).

Isotropic orientated microstructure:

$$x^2 + y^2 + z^2 = n_{iso}\sqrt{x^2 + y^2 + z^2} \tag{2.4}$$

Linear orientated microstructure:

$$x^2 + y^2 + z^2 = n_{lin}\sqrt{y^2 + z^2} \tag{2.5}$$

Areal orientated microstructure:

$$x^2 + y^2 + z^2 = n_{pla}\sqrt{z^2} \tag{2.6}$$

The orientation of the real spatial microstructure and the formulation of the ellipsoidal unit microbody. Real microstructures are very seldom ideally isotropic, ideally linear or ideally areal orientated systems. As explained above, the QMA assumes that the real mineral microstructure can be seen as superposition of the three elementary boundary systems with different parameter values, as shown at the orange example in Figure 2.24.

Hence, the two-dimensional roses of intersections of those systems are superpositions as well, which results in a smooth transition between a circular and a double circular shape. The spatial shape of the corresponding rose of intersections can then be seen as superposition of a sphere, a torus, and a double sphere. Hence, the equation for the combined spatial rose of intersections is formed as sum of the equations of the elementary bounding surface systems (Equation 2.7).

Combined orientated microstructure:

$$x^2 + y^2 + z^2 = n_{iso}\sqrt{x^2 + y^2 + z^2} + n_{lin}\sqrt{y^2 + z^2} + n_{pla}\sqrt{z^2} \tag{2.7}$$

The approximated three-dimensional rose of intersections is further used to calculate the shape of a unit microbody [210]. Therefore, it is assumed that all grains of the specific phase of interest have the same orientation and shape. Considering the volumetric proportion ϵ_V of the phase of interest, it is possible to calculate an average ellipsoidal shaped grain that satisfies the constraints given by the spatial rose of intersection (Equation 2.8). This unit ellipsoid, which is shown in Figure 2.25, is defined by its principal semi-axes a, b, and c (Equations 2.9 to 2.11).

$$\epsilon_V = \frac{2}{3}n_{iso}\sqrt{x^2 + y^2 + z^2} + \frac{\pi}{4}n_{lin}\sqrt{y^2 + z^2} + n_{pla}\sqrt{z^2} \tag{2.8}$$

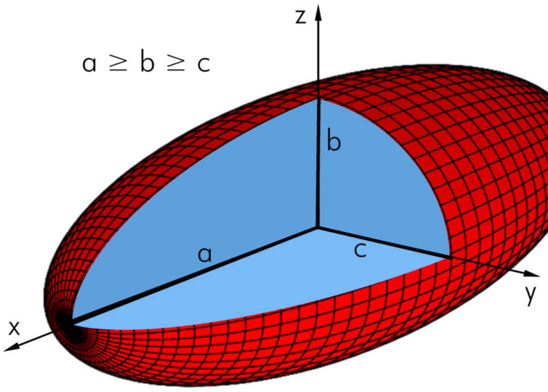

Fig. 2.25: Model for the grain shape: Ellipsoidal unit microbody with its principal semi-axes a, b, and c (Modified from [146])

$$a = \frac{3\epsilon_V}{2n_{is}} \tag{2.9}$$

$$b = \frac{\epsilon_V}{\frac{2}{3}n_{iso} + \frac{\pi}{4}n_{lin}} \tag{2.10}$$

$$c = \frac{\epsilon_V}{\frac{2}{3}n_{iso} + \frac{\pi}{4}n_{lin} + n_{pla}} \tag{2.11}$$

Spatial combination of the results of the orthogonal area analyzes. Combining the results of the planar area analysis to a three-dimensional set of data, again, is principally a straight forward averaging process. As for the spatial matrix of interfaces and for the point analysis, this approach gives satisfactory results as long as the three orthogonal planes are representative for the whole material of interest.

However, the results of the planar area analysis, which are the distributions of cut surfaces of the grains in the orthogonal planes, have to be transferred to a volumetric equivalent. A suitable spatial target value is the distribution of grain sizes in the volume, for example. For calculating this value, a stereological transformation has to be used, which is outlined together with the definition of the grain size parameter in the following section.

The Results of the QMA

The results of a QMA, which are shown in Figure 2.26, can be classified into parameters describing the mode and parameters describing the fabric (Table 2.1). The mode of a microstructure contains the type and the volume percentage of a phase in general. The fabric may be subdivided into texture and structure. Though textural characteristics refer to single

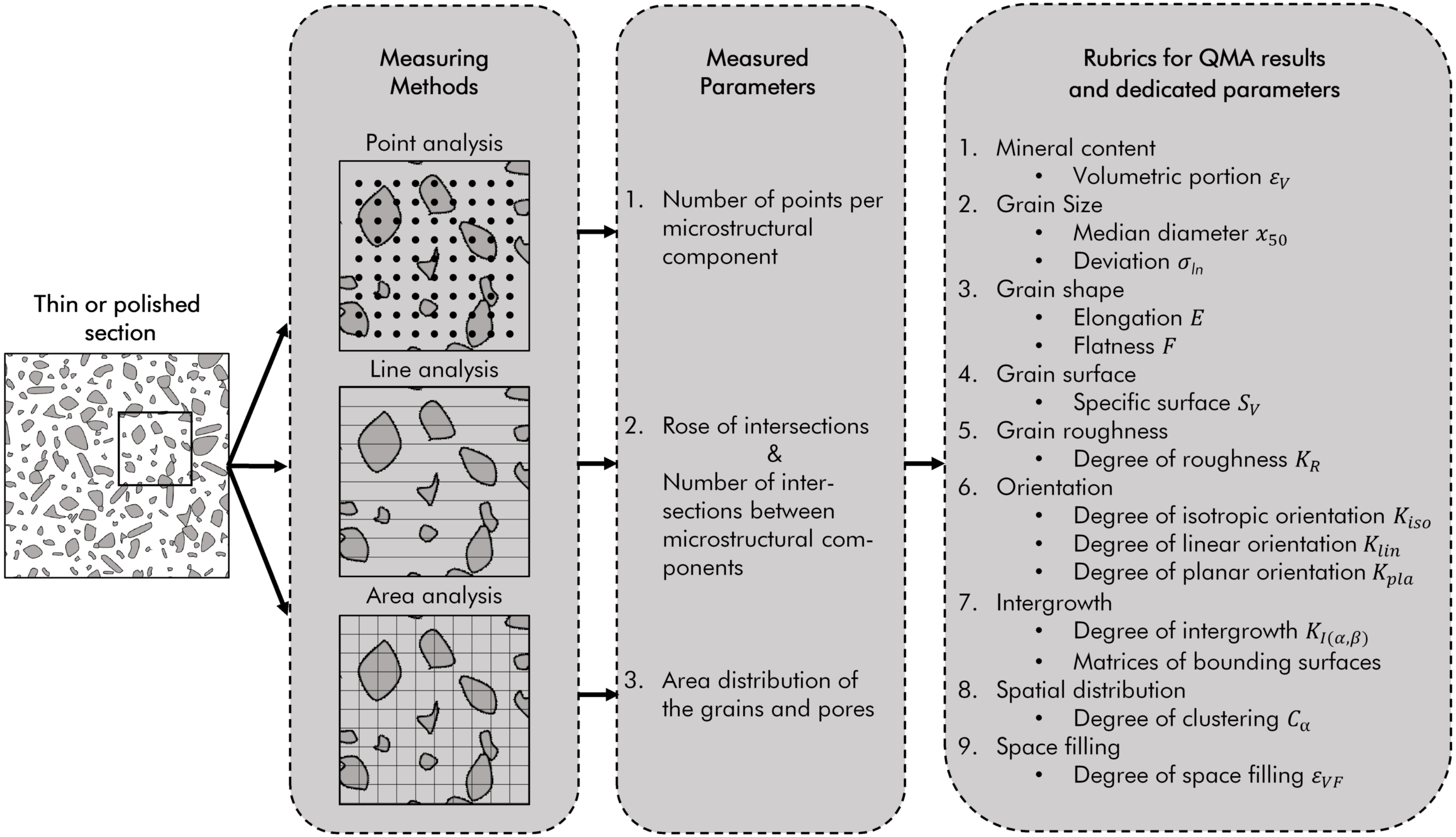

Fig. 2.26: Procedure of analyzing a thin section and generating quantitative parameters using QMA

grains, they are described in general. Therefore, parameters that describe the size, surface, shape, and roughness of the grains are calculated for each phase. In contrast, the structure describes the anisotropy of the spatial arrangement of the mineral constituents. For this reason, orientation, spatial distribution, and space filling are characterized as well.

Tab. 2.1: Parameters of the QMA for characterizing the rock properties. Modified from [147]

Raw material		
Mode	Fabric	
Volumetric portion	Texture	Structure
• Mineral phases, rock fragments organic matter, gas and liquid phases • Non-Differentiated Phase (NDP)	• Grain size • Grain shape • Grain surface • Grain roughness	• Orientation • Degree of intergrowth • Spatial distribution • Space filling

The mineral content. Every mineral microstructure component can be characterized first by volumetric proportion, which is the mineral content. This value is calculated directly from the spatial combination of the results of the point analysis. The QMA parameter, which is associated with the mineral content of a particular phase is the volumetric proportion ϵ_V of this phase relative to the total test volume of the sample.

In order to understand how the volumetric portion can be derived from point analysis, a basic relationship of stereology has to be used. Equation 2.12 states that, in a stereological context, the number of points belonging to a specific group of objects per test points P_P is equal to the volume of the same group of objects per unit test volume V_V. Furthermore, it is also equal to the area of these objects per test area A_A, and the length of these objects per unit test line L_L.

$$V_V = A_A = L_L = P_P \tag{2.12}$$

If this general approach is applied to the more specific problem of the QMA, it can be found that the volumetric portion ϵ_V of a certain phase is equal to the general stereological parameter V_V (Equation 2.13).

$$\epsilon_V = V_V \tag{2.13}$$

Furthermore, it can be found that the percentage of points belonging to the phase in relation to the sum of all analyzed points, which is measured during the point analysis is equal to the general stereological parameter P_P. Hence, with the help of Equation 2.12 it can be concluded that the volumetric portion of a specific mineral component ϵ_V is equal to the calculated parameter P_P of the point analysis (Equation 2.14).

$$\epsilon_V = P_P \tag{2.14}$$

The grain size. Based on the results of the area analyses it is possible to approximate the grain size for a specific phase. The general approach is to apply a stereological transformation on the two-dimensional data in order to get the size distribution of the spatial grains.

In detail, the cut surfaces of the grains of all three orthogonal slices are measured first. Additionally, the grain shape is taken into account as well. Therefore, the average grain shape of the phase of interest is approximated by a tri-axial ellipsoid (Figure 2.25). The cut surface distributions of all three orthogonal slices are then corrected using the principal semi-axes of the idealized ellipsoidal model grain.

In the second step, the distributions of the three orthogonal slices are combined and used for a stereological transformation in order to calculate the spatial distribution of the grains. In detail, this approach is based on the calculation of logarithmic diameter distribution of spherical microbodies as supposed by SALTYKOV [170]. Therefore, it is assumed that:

- The spatial distribution of the grains is uniform
- The grains do only differ in their size but have equal shapes
- The grains are randomly orientated in the space

This stereological transformation results in the log-normal probability density function of the spatial frequency distribution of the grain sizes $q_0(x)$ with its median $x_{50,0}$ and standard deviation σ_{ln}. This can be converted into the corresponding volume distribution by calculating the appropriate median $x_{50,3}$ using Equation 2.15 [135, 146], whereupon the dispersion parameter σ_{ln} is the same for both distributions.

$$x_{50,3} = x_{50,0} \cdot e^{3{\sigma_{ln}}^2} \tag{2.15}$$

Finally, the log-normal probability density function of particle size distribution can be described by its median $x_{50,3}$ and the dispersion parameter σ_{ln} as shown in Equation 2.16 [135, 146, 177, 198, 226].

$$q_3(x) = \frac{1}{\sigma_{ln}\sqrt{2\pi}} \cdot \frac{1}{x} e^{-\frac{1}{2}\left(\frac{\ln(x)-\ln(x_{50,3})}{\sigma_{ln}}\right)^2} \tag{2.16}$$

The dispersion parameter of the log-normal distribution σ_{ln}, which should not be confused with the standard deviation of the underlying normal distribution, has no unit and can be calculated by Equation 2.17.

$$\sigma_{ln} = \ln\frac{x_{84}}{x_{50}} = \ln\frac{x_{50}}{x_{16}} = \frac{1}{2}\ln\frac{x_{84}}{x_{16}} \tag{2.17}$$

The grain shape. Another important characteristic of a given grain is its shape. In terms of the QMA, the grain shape is approximated as a tri-ellipsoid with its principal semi-axes a, b and c (Figure 2.25). In order to define an easy to understand measure for the grain shape, it seems useful to utilize the ratio of the principal axes for this purpose. Considering the fact that the principal axes are always ordered by their size $a \geq b \geq c$, the ratio of the axes a and b can be described as the elongation El (Equation 2.18) of the unit ellipsoid, which in turn represents an abstraction of the grain shape. Accordingly, the ratio of the axes b and c can then be described as the flatness Fl (Equation 2.19).

$$El = \frac{a}{b} = \frac{\frac{2}{3}n_{iso} + \frac{\pi}{4}n_{lin}}{\frac{2}{3}n_{iso}} \tag{2.18}$$

$$Fl = \frac{b}{c} = \frac{\frac{2}{3}n_{iso} + \frac{\pi}{4}n_{lin} + n_{pla}}{\frac{2}{3}n_{iso} + \frac{\pi}{4}n_{lin}} \tag{2.19}$$

The real grain surface. In addition to the shape, the surface is also an important parameter that must be taken into account when describing the grain properties. By the means of the QMA the grain surface can be calculated in different approaches. It is noted, that the surface is always seen in relation to the volume of the corresponding grains, which results in the calculation a specific surface. The first approach is based on the fact that the total surface S_V of a stereological system is equal to the sum of its isometric, linear, and planar components (Equation 2.20) [40, 101].

$$S_V = S_{V,iso} + S_{V,lin} + S_{V,pla} \tag{2.20}$$

The elementary components $S_{V,iso}$, $S_{V,lin}$, and $S_{V,pla}$ are principally calculated from the numbers of intersection of the line analysis, which is done with different specific analysis orientations [40]. Due to the fact that the results of the line analysis are already used to calculate the spatial rose of intersections, it is possible to use the radii of the spatial elementary bounding systems n_{iso}, n_{lin}, and n_{pla} directly to calculate the specific surface. Therefore, the radii have to be multiplied with the factors, which take the behavior of elementary isotropic, linear and planar objects during line analysis into account.

$$S_{V,R} = 2n_{iso} + \frac{\pi}{2}n_{lin} + n_{pla} \tag{2.21}$$

This methodology allows to access the grain shape directly and therefore takes complicated shapes, like grains with many bays or a jagged contour into account as well. Hence, the calculated specific surface is called real specific surface $S_{V,R}$.

The ideal grain surface. In contrast, the specific surface can also be calculated from the grain size distribution. Based on the assumption of a log-normal grain size distribution, it is possible to apply the equations originally set up for log-normal particle size distributions (Equation 2.22) [135, 167]:

$$S_V = \frac{6\varphi e^{\frac{\sigma_{ln}}{2}}}{x_{50,3}} \tag{2.22}$$

Hence, the specific surface of a given phase is calculated with the help of its volumetric portion ϵ_V as follows in Equation 2.23.

$$S_{V,I} = \frac{6\epsilon_V \varphi e^{\frac{\sigma_{ln}}{2}}}{x_{50,3}} \tag{2.23}$$

The specific surface, which is calculated with the above-mentioned approach is based on the distribution of ideally shaped microbodies. Therefore, it does not consider the real measured contour of the grains. Hence, it can be interpreted as ideal surface $S_{V,I}$, taking only the ideal grain shape into account. The difference between both calculation approaches is schematically shown in Figure 2.27.

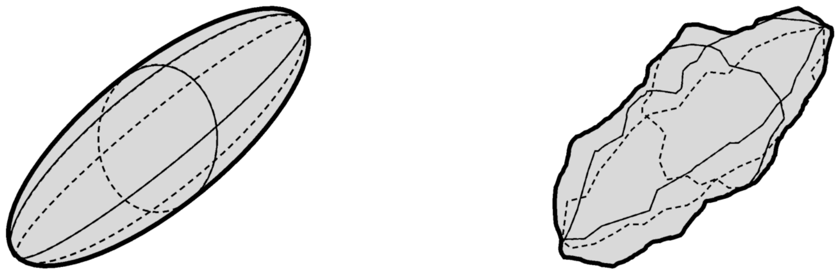
(a) Ideal grain surface $S_{V,I}$ (b) Real grain surface $S_{V,R}$

Fig. 2.27: Schematic representation of the ideal grain surface $S_{V,I}$ in contrast to the real grain surface $S_{V,R}$

The grain roughness. Considering the differences between the real and the ideal grain surface in Figure 2.27, it is further possible to define a grain roughness. For this, the difference of the real specific surface and ideal specific surface of the grains is set in relation to the real specific surface of the grains. Hence, the grain roughness can be calculated according to Equation 2.24.

$$K_R = \frac{S_{V,R} - S_{V,I}}{S_{V,R}} \tag{2.24}$$

Due to the different surface definitions, this parameter can be considered as a measure for the interlocking of the grains.

The grain orientation. As already mentioned, it is possible to classify the orientation of the grains of a given microstructure. The basis for this is the approximated spatial rose of intersections, which can be seen as superposition of the spatial roses of intersections of the three elementary bounding systems. According to the proportions of the individual elementary bounding systems on the combined real bounding system, it is possible to calculate characteristic numbers for the orientation of the microbodies. In detail, there are the degree of isotropic orientation K_{iso}, the degree of linear orientation K_{lin} and the degree of planar orientation K_{pla}.

$$K_{iso} = \frac{2n_{iso}}{2n_{iso} + \frac{\pi}{2}n_{lin} + n_{pla}} \tag{2.25}$$

$$K_{lin} = \frac{\frac{\pi}{4}n_{lin}}{2n_{iso} + \frac{\pi}{2}n_{lin} + n_{pla}} \tag{2.26}$$

$$K_{pla} = \frac{n_{pla}}{2n_{iso} + \frac{\pi}{2}n_{lin} + n_{pla}} \tag{2.27}$$

$$\tag{2.28}$$

The grain intergrowth. A further structure characteristic is the grain intergrowth. In general, it is used to describe the mineral associations within the mineral microstructure. From this the so-called degree of intergrowth $K_{I,(\alpha,\beta)}$ is derived. This parameter characterizes the frequency with which a specific type of grain boundary occurs, for example, between grains of phases α and β (Equation 2.29). Therefore, the specific surface of the interfaces between grains of phase α and grains of phase β, which is called $S_{V,(\alpha\beta)}$, is set in relation to the total specific surface of all interfaces present in the mineral microstructure $S_{V,all}$ (Equation 2.29). Based on this, the degree of intergrowth can also be considered quantifying how many times two particular types of grains border each other in relation to the total amount of grain boundaries.

$$K_{I,(\alpha,\beta)} = \frac{S_{V,(\alpha\beta)}}{S_{V,all}} \tag{2.29}$$

The parameter $S_{V,(\alpha\beta)}$ can be calculated with the means of the line analysis (Equation 2.30). For this, it is necessary to determine the number of intersections $N_{(\alpha,\beta)}$ between the grains of phase α and the grains of phase β on a line of the line analysis first. Furthermore, the distance between two parallel lines of the line analysis d, and the area of the measuring field of the line analysis a_0 has to be determined.

$$S_{V,(\alpha\beta)} = \frac{2 \cdot N_{(\alpha,\beta)} \cdot d}{a_0} \tag{2.30}$$

The specific surface of all interfaces $S_{V,all}$ is calculated as the sum of all specific surfaces of the possible grain pairings within a given mineral microstructure. For example, a mineral microstructure consisting of three different phases α, β, and γ can have six different types of grain boundaries. Three between grains of different phases (α-β, α-γ, and β-γ) and three more between grains of the same phases (α-α, β-β, and γ-γ).

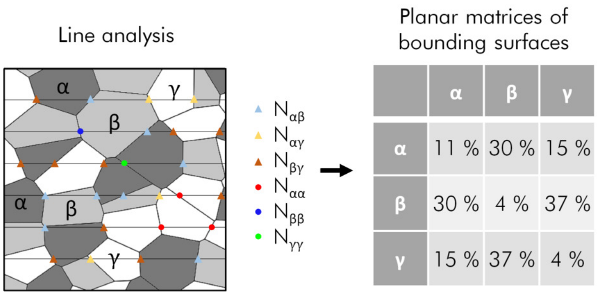

	α	β	γ
α	11 %	30 %	15 %
β	30 %	4 %	37 %
γ	15 %	37 %	4 %

Fig. 2.28: Exemplary line analysis of a mineral microstructure consisting of three different phases α, β, and γ with the six different types of grain boundaries and the corresponding matrix of bounding surfaces

The different possible degrees of intergrowth can then be displayed using the matrix of bounding surfaces, where all possible pairings between different microstructural constituents are incorporated (Figure 2.28).

The spatial distribution of the grains. As explained in Table 2.1, the spatial distribution is also an important structure parameter. In detail, the spatial distribution of the grains of a specific phase α can be described using the degree of clustering C_α, which is sometimes called contiguity [40, 50, 69, 101]. This analysis is done for each phase separately. There it is measured how often grains of the phase of interest α border on grains of the same phase and how often those grains border on other phases. For this reason, all grains belonging to other phases are summarized as grains of phase β.

If phase α tends to form clusters like in Figure 2.29a, significantly high numbers of bordering grains of phase α can be measured. In contrast, if the phase of interest does not form clusters, the number of bordering grains of phase α is insignificant in relation to the specific volumetric proportion of the phase ϵ_V. The specific volumetric proportion is insofar important as it affects the frequency of grains of the same phase bordering each other by random.

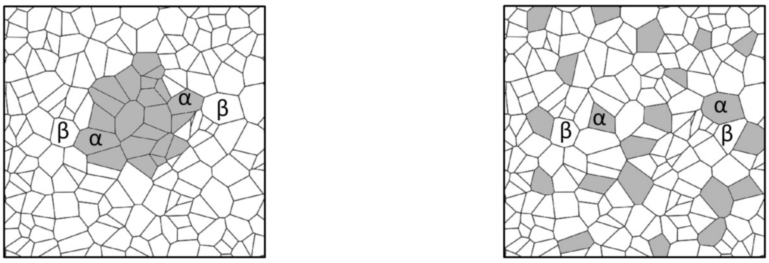

(a) Clustered microstructure $S_{V,I}$

(b) Distributed microstructure $S_{V,R}$

Fig. 2.29: Schematic representation of a clustered and a distributed packing of grains of phase α. All grains belonging to other phases are summarized as β

Assuming a mineral microstructure, where the phase of interest α has a volumetric portion ϵ_V of 90 %, it is natural that those grains border each other very frequently, even though it is totally random. But if the phase of interest has only a volumetric portion ϵ_V of 10 %, it is more likely that only very few grains of the same phase α are bordering each other if the phase does not tend to cluster as shown in Figure 2.29b.

According to the original definition of GURLAND [69], the degree of clustering or contiguity can be defined as the "average fraction of surface area shared by one grain of a phase with all neighboring grains". These considerations can be summarized in Equation 2.31, where the degree of clustering C_α is calculated from the specific surfaces of the interfaces between neighboring grains $S_{V,(\alpha\alpha)}$ and $S_{V,(\alpha\beta)}$. As those specific surfaces are directly proportional to the number of intersections between grain boundaries of neighboring grains, this can also be expressed with the parameters $P_{L,(\alpha\alpha)}$ and $P_{L,(\alpha\beta)}$. The factor 2 has to be used to compensate the fact that each interface of grains of the same phase is counted only once by the line analysis, while interfaces between different phases are counted twice [50, 69, 101].

$$C_\alpha = \frac{2S_{V,(\alpha\alpha)}}{2S_{V,(\alpha\alpha)} + S_{V,(\alpha\beta)}} = \frac{2P_{L,(\alpha\alpha)}}{2P_{L,(\alpha\alpha)} + P_{L,(\alpha\beta)}} \tag{2.31}$$

The space filling of the microstructure. Despite of the distinct phase related parameters, it is further necessary to characterize how much of the rock microstructure is interspersed with pores. This property is usually expressed with the degree of space filling ϵ_{VF} and is commonly seen as volumetric proportion of all crystallized, solid phases of the microstructure $\epsilon_{V,crystalline\,phases}$ (Equation 2.32). However, this value is technically also the complimentary set to the porosity ϕ of the mineral microstructure, which is the volumetric proportion of all pores $\epsilon_{V,pores}$ (Equation 2.33).

$$\epsilon_{VF} = \sum \epsilon_{V,crystalline\,phases} \tag{2.32}$$

$$\epsilon_{VF} = 1 - \phi = 1 - \epsilon_{V,pores} \tag{2.33}$$

However, it is mandatory to interpret the degree of space filling differentiated. Depending on the method of measurement, different types of pores are detectable. When doing a QMA, especially in combination polarized light microscopy, it is only possible to quantify pores that are located on the three orthogonal slices. Furthermore, those pores have to be big enough to be detectable using optical microscopes.

Other measuring methods like mercury intrusion porosimetry are more accurate, as they test volumetric samples. Those are more representative for detecting spatial captivities than the planar samples of the QMA. Furthermore, approaches using liquids can also detect invisible micro pores, which are not identifiable with optical microscopy.

2.2.2 Applied QMA in mineral processing

It is known that different possible structures of the fabric influence the processing behavior in general [148]. An example for this is the influence of the rock properties of the feed material of a comminution process on the shape of the product particles. As shown by POPOV; LIEBERWIRTH, and FOLGNER [147], this influence can be as high as 65 % for the particle shape of a product that was crushed with a vertical shaft impact crusher. Moreover, it is shown that other parameters like the grain size or the roughness have an immediate correlation to such important characteristics as strength, specific energy for grinding, or wear rate [148]. These correlations are further confirmed by SCHREIBER [176], who extensively studied the influence of the different microstructural characteristics on the rock strength. Furthermore, it can be demonstrated that the QMA results can also be used to reliably predict the wear rate of HPGR [73]. Consequently, the QMA has been successfully used to classify the processing characteristics of various hard rocks at the Institute of Mineral Processing Machines.

Concededly, obtaining these valuable characteristic numbers goes along with high labor input. The QMA so far needs a versed operator like a mineralogist, who can reliably determine various minerals. Most of the time is unfortunately needed to execute rather simple tasks such as counting the points and intersections or for doing the planimetry. In comparison, the determination of the components of the fabrics takes only a small amount of time.

In conclusion, it can be summarized that the QMA is a useful tool for characterizing minerals, which can be applied to far-reaching tasks in mineral processing. This is seen to be a good basis for the intended incorporation of realistic microstructures into DEM as it allows firstly to describe it in a quantitative and objective manner. For this reason, it is decided to further use the QMA as basis for the synthesis approach presented in this study.

However, significant improvements are possible if an intelligent software supports the operator. Already an automation of simple counting processes can relieve the operator significantly. As the following section may show, the efforts to synthesize fabrics of different hard rocks benefits the QMA at this point, since appropriate algorithms are developed.

2.2.3 Applicability of the QMA for the synthesis of realistic microstructures

Due to the fact that the QMA quantifies the microstructural properties of rock material at the grain size level, this method is regarded as a suitable basis for the synthesis of realistic digital twins with equal statistical characteristics. In addition, as explained in Section 2.2.1, the ability to differentiate between adjacent grains without doubt, even if they are of the same phase, is an absolute precondition for a reliable subsequent synthesis. However, this can by now not be guaranteed by the currently available solutions for automated mineralogy based on

X-ray spectroscopy. Although polarized light microscopy of thin sections requires a relatively high amount of manual work, it seems to be the most reliable basis for the subsequent microstructure synthesis. In addition, this study can draw on the extensive database of rocks from various deposits that have already been analyzed with the QMA at the Institute of Mineral Processing Machines.

3 Synthesis of realistic mineral microstructures for DEM simulations

The following chapter deals with the synthesis of realistic mineral microstructures on the basis of the QMA results of the real microstructures. However, in order to model realistic microstructures as basis for DEM simulations, some preliminary considerations have to be taken.

Basic considerations for the approach to be developed. Firstly, four basic requirements for the synthesis and the implementation of microstructures into DEM simulations are formulated. These requirements outline the general conditions for the method that is developed:

- The approach should be capable to create a mathematical model of a given mineral microstructure. This model has to represent a given mineral microstructure of a real sample in a statistically satisfying way.
- The approach should be able to create two- and three-dimensional models in principle.
- It should be possible to model a broad range of different structures and fabrics.
- The approach should have an open access interface so that the model can be used in arbitrary simulation environments.

Conclusions of these conditions. For realizing this project, these general requirements have to be specified. Hence, to comply with the required statistical certainty in the description of the microstructures, the analysis of a given real mineral microstructure is restricted to QMA. As explained in Section 2.2, this technique allows to quantitatively characterize the mineral microstructure. In contrast to the traditional approaches, which are mainly used by mineralogists, this method allows to describe the mineral microstructure objectively and to summarize the data to a format, which is understandable for computer programs. Therefore, the QMA is considered to be very suitable for this project, but also needs to be adapted for the processing of synthetic microstructures.

Since there are no comparable approaches in the literature, it is also necessary to first demonstrate the basic functionality of this approach as part of a proof of concept study. Therefore, it is useful to restrict the approach to two-dimensions, so that modeling of two-dimensional microstructures is used as starting point. The main advantage of this approach is that the basic procedure can first be checked in the two-dimensional case with manageable effort. If the results of the proof of concept study are positive, then the synthetic microstructure approach can later be extended to three-dimensional problems, without wasting resources.

Besides the lower complexity for the realization, there is another advantage for starting with the two-dimensional approach. It is a matter of fact that two-dimensional microstructural data can also be displayed in two-dimensional images. Hence, the comparability and analyzability of synthetically generated two-dimensional microstructures is higher and the evaluation is more understandable. In contrast, the validation of a three-dimensional model is significantly more complex and should not be done until the algorithms have been verified on two-dimensional problems. In addition, a two-dimensional synthesis environment is also seen to be more experiment-friendly. It is expected that it is easier to implement and test new algorithms for generating grain structures.

In order to ensure maximum comparability to the real model microstructures, the resulting two-dimensional synthetic microstructures shall further be analyzed with the methods of the QMA as well. Therefore, the originally three-dimensional QMA has to be adapted to be applicable for two-dimensional problems as well. However, the algorithms for executing QMA on images of synthetically generated two-dimensional microstructures may be applied for the analysis of real microstructures as well. As a side effect, this transfer may help to decrease the work for analyzing a sample and increase the objectiveness.

The resulting main work thesis. These specifications lead to the main work thesis, which is presented in Figure 3.1. The aim is to implement realistic synthetic two-dimensional mineral microstructures into DEM simulations using the characteristic numbers of the QMA as input parameters. The basis for this approach is of course a representative sample of a hard rock and it should result in a two-dimensional model of the microstructure. This can then be transferred into an arbitrary simulation environment.

Based on this work thesis, in Section 3.1 it is first discussed how the QMA can be adapted to the needs of the proposed synthesis approach. Subsequently, different possible synthesis strategies are presented and evaluated in Section 3.2. Based on this the implementation of chosen so-called grain-drawing method is explained in detail in Section 3.3. This chapter is completed by the introduction of the final program for the microstructure analysis and synthesis in Section 3.4.

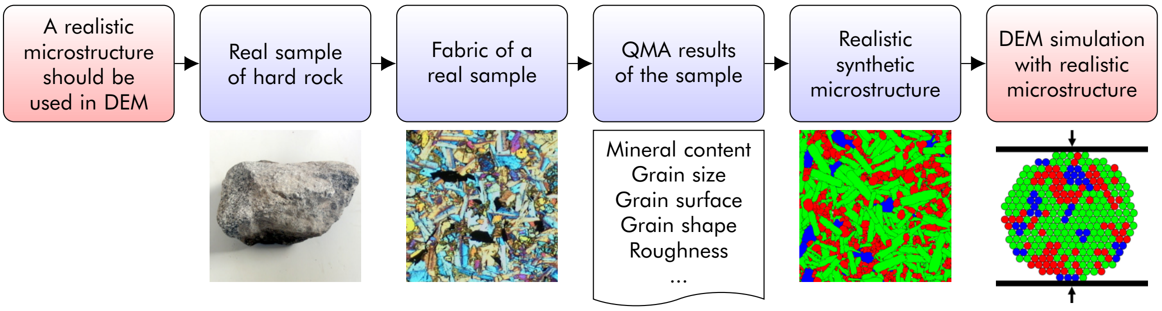

Fig. 3.1: Schematic procedure for synthesizing realistic microstructures that can serve as basis for DEM simulations with BPM

3.1 Development of a computer-assisted QMA for the analysis of real and synthetic mineral microstructures

In general, the conventional QMA, as described in Section 2.2.1, is seen as a suitable tool for an objective analysis of mineral microstructures. But, in order to use this tool for the synthesis of realistic mineral microstructures, it has to be adapted. The basic QMA is geared towards the manual analysis of real thin or polished sections using polarization microscopy. As the synthesized models of any mineral microstructure will exist only as a set of computer data, it is mandatory to develop the manual QMA towards a computer-assisted method, which is able to analyze synthetic mineral microstructures in the same way as real mineral microstructures.

3.1.1 Fundamentals of the computer-assisted QMA

Figure 3.2 shows the principal methodology for such an enhanced QMA, which can analyze real mineral microstructures as well as synthetic ones. The flowchart shows that it is hardly possible to conduct a direct comparative analysis on both the real and the synthetic microstructures. That is because of the differences in the actual shapes of the microstructures.

The real microstructure is given by the thin or polished sections, which can be accessed among others by polarization microscopy. In contrast, a synthetic microstructure is actually only a set of digital data. Hence, a direct analysis is not possible with the conventional QMA as it needs a physically existent microstructure.

In order to allow a QMA of synthetic microstructures, those have to be brought into a shape that can be processed by the algorithms of QMA. Therefore, it seems likely to use an image representation. If every phase is represented by an own unique color, this results in a simple false-color image of the microstructure, which is in principle appropriate for a QMA analysis.

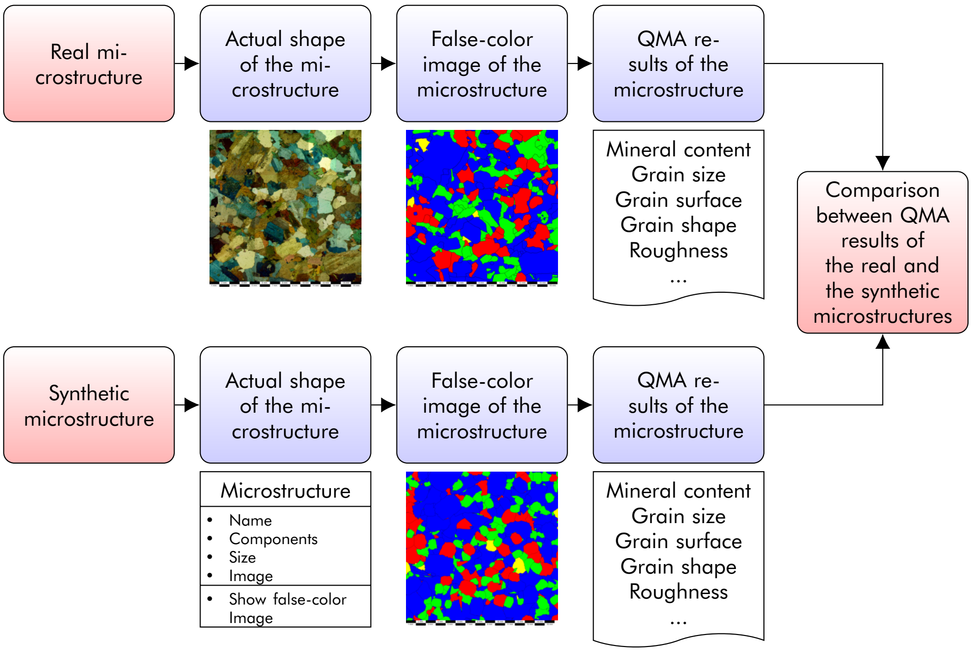

Fig. 3.2: Schematic comparison of an enhanced QMA that can analyze real and synthetic mineral microstructures on the basis of false color images

Because such a false-color image exists in a digital form, it is then directly accessible for computer algorithms. This makes it possible to carry out the actual analysis in a computer-aided manner, which makes the measurement and evaluation process much faster than with the traditional manual QMA. Moreover, since every part of the microstructure is uniquely determined by its color representation, such a digital false-color image is also biunique. Hence, it is not necessary that an operator interprets the mineral microstructure as would be required for a conventional QMA.

However, in order to make such a false-color image processable for automated measuring algorithms, the image has to meet several conditions. Those are briefly outlined in the following.

3.1.2 The requirements for the false-color image.

Based on the intended application of the false-color images, three main requirements can be found:

- The grain boundaries have to be represented with an own unique color.

- The grain boundaries have to be closed. That is because the QMA uses a strict definition of grains, which implies that every microbody is bounded by a completely closed interface. Without this condition, the measuring methods would not be applicable because the measurement itself as well as the assignment of specific measuring results to particular components of the microstructure would be inconclusive.

- The image has to be biunique in the sense that each color represents a specific phase and that every phase is only represented by one specific color. This applies for mineral phases, NDP, and pores.

The unique color for the grain boundaries. The first condition, which requires an own unique color for representing the grain boundaries is needed to ensure that there is no mix-up with the actual inside of the grains. For this purpose, the color black is reserved for the false-color representation of grain boundaries in this study.

The need for closed grain boundaries. Based on the decision to use black for the grain boundaries, Figure 3.3 and Figure 3.4 show the basic steps to convert a given microstructure with phases α and β into a biunique false color-color image. Using the original microstructure, a map of grain boundaries has to be generated first. It is mandatory that the map of grain boundaries is closed in order to meet the conditions of the QMA. To illustrate that, Figures 3.3b and 3.3c show the differences between correct closed grain boundaries and the result of an incorrect boundary detection with open grains.

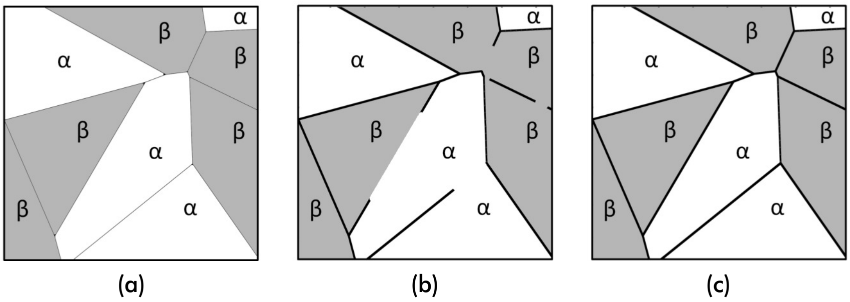

Fig. 3.3: Schematic illustration of incorrect and correct mapped grain boundaries of a given microstructure with phases α and β: (a) Given microstructure, which is the basis for the grain boundary detection; (b) Incorrect map with open boundaries; (c) Correct map with closed boundaries

The need for a biunique color coding of the grains. On the basis of a correct map of grain boundaries it is then possible to assign the biunique colors to the different grains (Figure 3.4a). The comparison between Figure 3.4b and Figure 3.4c shows what happens if the color assignment is faulty. If an incorrect false-color image like Figure 3.4b would be presented to an automated QMA, it would cause wrong analysis results as the assignments of colors for phase α and β are inconclusive.

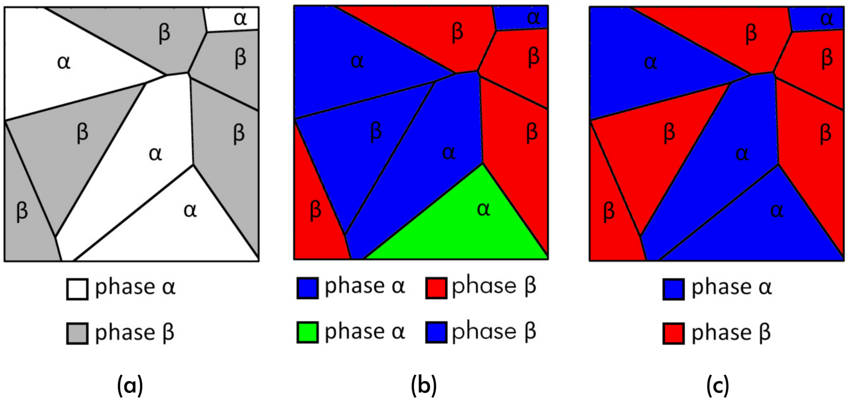

Fig. 3.4: Schematic illustration of incorrect and correct false-color conversions of a given microstructure with the phases α and β: (a) Basis for the color assignment; (b) Incorrect, inconclusive false-color image; (c) Correct, biunique false-color image

3.1.3 The conversion of a given real mineral microstructure into a false-color image

Because of the analysis of the real microstructure is the first step in the intended synthesis process, it is subsequently evaluated if and how false-color images of the real microstructure can be generated for the computer-assisted QMA.

As explained, it is necessary to convert a given real mineral microstructure into a false-color image that fulfills the above explained requirements, in order to allow comparative analysis. In general, this can be done by photographing the thin or polished section first. Subsequently, the photographs have to be transferred into false-color mode, which, by now, has to be done manually. The needed substeps for such a conversion process are enumerated in the following:

1. Preparation of a thin- or polished section
2. Taking pictures of the thin- or polished section using polarization microscopy or equivalent methods
3. Merging the single photographs of the polished section to an image of the whole sample
4. Creation of a map of grain boundaries according to Figure 3.3
5. Assignation of biunique colors to the grains according to Figure 3.4

Example approach for an automated microstructure conversion. Because of the general focus of this study it obvious to try to computerize this task. However, it is found, that with the technology currently available on the market the conversion is not fully automatable, as there are two major problems. The first one is the correct detection of grain boundaries. As explained in Section 3.1.2, this step has to be exact. Otherwise no correct QMA measurement can be conducted. The difficulties that arise when automated algorithms are used are exemplarily explained with the help of an example conversion in Figure 3.5.

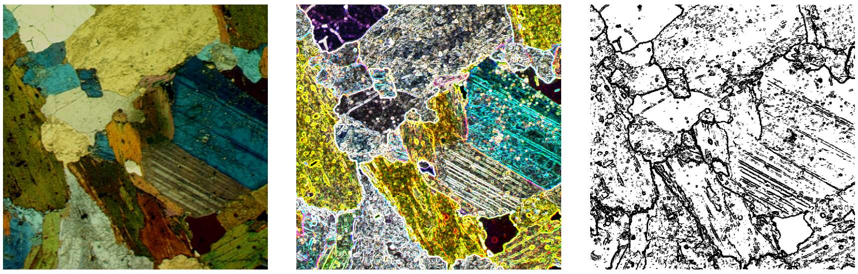
(a) (b) (c)

Fig. 3.5: Example of an automated edge detection algorithm: (a) Photography from a thin section of granodiorite from Kindisch, Saxony, taken under polarized light with a 16x magnification; (b) Exemplary result from sobel edge detection algorithm; (c) Binarized and inverted image from the sobel edge detection

Therefore, a photography of granodiorite from Saxony, Kindisch is taken as reference. It shows a small part of a thin section, which is taken under polarized light with 16x magnification (Figure 3.5a). Exemplary, a sobel filter was applied to this image, which is a common edge detecting algorithm [163] (Figure 3.5b). Because of the strict requirements for the false color-image conversion, the image with the detected edges has to be binarized, as every point in the image can either be an edge or not. In order to ease the interpretation, the binarized image is also inverted, making the detected edges black (Figure 3.5c)

Problems related to inadequate grain boundary detection. The comparison between the original photography and the image with the detected grain boundaries reveals the general problems of automated edge detecting for mineral microstructures. Due to little cracks inside the grains, impurities on the thin or polished section, twinning lamellae, and other structures, such algorithms usually detect a certain amount of false grain boundaries. In reference to test statistics, this can be seen as type II errors, because those edges are false positive findings.

In contrast, there are also areas where the algorithm does not detect edges or where the detected edges were suppressed during the binarization. These results can be seen as type I errors because those undetected grain boundaries are typical false negative findings.

Of course, it is possible to improve the quality of the edge detection by optimizing the filter and binarization parameters or by applying other filters, that might be more appropriate. Nevertheless, one should always keep in mind that any adjustment that will reduce type I errors will increase the probability to get type II errors and vice versa. An absolute elimination of these errors is not possible without the usage of further information. There can always be inconspicuous or invisible grain boundaries in the current view next to areas which have significant contrast to the surroundings, but which are no boundaries at all. These are circumstances, which make reliable and correct automated grain detection on the basis of single conventional photographs impossible as shown by LANGE and HILLMANN [102].

Problems related to inadequate phase detection. The second major problem is connected to the color assignment. The colors of the grains of the real photographs are not biunique with respect to the different phases in the microstructure [102]. For example, it is possible that two grains, which belong to different phases, have nearly the same color gradient while turning under polarized light. This characteristic makes differentiation for any algorithm impossible if no further information is used.

For distinguishing those, an experienced operator is needed. He has to use further, mostly experience-bound information in order to do correct assignments. This further information can be the general grain shape and size, its appearance under different polarization conditions, as well as the existence of twinning formation and twinning lamellae, pleochroism, shagreen, and relief. However, automation efforts for evaluating such additional data are difficult, since most of these parameters are not quantifiable till now.

Furthermore, it can be necessary to change the polarization and magnification conditions multiple times in order to determine single grains. Although polarization microscopes with automated rotary stages and object guides, which can autonomously scan given objects, are meanwhile on the market, there is no appropriate software that can access the additional required parameters. However, those are needed to determine the different phases and couple the underlying algorithms to the automated scanning and photographing of the probe.

Prioritization of a partly manual microstructure conversion. Due to the above presented shortcomings of the available technology and software, it is decided to forgo an automation of the conversion process for the time being. Because of the far-reaching problems of both the edge and the phase detection, a development of a reliable and correct conversion program is beyond the scope of this study.

For this, it is decided to rely on a manual conversion. This allows to keep the development effort for the adapted QMA moderate by ensuring that the converted false-color images meet the presented requirements.

3.1.4 Implementation of the point, line, and area analysis

In contrast to the conversion, the actual analysis could successfully be automated within this project. Therefore, a computer program was developed, which can perform the point, line, and area analysis on a given false-color image [96]. The program is written in the open source programming language Python [166]. Advantageously, this universal, higher script language is relatively powerful but simple to use. For the image analysis, the python package Pillow [25] is used as basis. Pillow is a fork of the Python Imaging Library (PIL) and provides extensive file format support. Its core is designed for fast data access and manipulation at the pixel level.

For using the three measuring methods, the user has to load a false-color image of the microstructure that has to be analyzed and pass it to the analysis functions. However, the functions are not restricted to mineral microstructures. As long as the passed false-color image fulfills the conditions explained in Section 3.1.2 it can be analyzed by the computer program automatically. Hence, the program could also be used for any other microstructure that meets the presented conditions. The actual implementation of the three measuring methods is shortly introduced in the following.

The automated point analysis

The implementation of the point analysis is based on the specification of the original QMA. The false-color image is sampled on a given raster first, as shown in Figure 3.6. Then, the function for the point analysis simply counts how many of the counted points belong to which phase. Based on this, it is possible to calculate the corresponding areal proportion ϵ_A.

However, due to the pixel format, it is possible that some points of the measuring raster fall on grain boundaries, which are represented by their black color. In order to keep consistency with the original stereological ideas, they have to be suspended from further evaluation. Otherwise the process would assign an areal proportion to the grain boundaries, which is not definable.

In the given example, two points of the current state of the analysis fall onto grain boundaries, which were marked by black circles. However, for the calculation of the areal proportion ϵ_A, only the valid measuring points, which are marked by the blue and red dots are counted.

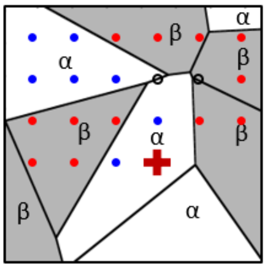

Fig. 3.6: Schematic example of the implementation of the automated point analysis: The process has analyzed about the half of the given microstructure. The current analysis point is marked with the dark red cross. Previous analysis points that belong to phase α are marked with blue dots and points that belong to phase β are marked with red dots. The two analysis points that fall onto grain boundaries are marked with black circles and are not used for further evaluation.

The automated line analysis

The process of the automated line analysis is a one to one conversion of the original idea of the stereology as well. As shown in the schematic example of Figure 3.7, the microstructure is scanned by a cursor, which is marked by a dark red cross. The cursor follows the predefined parallel analysis lines and counts the intersections between the grain boundaries $N_{(\alpha,\beta)}$. These were stored by type and are the basis for the further evaluation processes.

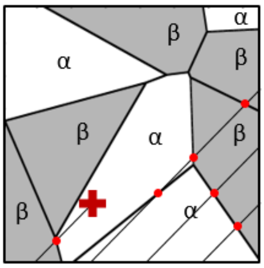

Fig. 3.7: Schematic example of the implementation of the automated line analysis: The cursor scans the microstructure following the predefined parallel lines. The current cursor position is marked with the dark red cross. Previously found intersections with grain boundaries are marked with red dots. For reasons of clarity this example does not distinguish between the different types of grain boundaries.

The automated area analysis

The automated area analysis is implemented differently from the original planimetry approach. In contrast to the manual analysis, it is possible to directly access the grain areas. For this, a simple implementation of a flood algorithm with 4-connected pixels is used [20]. This algorithm scans the microstructure for connected areas. In the function for the area analysis, the used flood fill algorithm is implemented so that all connected areas, which are the grains, are scanned one after each other. After completing a grain, the algorithm saves the number of pixels that belong to it by the type of phase.

After the process has analyzed all the grains, the program has a list for every phase. These lists store the number of pixels for each grain belonging to that specific phase. These particle sizes are then used for further evaluation.

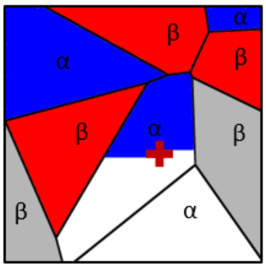

Fig. 3.8: Schematic example of the implementation of the automated area analysis: The flood fill algorithm scans all connected areas. At the current state of the process, the grain in the middle is scanned by the cursor, which is marked by the dark red cross. Areas, which are already scanned, are painted in blue for phase β and red for phase α. The function that controls the process saves the number of pixels belonging to the grains of each phase in a separate list automatically.

3.1.5 Selection of appropriate QMA parameters for analyzing two-dimensional microstructures

After the false-color image of the given real or synthetic microstructure was successfully analyzed with the above presented three automated methods, the results have to be evaluated in an appropriate way. Due to the fact that the focus is set on a two-dimensional approach in the first instance, it is necessary to narrow down the QMA results, which later serve as input parameters for generating the synthetic microstructures.

As explained in Section 2.2, the QMA is originally a method to measure and describe the texture and structure of three-dimensional mineral microstructures. Hence, not all the results are suitable for generating two-dimensional synthetic microstructures, as some of them describe three-dimensional characteristics only. Others, however, have to be adapted to two-dimensional structures.

Hence, the evaluation and the parameters of the QMA were adapted in this study in order to guarantee correct and reliable analysis results for the used two-dimensional microstructures. The resulting adaptations on the QMA parameters are explained in the following. For this, Table 3.1 first summarizes the parameters for the three-dimensional analysis and its associated two-dimensional equivalents, ordered by the general rubrics of the results of the QMA analysis.

Because of the similarities between these parameters, it is possible to build up an automated adopted QMA for two-dimensional microstructures, which uses the same basic measuring methods. Hence, the functions for doing the point, line, area analysis can be used as well.

Tab. 3.1: QMA parameters for two- and three-dimensional analysis

General QMA parameters	3D	2D
Mineral content	Volumetric proportion ϵ_V	Areal proportion ϵ_A
Grain size	Median grain size $x_{50,3}$ Standard deviation σ_{ln}	Median grain size $x_{50,2}$ Standard deviation σ_{ln}
Grain shape	Elongation El Flatness Fl	Elongation El
Grain surface	Specific grain surface S_V	Specific boundary line length C_A
Grain roughness	Degree of roughness K_R	Degree of roughness K_R
Orientation	Degree of isotropic orientation K_{iso} Degree of linear orientation K_{lin} Degree of planar orientation K_{pla}	Degree of isotropic orientation K_{iso} Degree of linear orientation K_{lin}
Intergrowth	Matrices of bounding surfaces	Matrices of bounding surfaces
Spatial distribution	Degree of clustering C_α	Degree of clustering C_α
Space filling	Degree of space filling ϵ_{VF}	Degree of space filling ϵ_{AF}

The difference in the post processing of the primary measuring values in comparison to the conventional QMA are explained in the following paragraphs.

The mineral content. The mineral content of a two-dimensional microstructure is comparably calculated as it is done for a three-dimensional microstructure. Therefore, the point analysis is used. The only difference is that no volumetric proportion ϵ_V, but an areal proportion ϵ_A is defined for two-dimensional structures. While ϵ_V corresponds to the volume of the objects per test volume V_V, ϵ_A is equal to the area of the objects per test area A_A. Nevertheless, this does not change the general approach since according to Equation 2.12 $V_V = A_A$ applies. Hence, it can be concluded that the areal portion of a specific mineral component ϵ_A is equal to the calculated parameter P_P of the point analysis (Equation 3.1).

$$\epsilon_A = P_P \tag{3.1}$$

The grain size. The size distribution of grains of two-dimensional microstructures is specified by the median grain size $x_{50,2}$ of the approximated log-normal area distribution and the dispersion parameter σ_{ln}. This is in principle similar like for a conventional three-dimensional

QMA, where the median grain size $x_{50,3}$ of the approximated log-normal volume distribution is used. Furthermore, the dispersion parameter σ_{ln} is the same for both distributions.

As the cut surfaces can be measured directly during the area analysis, it is not necessary to use stereological transformations for two-dimensional applications as work around like in Equation 2.15. Hence, it is possible to directly determine the desired median grain size of the cut surface distribution of the grains, which is equal to $x_{50,2}$.

However, for this reason a suitable diameter definition has to be found. As the analysis is two-dimensional anyway, the so called Heywood diameter seems to be the obvious choice. Therefore, it is assumed, that the size of an arbitrary shaped grain is the diameter of a size equivalent circle.

The advantage of this definition is that the equivalent diameter can be calculated relatively easy and straight forward. Other diameter definitions often imply more complicated analysis algorithms of the two-dimensional structures. However, it should be noted that basically any other size definition can be used at here. Finally, with this diameter assumption Equation 3.2 can be used to approximate the cut surface distribution of the grain sizes [198].

$$q_2(x) = \frac{1}{\sigma_{ln}\sqrt{2\pi}} \cdot \frac{1}{x} e^{-\frac{1}{2}\left(\frac{\ln(x)-x_{50,2}}{\sigma_{ln}}\right)^2} \tag{3.2}$$

The grain shape. In order to evaluate the grain shape in two-dimensional microstructures, its definition has to be adapted for planar analysis. In contrast to conventional three-dimensional analysis, it is not possible to approximate the grain shape by a tri-ellipsoid as no information about the spatial depth is measured. Based on the results of the analysis of only one plane, the grain shape can only be approximated by an ellipse with its principal semi-axes a and b. However, this can also be seen as a special form of a tri-axial ellipsoid, where the shortest principal semi-axis $c = 0$.

Due to this restriction, only the elongation El can be calculated because the flatness Fl is not defined for plane objects like an ellipse (Equation 3.3).

$$El = \frac{a}{b} = \frac{\frac{2}{3}n_{iso} + \frac{\pi}{4}n_{lin}}{\frac{2}{3}n_{iso}} \tag{3.3}$$

The real grain surface. In order to characterize the grain shape one has to keep in mind, that similar to the considerations for the grain shape, there is no three-dimensional but

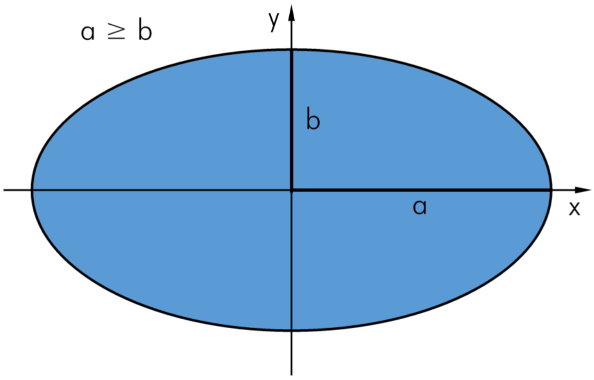

Fig. 3.9: Model for the grain shape at planar analysis: Elliptical unit microbody with its principal semi-axes a and b

a two-dimensional microbody, which has to be described. Taking this fact into account, the grain surface has to be defined using two-dimensional parameters as well. The corresponding equivalent to the specific surface S_V can be found in the specific boundary line length C_A. This parameter sets the circumference of the object of interest in relation to its area (Figure 3.10). The corresponding mathematical definition is shown in Equation 3.4.

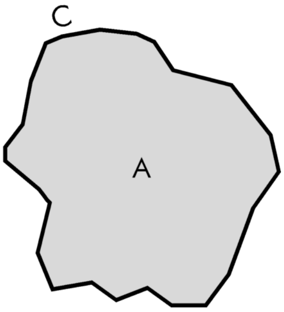

Fig. 3.10: Example of an arbitrary two-dimensional object with its area A and circumference C

$$C_A = \frac{C}{A} \tag{3.4}$$

According to the two different definitions for the specific surface S_V, it is possible to calculate a real specific boundary line length $C_{A,R}$ and an ideal specific boundary line length $C_{A,I}$ as well.

The so-called real specific boundary line length $C_{A,R}$ is calculated with the help of the approach for determination of the total line length in the plane using the random intersection lines method of SALTYKOV [170]. This method is based on Buffon's needle problem.

It can be shown that the specific line length of arbitrary thin objects like lines or curves in the plane, can be measured using a set of measuring lines, which are used to count intersections with the thin objects. This approach is bound to the condition that the used analysis method has to be able to measure every possible intersection angle between the measuring lines and the thin objects of interest with equal probability. This condition is fulfilled for the following three setups:

- The object of interest is isometric and the orientation of the system of measuring lines is discretionary. That also allows a set of parallel measuring lines that are orientated with an arbitrary angle.
- The object of interest is anisometric and the orientation of the system of measuring lines is random or uniformly distributed over the measuring angle.
- The object of interest is isometric and the orientation of the system of measuring lines is random or uniformly distributed over the measuring angle.

The line analysis of the QMA fulfills this condition as a set of parallel measuring lines is used in different uniformly distributed measuring angles. This guarantees that isometric and anisometric structures can reliably be analyzed. Hence, the specific boundary line length is calculated directly from the results of the line analysis.

Therefore, the parameter n is used, which is the number of intersections between the objects of interest and the lines of the line analysis in relation to the total length of the analysis lines. According to the solution of Buffon's needle problem, the total length of the thin objects in the given system in relation to a unit area, can directly be calculated from n [48, 170]. If the grain boundaries are considered to be these thin objects in Buffon's needle problem, subsequently Equation 3.5 can be used to calculate the real specific boundary length.

$$C^*_{A,R} = \frac{\pi}{2} n \tag{3.5}$$

Hence, this parameter characterizes how often the grain boundaries of interest are intersected by the measuring lines. As the total area of the field of measuring is the reference value for $C^*_{A,R}$, it can be described as real specific boundary line length referring to the total area of the field of measuring.

Thus, the real specific boundary line lengths of different phases cannot be compared with each other directly. The reason is that the number of measured intersections is associated to the areal proportions ϵ_A of the phases. In order to illustrate this, two phases A and B are assumed, whose grains have the same grain surface characteristics but different area proportions ($\epsilon_{A,A} < \epsilon_{A,B}$). The grains of a phase A, which make up the smaller part of the total structure are consequently less often intersected by the measuring lines than those of the other phase ($n_A < n_B$). Hence, the calculated real specific boundary line length of phase A is smaller than of phase B although both have the same grain surface characteristics ($C^*_{A,R,A} < C^*_{A,R,B}$).

For this reason, Equation 3.5 has to be normalized to the areal proportion of the specific phase ϵ_A, which leads to Equation 3.6:

$$C_{A,R} = \frac{C^*_{A,R}}{\epsilon_A} \tag{3.6}$$

By doing so, it is possible to analyze the real specific boundary line length detached from the frequency of occurrence of a specific phase in a mineral microstructure. Consequently, it is possible to compare the grain surface characteristics of two different phases directly with this parameter. Hence, this is the parameter, which is further used to specify the specific boundary line lengths of the different phases in the adapted QMA.

The indirect ideal grain surface. Comparably to the three-dimensional analysis, it is possible to calculate an ideal grain surface $C_{A,I}$ in addition to the real grain surface $C_{A,R}$. This can be done in two different approaches. The first one is to indirectly approximate the ideal specific boundary line length from the grain size distribution ($C_{A,I,approx}$). The detailed derivation of this approach, which also assumes that the area distribution of the cut surfaces is also log-normal distributed, is shown in Appendix A.1 for clarity reason.

Accordingly, Equation 3.7 represents the formula to approximate the ideal specific boundary line length, based on the median grain size $x_{50,2}$ and the standard deviation σ_{ln} of the approximated log-normal grain size distribution. The ideal specific boundary line length of the approximated grain size distribution $C_{A,I,approx}$ can be compared directly to its real counterpart $C_{A,R}$ as both of them are referred to the areal proportion of the specific phase ϵ_A.

$$C_{A,I,approx} = 4\left[3\frac{a+b}{4\sqrt{ab}} - \frac{1}{2}\right]\frac{1}{x_{50,2}}e^{\frac{{\sigma_{ln}}^2}{2}} \tag{3.7}$$

The difference between both the ideal and the real grain surface in the two-dimensional analysis is exemplarily shown in Figure 3.11.

If one is interested in the ideal boundary line length referred to the total area of the field of measuring, Equation 3.7 has to be normalized with ϵ_A as well (Equation 3.8).

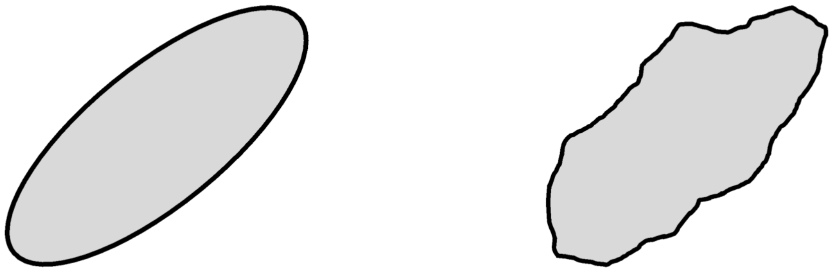

(a) Ideal grain surface $C_{A,I}$ (b) Real grain surface $C_{A,R}$

Fig. 3.11: Schematic representation of ideal grain surface $C_{A,I}$ in relation to the real grain surface $C_{A,R}$

$$C^*_{A,I,approx} = \epsilon_A \cdot C_{A,I,approx} \tag{3.8}$$

The direct ideal grain surface. However, a second method to determine the specific ideal boundary line length $C_{A,I}$ from the grain size distribution can be used as well. In contrast to the traditional QMA, where the particle size distribution can only be approximated by the area analysis, it is possible to directly access the exact grain area distribution in a false-color image. Hence, it is not necessary to calculate $C_{A,I}$ with the help of the approximated distribution parameters $x_{50,2}$ and σ_{ln}.

Instead, it is possible to calculate the circumference of an area equivalent circle for each grain. This data can then be used to determine the specific ideal boundary line length of the actual distribution, which called $C_{A,I,actual}$. For this, $C_{A,I,actual}$ is calculated as function of the sum of the areas A_i of the analyzed set of grains Ω and the ratio of the semi-axes El. These relations are specified in Equation 3.10. For the detailed derivation of this formula, it is referred to Appendix A.2.

$$El = \frac{a}{b} = const. \tag{3.9}$$

$$C_{A,I,actual} = \sqrt{\sum_{i \in \Omega} A_i \pi} \left(\frac{3}{2} \left[\frac{El + 1}{\sqrt{El}} \right]_1 \right) \tag{3.10}$$

Equivalent to the previous formulas, it is possible to transform Equation 3.10, so that it refers to the total area of measurement (Equation 3.11).

$$C^*_{A,I,actual} = \epsilon_A \cdot C_{A,I,actual} \tag{3.11}$$

The advantage of this direct approach to calculate the actual specific boundary line length $C_{A,I,actual}$ is that this parameter cannot be affected by any insufficiencies of the approximation of the particle size distribution. Hence, it is further used for the final adapted QMA, which is implemented in the program.

The grain roughness. The definition of the grain roughness in a two-dimensional analysis is similar to the three-dimensional approach. In principle, only the reference basis for the calculation changes from the specific surface S_V to the specific boundary line length C_A.

However, it is possible to calculate the roughness also on the basis of the specific boundary line length of the actual grain size distribution $C_{A,I,actual}$. This approach has the advantage, that the calculated roughness is not subjected to any uncertainty due to the approximation of the grain size distribution. Consequently, the calculated roughness based on the original estimation approach is further called $K_{R,estimated}$ (Equation 3.12). In contrast, the roughness based on the actual grain size distribution is called $K_{R,actual}$ (Equation 3.13).

$$K_{R,estimated} = \frac{C_{A,R} - C_{A,I}}{C_{A,R}} \tag{3.12}$$

$$K_{R,actual} = \frac{C_{A,R} - C_{A,I,actual}}{C_{A,R}} \tag{3.13}$$

As $K_{R,actual}$ is robust to approximation variances and therefore more accurate than K_R, Equation 3.13 is further used for the two-dimensional QMA.

The grain orientation. Like for the original QMA, the orientation of the grains in a plane can be deduced from the rose of intersections as well. Analogous to the spatial analysis, this is done by approximating the two-dimensional roses of intersections, which can be seen as combination of an ideal isotropic and an ideal linear bounding surface system (Figure 3.12). The individual proportions of the elementary bounding systems on the combined real bounding system can be calculated by means of Equations 3.14 and 3.15. However, due to the missing spatial component of the planar analysis, only the degree of isotropic orientation K_{iso} and the degree of linear orientation K_{lin} are relevant [170].

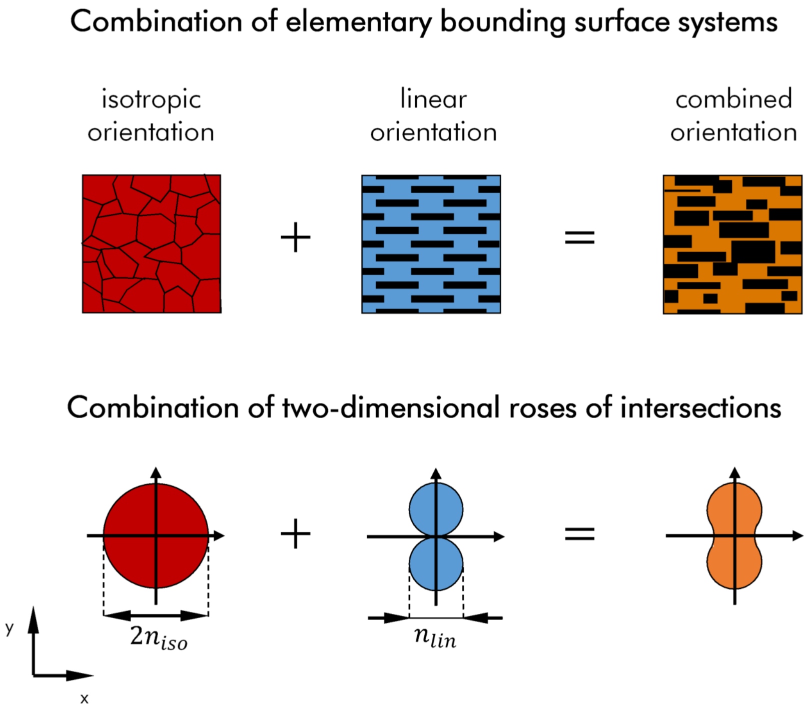

Fig. 3.12: Superposition of elementary surface boundary systems and the measured two-dimensional roses of intersections

$$K_{iso} = \frac{\frac{\pi}{2} n_{iso}}{\frac{\pi}{2} n_{iso} + n_{lin}} \tag{3.14}$$

$$K_{lin} = \frac{n_{lin}}{\frac{\pi}{2} n_{iso} + n_{lin}} \tag{3.15}$$

The grain intergrowth. Similar to the grain intergrowth definition of spatial systems, it is also possible to describe the mineral associations of two-dimensional mineral microstructures. Equally, this grain growth characterizes how often a specific type of grain boundary occurs in the analyzed system. In difference to the spatial analysis, the basis for the calculation is again the specific boundary line length C_A. Hence, the degree of intergrowth $K_{I,(\alpha,\beta)}$ between grains of phase α and grains of phase β is defined as the proportion of the specific boundary line length between the grains of the two phases $C_{A,(\alpha,\beta)}$ and the specific boundary line length of the whole mineral microstructure $C_{A,all}$ (Equation 3.16).

$$K_{I,(\alpha,\beta)} = \frac{C_{A,(\alpha,\beta)}}{C_{A,all}} \tag{3.16}$$

The specific boundary line length $C_{A,(\alpha,\beta)}$ for the pairing between grains of phase α and β is calculated with the means of the line analysis as well (Equation 3.17). In general, the calculation approach is similar to that of the spatial calculation (Equation 2.30). Like in the spatial definition the number of intersections $N_{(\alpha,\beta)}$ between grains of phase α and grains of phase β on the lines of the line analysis as well as the distance between two parallel lines of the line analysis d and the area of the measuring field of the line analysis a_0 are used as input parameters. However, in contrast to the original definition, the factor $\pi/2$ has to be used for the conversion of the number of intersections per measuring line length into the specific boundary line length as explained in Appendix A.3. In the consequence, $C_{A,(\alpha,\beta)}$ can be calculated by Equation 3.17.

$$C_{A,(\alpha,\beta)} = \frac{\pi \cdot N_{(\alpha,\beta)} \cdot d}{2 \cdot a_0} \tag{3.17}$$

The specific grain boundary length of all interfaces $C_{A,all}$ is the direct equivalent to the specific surface of all interfaces $S_{V,all}$. It is calculated as the sum of all specific grain boundary lengths of the possible grain pairings within a given mineral microstructure. These similarities result in a comparable evaluation and representation of the degrees of intergrowth for a plane analysis, which is also done in matrix form as it is shown in Figure 2.28 in Section 2.2.1.

The spatial distribution of the grains. In order to characterize the spatial distribution of the different grains in a plane microstructure, an approach can be used, which is equivalent to the three-dimensional definition. Thus the original definition for the degree of clustering can directly be taken from Section 2.2.1 as the only difference is again the basis of the calculation.

Instead of the specific surfaces of the grains S_V, the specific boundary line length C_A has to be used. However, it is noted that specific boundary line lengths are proportional to the number of intersections between grain boundaries of adjacent grains. Hence, the degree of clustering of a two-dimensional analysis C_α can also be directly expressed as function of $P_{L,(\alpha\alpha)}$ and $P_{L,(\alpha\beta)}$ (Equation 3.18).

$$C_\alpha = \frac{2C_{A,(\alpha,\alpha)}}{2C_{A,(\alpha,\alpha)} + C_{A,(\alpha,\beta)}} = \frac{2P_{L,(\alpha\alpha)}}{2P_{L,(\alpha\alpha)} + P_{L,(\alpha\beta)}} \tag{3.18}$$

The space filling of the microstructure. The last relevant parameter for the adapted planar QMA is related to the space filling of the rock material. For the two-dimensional analysis the definition of the degree of space filling ϵ_{AF} is in principle similar to the spatial definition shown in Section 2.2.1. The only difference is that the areal proportion of a phase ϵ_A is used instead of the volumetric proportion ϵ_V. However, the calculation of the areal degree of space filling is equivalent to its volumetric pendant.

$$\epsilon_{AF} = \sum \epsilon_{A,crystalline\,phases} \tag{3.19}$$

$$\epsilon_{AF} = 1 - \phi = 1 - \epsilon_{A,\,pores} \tag{3.20}$$

3.1.6 Summary of the principles of the adapted QMA

The presented methods and parameters of the adapted QMA are considered to be a straight forward transfer of the methods of the original three-dimensional QMA to the planar case. Due to the similarities, the analysis methods are the same. Both approaches use the point, line and area analysis as basis. However, the adapted QMA is designed so that biunique false-color images of the mineral microstructures are used as starting point. This allows to automate the basis analysis methods and let the computer do the counting work.

In addition, the actual parameter definitions were adapted to the planar problem. However, most of the definitions are quite similar as only the reference values have to be changed. Altogether, this adapted two-dimensional QMA is therefore considered to be a suitable basis for the intended development of the microstructure synthesis approach. However, the combination of this analysis method with the actual synthesis algorithms and their implementation in the final program are then explained in Section 3.4.

3.2 Analysis of possible strategies for the microstructure synthesis

As explained at the beginning of Chapter 3, the synthesis program should be capable of generating two-dimensional structures. However, there are different strategies conceivable, which can fulfill this task and should result in a realistic output. In general, the strategies to synthesize microstructures can be divided into models, which simulate the grain growth and in models that synthesize only the final appearance of the microstructure, neglecting the actual genesis.

Besides this classification of the modeling approach, the different strategies can be further classified by the used simulation technique and the simulation objective. The basic elements of these simulations can be as different as for example polygons or more general polyhedra based structures [12, 13, 17, 75, 103], cellular automata [58, 159, 228], and various tessellations procedures [105, 107, 200]. Also the fields of application for such microstructure synthesis approaches are very broad. They range from natural grown mineral microstructures [12, 17, 75] to cell structures of living tissue [13] and man-made microstructures in alloys [58, 159, 228].

Due to this diversity, an all-embracing review of synthesis strategies is not useful in this context. Therefore, the following summary concentrates on the two strategies that have comparable study subjects to the intended synthesis approach, so that possible advantages can be adopted.

Grain growth simulations

Models that simulate the grain growth are popular in material science, especially for the analysis of alloys. Such models are often used to understand the formation processes of the grains, which have great influence on the material properties. For example, RAABE [159] uses a three-dimensional cellular automaton for simulating the evolution of the crystallographic texture during recrystallization of aluminum. In a comparable approach GASNIER et al. [58] uses a more sophisticated grain growth model for the simulation of a polycrystalline microstructure. These approaches can also be adapted to model the microstructure evolution in more complex production processes like cold-rolling of dual phase steels [228].

The presented studies use grain growth simulations because the analyzed materials originate from productions processes, which are directly controlled or influenced by the process design. Hence, these simulations can be used to explain how and why a microstructure evolves the way it is observed in real processes. On the basis of such simulations, it is also possible to improve the production processes so that the microstructure of the final product guaranties better material properties.

Grain growth models are also popular in geology science, for example for the analysis of the microstructure evolution in veins [12, 17, 75]. However, in contrast to the presented approaches of material science, no cellular automata were used. The presented geological studies simulate the actual microstructure directly with polygons, which represent the different mineral constituents. This approach has the advantage that the growth conditions of the different grains can directly be influenced by changing the associated parameters for the specific grains. This is hardly possible in cellular automata, as such simulations usually use global, indirect parameters to drive the simulations.

Direct synthesis of final microstructures

The direct synthesis of microstructures is used, if not the actual genesis but only the final appearance is of interest. This can especially be the case for geotechnical studies like simulations of uniaxial compression and tensile strength tests [107] or Brazilian test [200]. In this case, it is not the aim to explain how a certain mineral microstructure was formed but to analyze how this microstructure influences the mechanical behavior of the rock.

Hence, such simulations do not have to take the actual evolution process into account. As a result, the mineral microstructure is modeled on the basis of Voronoi diagrams in both studies. The individual Voronoi cells are then assigned to specific mineral phases, as already explained in Section 2.1.3. This actual assignment process is based on a one-to-one copy of the microstructure observed with optical microscopy. The final Voronoi diagram with the Voronoi cells assigned to the different phases then serves as model for the mineral microstructure.

Development of a preferred synthesis strategy

The requirements for the synthesis of realistic mineral microstructures in the context of mineral processing are comparable to those of the geotechnical studies [107, 200], which use the Voronoi approach. Also for the intended microstructure synthesis, it is not necessarily useful to simulate the genesis of the mineral microstructure. As a matter of fact, only the current existing rock material and its characteristics are essential for mineral processing applications.

Of course, it can be argued that the mineral microstructure and properties of any present rock material are the result of petrogenetic processes, which occurred before. But for this application it is seen to be acceptable to consider the actual mineral microstructure detached from its petrogenesis. Due to the huge diversity of petrogenetic processes, including the formation of igneous rock, metamorphic rock, and sedimentary rock, it is not useful to simulate the actual petrogenesis processes, as only the final result of the evolution process is of interest for most mineral processing simulations.

Nevertheless, as already mentioned in Section 2.1.3, the approaches proposed by LI; KONIETZKY, and FRÜHWIRT [107] and TAN; KONIETZKY, and CHEN [200] are relatively inflexible as they are only suitable for a limited number of mineral microstructures. Furthermore, the presented modeling technique, which is based on Voronoi tessellations has also some disadvantageous limitations for the synthesis of microstructures.

On the one side Voronoi diagrams are relatively easy to simulate and can be adjusted to imitate many different structures. On the other side, however, one has to keep in mind that tessellations can only be used to imitate structures that agree with their formation conditions. It is noted, that a Voronoi cell is by definition the set of all points, whose distance to a given seed point is not greater than their distance to any other seed point in the considered space. Hence, it is a suitable tool to simulate relatively homogeneous, isotropic structures. However, in return it is not possible to create more complex structures like:

- Concave grains (Figure 3.13a)
- Grains that are embedded into other grains (Figure 3.13b)
- Adjacent grains of very different size or shape (Figure 3.13c)

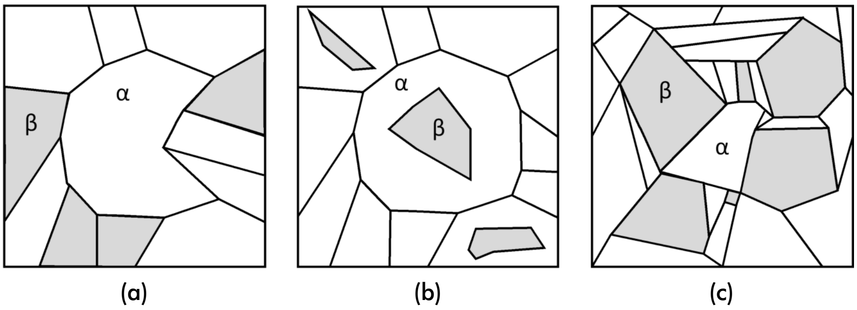

Fig. 3.13: Examples for complex mineral microstructures consisting of phases α and β, which cannot be synthesized with Voronoi tessellation: (a) Concave grains; (b) Grains that are embedded into other grains; (c) Neighboring grains of very different size or shape

This, however, is an unfavorable restriction because the mineral microstructures that are of interest for mineral processing simulations are seldom homogeneous and isotropic. In fact, it is very often the complexity of the mineral microstructure that justifies simulative efforts, since the mineral processing behavior cannot be derived from standard textbook knowledge. For this reason, tessellations approaches such as those based on Voronoi cells are discarded because they are always bound to their formation conditions and therefore are not flexible enough for the approach of this study.

As the final synthesis algorithm has to be able to create complex microstructures as well, a universal approach is chosen for the intended synthesis. Therefore, it is decided that the most appropriate way would be to draw the mineral microstructure on the basis of QMA results. The synthesis method developed from this idea is presented in the following.

Introduction of the drawing method

The basic idea of the proposed drawing method is adopted from a possible human drawing process. Let us assume that the mineral microstructure in Figure 3.14 is the original, which serves as pattern for drawing. In detail, it consists of NDP, which can be seen a matrix α and an embedded crystalline phase β.

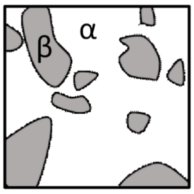

Fig. 3.14: Exemplary original microstructure, which is a pattern for drawing a synthetic microstructure

If one is faced with the task to draw a picture of this microstructure, which should not be a simple copy, but a statistical equivalent synthetic microstructure, the following procedure is possible:

1. Examine the original microstructure and determine the microstructural properties like grain size and grain shape.
2. Draw of grains with suitable properties on a blank sheet of paper.
3. Cut off a stripe of each image edge in order to eliminate the edge effect on the drawing process.
4. Compare the properties of the drawn synthetic microstructure with the properties of the original.
5. If the result of the comparison is insufficient, analyze which properties are drawn inadequately and restart the drawing process with improved focus on those properties.

In addition to this, Figure 3.15 shows the actual drawing process schematically for the given example. Starting from a blank sheet of paper, the grains of phase β are drawn until the visual appearance is satisfactory. The remaining blank area is considered NDP, which is phase α. Finally, the image is cropped so that the remaining part is free of any edge effect. If the comparison between the original pattern in Figure 3.14 and the cropped result in Figure 3.15c is satisfying, then a two-dimensional synthetic microstructure has been created that fulfills the own visual, subjective quality check.

As this creation procedure is based on a free drawing process, it is in principle possible to synthesize every two-dimensional microstructure. There are no restrictions so that also complex, concave and embedded microstructures can be synthesized in principle. Hence, this approach is seen to be suitable for synthesizing mineral microstructures as base for computational simulations like DEM.

However, it should be mentioned, that the freedom of the drawing process and the manifold possible drawing strategies make this approach also challenging. In contrast to the tessellation based synthesizing strategies, there is no unambiguous mathematical rule for constructing

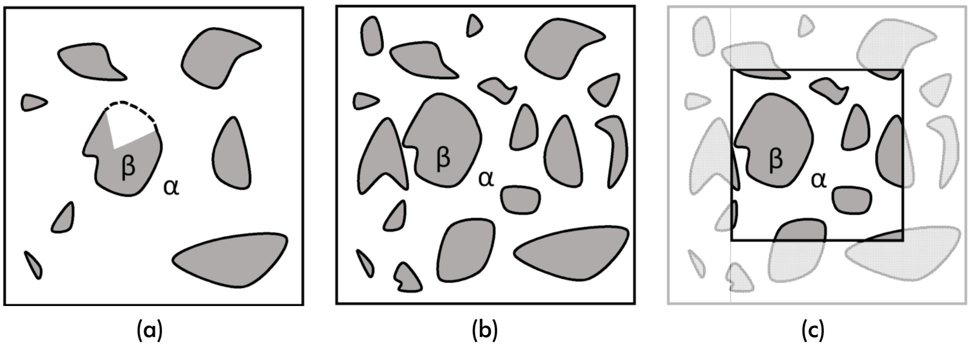

Fig. 3.15: Schematic ideal drawing process of a two-dimensional synthetic microstructure consisting of a matrix α and an embedded crystalline phase β: (a) Drawing of grains with suitable properties on a blank sheet of paper - The grain in the middle is being drawn at the moment.; (b) Image after completed drawing process; (c) Cropping the image in order to eliminate the edge effect on the drawing process

the synthetic microstructure. Instead, it is up to the drawer to find and use a suitable drawing strategy. While one drawer may begin to draw randomly distributed big grains and then proceed with the smaller ones, another could fill the image from left to right simultaneously with small and big grains. Hence, a variety of different drawing approaches is conceivable. They can produce similar results but also have discrepancies that can be explained by the different strategies.

3.3 Implementation of the drawing method

The implementation of the drawing method is done in the open source computing language Python and the imaging library PIL. The actual procedure of the program for creating a two-dimensional synthetic microstructure is comparable to the basic concept, which is presented in Section 3.2. But in contrast to the explained exemplary procedure of a human drawer, the implemented algorithms cannot rely on the learned human experience in analyzing and drawing of pictures. Instead, the program needs explicit instructions, how it has to proceed.

Therefore, the following section is dedicated to the drawing process. At the beginning, in Section 3.3.1 the synthesis of single grains is introduced. Based on this, it can be explained how the drawings of multiple grains can form a synthetic microstructure in Section 3.3.2. The more sophisticated synthesizing of microstructures consisting of multiple phases is described subsequently in Section 3.3.3.

The evaluation of the drawn structures is separated from the drawing process in the program. In contrast to a human drawer, who is able to evaluate and improve the drawing process on the fly, the program has to finish the synthesis first. The examination of the original microstructure and determination of the microstructural properties like grain size and grain shape is then done with the help of the QMA. Therefore, the two-dimensional adaption is used, as only two-dimensional microstructures are in focus of this study. The characteristics of the adapted QMA are not further discussed at this place, as they are already explained in Section 3.1.5. However, the combination of the drawing approach and the adapted QMA form the actual evaluation cycle. This is explained in more detail in Section 3.4, where the final program is introduced.

3.3.1 Drawing of a single grain

The actual drawing is done with polygons as it is possible to create every possible two-dimensional structure with this type of figure. Therefore, the PIL function `polygon` is used. This function allows to draw an arbitrary polygon. It consists of straight lines, which connect the given vertices `xy`. The vertices `xy` are provided as sequence of 2-tuples in the form `[(`x_1`, `y_1`), (`x_2`, `y_2`), ..., (`x_i`, `y_i`)]`. The color of the outline and the color of the polygon filling can be specified with corresponding parameters `outline` and `fill`.

```
ImageDraw.ImageDraw.polygon(xy,fill=None, outline=None)
```

For the purpose of drawing synthetic two-dimensional mineral microstructures, the drawn polygons are considered to represent single grains. Therefore, the polygons are drawn with black outlines, which is reserved for grain boundaries as explained in Section 3.1.2. Accordingly, the color of the filling is used as identifier for the phase of the grain. Therefore, a biunique color is assigned to every grain of a specific phase. This process is schematically shown in Figure 3.16 for a single grain that is drawn with gray filling. As the polygon is drawn on blank space, there are no external influences, which have to be considered yet.

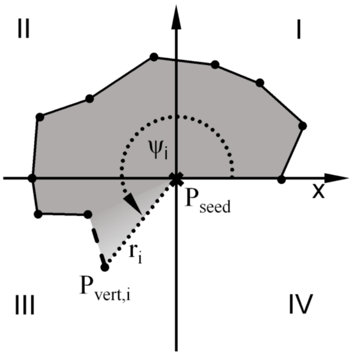

Fig. 3.16: Schematically drawing procedure of a single grain

The polygon is drawn around a preliminary chosen seed point P_{seed}. Based on this seed point, the drawing space, which also called canvas, is internally divided into four quadrants. The vertices, which form the polygon are then created counterclockwise. For each vertex, the corresponding drawing angle ψ_j and drawing radius r_j are calculated on the basis of a set of internal creation routines. Each vertex $P_{vert,j}$ is buffered until the coordinates of all vertices that belong to the polygon are calculated. Afterwards, the coordinates of the vertices are given as input parameter `xy` to the function `polygon`, which finally draws the grain.

As mentioned, the actual drawing process of the polygons is controlled by a set of internal creation routines and parameters as shown in Figure 3.17.

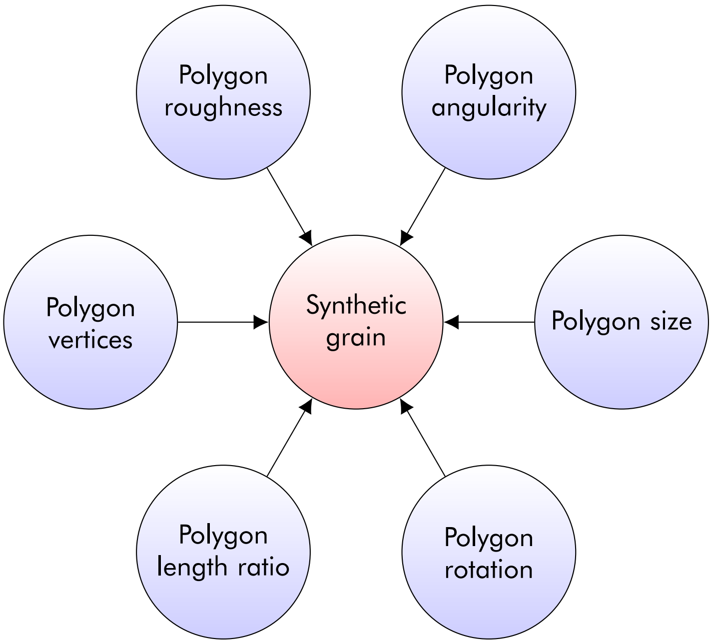

Fig. 3.17: Parameters for drawing a synthetic grain

In order to create the desired shape of a grain, the program can for example adjust the number of vertices and the size of the polygons. In order to allow variation of the grain shape, these parameters are coupled to additional deviation parameters. Furthermore, for the creation of elongated grains, a parameter that specifies the ratio of the semi-axis is used. In contrast, the transition from angular to rounded particles is defined by an internal factor for the degree of angularity and the grain boundary is further affected by a parameter for the polygon roughness. The possible different adjustments considered in the model are presented in the following.

Polygon size. Figure 3.18 shows exemplarily simple quadratic grains, which are all drawn by the `polygon` function. The different grain sizes are due to variations of the internal polygon size parameter $poly_{size}$. This parameter can be seen as basis for calculating the radius r_j with which the polygon is drawn at a certain drawing angle ψ_j. It is noted, that the slightly rounded corners are due to the finite number of vertices, which are used to draw the polygon. Hence, slightly rounded corners are considered to be typical for this approach. However, if necessary, this can be reduced by increasing the number of vertices.

Polygon angularity. Changing the general grain shape from angular to circular can be done through the internal synthesis parameter for the grain angularity $poly_{angular}$. As shown in Figure 3.19 the shape can infinitely be varied between a square and a circle.

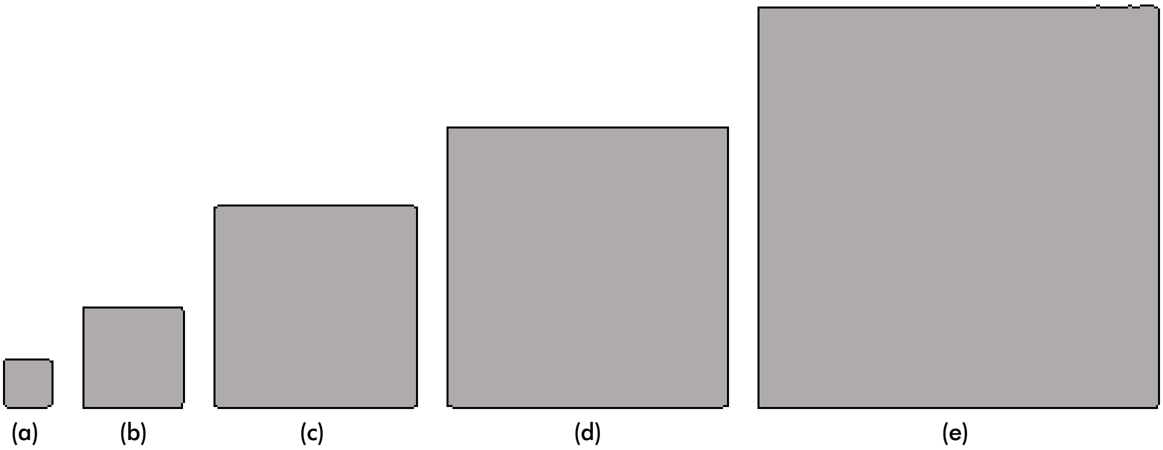

Fig. 3.18: Exemplary grains drawn with different polygon sizes $poly_{size}$ by the `polygon` function: (a) $poly_{size}$ = 12 pixels; (b) $poly_{size}$ = 25 pixels; (c) $poly_{size}$ = 50 pixels; (d) $poly_{size}$ = 75 pixels; (e) $poly_{size}$ = 100 pixels

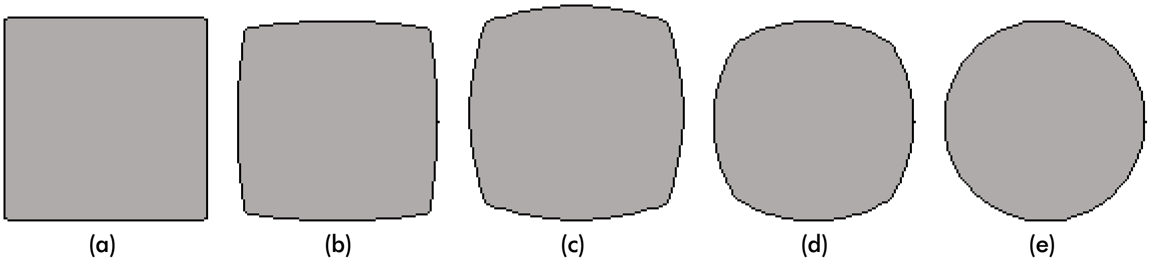

Fig. 3.19: Exemplary grains drawn with different polygon angularities $poly_{angular}$: (a) $poly_{angular}$ = 100 %; (b) $poly_{angular}$ = 75 %; (c) $poly_{angular}$ = 50 %; (d) $poly_{angular}$ = 25 %; (e) $poly_{angular}$ = 0 %

Polygon roughness. Based on the simple grain, it is possible to create more rough structures by increasing the polygon roughness (Figure 3.20). Therefore, the radii for calculating the single vertices of the grain are multiplied with a random factor. The range of the magnitude of this factor is an internal parameter that can be altered by the user, which results in different grain surfaces. In order to achieve a size independent result, the roughness parameter is set relation to the grain size.

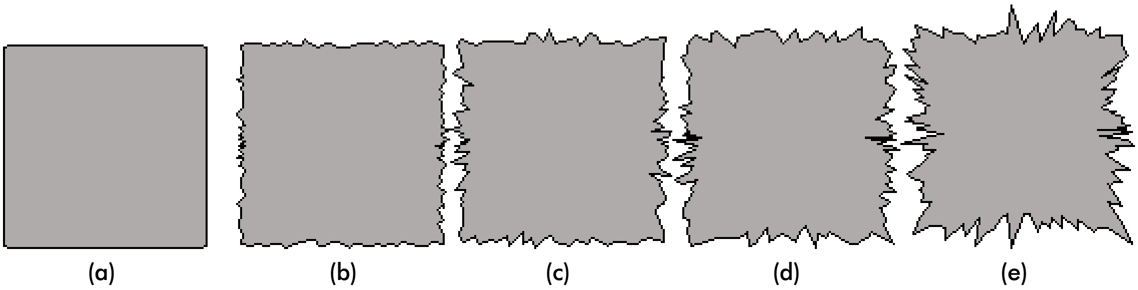

Fig. 3.20: Exemplary grains drawn with equal polygon sizes but different factors for the magnitude of the grain roughness $poly_{rough}$: (a) $poly_{rough}$ = 0 %; (b) $poly_{rough}$ = 2.5 %; (c) $poly_{rough}$ = 5 %; (d) $poly_{rough}$ = 7.5 %; (e) $poly_{rough}$ = 10 %

Polygon vertices. The influence of the number of vertices on the resulting grain shape is shown in Figure 3.21. Therefore, grains with an equal size $poly_{size}$ = 50 pixels and relative roughness $poly_{rough}$ = 10 % are drawn with different number of vertices. In order to make the result of this adjustment size independent, the number of vertices $poly_{vert}$ is set in relation to the grain size as well.

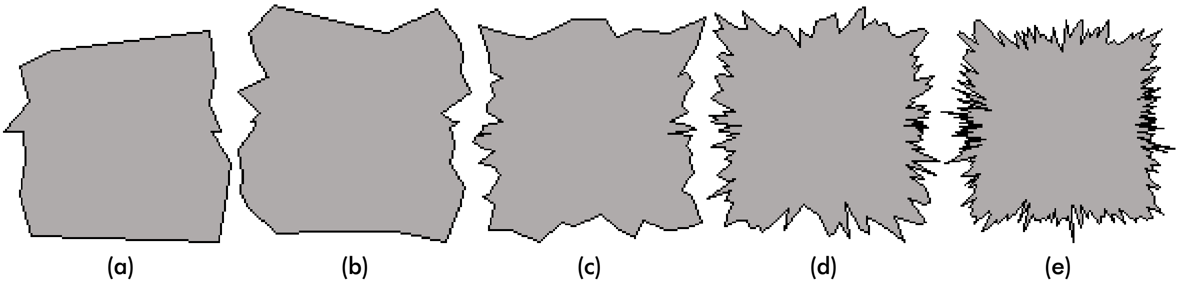

Fig. 3.21: Exemplary grains drawn with equal sizes and roughnesses but different relative numbers of vertices: (a) $poly_{vert}$ = 1 %; (b) $poly_{vert}$ = 10 %; (c) $poly_{vert}$ = 20 %; (d) $poly_{vert}$ = 50 %; (e) $poly_{vert}$ = 100 %

However, in contrast to the roughness parameter $poly_{rough}$, the circumference of the grain is used as reference. Since the circumference cannot be calculated before the drawing of the grain is completed, it is estimated by the circumference of an ellipsis with equal radii Equation 3.21.

$$C_{Ellipsis} = \pi(3\frac{a+b}{2} - \sqrt{ab}) \tag{3.21}$$

The calculated number of vertices is further altered by an additional normally distributed random number of vertices. For this a standard deviation $\sigma = 3$ is used. Depending on the sign of this random number, the rounded additional number of vertices is added or subtracted from the initial calculated number of vertices. This variability in the number of vertices for each grain is necessary to prevent undesired anisotropy effects. This would happen if all grains belonging to a specific phase would be drawn with the same number of vertices and at the same angles.

However, in order to avoid the accidentally creation of polygons with very few vertices, a lower limit is implemented. This prevents the creation of polygons with less than three vertices per quadrant. Hence, every synthetic grain consists of at least twelve vertices.

Polygon length ratio. The shape of the grains can further be controlled by the parameter for the length ratio of the grain (Figure 3.22). Grains with a length ratio of one tend to be equilateral, while lower ratios will result in elongated grains. This parameter has also a lower limit that prevents the program from drawing grains that are thinner than 10 pixels.

The influence of this limit can be seen in Figure 3.22e. A length ratio $poly_{ratio}$ = 0 % would result in infinite thin grains, which are impossible to draw. Consequently, this is prevented by the lower limit of $poly_{ratio}$, which instructs the drawing process to synthesize a grain with the thickness of 10 pixels instead.

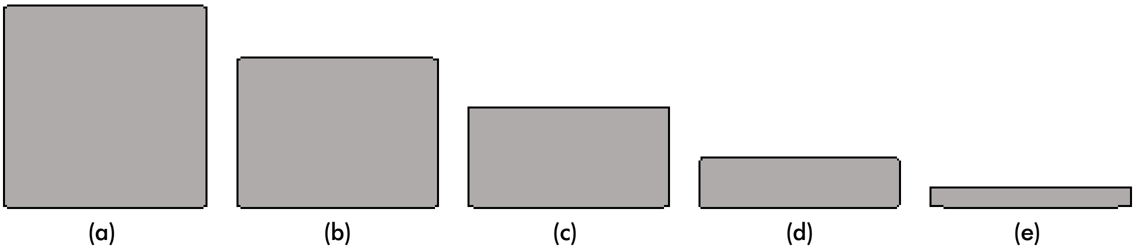

Fig. 3.22: Exemplary grains drawn with equal sizes but different length ratios: (a) $poly_{ratio} = 100\,\%$; (b) $poly_{ratio} = 75\,\%$; (c) $poly_{ratio} = 50\,\%$; (d) $poly_{ratio} = 25\,\%$; (e) $poly_{ratio} = 0\,\%$

Polygon rotation. In order to control the orientation of the grains in a synthetic microstructure, it is possible to rotate the polygons. Figure 3.23 shows grains, which are drawn with identical dimension parameters but different values for the polygon rotation $poly_{angle}$.

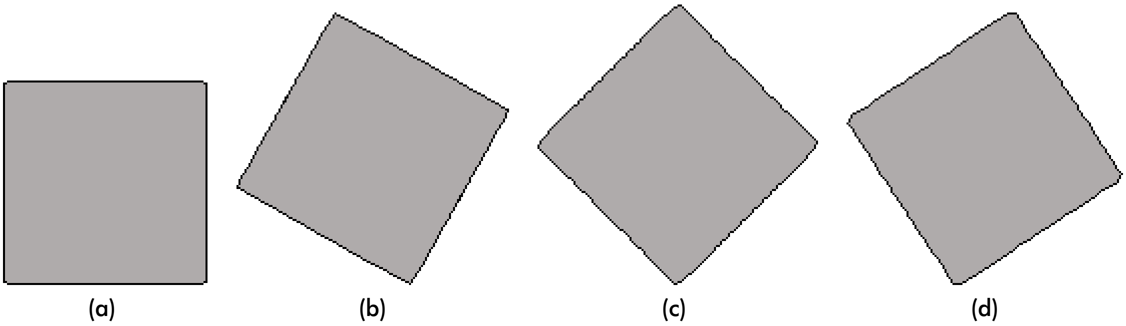

Fig. 3.23: Exemplary grains drawn with identical dimensions but different orientation angles $poly_{angle}$: (a) $poly_{angle} = 0°$; (b) $poly_{angle} = 22.5°$; (c) $poly_{angle} = 45°$; (d) $poly_{angle} = 67.5°$

Superimposition of the polygon parameters. In order to allow the synthesis of realistic mineral microstructures, the provided parameters for drawing different grain structures can be combined without restrictions. Hence, the program can generate a multitude of individual grain shapes. With regard to the diversity of possible parameter combinations, it is not intended to show all synthesizable grain shapes. Instead, Figure 3.24 shows some exemplary grains, which illustrate the manifold possibilities of the drawing method.

3.3.2 Drawing of multiple grains, which form a synthetic microstructure

As explained in the introduction (Section 1.1), mineral microstructures usually do not consist of a single grain but of a multitude of grains. Hence, in order to synthesize such a realistic mineral microstructure, it is mandatory to draw multiple grains one after each other, and fill the provided blank space. In general, it is started with drawing of the first grain, which is done on a blank space, as previously explained. The subsequent following grains are drawn

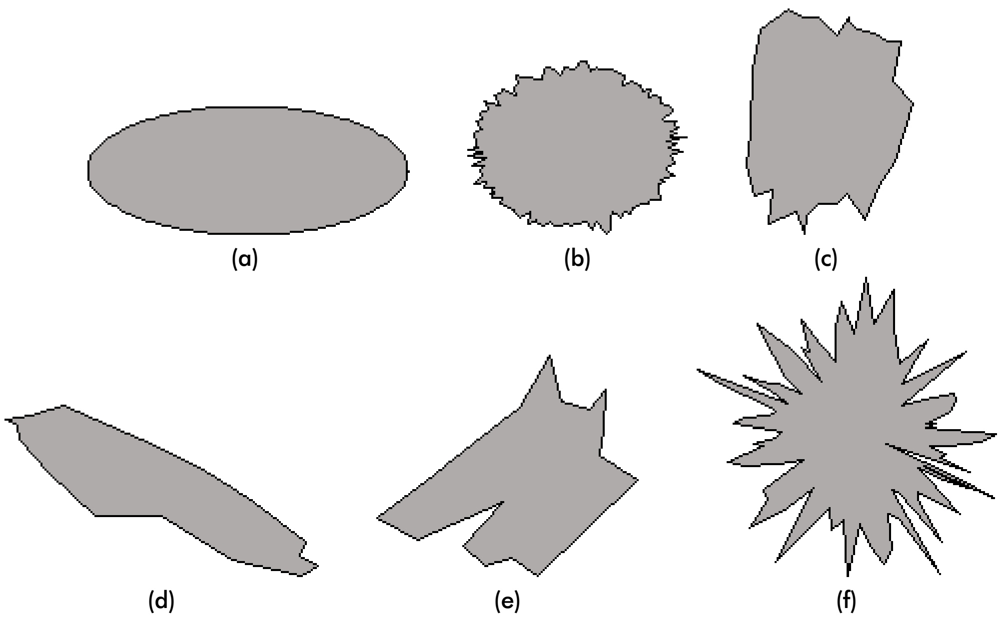

Fig. 3.24: Single grains, which are exemplarily drawn with different parameter combinations: (a) Smooth elliptical grain; (b) Rough rounded grain; (c) Cubical angulated grain; (d) Elongated angulated grain; (e) Grain with distinct concave edges; (f) Starlike grain;

on remaining blank areas of the space. The general procedure, which is used to synthesize a grain on a partially occupied canvas is shown in Figure 3.25.

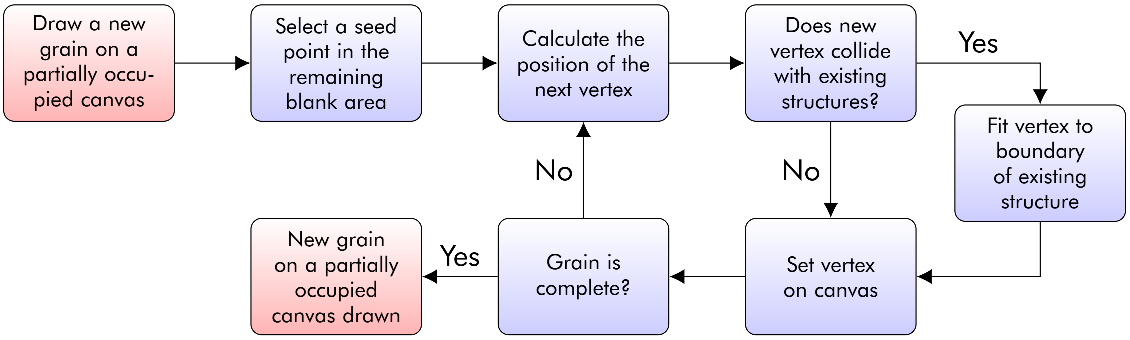

Fig. 3.25: Schematic procedure for drawing a new grain on a partially occupied canvas

Assuming that the program has to draw a new grain on the partially occupied canvas in Figure 3.26a, the first step is to randomly chose a new seed point P_{seed} in remaining blank area. Then the actual drawing of the new grain is done on the basis of the explained internal routines and parameters that are given as input parameters to the function `polygon` (Figure 3.26b).

The main difference is, however, that the program must take into account the already existing grains. Therefore, the program checks always if there are existing structures between the seed point P_{seed} and the next vertex $P_{vert,j}$. If there is an existing grain that prevents the program being able to draw the new grain undisturbed, the contour of the new grain is automatically aligned with the grain boundary of the existing grain.

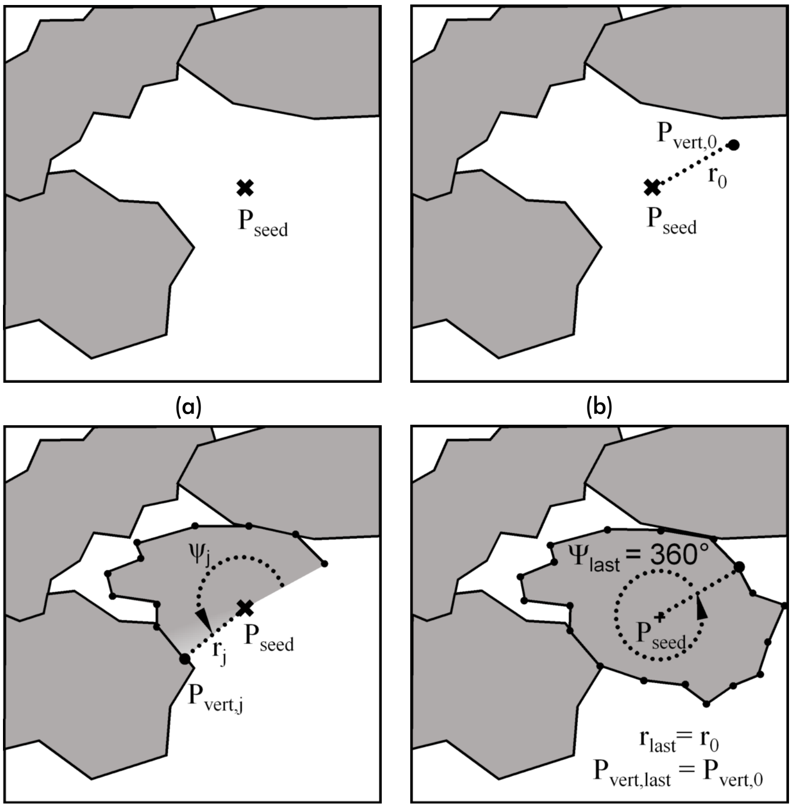

(a) (b)

(c) (d)

Fig. 3.26: Exemplary procedure for drawing a new grain in a partially occupied canvas with three grains present: (a) A new seed point P_{seed} is randomly set in the remaining blank area; (b) The first vertex $P_{vert,0}$ of the new grain with the radius r_0 is set undisturbed in the blank area; (c) The radius r_j of the Vertex $P_{vert,j}$ is adjusted so that $P_{vert,j}$ can be set exactly onto the existing grain boundary; (d) The drawing process of the grain is finished by closing the polygon

This situation can be seen in Figure 3.26c. The position of the new vertex $P_{vert,j}$ is adjusted, so that it does not overlap the existing grain. This procedure ensures two important conditions of the synthesis process. Firstly, it is prohibited that already existing grains are overlaid, which would change the characteristics of the already drawn grains. Secondly, the implemented algorithms, which are used to fit the new vertex to the existing grain boundaries, minimize the creation of small undesired voids between the existing and the new grains.

This procedure is continued as long as other grains are blocking the free drawing process. Otherwise the program proceeds with unhindered drawing until the polygon is closed as shown in Figure 3.26d. In this case, the drawing process of the actual grain is finished and the program continues by selecting the next seed point P_{seed} for the next new grain.

In addition to the parameters that affect the appearance of single grains, there are yet two other parameters implemented. Those can be used to change the characteristics of a microstructure that is formed by multiple grains of a specific phase. As they are important for the appearance of the final microstructure, they are explained in the following.

Deviation of the polygon size. The first parameter $poly_{\Delta size}$ can be used to control the deviation of the grain size distribution. Figure 3.27 shows the effect of this parameter on a synthesized monomineralic microstructure. If $poly_{\Delta size}$ is set to 0 % the grain sizes of the resulting microstructure are only affected by the preset grain size $poly_{size}$. The noticeable variations of the grain sizes and shapes are effects of the successive drawing procedure.

As shown in Figure 3.26 the synthesis process inserts the new grains in blank areas in between the existing structures. This results in the creation of smaller grains at the end of the synthesis process, since the remaining blank areas with decreasing sizes have to be filled as well. This random behavior is characteristic for the synthesizing program and cannot be directly influenced. Hence, every synthesized microstructure will have a minimum grain size deviation, which results from the generation process and depends on the other generation parameters. However, it is possible to actively increase the grain size deviation with the parameter $poly_{\Delta size}$, as it is shown in Figure 3.27b.

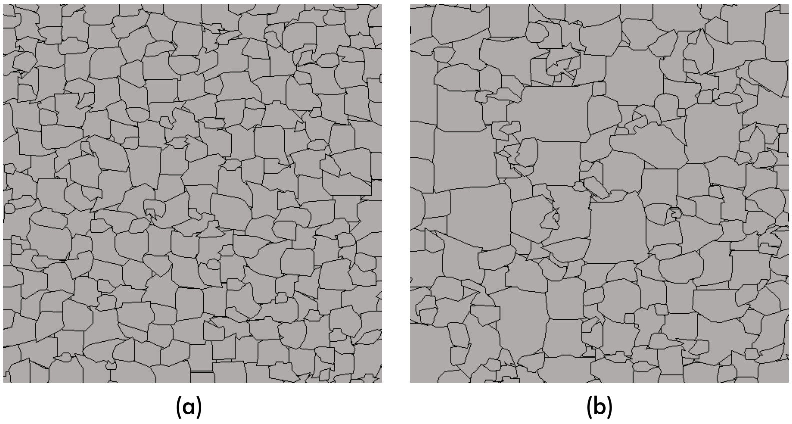

Fig. 3.27: Exemplary synthetic microstructures with different values for the deviation of the polygon size $poly_{\Delta size}$ but a constant value for the polygon size ($poly_{size} = 20$ pixels): (a) $poly_{\Delta size} = 0$ %; (b) $poly_{\Delta size} = 100$ %

Deviation of the polygon orientation. With the help of the second parameter $poly_{\Delta angle}$, it is possible to control the deviation of the orientation angle of the grains of a specific phase. This parameter can be interpreted as standard deviation for the orientation angle.

Figure 3.28 shows a synthetic monomineralic microstructure, which was created with different values for the deviation of the grain orientation angle. In order to increase the visibility of its effect, elongated grains with $poly_{ratio} = 20$ % were used as basis. If the deviation parameter is set to $poly_{\Delta angle} = 0°$, the program synthesizes an anisotropic microstructure with all the grains orientated in the same direction. However, with an increasing deviation parameter $poly_{\Delta angle}$, the degree of orientation decreases as can be seen in Figures 3.28b to 3.28d. Consequently, setting $poly_{\Delta angle}$ to 90° would result in an isotropic microstructure.

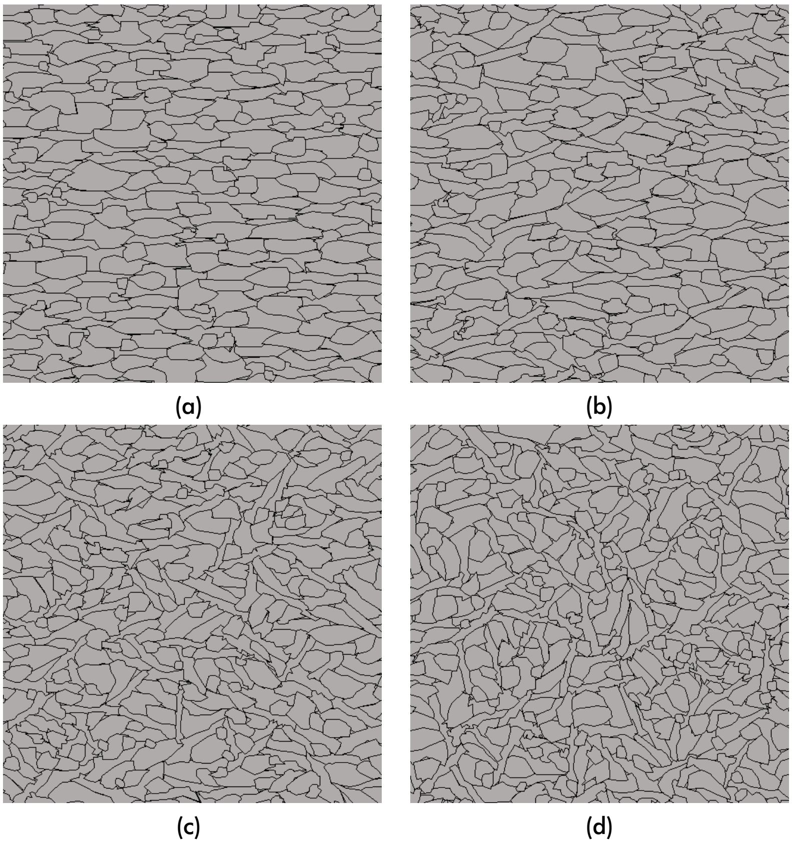

Fig. 3.28: Exemplary synthetic microstructures with different parameters for the grain orientation angles $poly_{\Delta angle}$: (a) $poly_{\Delta angle} = 0°$; (b) $poly_{\Delta angle} = 15°$; (c) $poly_{\Delta angle} = 30°$; (d) $poly_{\Delta angle} = 45°$

3.3.3 Synthesizing mineral microstructures consisting of multiple phases

As shown in the previous sections, it is possible to synthesize various different grain structures in principle. However, in order to allow the synthesis of realistic mineral microstructures, the program has to able to draw structures consisting of different mineral phases that have different characteristics. For this the parameter $poly_{color}$ and the so-called polygon density $poly_{desity}$ are introduced. Furthermore, the options for the purposefully synthesis of microstructures with pores or NDP, are explained in the following as well.

Synthesis of multiple mineral phases

Polygon color. Based on the proposed drawing approach, synthesis of more than one phase is possible without problems. Hence, it is only necessary to use different colors for the grain fillings. For this, the parameter $poly_{color}$ is introduced. By doing so, the number of phases is not limited. However, it is noted that any mineral microstructure to be synthesized has to consist of at least one phase, since a microstructure without mineral content is not defined.

Polygon density. A real mineral microstructure that consists of multiple constituents can be characterized by the specific area content ϵ_A of each constituent (Section 3.1.5). Hence, it is mandatory to enable the program to synthesize microstructures with predefined proportions of the different phases.

Unfortunately, it is not possible to predefine ϵ_A of each phase directly as the drawing procedure is based on randomized algorithms. Hence, the surrogate $poly_{desity}$ has to be used. This hypothetical value represents the proportion that the pixels of all grains of a specific phase would cover, if the grains could be drawn without any interference (Equation 3.22) on an empty canvas with the free drawing area A_{canvas}. The resulting unit is [%]. This can be calculated by using the estimated number of seeds for drawing polygons of a certain phase $poly_{seeds}$ the estimated average size of such a polygon $poly_A$.

$$poly_{desity} = poly_{seeds} \cdot \frac{poly_A}{A_{canvas}} \cdot 100\% \tag{3.22}$$

Therefore, the area covered by a single grain $poly_A$ is internally estimated by its average grain size $poly_{size}$ and aspect ratio $poly_{ratio}$ (Equation 3.23).

$$poly_A = {poly_{size}}^2 \cdot poly_{ratio} \tag{3.23}$$

Based on this, it is then possible to estimate the needed probability $poly_{Pr}$ for setting a grain seed of a particular phase with Equation 3.24. Therefore, the number of seeds for the grains of a specific phase $poly_{seeds,\,phase}$ is set in relation to the total number of seeds for the grains of all phases $\sum poly_{seeds,\,i}$. The actual selection of which phase the next grain is to be drawn is made randomly, based on these seed probabilities. The interplay of this selection mechanism and the other synthesis procedures is explained in more detail at the end of this section (Figure 3.31).

$$poly_{Pr,\,phase} = \frac{poly_{seeds,\,phase}}{\sum poly_{seeds,\,all}} \tag{3.24}$$

Hence, in combination with the parameter for the biunique color representation $poly_{color}$ and the multiple other drawing parameters (Sections 3.3.1 and 3.3.2), it is then possible to synthesize a complex microstructure as shown exemplarily in Figure 3.29.

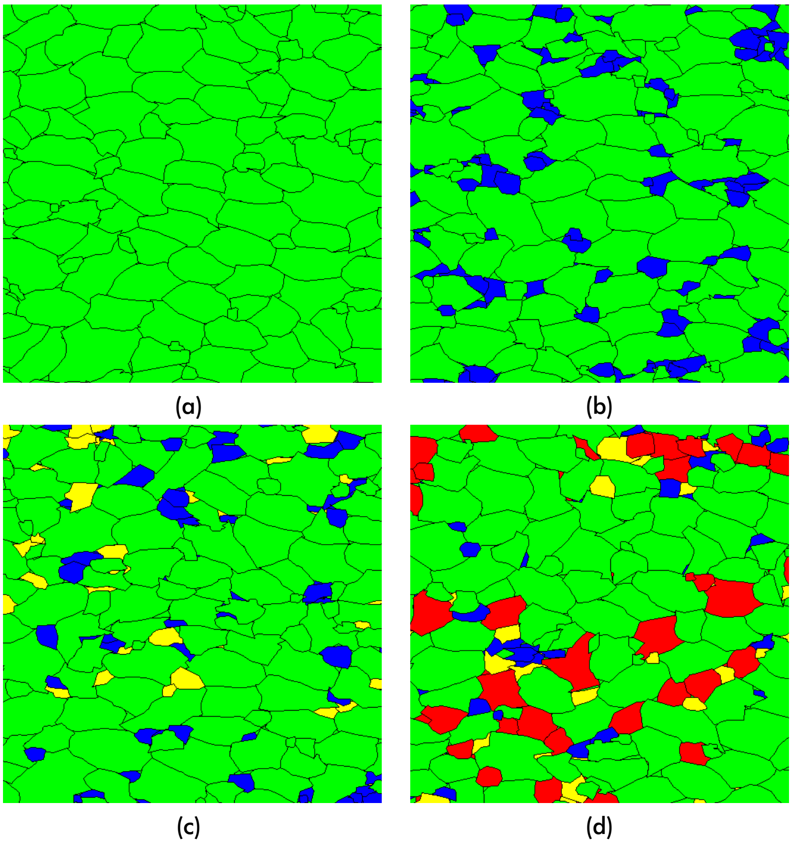

Fig. 3.29: Exemplary synthetic microstructures with different numbers of crystalline phases: (a) One phase; (b) Two phases; (c) Three phases; (d) Four phases

The synthesis of pores and NDP

The synthesis of pores is similar to the synthesis of crystalline phases in principle. For their synthesis, the color gray is reserved. Since it is irrelevant for the program whether the drawn polygon represents a crystalline phase or a void in the mineral microstructure, the same routines are used. Hence, the gray colored pore structures in Figure 3.30a are subjected to the same drawing conditions as the green colored mineral phase. The differences are only due to the very small size of the pore polygons $poly_{size}$ and the lower areal portion of a pores $\epsilon_{A,pores}$.

In contrast, the synthesis of NDP is not based on the drawing of polygons. The drawing of immeasurable small structures with the polygon approach makes no sense. It is more useful to handle the NDP like a contiguous phase that has no grain size. Hence, the synthesis can be done by filling the provided space with crystalline phases and pores until the left blank space is equal to the area content ϵ_A of the NDP. The synthesis is then interrupted and the remaining area is filled with the biunique color of the NDP. The outcome of such a synthesis process is shown in Figure 3.30b.

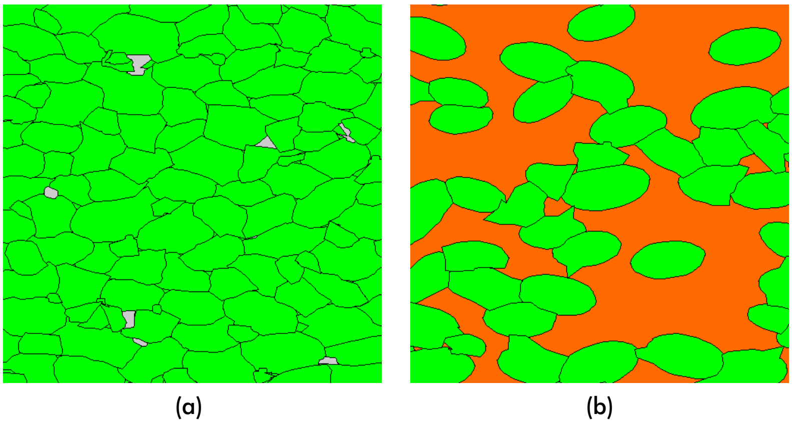
(a) (b)

Fig. 3.30: Exemplary synthetic microstructures of one crystalline phase in combination with pores and NDP: (a) Pores (gray) in monomineralic microstructure (green); (b) A crystalline phase (green) embedded in NDP (orange)

The interplay of the different synthesis steps

In order to generate a two-dimensional microstructure, the various presented synthesis steps and algorithms have to act together. This is schematically shown in Figure 3.31. For clarity reasons, this illustration is restricted to the main procedures.

In general, the synthesis cycle starts with a given set of synthesis parameters. These are for example the phases, possible pores, or NDP with the specific, associated polygon parameters, colors and seed probabilities. Furthermore, parameters defining the size of the drawing canvas or the length scale are provided.

Based on this, a canvas is created and a first phase for drawing a grain is chosen. This is done by random drawing according to the seed probabilities. Subsequently, a random seed point of the blank area is selected and the program starts to draw a grain according to the algorithms explained in Section 3.3.1. Afterwards, the remaining blank pixels of the canvas are determined, as they form the pool from which the next seed can be selected.

If the remaining blank area is equal or below the estimated areal proportion of the NDP, the remaining area is filled with NDP and the synthesis is finished. If this is not the case or there is no NDP to be synthesized it is further tested whether the remaining blank are is less than 5 % of the size of the initial blank canvas. If this is not the case the synthesis cycle continues with choosing the next phase for drawing a new grain.

In contrast, if the remaining free drawing area is small enough, the drawing cycle is stopped. It was found that, in this case, it is possible to assign the phases directly to the remaining voids according to their seed probabilities. This saves the program from fitting the new grains in the small remaining voids with the grain drawing approach, since the final shape of these grains is determined by the shape of the voids. Hence, the synthesis process can significantly speed up, without a change in the synthesis result.

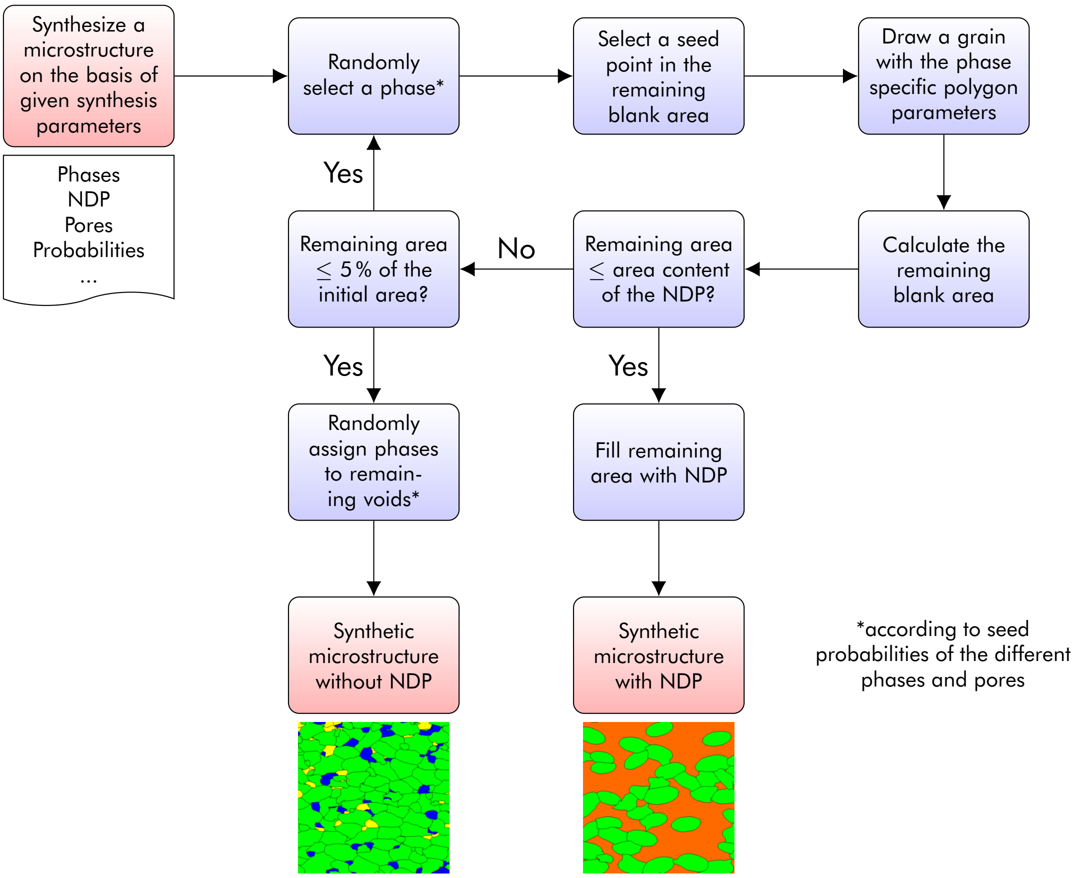

Fig. 3.31: Schematic drawing cycle for the synthesis of a microstructure

The above presented schematic cycle represents the synthesis procedure, which is further used. Nonetheless, it should be noted that this is not necessarily the optimal setup. It has proven to be a robust synthesis cycle design, which allows to generate various different microstructures. However, due to the modular, object orientated programming approach it easily is possible to change parameters like the threshold for filling the voids, alter the order of the sub-steps or even to integrate new processes.

3.4 The final program for microstructure analysis and synthesis

Altogether, the presented drawing cycle and the different parameters for the adjustment of the single grains as well as the parameters for drawing multiple grains and different phases are a solid basis for the intended synthesis of realistic mineral microstructures for DEM simulations. However, in order to synthesize realistic two-dimensional mineral microstructures, it is necessary to couple the artificial two-dimensional structures to the properties of real microstructures. An important parameter for doing so is the length scale S_L, which has to be provided by the user. This factor characterizes the size relationship between digital Pixel based false-color images and the real mineral microstructure.

With this parameter it is possible to connect synthesis and analysis approaches. For this reason, a python program has been created, which combines the original three-dimensional QMA, the adopted two-dimensional QMA, and the two-dimensional synthesis algorithms as well as a couple of additional functions for handling, inspection, import and export of synthetic and real microstructures. To make it easy to work with all its features, the applications are all linked to a Graphical User Interface (GUI) which is created with python library for creating graphical user interfaces on the basis of Qt (PyQt).

However, since the focus of this study is on the two-dimensional approach, only the essential program features, which are necessary for this, will be explained. A more general overview of the actual program and the setup of the GUI can be found in the Appendix B.

3.4.1 Synthesis and analysis of an example microstructure

For the evaluation of the principle functionality of the program, it is useful to work with an artificial example first. Based on this, it is also possible to analyze the reproducibility of the synthesis process. For this, the synthesized microstructures are analyzed with methods of the adapted QMA.

Analysis of a single microstructure

At the beginning, a single microstructure is synthesized only. This is used to focus on the performance of the drawing method in combination with a set of artificial input parameters.

The artificial example microstructure. Exemplary, such a synthetic microstructure consisting of four crystalline phases A, B, C, and D is examined in more detail. Therefore, it is synthesized with the input parameters shown in Table 3.2. Although the native unit for the average polygon size is Pixel, it is presented in mm as well for reasons of comparability. The initial size of the canvas is 5200 Pixels × 5200 Pixels including a margin of 100 Pixels at each side of the frame. After the drawing process, the margin is cropped, which results in a final canvas size of 5000 Pixels × 5000 Pixels. For this exemplary purpose a length scale of $S_L = 114\,\frac{\text{Pixel}}{\text{mm}}$ is used.

Qualitative evaluation of the synthesized example microstructure. The resulting false-color image of this synthetic microstructure is shown in Figure 3.32. Due to the final synthesis size of 5000 Pixels × 5000 Pixels it is difficult to plot the whole microstructure in a way that all

Tab. 3.2: Synthesis parameters for the example microstructure consisting of four crystalline phases in its native pixel based units. For reasons of comparability, the average polygon size is presented in mm as well.

Synthesis Parameter	Symbol	Unit	Phase A	Phase B	Phase C	Phase D
Color	$poly_{color}$	[–]	Blue	Green	Yellow	Red
Grain density	$poly_{desity}$	[%]	0.77	85.62	0.77	12.84
Seed probability	$poly_{Pr}$	[%]	11.77	58.82	11.77	17.65
No. vertices	$poly_{vert}$	[%]	100	100	100	100
Avg. size	$poly_{size}$	[Pixel]	15	50	15	25
		[mm]	0.13	0.44	0.13	0.22
Dev. size	$poly_{\Delta size}$	[%]	20	20	20	20
Roughness	$poly_{rough}$	[%]	0	10	0	30
Aspect ratio	$poly_{ratio}$	[%]	25	50	25	100
Angularity	$poly_{angular}$	[%]	100	0	100	0
Avg. orientation	$poly_{angle}$	[°]	0	0	0	0
Dev. orientation	$poly_{\Delta angle}$	[°]	3	15	3	15

the details are easily recognizable. Hence, an enlarged section of 1000 Pixels × 1000 Pixels is shown as well.

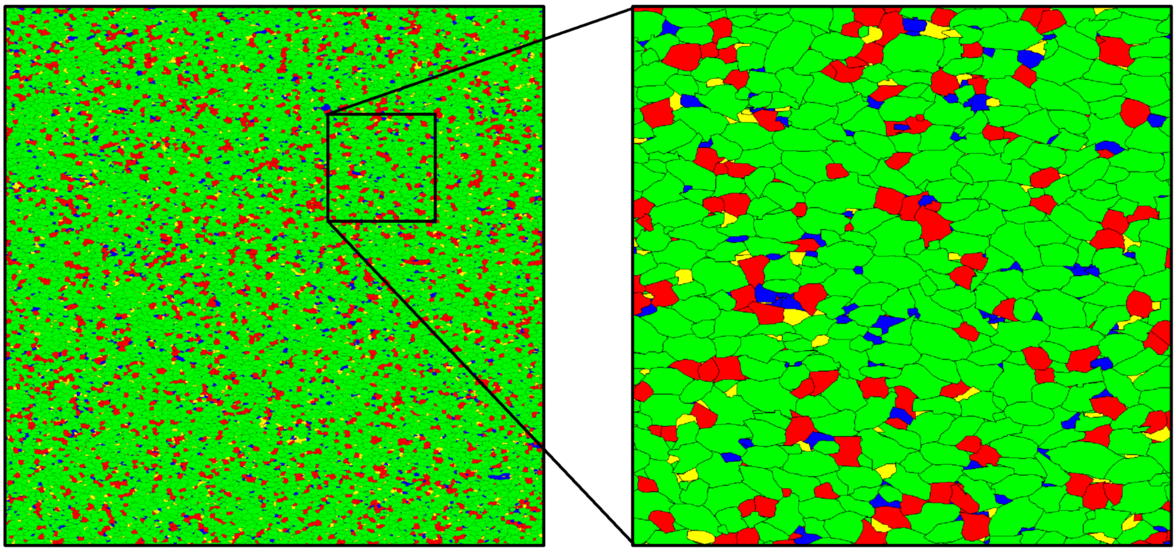

Fig. 3.32: Synthesized example microstructure: Original view of the size of 5000 Pixels×5000 Pixels (left); Example section of the size of 1000 Pixels × 1000 Pixels (right)

As can be seen from this figure, the program successfully finished the synthesis process. At first glance, the presented two-dimensional microstructure seems to fit the intended parameter setting. According to these, grains with four different colors were synthesized, which correspond to the preset color parameters. Furthermore, it can be seen that most of the synthesized microstructure is filled with green grains. This is also logical, since the grain density of the corresponding phase B has the highest value compared to the others.

Quantitative evaluation of the synthesized example microstructure. However, for a more detailed evaluation, it is necessary to analyze the QMA results. As explained, the characteristics of the two-dimensional microstructures are evaluated with the adopted QMA. In the program, the calculated analysis results are summarized in the corresponding tab (Figure B.3). However, in order to allow a consolidated evaluation, the results are discussed in the following in detail.

For this, the results of the adapted QMA are presented in Table 3.3. It should be noted that it is not possible to directly compare these results with the input parameters of Table 3.2. This is because of the superimposition of the various parameters for drawing the polygons of the different phases, which results in certain deviations of the final QMA parameters. However, it is possible to qualitatively compare the QMA results with the synthetic microstructure in Figure 3.32 and the input parameters.

Tab. 3.3: QMA results of a single synthesized example microstructure

QMA Parameter	Symbol	Unit	Phase A	Phase B	Phase C	Phase D	$\sum$
Areal proportion	ϵ_A	[%]	2.69	81.63	2.63	13.05	100.00
Median grain size	$x_{50,2}$	[mm]	0.22	0.54	0.22	0.38	0.50
Standard deviation	σ_{ln}	[-]	0.70	0.43	0.73	0.44	0.45
Elongation	El	[-]	2.11	1.59	1.63	1.51	1.49
Boundary line length	C_A	$[\frac{\mathrm{mm}}{\mathrm{mm}^2}]$	28.50	10.26	30.78	13.68	11.40
Deg. of roughness	K_R	[%]	18.00	17.71	27.66	13.20	18.82
Deg. of iso. orientation	K_{iso}	[%]	62.47	75.89	74.54	78.30	79.20
Deg. of lin. orientation	K_{lin}	[%]	37.53	24.11	25.46	21.70	20.80
Deg. of clustering	C_α	[%]	13.00	73.37	12.17	19.38	63.09
Deg. of space filling	ϵ_{AF}	[%]	—	—	—	—	100.00

Based on this, it is found that the general QMA parameters seem to confirm the visual evaluation of the synthetic microstructure in Figure 3.32. In total, four different phases were detected. The areal proportion ϵ_A of phase B is indeed the highest. It is followed by phase D, which was also synthesized with the second highest grain density. The same applies for the grain sizes of the phases B and D. These general parameters are complemented by the matrix of the bounding surfaces, which is shown in Table 3.4.

Tab. 3.4: Degrees of intergrowth $K_{I,(\alpha,\beta)}$ [%] for a single synthesized example microstructure

	Phase A	Phase B	Phase C	Phase D
Phase A	1.08	5.53	0.59	1.11
Phase B	—	66.83	5.69	13.03
Phase C	—	—	1.06	1.35
Phase D	—	—	—	3.73

However, in order to evaluate this in more detail it is beneficial to analyze the actual measured grain sizes. For this, additional information like the two-dimensional roses of intersections and plots of the grain size distributions are presented by the program as well. Besides the general parameters of the adapted QMA, these are also calculated automatically and presented to the user. The corresponding tabs with the results for this example microstructure are shown exemplarily in Figures 3.33 and 3.34. Hence, it is possible to evaluate the synthesis in more detail.

Evaluation of the grain size distributions. The more detailed analysis is started with the evaluation of grain size distributions, which were measured with the adapted QMA. These are plotted in Figure 3.33 in separate diagrams for each of the four phases and the sum of all microbodies. Each of the plots contains both, the frequency number distribution of the grain size $q_0(x)$ in shape of histograms and the cumulative area distribution of the grain size $Q_2(x)$.

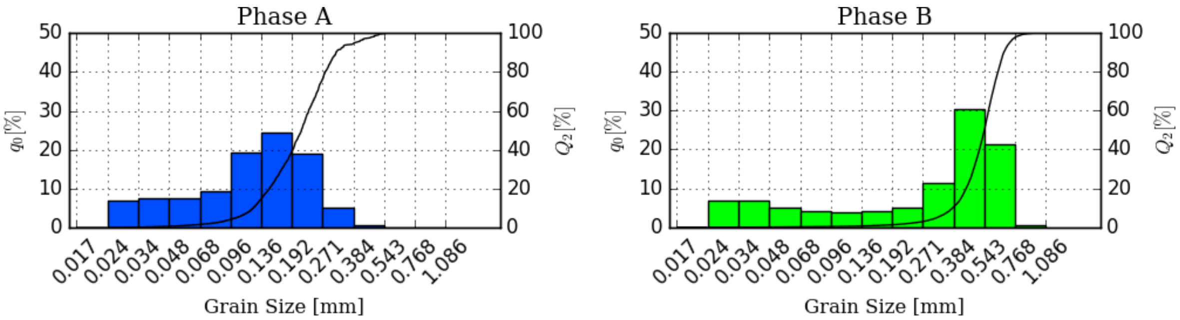

(a) Grain size distribution of phase A

(b) Grain size distribution of phase B

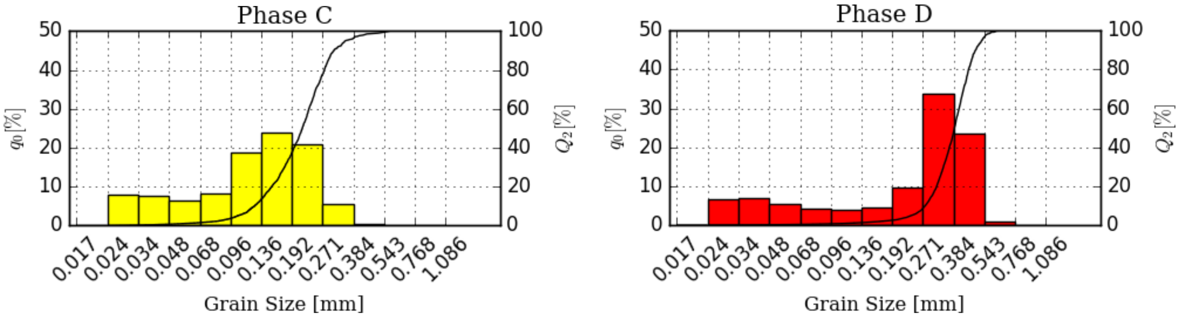

(c) Grain size distribution of phase C

(d) Grain size distribution of phase D

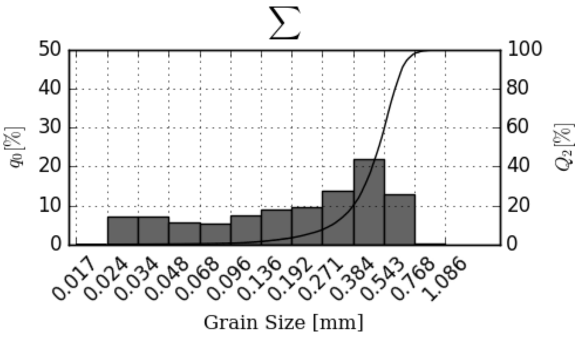

(e) Grain size distribution of the sum of the microbodies

Fig. 3.33: Grain size distributions of the synthesized example microstructure: (a) Phase A; (b) Phase B; (c) Phase C; (d) Phase D; (e) Sum of the microbodies

It is again noted, that there is no analytical relationship between the measured grain sizes and the input parameters for the average polygon sizes. Because of the superimposition of the various synthesis parameters during the drawing process on a continuously filled canvas, any correlations are subjected to certain deviations. Nevertheless, it is possible to do a qualitative assessment of the results.

For example, the evaluation of the cumulative area and the frequency number distributions reveals, that most of drawn grains are in the size ranges, which were defined by the synthesis parameters of the grain sizes $poly_{size}$ and its deviations $poly_{\Delta size}$. This is also the reason for the occurrence of the maxima at the coarse ends of the particle size distributions, which are clearly visible in the histograms of frequency distributions. A higher initial synthesis parameter for the grain size $poly_{size}$ results consequently in higher measured grain sizes like for phase B in Figure 3.33b.

The grains that are significantly smaller than those of the explained maxima at the coarse end, are the result of the interferences of the drawing process. On account of the fact that the generator draws new grains only on free area, small blank areas can occur between grain boundaries. These residuals usually remain until the end of the process. At this point, the algorithm has to fill these small relicts, although the fresh grains do not meet the preset grain distribution. Nevertheless, these discrepancies seem to be negligible with respect to the resulting cumulative grain area distribution $Q_2(x)$. If one considers the grain size distributions of the sum of all microbodies in Figure 3.33e as example, it can be seen that the cumulative area of all grains that are smaller than 0.096 mm is less than 1 %. Accordingly, the area of these small remains is insignificant compared to the area of the proper grains.

Evaluation of the roses of intersections. Besides that, further details can be found in the plots of the roses of intersection in Figure 3.34. Like for the grain size distributions, there is again one plot for each phase and an additional one for the sum of the microbodies.

Within each of these plots, there are two different curves plotted. The black represents an estimation of the program and the colored is the actually calculated two-dimensional rose of intersections. The program automatically plots the estimated rose of intersections for control purposes. Internally, it is used as a first guess for the approximation process for the final rose of intersections and is not taken into account for further discussion.

On the basis of these detailed analysis results, further synthesis parameters can be identified that influence the synthesis results. These may be, for example, the grain aspect ratio $poly_{ratio}$, the average grain orientation $poly_{angle}$, and the corresponding deviation $poly_{\Delta angle}$, which in combination seem to effect the shape of the rose of intersections.

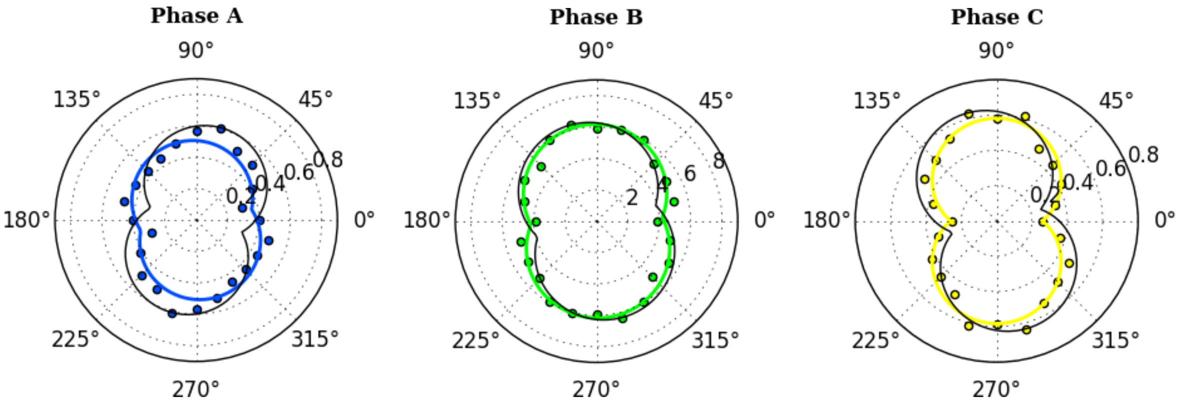

(a) Rose of intersections of phase A **(b)** Rose of intersections of phase B **(c)** Rose of intersections of phase C

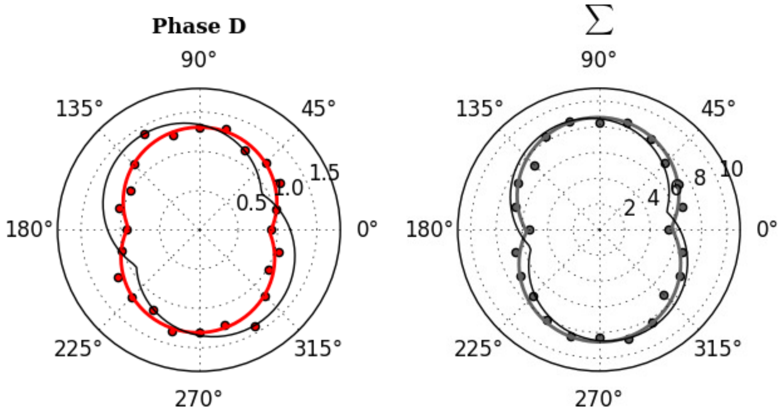

(d) Rose of intersections of phase D **(e)** Rose of intersections of the sum of the microbodies

Fig. 3.34: Two-dimensional roses of intersections [intersections /mm] of the synthesized example microstructure. The black curve is the estimated by the program automatically as first guess for the approximation process. The colored represents the final approximation: (a) Phase A; (b) Phase B; (c) Phase C; (d) Phase D; (e) Sum of the microbodies

A good example for such correlations can be found for phase C in Figure 3.34c. In this plot, the calculated curve is noticeably bounded at approximately 0° and 180°. This means, that significantly less intersections between grains of Phase C and any other grains were measured in horizontal direction.

The reason for this can be found in the special combination of the three mentioned parameters. First, the relatively low chosen aspect ratio for the grains ($poly_{ratio,C} = 0.25\,\%$) results in slightly elongated grains, which is indicated by its increased degree of elongation ($El_C = 1.513$). Hence, in combination with the low deviation of the orientation angle ($poly_{\Delta angle,C} = 3°$) around the major orientation direction, which is horizontal ($poly_{angle,C} = 0°$), this results in such a slightly orientated grain arrangement.

Analysis of the reproducibility of the synthesis process

For the purpose of evaluating the synthesis characteristics concerning possible correlations and reproducibility, the above mentioned example microstructure is synthesized additional eight times with equal synthesis parameters. This results in nine different synthetic microstructures in total, which, however, should have comparable microstructural characteristics. For evaluation, the average QMA results of the nine final synthetic microstructures are shown in Table 3.5.

Tab. 3.5: Arithmetic mean (AM) of the QMA results of the nine synthesized example microstructures

QMA Parameter	Symbol	Unit	Phase A	Phase B	Phase C	Phase D	$\sum$
Areal proportion	ϵ_A	[%]	2.48	81.89	2.48	13.16	100.00
Median grain size	$x_{50,2}$	[mm]	0.21	0.54	0.21	0.38	0.50
Standard deviation	σ_{ln}	[-]	0.69	0.44	0.70	0.43	0.45
Elongation	El	[-]	1.90	1.67	1.72	1.32	1.59
Boundary line length	C_A	$[\frac{\text{mm}}{\text{mm}^2}]$	29.77	10.26	30.40	14.06	11.78
Deg. of roughness	K_R	[%]	19.73	16.60	23.05	16.47	17.64
Deg. of iso. orientation	K_{iso}	[%]	67.75	73.61	72.69	85.35	75.91
Deg. of lin. orientation	K_{lin}	[%]	32.25	26.39	27.31	14.65	24.09
Deg. of clustering	C_α	[%]	12.46	74.13	12.21	21.90	64.01
Deg. of space filling	ϵ_{AF}	[%]	—	—	—	—	100.00

Evaluation of the averages of the general QMA parameters. The table of the general QMA results shows, that the analysis of the averaged results confirms the previous findings. For example, the measured median grain size $x_{50,2}$ correlates to a certain degree with the corresponding synthesis parameter $poly_{size}$. Hence, the grains of phases A ($x_{50,2,A} = 0.21$ mm) and C ($x_{50,2,C} = 0.21$ mm) are considerably smaller than those of phases B ($x_{50,2,B} = 0.54$ mm) and D ($x_{50,2,D} = 0.38$ mm). However, in comparison to each other, the grain sizes of phases A and C are identical. This is considered to be a direct result of the identical synthesis parameter for the grain sizes $poly_{size}$ for these two phases ($poly_{size,A} = poly_{size,C} = 0.13$ mm).

Nevertheless, the comparison between the measured grain sizes of Phases B and D proofs, that there is no direct analytical relationship. Although the size parameter for phase B ($poly_{size,B} = 0.44$ mm) is twice the parameter for phase D ($poly_{size,D} = 0.22$ mm), the resulting median grain size of phase B is only 42 % higher than for phase D.

Analogous evaluations can be done for other parameters like the degrees of orientation. Such an example is the synthesis parameter for the grain aspect ratio of phase D. $poly_{ratio,D} = 100\,\%$ means that the program tries to synthesize equilateral grains. The influence of this setting on the synthesis result is evident from the relatively high degree of isotropic orientation

($K_{iso,D} = 85.35\,\%$) for this phase. In turn the corresponding degree of linear orientation is relatively low ($K_{iso,D} = 14.65\,\%$).

Evaluation of the variation of the general QMA parameters. The reproducibility of the synthesis process can be evaluated with the standard deviation (SD) and coefficients of variation (CV). These measures of variations are listed in Tables 3.6 and 3.7. The statistic evaluation shows that the synthesis of the example microstructure is satisfactory in terms of comparability.

Tab. 3.6: Standard deviations (SD) of the QMA results of the nine synthesized example microstructures

Standard deviation of...	Symbol	Unit	Phase A	Phase B	Phase C	Phase D	$\sum$
Areal proportion	ϵ_A	[%]	0.097	0.402	0.089	0.298	0.000
Median grain size	$x_{50,2}$	[mm]	0.005	0.004	0.004	0.004	0.004
Standard deviation	σ_{ln}	[-]	0.015	0.011	0.016	0.008	0.010
Elongation	El	[-]	1.058	0.000	1.710	0.570	0.570
Boundary line length	C_A	$[\frac{\text{mm}}{\text{mm}^2}]$	0.265	0.071	0.269	0.104	0.050
Deg. of roughness	K_R	[%]	3.286	0.818	5.474	1.855	0.657
Deg. of iso. orientation	K_{iso}	[%]	6.668	2.061	6.831	4.043	1.568
Deg. of lin. orientation	K_{lin}	[%]	6.668	2.061	6.831	4.043	1.568
Deg. of clustering	C_α	[%]	1.394	0.534	1.638	1.420	0.725
Deg. of space filling	ϵ_{AF}	[%]	—	—	—	—	0.000

Tab. 3.7: Coefficients of variation (C_A) of the QMA results of the nine synthesized example microstructures

Coefficient of variation of...	Symbol	Unit	Phase A	Phase B	Phase C	Phase D	$\sum$
Areal proportion	ϵ_A	[%]	3.94	0.49	3.61	2.27	0.00
Median grain size	$x_{50,2}$	[%]	2.54	0.82	1.99	1.12	0.77
Standard deviation	σ_{ln}	[%]	2.14	2.52	2.29	1.81	2.23
Elongation	El	[%]	13.94	4.25	15.66	7.86	3.13
Boundary line length	C_A	[%]	3.55	0.00	5.63	4.05	4.84
Deg. of roughness	K_R	[%]	16.65	4.93	23.75	11.27	3.72
Deg. of iso. orientation	K_{iso}	[%]	9.84	2.80	9.40	4.74	2.07
Deg. of lin. orientation	K_{lin}	[%]	20.68	7.81	25.01	27.59	6.51
Deg. of clustering	C_α	[%]	11.19	0.72	13.42	6.49	1.13
Deg. of space filling	ϵ_{AF}	[%]	—	—	—	—	0.00

With regard to the coefficients of variation, it can be said that the areal proportions ϵ_A of all phases vary in the lower single-digit percentage range. The same yields for the texture parameters like grain size, shape, and surface, which are negligible.

The evaluation of the other parameters, shows relatively low coefficients of variation for phase B in contrast to those of the other phases. This outcome is considered to be related to the high areal proportion of this phase ($\epsilon_{AB} = 81.89\,\%$). Due to this, significantly more grains are included in the analysis process, so that the results are statistically more reliable. For the other phases with significantly lower numbers of grains, this results in increased coefficients of variation.

Hence, it is reasoned, that the variation of QMA parameters of the other phases could be reduced by increasing the number of grains of these phases, which would then be taken into account by the analysis. This can be achieved, for example, by increasing either the overall size of the synthesized microstructure or the areal proportion. However, it should be noted, that the latter would also result in new synthetic mineral microstructure with different characteristics.

However, the evaluation of the coefficients of variation for the whole microstructure, which is the sum of all microbodies, reveals sufficient low variations for all QMA parameters. In detail, all coefficients of variations except that for the degree of linear orientation K_{lin} are below 5 %, which is seen to be satisfactory. This assessment is supported by the comparison with POPOV [146]. In this study four different hard rocks, three granites and one gneiss, were analyzed with the original three-dimensional QMA three times each for comparison purposes. The variances of these real analyzes are all in the range or even a bit higher than the those of the example microstructure in Table 3.7. For illustration, the grain size of the sum of the microbodies is selected as an example. This parameter has a coefficient of variation of 0.77 % for the example above. The corresponding variations of the real test are between 2.69 to 39.29 %. This clearly shows that the proposed method can synthesize mineral microstructures relatively reproducibly if the drawing area is sufficiently large. Higher degrees of variation could be achieved if the observation area were more limited as in the real tests.

The relatively high coefficient of variation of the degree of linear orientation is kind of misleading in this case. As the sum of the degrees of isotropic and linear orientation is always 100 %, the variation of both parameters is coupled. Hence, both have the same standard deviation ($SD(K_{iso,sum}) = SD(K_{lin,sum}) =$ 4.04 %). However, as the references are different, both coupled values have different coefficients of variation ($CV(K_{iso,sum}) =$ 2.07 %; $CV(K_{lin,sum}) =$ 6.51 %). Hence, both have always to be seen in relation to each other.

Evaluation of the additional QMA parameters. Analogous to the general QMA parameters, it is furthermore possible to evaluate the degrees of intergrowth. For this reason, Table 3.8 shows the average degrees of intergrowth between the different phases for the nine example microstructures in the shape of an upper triangular matrix. The average results shown correspond to the results of the individual example microstructure, without any further knowledge being gained.

Tab. 3.8: Arithmetic mean (AM) of the degrees of intergrowth $K_{I,(\alpha,\beta)}$ [%] of the nine synthesized example microstructures

	Phase A	Phase B	Phase C	Phase D
Phase A	0.98	5.21	0.50	1.15
Phase B	—	67.34	5.28	13.02
Phase C	—	—	0.98	1.22
Phase D	—	—	—	4.32

However, Table 3.10 show, that the degrees of intergrowth are also subjected to more variation, if the frequency of occurrence of the associated phases is low. Exemplary for this are the results for phases A and C. However, the overall evaluation of these results confirms that the synthesis outcome is satisfying, as the variations for the mean components are insignificant.

Tab. 3.9: Standard deviation (SD) of the degrees of intergrowth $K_{I,(\alpha,\beta)}$ [%] of the nine synthesized example microstructures

	Phase A	Phase B	Phase C	Phase D
Phase A	0.14	0.14	0.05	0.07
Phase B	—	0.68	0.27	0.33
Phase C	—	—	0.15	0.09
Phase D	—	—	—	0.40

Tab. 3.10: Coefficients of variation (CV) of the degrees of intergrowth $K_{I,(\alpha,\beta)}$ [%] of the nine synthesized example microstructures

	Phase A	Phase B	Phase C	Phase D
Phase A	14.29	2.69	10.00	6.09
Phase B	—	0.99	5.11	2.53
Phase C	—	—	15.31	7.38
Phase D	—	—	—	9.26

Conclusions on the artificial example

Altogether, the overall results of this example test series are satisfactory. It has been demonstrated that an artificial synthetic microstructure can successfully be synthesized and analyzed with the created program. The synthesized microstructure is then displayed by the program for visual inspection and can be exported as image for further use. For the primary evaluation, the program provides the user with the general QMA results. In addition, a more detailed evaluation can be made on the basis of the matrix of bounding surfaces as well as on the plots of the grain size distributions and the roses of intersections.

With respect to the presented artificial four-phase example, the analysis results were used to prove that the synthesis is reproducible. Furthermore, these suggest that there are correlations, but no analytical relationships, between the synthesis parameters and the QMA results of the corresponding phases. Hence, the program itself as well as the implemented synthesis and analysis algorithms are considered to be suitable in principle for a systematic microstructure synthesis. However, in order to be able to synthesize a realistic mineral microstructure based on the real microstructure sample, a specific procedure has to be used, which is explained below.

3.4.2 Procedure for generating a realistic synthetic microstructure of a given real microstructure

The previous example shows that the synthesis process is reproducible and that there are correlations between the synthesis parameters and the QMA results. However, in order to determine the appropriate synthesis parameters for synthesizing a realistic microstructure, it is necessary to find unambiguous quantifiable correlations between the synthesis parameters on the one hand and the characteristics of the synthetic microstructure on the other. Unfortunately, a direct calculation of the synthesis parameters on the basis of the QMA results of the real example microstructure is not possible.

Parameter estimation based on computer experiments. The reason for this are the numerous interdependencies between these parameters. For example, the final grain size $x_{50,2}$ is of course mainly determined by the corresponding size parameter of the synthesis algorithm $poly_{size}$. Though, there are also other parameters that have direct or indirect influence. In case of the grain size, the aspect ratio $poly_{ratio}$ and angularity $poly_{angular}$ must also be taken into account, as they affect the final grain area and thus the measurable grain size. Furthermore, indirect influences of other synthesis parameters of the same or even of other phases cannot be excluded without doubts.

In order to help the user with finding the right set of synthesis parameters, the program is able to estimate those on the basis of predefined models. This approach is based on Design of Experiments (DoE) for computer experiments and consecutive regression analysis and modeling. The details of this methodology are explained in Appendix B.6.

The final synthesis procedure. The general approach for the synthesis of a microstructure that reflects a real example microstructure appropriately is shown in Figure 3.35. The starting point is always the adapted QMA of the real microstructure, which forms the basis of the estimation process. Alternatively, it is possible to import the results of a microstructure that has been analyzed previously or enter the QMA parameters manually.

At this point, the user has the choice of whether the program should automatically estimate the synthesis parameters on the basis of the computer experiment or whether he wants to

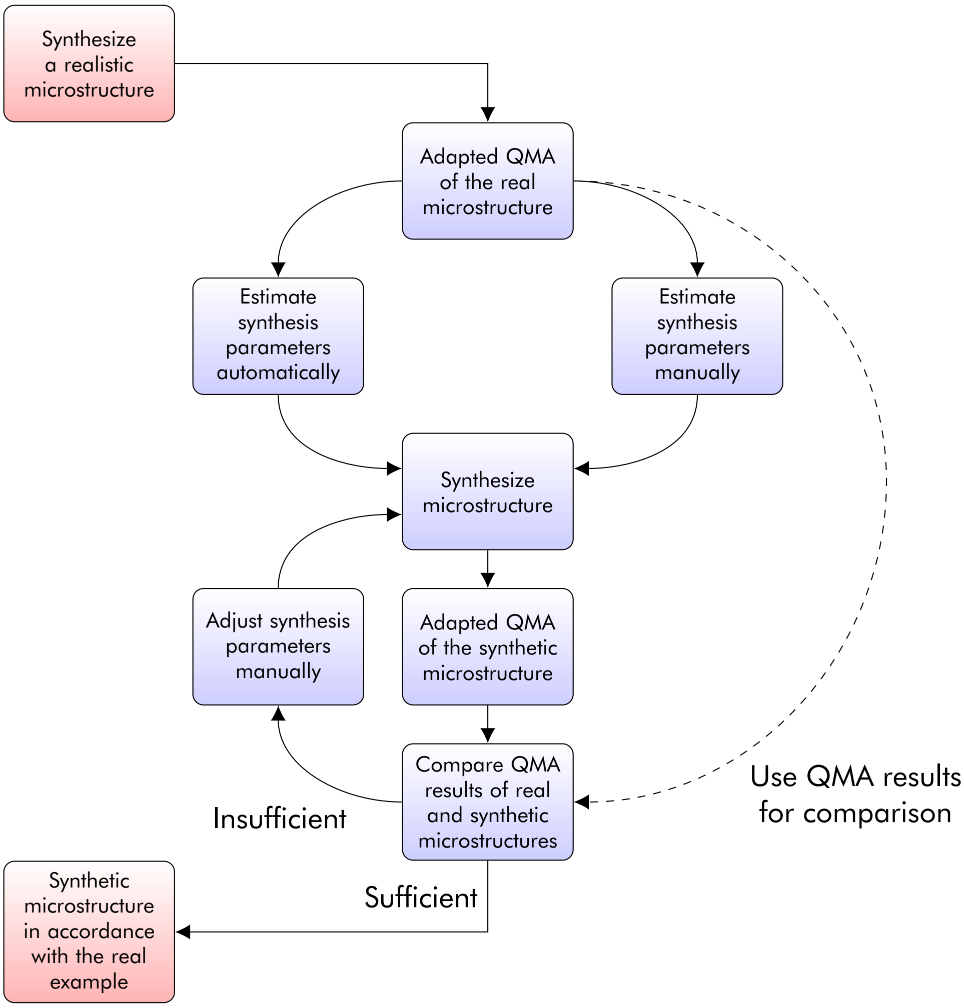

Fig. 3.35: The final procedure for synthesizing a realistic microstructure on the basis of the adapted QMA of a real sample

enter his own parameters manually. The latter, however, is only a useful, if the operator has previous knowledge about the needed synthesis parameters. This can be the case, if, for example, an older synthesis should be repeated on the basis of the corresponding synthesis parameters without synthesizing these again.

Subsequently, a microstructure will be synthesized in a first trial using those estimations. This microstructure is also analyzed with the adapted QMA and the results are compared to those of the real sample microstructure. If the comparison reveals discrepancies between both microstructures, which are unacceptable for the user, he has to adjust the synthesis parameters and restart the actual microstructure generation.

Due to the interdependencies of the synthesis parameters, this is an iterative process. Nevertheless, testing the program has shown that optimizing the results is usually an uncomplicated process. Since the user can directly see from the changes in the QMA of the newly synthesized microstructure whether his parameter changes have improved the correspondence between the two microstructures, he can identify the parameters relevant for the fine tuning relatively quickly. Based on this, that iterative cycle is repeated until the results are found to be satisfactory.

The criterion according to which the results are classified as satisfactory, however, depends on the respective application. It is conceivable to optimize the parameters until a single microstructure was synthesized, whose differences in the QMA results are below individual limit values. In addition, it is also possible to synthesize a series of microstructures with the same input parameters and consult the averages and variation measures. At this point, the user has to decide, what degree of agreement between the real and the synthetic microstructure is required for the appropriate further use of the synthetic.

In summary, this synthesis procedure is seen to be suitable for the synthesis of a realistic mineral microstructure as it is intended by this study. However, there is of course potential for further development. For example, it should be possible to automate the adjustment of the synthesis parameters after the comparison of the results. For this purpose, machine learning algorithms such as those based on artificial neuronal networks could be used. However, this would go beyond the scope of this study. In order to justify such far-reaching further developments, the synthetic microstructure approach has to be validated first. If the results are positive, it is possible to enhance the synthesis with such features.

4 Validation of the synthesis approach

As shown with the example in Section 3.4, it is generally possible to synthesize two-dimensional microstructures with the proposed grain drawing approach. Moreover, the example verifies the reproducibility of such microstructures. However, in order to use this approach for real simulations tasks, it is mandatory to prove its applicability in a real environment. This shall be done in a proof of concept study, which is presented in this chapter.

For this purpose, some general methodical considerations are made first, which are the basis for determining the structure of this study (Section 4.1.1). Subsequently, the individual experiments and the corresponding simulations are presented and evaluated separately in Sections 4.2 to 4.4.

However, it is noted, that although it is intended to analyze the experiments as comprehensive as possible, the main emphasis is set on the evaluation of the applicability of the proposed synthetic microstructure approach. Following this, the findings and conclusions of these distinct tests are then summarized in Chapter 5, where the general applicability of the synthetic microstructure approach is evaluated.

4.1 Methodical considerations

The selection of the tests for this proof of concept study is oriented to the needs for evaluating the synthetic microstructure approach. Therefore, it is suggested to use a comparison based validation procedure. The characteristics of the real and the simulated experiments are deduced from this experimental procedure and explained in the following.

4.1.1 The basic idea of the validation procedure

For the purpose of validation, a two-parted comparison procedure is considered in general. This approach consists of a real comminution experiment and a simulative twin, which is done in parallel, as shown in Figure 4.1. The basic idea is to conduct a real experiment, where the influence of the mineral microstructure becomes apparent. The experiment is then simulated with a realistic mineral microstructure, which is generated with the developed synthesis program. Finally, the results of both parts of the validation approach are compared with each other.

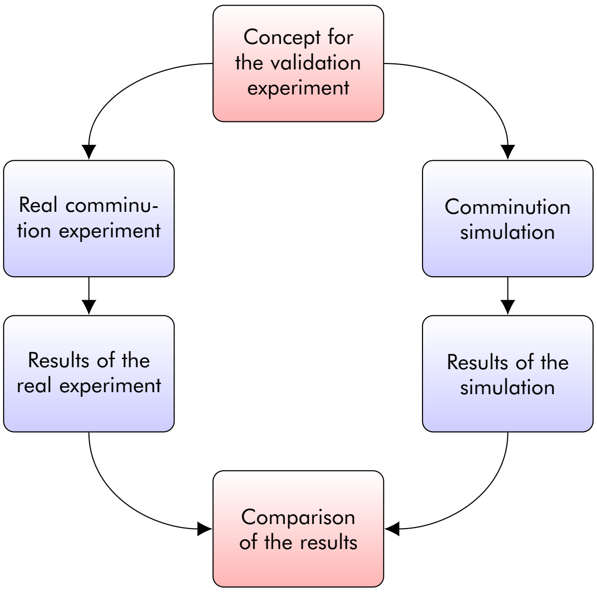

Fig. 4.1: Schema for a parallel fracture test and simulation

For the comparison, the focus is set on verifying the applicability of the synthetic microstructure approach. Therefore, the influence of the mineral microstructure on the comminution process is analyzed. The results of this process are then used as basis to evaluate whether the suggested synthesis approach is expedient or not in order to reproduce the comminution characteristics in simulations. However, as this study is designed as proof of concept, it is noted that the aim is not to fully reproduce the exact physical behavior of the real experiment.

Considerations for the real comminution experiments

The success of this approach relies on the appropriateness of the chosen real benchmark fracture test. In order to compare and evaluate the fracture behavior of a two-dimensional synthesized mineral microstructure, the chosen experimental setup has to meet specific requirements. The basic idea is to use a setup that allows best comparability between the real and the simulated fracture test with DEM. Hence, the dimensionality of the real and the simulated test should be the same. Given that the dimensionality of the simulation is limited by the two-dimensionality of the synthesized microstructure, the real setup has to be at least quasi-two-dimensional as well.

Further, for the sake of an easy to monitor fracture process, the test has to be quasi-static. This requirement benefits also the comparability to the BPM simulation, since the simulation models, which are typically used for minerals, do not take the influence of the load rate into account. In addition, the test setup needs to allow the measurement of characteristic test parameters.

Although many existing fracture tests for rock, like the Brazilian test or the Unconfined Compressive Strength (UCS) test, are quasi-static and do allow measurements of significant parameters, none of them meets the required two-dimensionality. Hence, as this two-dimensionality is essential to allow a reliable comparison between the simulated and the real experiments, these tests drop out.

For this reason, customized fracture tests will be developed. It is found that the advantages for the evaluation quality that came along with such tailored setups outweigh the disadvantages of the relatively high expenses for the test design. Consequently, it is also possible to consider restrictions resulting from the simulation capabilities for the test design.

Considerations for the comminution simulations

In order to utilize the synthetic microstructure for the purpose of comminution simulations, the chosen DEM environment has to be capable to simulate such a microstructure in general. By now, neither the commercial nor the open-source software projects provide this feature. Hence, it is necessary to develop a suitable DEM feature first.

The used DEM software. For this purpose, the open source framework Yet Another Dynamic Engine (YADE) [192] is predestined. It is a simulation environment, which has its origin in geomechanics and associated fields of research. According to this, it uses the Newtonian motion equations for the calculation of the particle motion. In combination with its predefined soft sphere approach for the particle contact, it is a classical representative for simulation environments on the basis Time-Driven Methods (TDM). Though the underlying DEM code used by YADE is not very fast, it is stable and reliable. Furthermore, YADE also has a user-friendly environment, which allows easy access via Python, which is used at the front end. Therefore, it is easy to implement own new features and test them immediately.

The final implementation in YADE is of course dependent on the actual experimental setup, which has to be simulated. However, there are some general characteristics that apply for all the following simulations of this proof of concept study.

Simulation dimensionality. As YADE is originally a pure three-dimensional environment, it is adapted to the needs of this study. Therefore, the simulation is manually restricted to the xy-plane, by blocking all motions, forces, and momentums along the z-axis. This results in a pseudo two-dimensional simulation environment. Although, all simulation objects have three-dimensional properties, they act like their planar equivalents. Hence, the spheres, which are typically used in YADE as discrete elements, act physically like circles in a plane, because any physics in the z-plane is suppressed.

General mapping procedure. For the presented program and its synthesis outcome, a possible mapping procedure is outlined in the following. For this, the exported image of the synthetic microstructure to be used in the DEM simulation is the basis. The actual process of mapping a synthesized two-dimensional microstructure into a DEM environment is exemplarily shown in Figure 4.2.

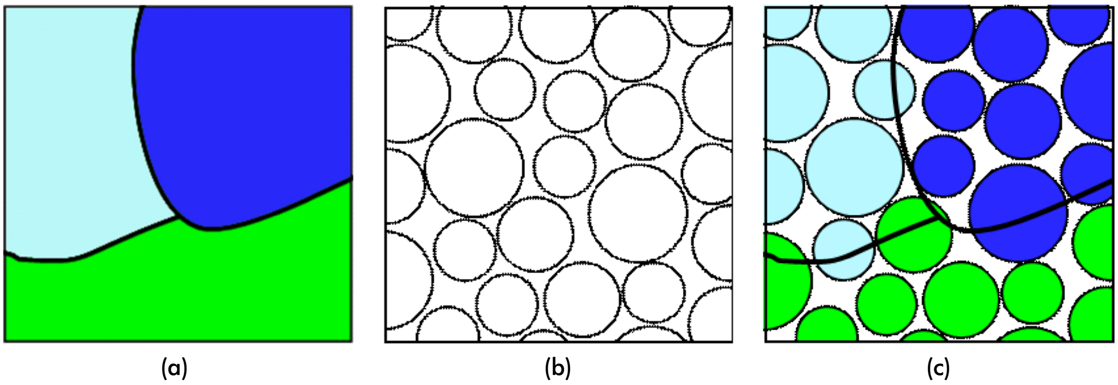

Fig. 4.2: Schema for mapping a two-dimensional microstructure onto a packing of circles: (a) Example microstructure with three adjoining grains; (b) Random raw packing of circles; (c) Final packing of circles with assigned material properties according to the example microstructure

Therefore, also an appropriate raw packing of discrete elements, like the circles in Figure 4.2b, is needed. For this validation study, the GenGeo library is used to generate such raw packings [60]. After their generation, they are imported into the YADE simulation. If the raw packing is ready, the mapping can be started.

For the explained mapping procedure, a python based extension for YADE was programmed. It handles the import of both the synthetic microstructure and the raw packing and controls the actual mapping process. During this, the program uses the synthetic microstructure as a template for the material assignment within the simulation. The assignment process analyzes, which grain is situated at the corresponding coordinates of each discrete element of the synthetic microstructure and assigns the associated material type to the discrete element.

Implementation of particle breakage. In the scope of this mapping procedure, it is further mandatory to implement the microstructure on the physical level of the simulation. Therefore, it is decided to use a BPM based approach. As explained in Section 2.1.2, this allows to model deformable composite particles in general. For the intended purpose, it is useful to make the bondings breakable so that the fracture process can be simulated explicitly. This means, that the given mineral material is represented by an arrangement of bonded discrete elements. These, however, can break, if the load on the bondings exceeds the predefined bonding strength, which is advantageous for simulating the comminution processes of the real experiments.

Particle contact model. The BPM approach has to be realized with a suitable model for the particle contact. Inside YADE, this can be done with different enhanced implementations of the classical linear elastic-plastic law of CUNDALL and STRACK [38]. The class `Law2_ScGeom6D_CohFrictPhys_CohesionMoment()` provides an implementation that adds the possibility of cohesive bondings for interactions between spheres to the classical law. Although this model is originally designed for spatial contacts, it can be used for two-dimensional models as well. As already discussed, the z-axis is blocked for this reason.

Resulting bonding types. With this particle contact model, the program can create the bondings between all neighboring discrete elements. Regarding the mapped mineral microstructure, it is possible to distinguish between inter- and intragranular bondings, in general. In addition, the intergranular bonds can be further distinguished in bondings between different grains of the same material and bondings between grains of different materials.

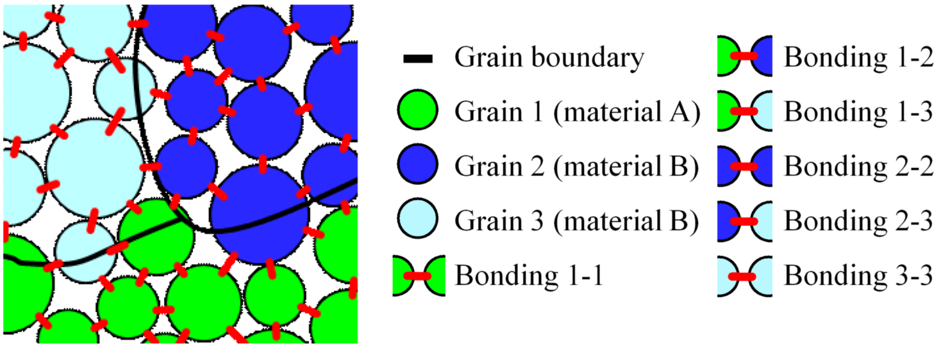

Fig. 4.3: Schematic illustration of possible bonding types between two grains of material A and one grain of material B

Figure 4.3 demonstrates the extent of diversity, which can be determined using this differentiation method. Therefore, a synthesized two-dimensional microstructure with three grains is shown exemplarily. It is assumed, that the green part represents a grain of phase A, while the two different shades of blue represent two different grains of phase B. Hence, of the resulting bonding types, three are intra- and three intergranular.

In order to realize the mineral microstructure in the simulation, the actual bondings have to be adapted based on this classification. Otherwise the physical behavior would not be affected by the mapped microstructure. This, however, can be realized in various ways. It is thus possible, to specify the physical properties of all bondings with regard to the bonding partners or to adjust only selected, specific bondings. The final implementation should therefore be done with regard to the actual experiment and the used material and is not generalized here.

However, with regard to the focus of this study, it is obvious to restrict the adaption of the bondings to a selection, since first of all the general applicability should be proven.

4.1.2 The experimental realizations

Based on the presented general considerations, it is decided to use a two-staged experimental concept. In this, a newly developed indenter fracture tests will be the basis in the first stage. Within this, the synthetic microstructure approach shall be tested first with controlled conditions. As shown in Figure 4.4, the second stage is then used to increase the complexity of the experiments with respect to the actual fracture process, as well as in the complexity of the mineral microstructures of the test materials.

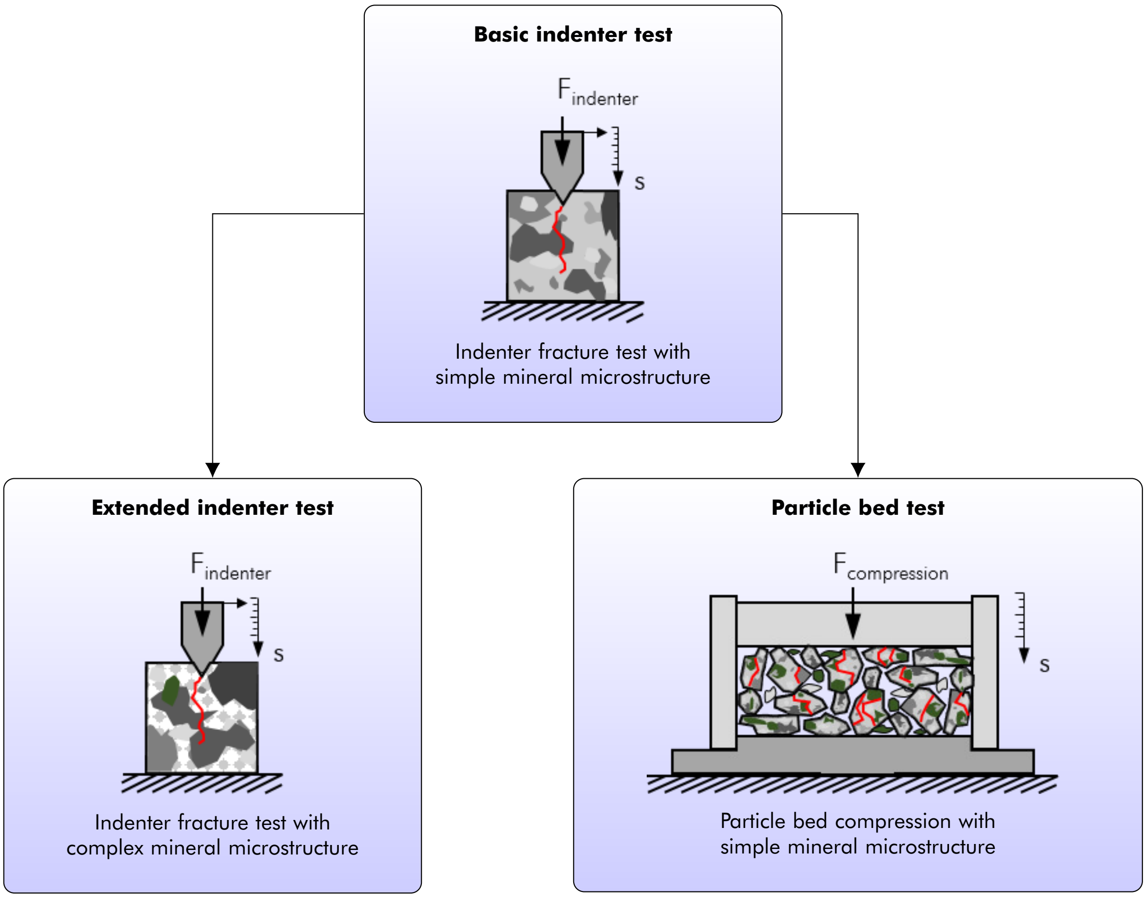

Fig. 4.4: Two-staged experimental concept

The first stage. In the first stage, a newly created indenter fracture test is used in combination with a relatively simple mineral microstructure. The purpose of this first stage is to evaluate the general applicability of synthetic mineral microstructures. For this reason, a new experimental setup was created. It is intended to ensure comparable fracture conditions in the scope of a setup, which can be transferred reliably to a two-dimensional BPM simulation.

In order to minimize other influences, this test shall be done with a material that has a relatively simple, homogeneous, and isotropic microstructure. Furthermore, it is seen to be important that it is easy to synthesize. The details of this basic validation experiment are explained in Section 4.2

The second stage. The experiments in the second stage build on the first stage. As already mentioned, they are used to check the applicability of the synthetic microstructure method in combination with more complex conditions. For example, the extended indenter test uses the same setup as the basic indenter test in combination with a test material that has a more complex mineral microstructure.

In contrast, the particle bed test transfers the synthetic microstructure approach to a test setup, which is closer to real comminution applications. However, in order to keep the link to the first stage, the same material with the simple mineral microstructure will be used. Both experiments as well as their simulative realizations are explained and discussed in more detail in Sections 4.3 and 4.4.

4.2 Basic indenter test

As already explained, the experiment of the first stage of this validation study is the basis for the proof of concept of the synthetic microstructure approach. In order to allow an evidence-based and comprehensible evaluation of this approach, the considerations for the test design as well as the real and simulative realization are explained in more detail below. For this, the ideas presented in Figure 4.1 of Section 4.1.1 are the decisive factors.

4.2.1 Considerations for the basic indenter test

As shown in Figure 4.5, the starting point for the setup will of course be a representative sample of the real test material. Based on this, a real physical fracture test is performed, on the one hand. On the other hand, the microstructure of the real specimen is analyzed and synthesized using the two-dimensional QMA and the synthesis program.

This two-dimensional synthetic structure is then transferred to YADE, where the fracture test is simulated. The focus is on the influence of the synthetic microstructure on the fracture pattern. The comparison of the results is then used as a standard to demonstrate the basic capabilities of the approach of synthetic mineral microstructures in DEM simulations.

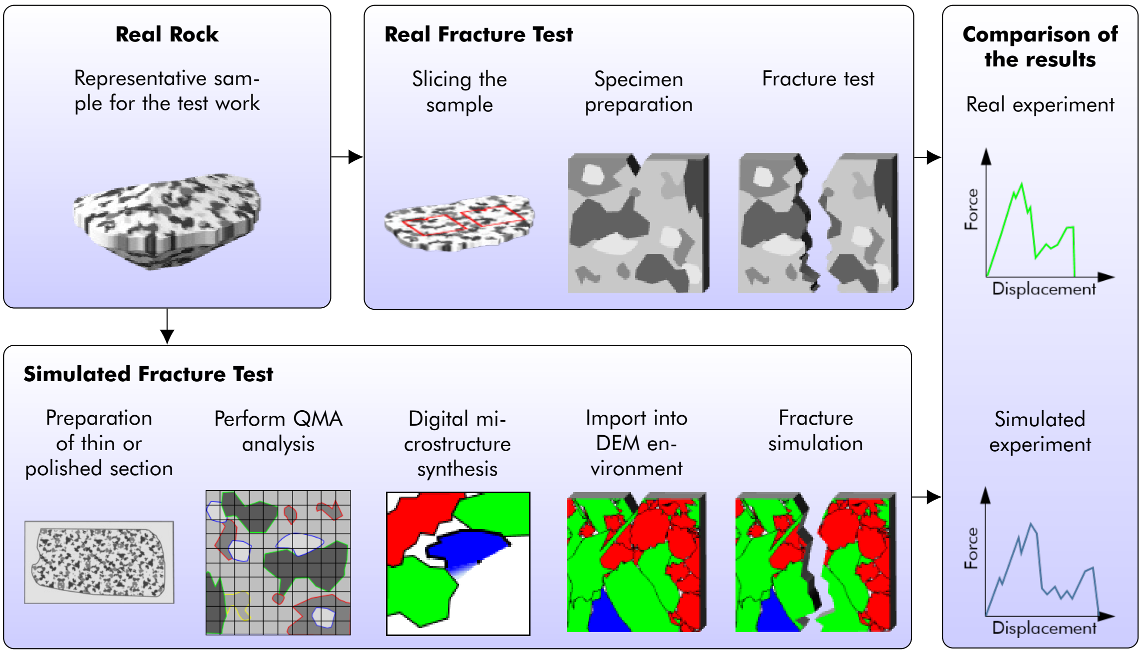

Fig. 4.5: Schema for the basic indenter test

Basic test setup

Altogether, the presented boundary conditions lead to the concept of a new fracture test setup, which is adjusted to the characteristic requirements of this study. Because of this, the new test was not designed for the determination of material parameters like most of the established fracture tests. Instead, it is intended to be used for pure validation and comparison purposes only.

The basic idea is to fracture a well-defined plate slowly with a wedge shaped indenter, which is shown in Figure 4.6. The plate is rigidly supported at the front and rear side but may freely move in the plane. During the test, the load on the specimen and the displacement of the indenter are continuously monitored. Additionally, a high-speed camera captures the fracturing itself, making it possible to evaluate the fracture behavior. The new setup is implemented into a hydraulic piston die press of the type MTS 20 with a capacity of 100 kN.

However, for a more detailed specification of the tests setup, especially concerning the final specimen dimensions, a suitable material has to be chosen first.

Selection of the test material

Conditions for the test material. In order to be able to guarantee results, which can be used to evaluate the appropriateness of the synthetic microstructure approach, the test material must meet certain requirements. Due to the dimensional restrictions, it is advantageous,

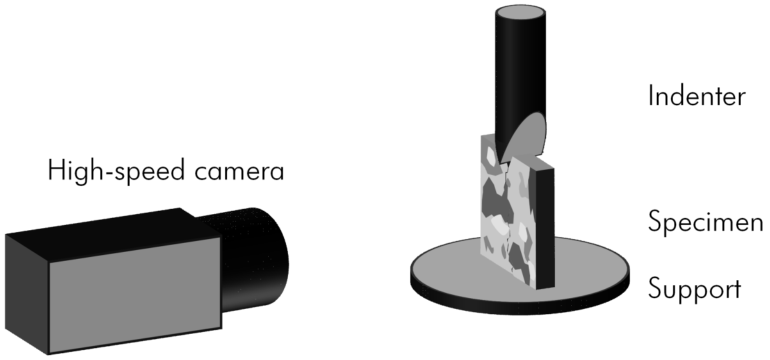

Fig. 4.6: Experimental setup of the new fracture test. The supports at the front and rear side of the specimen are not shown for reasons of clarity

if the mineral microstructure is homogeneous and isotropic. For this first stage experiment, this minimizes the influence of the orientation of the material during the test on the fracture process.

Furthermore, the microstructure should be middle to coarse-grained, based on the classification of TEUSCHER [204]. This fact is of importance insofar as in these cases the optical identification of crack paths during the real fracture test is significantly easier than for a fine-grained rock. Using testing material of this grain size makes it possible to determine where the crack propagates along a specific grain boundaries and where it propagates straight through the grains, using camera technology with standard magnification.

The chosen test material. Based on the above presented side conditions, the granite from Meissen, Saxony is shortlisted. This material has a typical reddish color and was historically used as natural building material. For the material characterization, the unconfined compressive strength $UCS = 168.10\,\text{MPa} \pm 6.27\,\text{MPa}$ and the Brazilian tensile strength $\sigma_{tB} = 8.25\,\text{MPa} \pm 0.94\,\text{MPa}$ were determined. Further measurements showed, that the granite has a porosity of about 0.7 % and an average dry particle density of $2.62\,\text{g}\,\text{cm}^{-3}$.

The corresponding results of the original QMA, including the measurement of the grains of three orthogonal thin sections, are shown in Table 4.1. Three different phases: quartz, feldspar and mica, are dominant. Little ore grains, representing an overall volumetric proportion of less than 0.5 %, are negligible for this investigation. Despite the results of the porosity test, no pores were measurable at the scale of the QMA. With an average grain size between 3.307 mm for quartz and 0.780 mm for mica, this granite is classified as a middle- to coarse-grained material.

As it can be seen by the low values for the elongation and flatness of the grains, the granite has a rather isometric texture. Moreover, the orientation parameters indicate an isotropic structure as well. Overall, the granite has a uniform fabric and its properties can be considered as independent of orientation.

Tab. 4.1: QMA results for the granite from Meissen, Saxony

QMA Parameter	Symbol	Unit	Quartz	Feldspar	Mica	$\sum$
Volumetric portion	ϵ_V	[%]	27.00	70.00	3.00	100.00
Median grain size	$x_{50,2}$	[mm]	3.31	1.48	0.78	1.97
Standard deviation	σ_{ln}	[–]	0.83	0.32	0.37	0.47
Elongation	El	[%]	1.05	1.14	1.09	1.13
Flatness	Fl	[%]	1.09	1.05	1.01	1.07
Grain surface	S_V	[mm^2/mm^3]	29.77	10.26	30.40	11.78
Deg. of roughness	K_R	[%]	15.00	8.00	31.00	11.00
Deg. of iso. orientation	K_{iso}	[%]	92.00	88.00	94.00	93.00
Deg. of lin. orientation	K_{lin}	[%]	4.00	10.00	6.00	6.00
Deg. of pla. orientation	K_{pla}	[%]	4.00	2.00	0.00	1.00
Deg. of clustering	C_α	[%]	31.00	68.00	1.00	56.00
Deg. of space filling	ϵ_{AF}	[%]	—	—	—	100.00

Based on the results of the above shown material analyses, the applicability of the granite from Meissen for the intended validation test is confirmed. It is seen to be a suitable material for the intended quasi two-dimensional test work. Hence, as there are no other negative factors and due to the good availability of the material and its deposit, this granite is chosen.

Detailed test setup

In order to evaluate the test setup and to find appropriate sample dimensions, preliminary tests were done. Those have shown, that this experimental setup guarantees, that the initial crack does not propagate through the whole granite sample at once. On the contrary, the fracture can be divided into a distinct primary crack that stops within the specimen and subsequent following cracks until the sample is fully broken. Therefore, energy losses at the initial crack due to conversion into kinetic energy of fracture fragments can be excluded. This makes the determination of the fracture energy more precise.

The details of the final setup are shown in Figure 4.7. The prismatic specimens have a quadratic cross section with an edge length of 50 mm. A V-shaped notch with an angle of 60° is machined from the top side of the specimens to a depth of 5 mm. For the sake of comparability between experiment and simulation, the plates are intended to be extra thin. The actual thickness, however, depends on the texture of the test material, its stability, and its machinability. For the middle- to coarse-grained granite from Meissen a specimen thickness of around 3.5 mm gives satisfactory results. This low thickness guarantees that only one or two grains of the granite are arranged back-to-back in most cases. Consequently, the condition of quasi two-dimensionality is achieved.

Further details of the indenter geometry are shown in Figures 4.7c and 4.7d. The indenter, which actually is a chisel with a wedge shaped edge, acts as counterpart to the specimen and

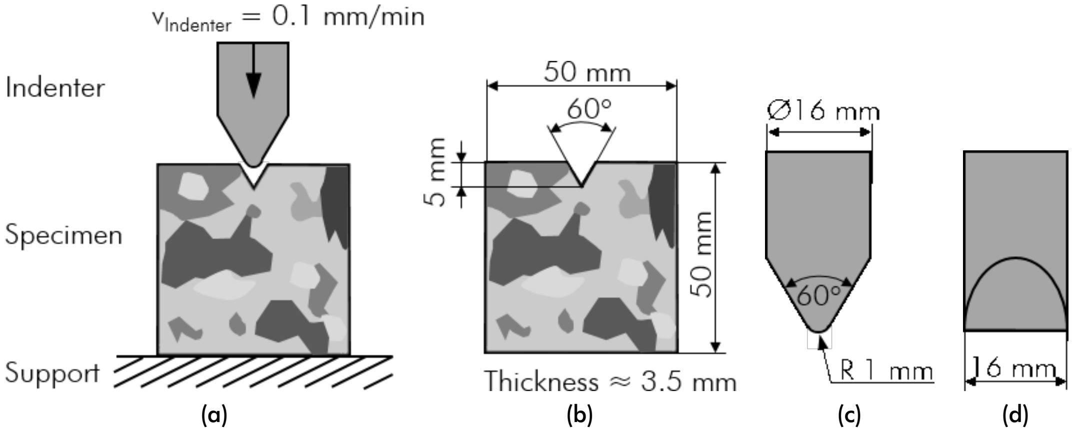

Fig. 4.7: Details of the experimental setup of the basic indenter test: (a) Arrangement of indenter and specimen; (b) Dimensions of the specimen; (c) Enlarged frontal view of the indenter with the wedge-like edge; (d) Enlarged side view of the indenter with the wedge-like edge

transmits the load from the hydraulic press into the notch of the plate. This edge of the chisel has the same angle as the notch. However, in order to prevent premature contact between the indenter and the root of the notch, the indenter has a radius of 1 mm at its front edge.

The required monitoring of the actual fracturing is done with a Miro M340 high-speed camera. It is positioned directly in front of the specimen and records all fracture events with 9296 fps, an exposure time of 1 µs, and a resolution of 512 Pixels × 512 Pixels. The high-speed recordings guarantee, that the details of the fracturing process are later reproducible.

Altogether, this new test setup is found to meet the requirements: It is quasi-two-dimensional, works quasi-static, and the ability to use high-speed recordings also has a positive effect on the evaluation process. It is also suitable for simulative test work as the key geometries are easy to implement into every DEM environment.

The test procedure

The test procedure is shown in Figure 4.8. At the beginning, an intact specimen is placed underneath the indenter. The test starts then with lowering the indenter until it touches the specimen in the notch. Next, the specimen is loaded by monotonically lowering the indenter until the fracture force F_{crack} is reached, which causes the initial macroscopic crack. At this point, the loading is stopped, so that test data like the high-speed recordings and force-displacement data can be saved to the hard drive. Afterwards, the loading is continued, until the crack reaches the bottom edge of the plate and the specimen is fully separated. During this process, the test is again paused after each macroscopic cracking event, to save the recorded high-speed video and force-displacement data of the preceding crack propagation on the hard disk.

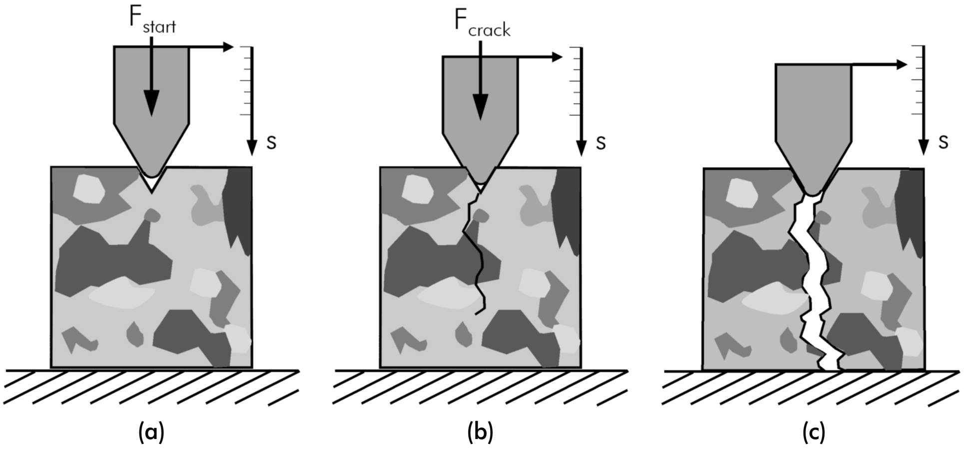

Fig. 4.8: Schematic experimental procedure of the basic indenter test: (a) Intact specimen with indenter stressing the notch; (b) Cracked specimen with indenter continuously stressing the notch; (c) Finally broken, stress-free specimen

4.2.2 Realization and evaluation of the real basic indenter test

The main aspects of the implementation and evaluation result from the very specific considerations of the basic indenter tests. However, due to unusual techniques, which are applied to prepare the specimens, special emphasis is set on this topic. Furthermore, since it is the basis for the comparison with the simulation, the evaluation procedure as well as the results are explained in detail.

Preparation of the granite specimens

Both, the special shape, which is required for the test as well as the global conditions of this study, presuppose very careful specimen preparation and pretreating. The main requirement is to machine the test material gently in order to minimize the pre-damage of the later specimen. This aspect is particularly important because of the thinness of the specimens.

As a result of these conditions, the designated rock for the specimen preparation is cautiously cut with a diamond saw to plates of about 5 mm thickness. The cut raw plates are further ground to the final thickness of about 3.5 mm on a vibrating surface grinding and polishing machine using a P180 silicon carbide abrasive powder. The front and backsides of the plates are treated equally. After grinding, the final outer shape of the specimens is prepared by water jet cutting.

Specimen characteristics. In total 16 granite specimens were successfully prepared for the basic indenter test. Compared to the minimum amount of about 10 specimens required for the UCS test [136], this number seems to be adequate for this first stage validation experiment.

The final thickness of the granite plates is on average 3.4 mm and ranges from 2.1 mm for the thinnest plate to 4.1 mm for the thickest plate. The differences between the thicknesses of the plates are due to the limited machining accuracy and precision of the grinding process. Due to the fragility of the plates, it is not possible to check the grinding progress as often as required during the machining. Hence, a certain variance is inevitable. However, since all plates are in a range of the quasi-two-dimensionality, the results are still considered satisfactory. Furthermore, preliminary tests have shown that the it is possible to reliably test granite specimens of at least 10 mm thickness with the indenter setup so that no further negative effects are expected.

Additionally, the deviation for the individual plates was evaluated as well. For this, the thicknesses near the four corners and the middle of each plate was measured. Overall, the deviation per plate is on average 0.14 mm, which is seen to be sufficient low.

Fluorescent liquid penetrant testing. In order to assess the pre-damage of the final specimens, each one is subjected to a non-destructive surface crack detection technique. In particular, liquid penetrant testing with Tiede® AP-11 is performed. This is a pH-neutral, water washable fluorescent penetrant of level 1 sensitivity that is certified according to the AMS 2644 [156, 184]. It is designed for general use in fluorescent penetration testing to find material defects open to the surface. However, due to its reliability and it compatibility, it can even be used for testing materials and alloys of the automotive and aviation industries. The ingredients are petroleum distillates, alcohol alkoxylates, alcohol ethoxylates alcohol ethoxylates, terpineol, and fluorescent dyestuff. Chemical interactions with common rock forming minerals are not known. Since preliminary tests have shown the applicability with the granite and no effects on the fracture behavior could be determined, this penetrant is considered suitable for this purpose.

The evaluation of these tests reveals, that no increase of pre-damages in the material is measurable, since no noticeable crack structures were found. Hence, it can be noticed, that the used mild machining processes for the sample preparation fulfill their purpose. However, it is further found that the penetrant can be used to make the grain boundaries of the granite visible (Figure 4.9). Obviously, it penetrates along grain boundaries into the whole volume of the rock sample through capillary forces. It can therefore be concluded that the boundaries between the grains of this granite are not really rigid interfaces, but actual domains that can transport liquids to a certain extent. This confirms ideas of hydrothermal systems in rocks and ore bodies in geological sciences.

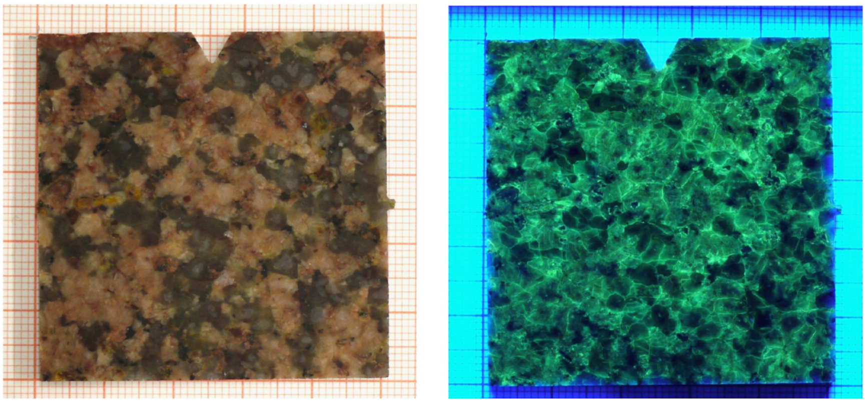

(a) (b)

Fig. 4.9: Preparation of the specimen of the basic indenter test with the fluorescent liquid penetrant: (a) Original specimen under visible light; (b) Specimen impregnated with fluorescent dye under ultraviolet (UV) light

Irrespective of these side findings, this feature is also of practical use for the evaluation of the fracture pattern. As it eases the discrimination between grains and grain boundaries, where the liquid dye penetrated the specimen, it is used as pretreatment. Hence, pictures of all unbroken specimens are taken under visible and UV light.

Realization of the real fracture tests

The 16 prepared specimens are fractured with the explained test procedure. Figure 4.10 shows the real test setup exemplary with a specimen fixed on the specimen holder just before the test starts.

In order to minimize the influence of friction, the chisel, the indenter, and the bottom plane of the thin specimen were prepared with an open gear lubricant on graphite basis. The supports, which hold the specimen at the left and right side are only loosely leaned against the specimen. This ensures that the supports do not absorb any forces or friction. They have to ensure the correct position of the specimen at the beginning and support it only until it is loaded by the indenter. Then the specimen is clamped between the indenter and the ground support. Since the specimens have no tendency to buckle, no further support is needed.

The fracture states. Figure 4.11 shows exemplarily a sequence of consecutive photos of the test procedure with a granite specimen taken with an additional digital camera. These show different states of the specimen, which can be examined during the experiment. According to the preliminary considerations in Figure 4.8, the test procedure can be distinguished into three states. The first one is the pre-failure state at the beginning of the test. The second stage is characterized by the primary crack and possible following subsequent cracks inside the specimen. The last state is the final failure.

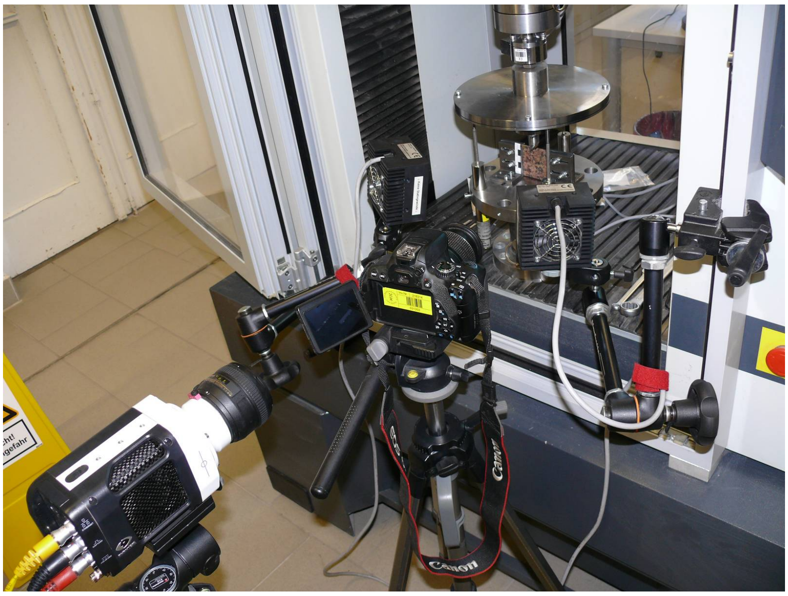

Fig. 4.10: Photo of the real experimental setup of the basic indenter test: The specimen is fixed on the specimen holder in the hydraulic piston die press. The indenter is already in the starting position, just above the ground of the notch of the specimen. The high-speed camera and a digital camera are positioned in front of the specimen. The switched-off lamps for the high speed camera are positioned at the left and at the right so that they can evenly light the specimen.

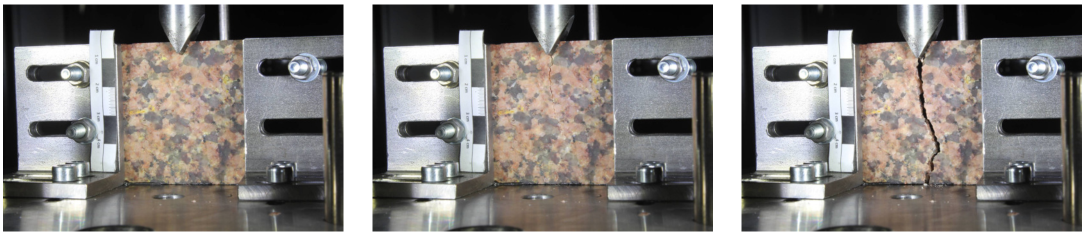

(a) (b) (c)

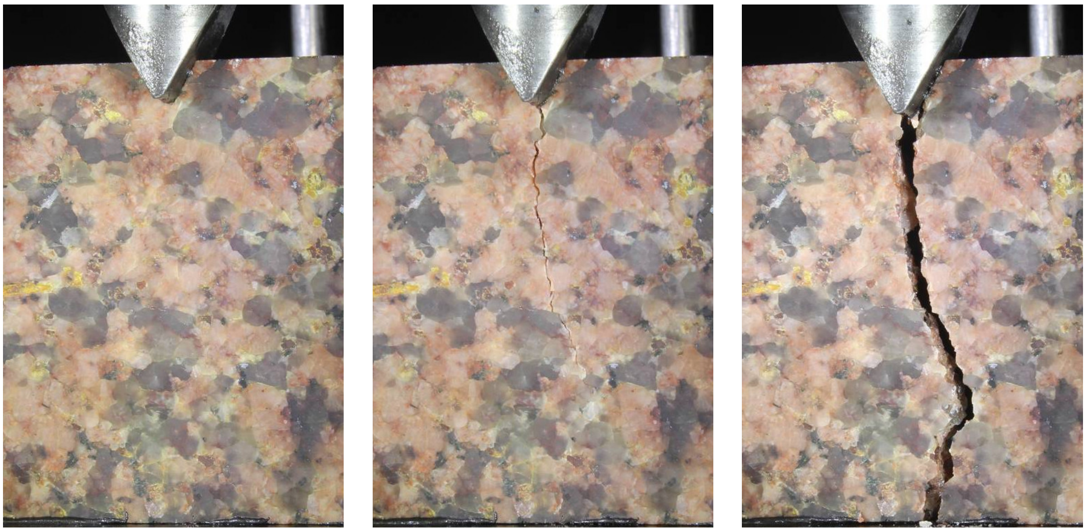

(d) (e) (f)

Fig. 4.11: Sequences of a basic indenter test: (a) Specimen at the beginning of the test; (b) Specimen with primary crack; (c) Finally broken specimen; (d) Detailed view on the initial microstructure; (e) Detailed view on the primary crack; (f) Detailed view on the final crack

Evaluation of the real fracture tests

The evaluation of the basic indenter test is done with emphasis on the influence of the mineral microstructure on the fracture behavior. Since this is a newly developed test procedure, unfortunately there are no references or experiences for the evaluation. Hence, the focus is set on the analysis of the broken specimens, the high-speed recordings, and the force-displacement measurements. All of them are used to evaluate the influence of mineral microstructure on the fracture.

Procedure for the evaluation of the broken specimens. As with the sample preparation, pictures of the broken specimen are taken under both visible and UV light. In combination with the pictures of the unbroken specimen, the crack paths are determined as shown in Figure 4.12.

Hence, it is possible to determine the real crack length l_{crack} by measuring the crack edge. Moreover, in combination with the thickness $d_{specimen}$ of the specimen, this allows a rather precise estimation of the newly created fracture surface A_{crack} to be calculated according to Equation 4.1.

$$A_{crack} = l_{crack} \cdot d_{specimen} \tag{4.1}$$

Due to the conspicuous texture of the granite and with the help of the UV-pictures, the different grains are easily distinguishable. Based on this, it is possible to differentiate between breakage through existing interfaces like the grain boundaries and breakage through intact grains. This is shown at Figure 4.12c, where the yellow part of the crack path represents intragranular fracture and the blue part represents fracture along grain boundaries. This information is used to estimate the proportion of the length of grain boundary cracks of the total crack length $p_{boundary}$ (Equation 4.2).

$$p_{boundary} = \frac{l_{crack,boundary}}{l_{crack}} \tag{4.2}$$

However, further interpretations, such as which grains are exactly affected, are not possible, since such macroscopic images cannot be used to reliably detect and distinguish all the grains. This would require more labor-intensive approaches such as polarization microscopy, which would go beyond the scope of this study.

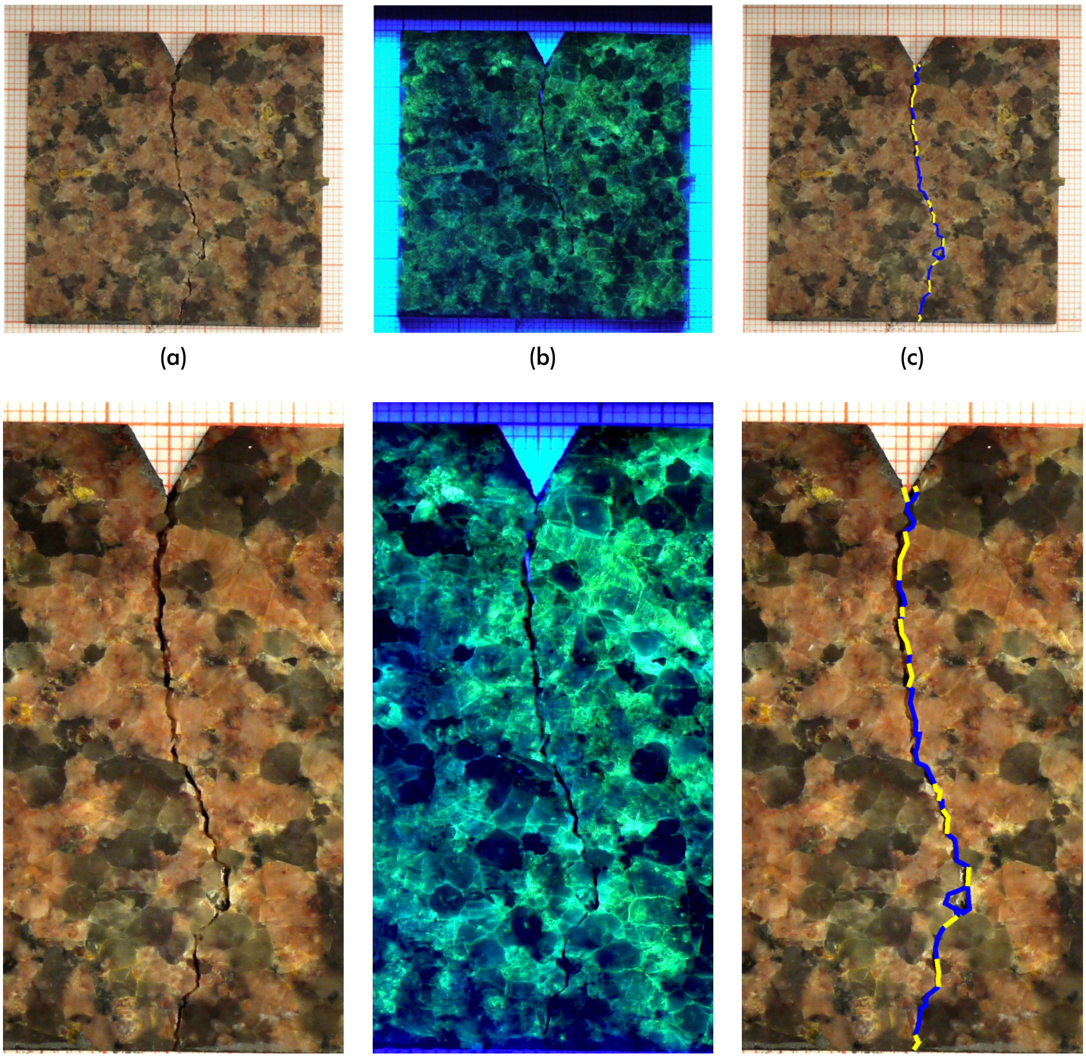

(a) (b) (c)

(d) (e) (f)

Fig. 4.12: Fractured specimen: (a) Broken specimen under normal lighting; (b) Broken specimen under UV lighting; (c) Broken specimen under normal lighting with highlighted crack path; Blue – Fracture along a grain boundary; Yellow – Fracture through a grain (d) Detailed view under normal lighting; (e) Detailed view under UV lighting; (f) Detailed view under normal lighting with highlighted crack path

Procedure for the evaluation of the high-speed recordings. Next, the high-speed recordings are used to determine the different, distinct cracking events. Fortunately, these events follow a typical pattern. They usually start with the continuous loading of the specimen, which is followed by the first initial crack. In most cases, this first crack stops within the sample. Its physical appearance is often characterized by a milky veil, which runs through the specimen (Figure 4.13a).

This event is followed by a phase of crack opening, where the indenter proceeds with little resistance through the material. This phase is marked by the change of the appearance of the primary crack from a milky veil to a slightly opened cleavage (Figure 4.13b). Typically, small force peaks and faint fracture noises accompany this process. It is assumed that those small-scale events mark processes, where remaining mechanical bondings as well as possible undercuts of the opposite fracture surfaces or roughness, are overcome. Although the crack width is increasing during this phase, the overall crack length seems to remain constant.

In the next phase, a noticeable increase in load is followed by a major cracking event, propagating the initial crack. If the newly formed crack fully separates the entire sample, then the test is finished. In contrast, if the new crack forms a secondary crack, which again stops inside the specimen, the order of the subsequent events is comparable to those after the initial crack. However, since such secondary cracks are typically smaller than the first one, the characteristics of the events are mitigated too. These subsequent cracks can occur multiple times in a row, but in most cases only one secondary, and in very few cases more than one were registered.

Besides, it is noticed, that there is a smooth transition between the small-scale events of crack opening and further fracturing events at the tip of the crack. Hence, a distinction of the two types of cracks is not always possible even with the high-speed recordings.

Procedure for the evaluation of the primary cracks. For the evaluation and comparison with the results of the simulation, the experimental data of the primary cracks are of particular interest. In this way, consistent test conditions are guaranteed. The fracturing processes after the primary crack are only qualitatively comparable since the breakage state of the specimen varies. Furthermore, the opening of the primary crack changes the way the indenter touches the specimen. While it is a full surface contact for the intact specimen, it changes to a line contact when the first crack opens due to pressing the notch open. For the same reason, it can happen that the tip of the indenter touches the root of the notch if the crack is opened wide enough.

Hence, the tests are evaluated with regard of the peculiarity of the primary cracks. Out of 16 specimen made of granite, which were initially prepared for this test series, 15 were successfully tested. One specimen broke prematurely, as the indenter was moved to the start position. Unfortunately, the first crack of another test was a mixture of crack propagation and crack opening. During this same test, the tip of the indenter also touched down on the root of the notch. Thus, in compliance with the strict requirements for comparison, only the 14 tests with clear primary cracks were considered for the following evaluation.

As Figure 4.13c shows, it is helpful to visualize changes in the high-speed recordings with special image processing methods. In this case, differences between the high-speed pictures before and after the initial crack are brightened and darkened, whereas areas with no changes are presented in gray, respectively. This technique allows to reliably recognize the progress and length of each distinct cracking event. Using this, the primary cracks of all completed tests are measured. Due to the hackly and fractal form of the crack path, the length of the first crack can exceed 50 mm even though it does not go through the whole specimen.

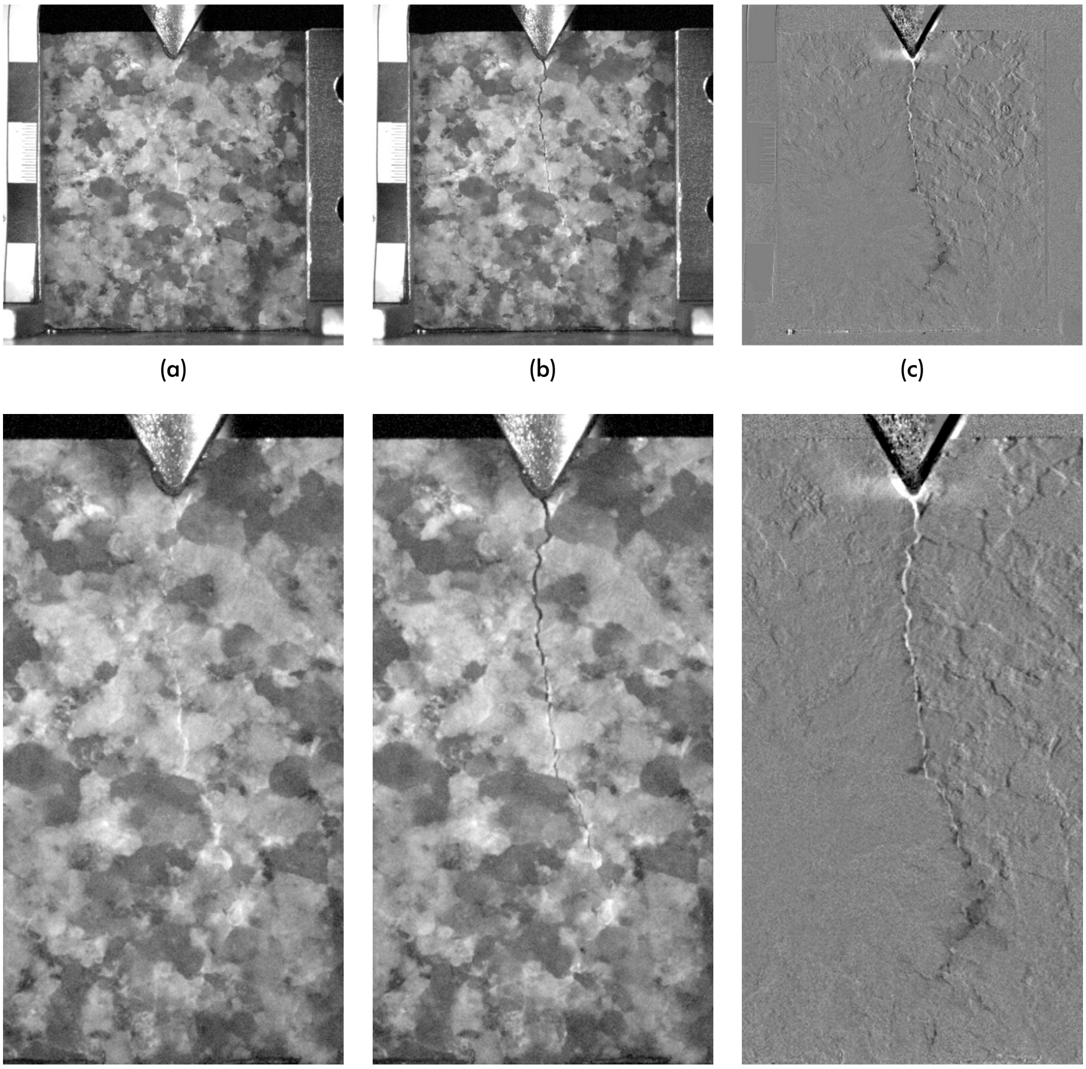
(a) (b) (c)

(d) (e) (f)

Fig. 4.13: High-speed recordings of a granite specimen after the primary crack: (a) Primary crack is recognizable by its milky veil; (b) Primary crack is opened; (c) Visualization of the path of the primary crack in the high-speed records using image analysis methods (d) Detailed view on the milky veil; (e) Detailed view on the opened primary crack; (f) Detailed view on the primary crack using image analysis methods

Procedure for the evaluation of the force-displacement data. Additionally, the measured force F, which is loading the specimen, and the displacement of the indenter s are evaluated. It is, therefore, possible to calculate the deformation work W, which is done by the indenter as integral of the force F over the displacement s (Equation 4.3). For the further evaluation and interpretation, it is noted, that this work corresponds to the energy that is absorbed due to fracturing.

$$W = \int F(s)\, ds \tag{4.3}$$

The plots in Figure 4.14 exemplarily display the measured values corresponding to the fracturing test of the specimen, which is shown above (Figure 4.13). To facilitate the understanding, the ranges of the different cracking events are additionally marked. The offset between these ranges in the plots over the time are the test pauses due to the time, which is needed to save the high-speed recordings. These areas are nonexistent in the plots on the right side, since no displacement occurred during these periods. Hence, the specimen absorbed no energy during this time.

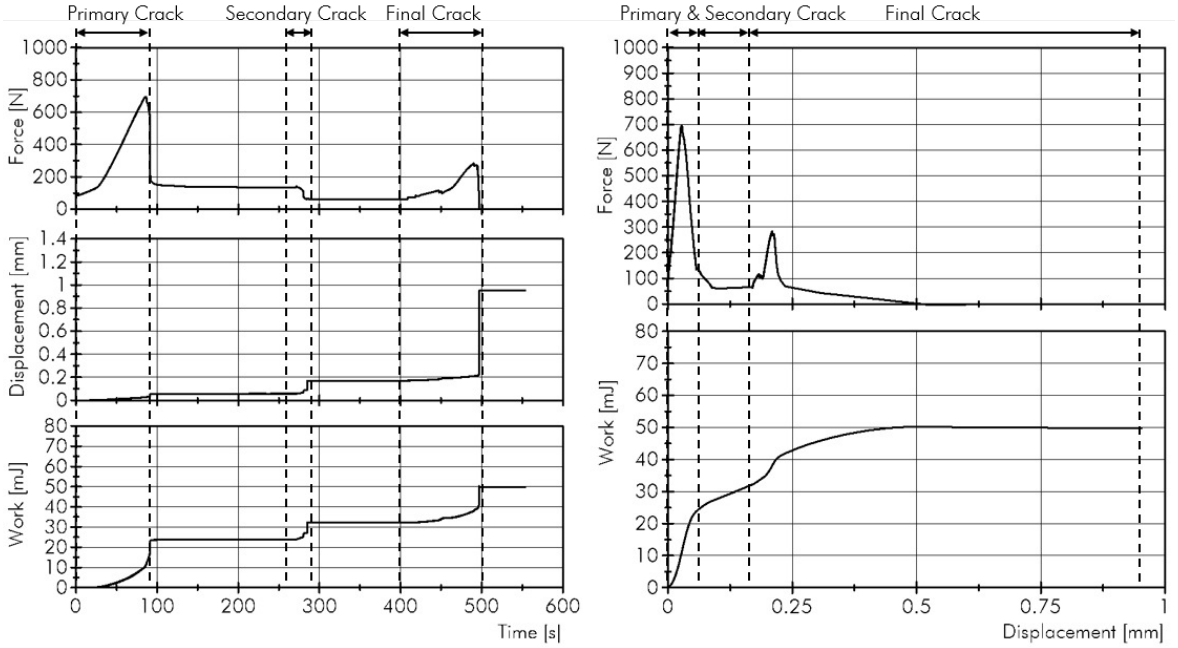

Fig. 4.14: Exemplary plots of the data of a basic indenter test: Force, displacement, and fracture work as function of the experimental time (left); Force and fracture work as function of the displacement (right)

In conclusion, the obtained data is used to deduce specific values, which help to characterize the cracking processes during these fracture tests. One of them is the fracture force F_{crack} for the primary crack, which is the maximum force that is reached just before the crack starts to propagate. Furthermore, the energy, which is absorbed by the propagation of the primary crack W_{crack} is calculated using Equation 4.4. In this case, the interval $[s_0,\ s_{crack}]$ has to be used. It represents the range between the displacement of the indenter at the beginning of the crack propagation s_0 and displacement just after the primary crack has stopped s_{crack}.

$$W_{crack} = \int_{s_0}^{s_{crack}} F(s)\ ds \tag{4.4}$$

The high-speed records were further used to determine the time Δt_{crack}, which elapsed between the first signs of crack propagation and the end of the cracking events. Using this information, the speed of the crack v_{crack} can be estimated. Therefore, the length of the primary crack l_{crack} is used as reference.

$$v_{crack} = \frac{l_{crack}}{\Delta t_{crack}} \tag{4.5}$$

Summary of the results. The raw data for the 14 tests with distinct primary cracks is shown in Table 4.2. The presented parameters are the thickness of the specimens $d_{specimen}$, the fracture force F_{crack}, the total crack length l_{crack}, the newly created fracture surface A_{crack}, the proportion of the length of grain boundary cracks of the total crack length $p_{boundary}$, the fracture work that was done during the crack propagation W_{crack}, the time that elapsed during the crack propagation Δt_{crack}, and the calculated crack speed v_{crack}.

Additionally, the corresponding arithmetic average AM, the standard deviation SD, and the coefficient of variation CV are tabulated as well. In this case, however, the informative value of these stochastic measures is limited, since the specimen thickness, which is the only independent variable, is not constant. Hence, in addition to the evaluation of the crack speed and the proportion of boundary breakage, which appear to be independent of the specimen thickness, special emphasis is set on the evaluation of the correlations between the different parameters.

Tab. 4.2: Raw measurement data for the basic indenter test: Shown are the results of the 14 tests with distinct primary cracks. The values represent the status of specimens just after propagation and stoppage of the primary crack. Values, which are not available, are labeled with n.a.

No.	$d_{specimen}$ [mm]	F_{crack} [N]	l_{crack} [mm]	A_{crack} [mm^2]	$p_{boundary}$ [%]	W_{crack} [J]	Δt_{crack} [s]	v_{crack} [mm/s]
1	2.4	422	34.7	84	65.2	9.9	0.20	177
2	2.8	404	68.2	189	58.1	20.4	n.a.	n.a.
3	3.0	555	53.0	157	78.1	17.7	0.12	451
4	2.5	350	34.8	87	68.7	7.4	0.26	133
5	3.7	846	56.7	210	52.6	27.3	0.22	254
6	2.2	217	22.1	49	45.6	6.5	0.27	81
7	3.5	278	13.6	48	35.7	5.6	0.21	66
8	3.9	600	38.4	150	58.3	21.1	2.01	19
9	3.7	657	40.4	151	41.1	24.8	0.09	456
10	3.9	847	57.5	222	46.6	31.7	0.14	410
11	3.8	695	49.0	185	63.1	23.8	0.19	256
12	4.0	644	41.7	166	60.9	21.0	1.85	23
13	4.1	809	57.3	235	55.5	31.2	1.63	35
14	4.0	927	64.5	255	49.6	38.1	1.69	38
AM	3.4	589	45.1	156	55.7	20.5	0.68	185
SD	0.7	227	15.8	67	11.4	10.1	0.78	166
CV	19.6	38.5	35.0	41.8	20.6	49.5	113.9	90.6

Evaluation of the crack speed It is noticeable that the determined speed of the crack propagation is very low compared to the typical values for the critical speed of crack propagation in minerals indicated in the literature. For comparison, TROMANS [208] calculates a maximum separation velocity of $1297\,\mathrm{m\,s^{-1}}$ at the crack tip for α-quartz. However, the maximum speed that a single crack can reach and the average speed of all crack events that occur in a complex structure, such as in the granite being tested, need to be differentiated. Even if only one crack in an ideal homogeneous environment is in the focus of consideration, the average crack speed is always lower than the maximum crack speed since the crack first has to speed up [100].

The physical situation within the tested specimen, however, is far more complex. The recorded fracturing events cannot be equated with cracking in homogeneous environments. It is assumed that the observed primary cracks are themselves the macroscopic appearances of a diversity of microscopic crack propagations, stopping and connection events. The macroscopic crack must encounter many different obstacles as it finds a path through or along many different grains. An example of such obstacles are grain boundaries, which alter the stress setting on the crack tip and cause reorientation and deviation of the crack path.

Evaluation of correlations. For further evaluation of the experimental results and for the comparison with the simulations, not only the measured raw data are of interest, but also potential correlations have to be considered. Therefore, Spearman's rank correlation test is used to analyze the data. This test, which results in Spearman's rank coefficient $\rho_{spearman}$, has the advantage, that not only normally distributed parameters can be tested. This is of special interest, since only the parameter for the boundary breakage $p_{boundary}$ is verifiably normally distributed. Hence, the other parameters like $d_{specimen}$ from the presented raw data, which are not normally distributed, can be tested as well.

For reasons of clarity, Table 4.3 shows only the results of pairings, where correlations are indicated. According to the classification of the effect size by COHEN [34, 35], it is possible to find strong correlations for the pairings $F_{crack} \sim A_{crack}$, $F_{crack} \sim W_{crack}$, $l_{crack} \sim A_{crack}$, and $W_{crack} \sim A_{crack}$, as well as a weaker correlation for $F_{crack} \sim d_{specimen}$. Additionally to the results of the correlation tests, the pairings are plotted in Figure 4.15 for visual verification. As it is of later interest, the pairing $W_{crack} \sim p_{boundary}$ is plotted as well, although there is no correlation ($p - value = 0.523$, $\rho_{spearman} = -0.187$) detectable.

Tab. 4.3: Spearman's rank correlation coefficients $\rho_{spearman}$ and the corresponding $p - values$ for specific data pairings of the basic indenter test

pairing	$F_{crack} \sim d_{specimen}$	$F_{crack} \sim A_{crack}$	$F_{crack} \sim W_{crack}$	$l_{crack} \sim A_{crack}$	$W_{crack} \sim A_{crack}$
$p - value$	0.003	0.000	0.000	0.000	0.000
$\rho_{spearman}$	0.745	0.895	0.969	0.938	0.890

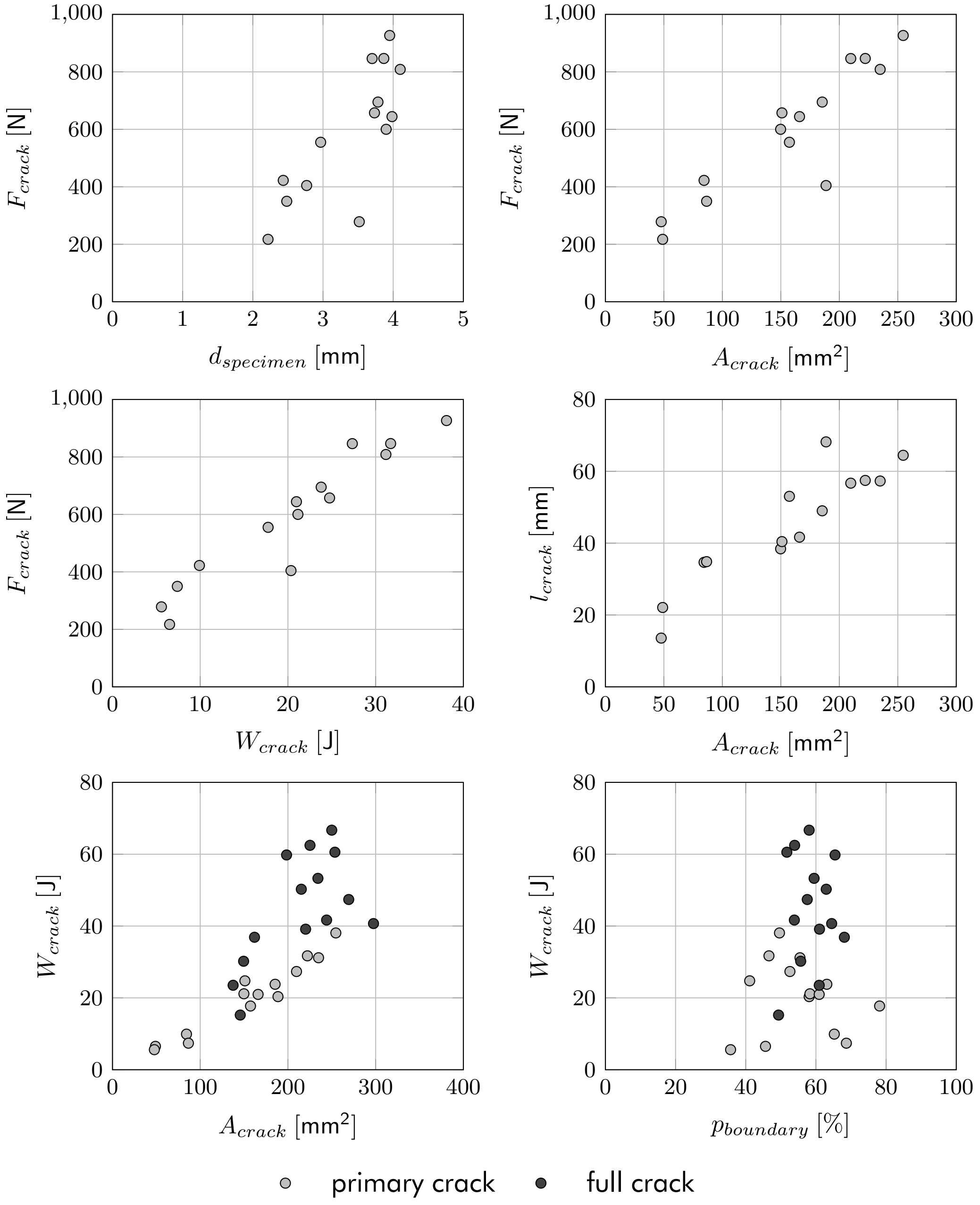

Fig. 4.15: Plots of possible correlations between the measured data

The relation between the crack length l_{crack} and the newly created fracture surface A_{crack} is obvious, since the crack length is the determining parameter for the calculation of A_{crack}. The pairing $F_{crack} \sim W_{crack}$ does have a comparable interrelationship. Hence, these two trivial correlations are negligible for further considerations. The correlation between F_{crack} and $d_{specimen}$ supports our understanding of rock fracture processes, since it means that the absolute force needed to fracture a particle depends on the size of the particle. Interestingly, linear relationships can be observed for this limited parameter field if the fracture force is set in relation to a size parameter like the specimen thickness $F_{crack}/d_{specimen}$ or the newly created fracture surface F_{crack}/A_{crack} (Figure 4.15).

The correlation between W_{crack} and A_{crack} is of particular interest. It confirms that the energy that is absorbed by the crack propagation is proportional to the newly created fracture surface A_{crack}. This interrelation becomes all the clearer in comparison with the results of the measurements for the complete cracks. In contrast, the measured energies of the complete cracks are subjected to more fluctuation due to the mixed, not quantifiable influences of the other test stages like crack opening and friction.

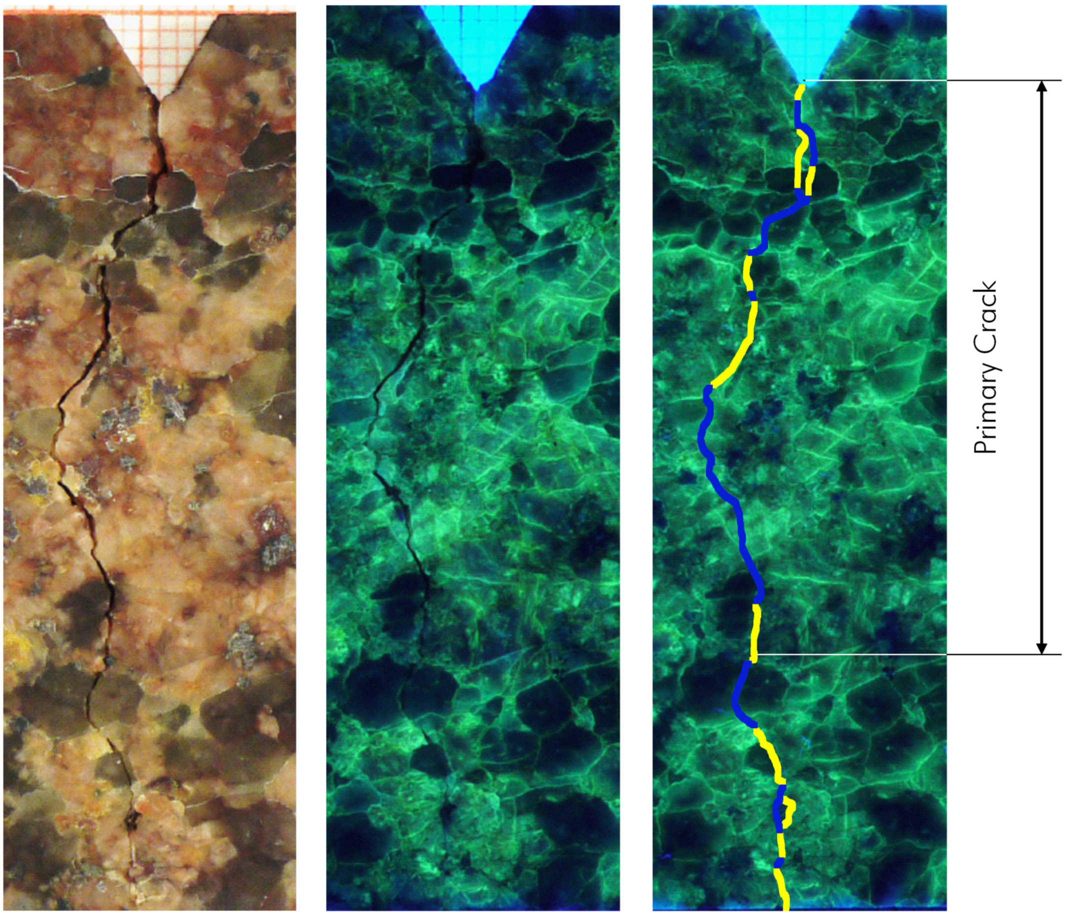

(a) (b) (c)

Fig. 4.16: Exemplary crack path in a granite specimen: (a) Normal lighting; (b) UV-lighting; (c) UV-lighting of the unbroken specimen with highlighted crack path; Blue – Fracture along a grain boundary; Yellow – Fracture through a grain

Evaluation of the intergranular breakage. Although no significant correlations can be found for $p_{boundary}$, the evaluation of the proportion of the length of grain boundary cracks with respect to the total crack length reveals an interesting feature. On average about 55.7 % of the crack length of the primary crack propagated along grain boundaries. Even when the total range between 35.7 % and 78.1 % is considered for this value, it can be assumed that this is not a random breakage. The relatively high values indicate, that a preferred breakage along grain boundaries, so called interfacial breakage, occurs.

This hypothesis is supported by a close look at the fracture pattern of the broken specimens. Figure 4.16 shows exemplarily the magnified image sections of the crack through a specimen.

It becomes evident, that significant parts of the crack path are clearly oriented along the grain structure. Furthermore, the crack did not propagate along the shortest path through the specimen. Instead, it propagates laterally in some regions. This can only be explained by the fact, that the crack propagates laterally through areas with lower resistance to crack propagation even if the path is longer.

In the context of this validation study, this breaking behavior is regarded as a good object of investigation. As the aim is to use synthetic microstructures in the simulation environment, it should be possible to use this feature as reference to evaluate the applicability and the potential of this approach. Therefore, the focus for the comparison with the simulation is on the evaluation of the proportion of the intergranular breakage.

4.2.3 Realization and evaluation of the simulated basic indenter test

According to the general considerations for the comminution simulations (Section 4.1.1) and the results of the real test, the basic indenter test is transferred into the YADE simulation environment. For doing this, the granite has to be synthesized first. The realistic synthetic twin is then used to map the microstructure to YADE, where the fracturing of the notched specimens is simulated.

Synthesis the Granite from Meissen

In order to synthesize the granite from Meissen, it has to be analyzed with the two-dimensional QMA. Therefore, however, a representative sample of the microstructure has to be digitalized first. Based on this, it is possible to calculate those characteristic numbers and generate a synthetic microstructure, which has statistically the same characteristics as the original.

Digitalization and analysis of the real microstructure. As already explained in Section 4.2.1, the chosen granite is very isotropic and homogeneous. For this reason, it is decided to use a single thin section as basis for the adapted QMA. Considering the existing analysis data, it can be emanated that no significant changes would be measured, if further thin sections, with other spatial orientations, were analyzed. However, this would require extensively more manual effort to bring those other references in a format, so that they can be used by the synthesis program. Hence, this is waived. Within the scope of these proof of concept experiments, it is assumed that this is a reasonable compromise.

However, in contrast to the conventional QMA, the ore grains are taken into account as well. Therefore, a thin section of the granite with an approximated size of 35 mm × 21 mm is digitized firstly, using a resolution of 114 Pixels mm^{-1}. Figure 4.17 shows a stitched view of the images from this thin section, taken with a polarized microscope, and the corresponding false color map. Therefore, all grains of the same material are filled manually with the same unique color, whereas grain boundaries are painted black. This false color map is then used as basis for computer-assisted QMA.

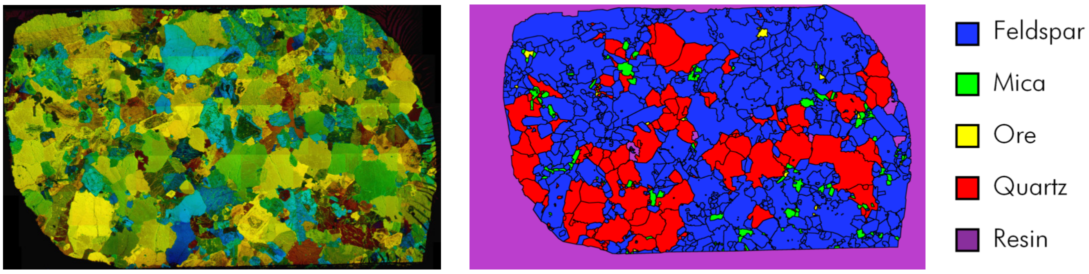

(a) (b)

Fig. 4.17: Map of the 35 mm × 21 mm thin section of the granite from Meissen for the two-dimensional QMA: (a) Stitched view under polarized microscope with 16-x magnification - contrast and brightness of the colors are post processed for recognizability reasons; (b) Corresponding false color map with legend for the different phases

The two-dimensional QMA results of the original thin section are shown in Table 4.4. Although it is not possible to directly compare the two-dimensional results with the three-dimensional ones in Table 4.1, the similarities in the characteristic numbers become apparent. The only abnormality are the values for the ore phase. This, however, is due to the very low number of the ore grains on the thin section. Because of this, the analysis algorithms are subjected to the typical uncertainties, which are explained exemplarily in Section 3.4.1. It is self-explanatory, that the real degree of roughness K_R of the ore phase has to be non-negative.

Tab. 4.4: Results of the planar QMA for the XY-plane of the granite from Meissen

QMA Parameter	Symbol	Unit	Feldspar	Mica	Ore	Quartz	$\sum$
Areal portion	ϵ_A	[%]	68.73	2.42	0.26	28.59	100.00
Median grain size	$x_{50,2}$	[mm]	1.97	0.61	0.45	2.37	2.05
Standard deviation	σ_{ln}	[mm]	1.55	0.97	1.12	0.80	1.32
Elongation	El	[-]	1.04	1.58	1.00	1.49	1.09
Boundary line length	C_A	$[\frac{\text{mm}}{\text{mm}^2}]$	4.75	9.73	12.97	4.00	4.76
Deg. of roughness	K_R	[%]	35.88	13.75	18.87	42.22	37.76
Deg. of iso. orientation	K_{iso}	[%]	98.02	76.04	100.00	79.12	95.43
Deg. of lin. orientation	K_{lin}	[%]	1.98	23.96	0.00	20.88	4.57
Deg. of clustering	C_α	[%]	75.86	9.88	12.77	45.05	65.29
Deg. of space filling	ϵ_{AF}	[%]	—	—	—	—	100.00

Generation and analysis of the synthetic microstructure. The analysis data of the real microstructure is used as input for the synthesis program. Resin, which is located in small defective areas of the real thin section, comes from damage during the preparation. It is, of course, ignored in the synthesizing process, as the synthetic rock material is assumed to have zero porosity.

For the purpose of guaranteeing a satisfying confidence level, a microstructure of the size of 10 000 Pixels × 10 000 Pixels is synthesized. In combination with the resolution of 114 Pixels mm^{-1}, this equates to a quadratic section with approximately 87.7 mm edge length and provides comparably low coefficients of variation as in the example presented in Section 3.4.1.

A section of the final result of the synthesis process can be seen in Figure 4.18. It can be directly compared with an image section of the real thin section, as both are rendered in false colors.

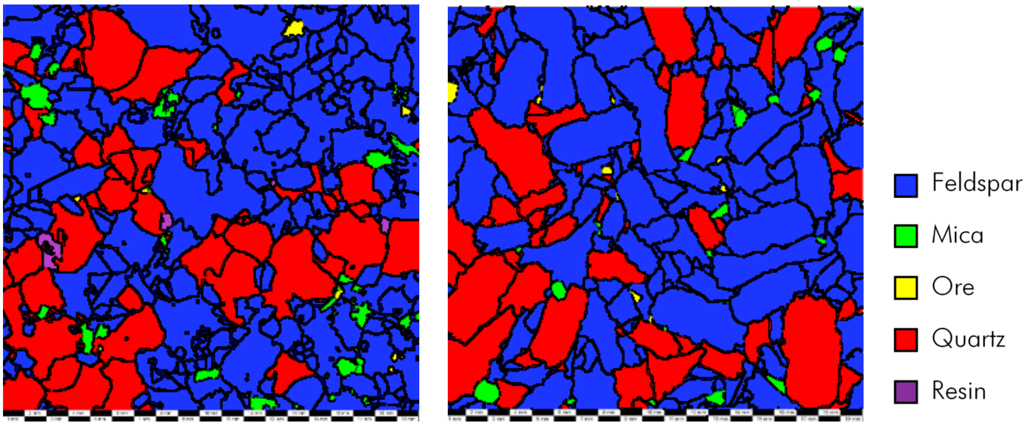

(a) (b)

Fig. 4.18: False color images of the mineral microstructure of the granite from Meissen: (a) Image of a real thin section; (b) Image of the synthesized equivalent

Additionally, Table 4.5 shows the corresponding planar QMA results of the synthesized sample, which represents a microstructure with a size of 87.7 mm × 87.7 mm. The visual comparison of both image sections and the evaluation of the QMA results indicates, that the synthesized microstructure is statistically equivalent to the real mineral microstructure, since only little deviations are ascertainable. Merely, the degrees of orientation of the mica and ore phase are significantly divergent from the original. However, this is due to the low areal portion of the two phases. In combination with the limited analysis area of the original thin section, this causes the explained uncertainties.

Despite this, the comparison of the planar QMA results of the synthetic microstructure with its three-dimensional counterpart of the real microstructure (Table 4.1) confirms, that the synthesized twin is a solid basis for further simulations. This conclusion is supported by the additional details of the QMA analyses in Appendices B.8 and C.1, as those confirm the good agreement.

Tab. 4.5: Results of the planar QMA for the synthesized mineral microstructure of granite from Meissen

QMA Parameter	Symbol	Unit	Feldspar	Mica	Ore	Quartz	$\sum$
Areal portion	ϵ_A	[%]	72.20	1.22	0.53	26.05	100.00
Median grain size	$x_{50,2}$	[mm]	1.98	0.60	0.49	2.13	2.00
Standard deviation	σ_{ln}	[mm]	0.93	0.84	0.71	0.89	0.92
Elongation	El	[-]	1.05	1.57	1.15	1.07	1.10
Boundary line length	C_A	$[\frac{\text{mm}}{\text{mm}^2}]$	4.00	11.40	14.40	3.66	4.05
Deg. of roughness	K_R	[%]	31.23	20.22	29.08	30.14	30.58
Deg. of iso. orientation	K_{iso}	[%]	97.36	76.52	92.36	96.37	94.90
Deg. of lin. orientation	K_{lin}	[%]	2.64	23.48	7.64	3.63	5.10
Deg. of clustering	C_α	[%]	73.64	13.30	12.99	30.14	61.24
Deg. of space filling	ϵ_{AF}	[%]	—	—	—	—	100.00

Setup of the basic indenter test in YADE

Setting up the basic indenter test in YADE can be divided into different steps. On the one side there is the mapping process, which is used to transfer the microstructural information into YADE. On the other side there is the parametrization of the actual DEM models inside YADE, which are needed to describe all the interactions between the discrete elements.

Mapping the synthetic microstructure to the simulation environment. However, before the actual mapping can start, the initial raw packing has to be generated first with the GenGeo library. For this, the original specimen contour is loaded as polygonal line into this package. It is used as shape, which limits the area, where the raw packing is generated. The actual packing is done with spheres, which have diameters ranging between 0.1 mm to 0.5 mm. The chosen diameters are a compromise between a sufficient high resolution of the microstructure and practicable computation time for the final fracture test simulation.

In the scope of preliminary tests, it was found, that this size distribution ensures that most of the granite grains are simulated by at least 10 to 20 discrete elements. Higher resolutions can easily be achieved if the size of the spheres of the initial raw packing is decreased, for the price of increasing computational effort during the final simulation. However, it turned out, that a further improvement in the resolution accuracy does not benefit the validation process, as the quality of the results is already sufficient for the intended proof of concept.

Hence, the final raw packing for this example specimen consists initially of 12 623 elements. For this experiment, the spheres are arranged in a densely packed single layer. Therefore, the physics of the simulation is restricted to the two-dimensional case and the spheres are transformed into cylinders as well. These operations are done automatically by the program of the fracture test simulation. The calculative length of the cylinders is set to 3.5 mm, which corresponds to the average thickness of the real specimens. Rigid facets simulate both the indenter and the support.

Afterwards, the synthesized microstructure of the granite is mapped to the raw packing of the discrete elements, as explained in Figure 4.2 of Section 4.1.1. The realization of this process, in the scope of the basic indenter test with the synthetic twin of the granite from Meissen, is presented in Figure 4.19. With this method, each grain in the model is composed of a number of individual elements (cylinders), with diameters in the range of 0.1 mm to 0.5 mm, but otherwise identical parameters.

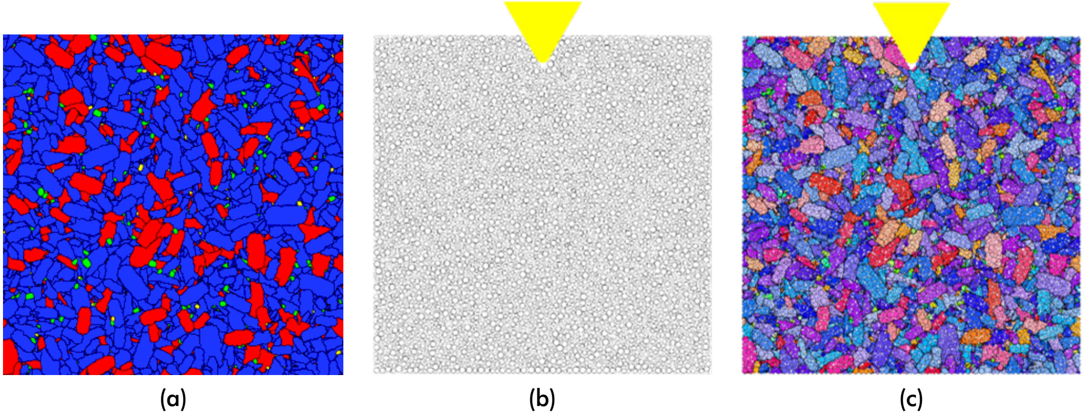

Fig. 4.19: Implementation of the synthetic granite microstructure into the DEM environment: (a) Picture of the synthetic granite with the size of the specimen; (b) Raw single-layered dense packing of cylinders with the indenter; (c) Final experimental setup in the DEM environment – For better demarcation, grains of the same material are painted in variations of the paired base color. Additionally, the grain boundaries are also drawn into the picture. The ground support is not visible since it is a plane that is orthogonal to the view.

Challenges for the parametrization of the DEM model. In the next step, the assignment process creates the bondings between all neighboring discrete elements, like exemplarily shown in Figure 4.3 of Section 4.1.1. As already explained, it is possible to distinguish between inter- and intragranular bondings. For the synthesized granite from Meissen with its four distinct phases, this makes four different intragranular and additionally six intergranular bonding types, which have to be parametrized. Unfortunately, there is only little information about, what the relevant physical properties of the grains for comminution simulation are and how they can be measured. Whereas for matrix properties of specific minerals at least some values can be derived from hardness and fracture toughness research, an experimental or analytical justifiable determination of their boundary properties is yet not possible.

Furthermore, one of the main limitations of the DEM, as presented in Section 2.1.3, has to be considered at this point. Usually, it is mandatory to calibrate the micro parameters of the particle contact model, so that the final simulation of the desired fracture process corresponds to its real role model. This is valid for commercial software like Particle Flow Code (PFC) as well as for open-source projects like YADE. It is state of the art to model the hard rock in BPM fracture simulation using an integral approach, which summarizes the mechanic properties of all individual microstructural properties of a given material. This is a historically grown procedure, as it simply adapts the typical geomechanical parameters like the Young's modulus or the compressive strength, which are usually determined for the whole rock material in standardized tests.

However, the micromechanic parameters are not equal to those typical geomechanical parameter, which are used to describe the loading and fracture behavior of hard rock. Model parameters like the contact stiffness and the cohesion in YADE, of course, do have related real parameters like the Young's modulus and the tensile strength. But, there is no generalized way to convert the parameters, gained from real geomechanical test work, into mircomechanic DEM parameters or vice versa. Besides the influences of the microstructure, which are only indirectly taken into account, this also highly depends on the actual model implementations. For this reason, the DEM parameters are typically stepwise optimized, until the simulated behavior imitates the real role model experiment in a satisfying manner.

The following brief digression shall help to understand the challenges of parameterizing such DEM models. An often used example material for DEM simulations of fracturing hard rock is the Lac du Bonnet granite, which was extensively analyzed and simulated in different studies [24, 72, 118, 149, 150, 173, 216]. Within those, the authors have used very different model parameters to simulate one and the same material in the UCS test setup. Based on the real Young's modulus of $E = 96\,\mathrm{GPa}$ and the real unconfined compressive strength $UCS = 200\,\mathrm{MPa} \pm 22\,\mathrm{MPa}$ [150], the finally used equivalent model parameters range between $E = 49$ to $100\,\mathrm{GPa}$ and $\sigma_n = 162\,\mathrm{MPa} \pm 44\,\mathrm{MPa}$ to $\sigma_n = 200\,\mathrm{MPa} \pm 50\,\mathrm{MPa}$, only for PFC2D based studies [24, 72].

However, those parameters can be even more different for other simulation environments. SCHOLTÈS and DONZÉ [173] showed, that the same material can be satisfactorily simulated using YADE with equivalent parameter ranges of $E = 68$ to $230\,\mathrm{GPa}$ and $\sigma_n = 70$ to $220\,\mathrm{MPa}$ respectively. Thereby, only the range for the bonding creation during the model initiation was changed.

It is therefore concluded that even if the same Lac du Bonnet granite had been used in this basic indenter test, it would not be possible to adopt the model parameters from the studies mentioned. The reason for this is, that they are typically only validated for the UCS test setup, which is used in these studies. Due to the lack of understanding of the correlations of all micro model parameters and the real physics, it can cause wrong results, if the test setup is changed to that of the indenter test.

At this point, the current limitation of the synthetic microstructure comes apparent. Although it is technically possible to provide a realistic microstructure to the simulation environment and independently parameterize all components via the different bonding types, it is not possible to fully utilize the potential, which arises from this approach. At the moment, we can neither reliably determine the physical properties of the microstructural components nor use integral values for the whole granite material, gained from typical geomechanical tests, as those are only valid for the test setups, where they are calibrated for.

Based on this, the only option for getting a model, which reproduces the macroscopic physical behavior of the real basic indenter test correctly, would be to stepwise optimize the parameters, until the simulation fits to the real measurements. However, following the above example, it is clear, that this approach would not help in the case of the intended proof of concept, as it would add only marginal value to the result.

It is obvious, that a given DEM model can be calibrated to fit a given role model experiment in almost every case. The informative benefit of such a simulation, however, is seen to be very limited. This is because the used model parameters can be physical nonsense at the micro level, although they might correctly imitate the physics on the macroscopic level of the actual experiment. Hence, it would not be possible to use the results in any other simulation setup, as they are bound to this specific application.

Abstract integral parametrization approach for the granite. Due to this unsolved challenges, it is decided to forgo a detailed physical model of the granite. In full awareness of the resulting limitations, the following simulation will not utilize the option of giving distinct material properties to every single grain and grain boundary at the moment. Furthermore, the simulation will willfully be set up with an abstract integral material model. As a start, this treats the granite like a generalized hard rock. A more adjusted, but not verifiable parameterization, would not benefit the proof of concept of the synthetic microstructure approach, which is actually in the focus. Hence, the chosen parameters are orientated in main features towards the presented Lac Du Bonnet granite. Following, the final parameters, which are shown in Figure 4.20, can be seen as placeholders for future improvements in the parametrization.

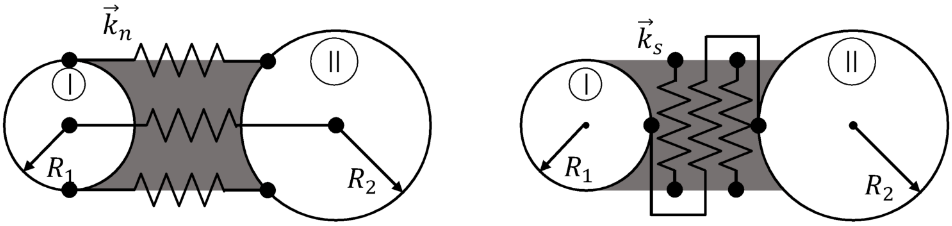

Young modulus $E = 50 \cdot 10^9$ N/m^2

Poisson ratio $\nu = 0.25$

Normal stiffness $k_n = \frac{2 \cdot E \cdot R_1 \cdot R_2}{(R_1 + R_2)}$

Shear stiffness $k_s = \nu \cdot k_n$

Rolling stiffness $k_r = 2 \cdot k_s \cdot R_1 \cdot R_2$

Normal strength $\sigma_n = 22$ MPa

Shear strength $\sigma_s = 22$ MPa

Rolling strength $\sigma_r = \infty$

Contact friction angle $\alpha = 0.5$ rad

Density $\rho = 2700$ kg/m^3

Fig. 4.20: Parameters for the bonding model of the granite from Meissen in YADE

In this final configuration, the bonding can be loaded by normal and shear forces as well as rolling moments. Twisting moments, however, do not occur due to the restriction to two dimensions. The reference for the shear and the normal strengths is always the area that is spanned between the diameter of the smaller cylinder and the thickness of the specimen. The bond breaks, if the maximum shear or normal force exceeds the maximum permissible strength. A full breakage due to rolling moments is not possible with the current bonding model. Exceeding the rolling strength would result in losing the moment bonding only. As this type of failure is atypical for minerals, the moment bonding is set unbreakable ($\sigma_r \approx \inf$).

The grain boundary factor. In order to allow the proof of concept, the grain boundary breakage of the fracture test shall be investigated exemplary. As can be seen from the results of the real fracture tests, about 50 % of the length of the crack paths is orientated along grain boundaries. Thereby it has propagated sometimes even laterally and out of the loading direction. As already explained, this can only be due interfacial breakage. The detailed data from the real tests predetermined this feature for the exemplary investigation.

On this data basis, it is decided to vary the grain boundary strength of the model in order to imitate the real fracture behavior. This approach is already applied by BEWICK; KAISER, and BAWDEN [14] to analyze the influence of grain structure during fracture. With the synthetic microstructure approach it is possible to overcome one of the main challenges that was identified by the authors themselves. They correctly ascertained, that they are not able to realistically simulate the microstructure, which is a reasonable simplification at this point of simulation.

Hence, for the proof of concept in this first stage experiment, the normal and shear strengths of relevant bondings are multiplied with a so-called grain boundary factor $z_{boundary}$ in the range of 0.6 to 1.4. Although a combination of different grain boundary factors for the normal and shear strengths is possible, the variation is applied to both strengths similarly in this study, for clarity reasons.

The indenter speed. The speed of the indenter in the simulation is set to 0.05 $\mathrm{m\,s^{-1}}$, which is significantly faster than the speed of the indenter in the real test setup (0.1 $\mathrm{mm\,min^{-1}} \approx$ 0.000 001 7 $\mathrm{m\,s^{-1}}$). However, this load rate is still low enough, so that the influence of the inertia of mass is insignificant for the model response.

Furthermore, it is noted that the bonding model itself is independent of the speed of the load. For this reason, there is no difference in the results between the simulations with 0.05 $\mathrm{m\,s^{-1}}$ and 0.000 001 7 $\mathrm{m\,s^{-1}}$ except the computation time. This is logical because more time steps are required for simulating the same displacement as the indenter itself is moved slower. The speed of the indenter is only restricted by the model stability. If the indenter is too fast, the model moves further away from the equilibrium state, which results in intensified vibrations in the simulated specimen. In the most extreme case, the vibrations become overcritical and the model can collapse.

In order to find a good indenter speed, preliminary tests were done. Their results show, that an indenter speed of 0.05 $\mathrm{m\,s^{-1}}$ is a good trade-off between reducing the simulation time and having a sufficient high model stability with enough reserves, till the model state becomes critical.

Evaluation of the simulated basic indenter test

The simulations with different factors for the strength of the grain boundaries show, that this parameter does influence the appearance of the fracture significantly. In Figure 4.21 the results of simulations are presented.

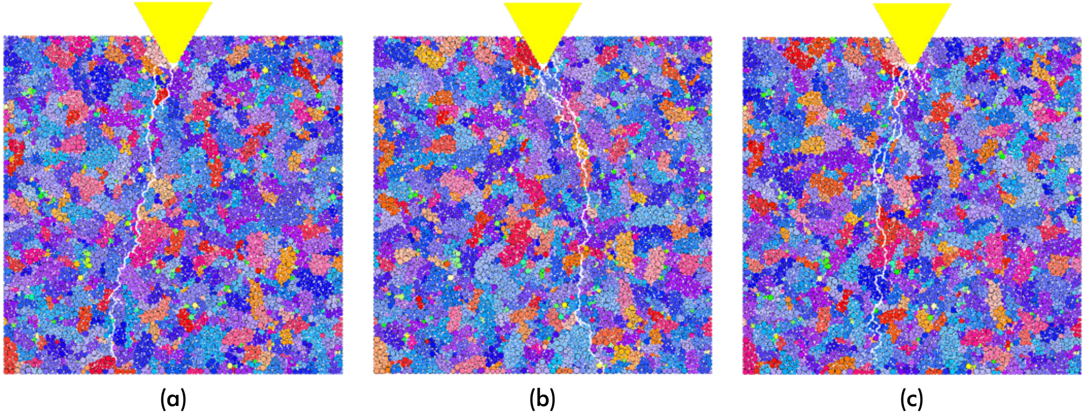

(a) (b) (c)

Fig. 4.21: Broken basic indenter test specimen with different grain boundary factors $z_{boundary}$ and the resulting portion of boundary breakage $p_{boundary}$: (a) $z_{boundary} = 0.6$, $p_{boundary} = 82\,\%$; (b) $z_{boundary} = 1.0$, $p_{boundary} = 35\,\%$; (c) $z_{boundary} = 1.4$, $p_{boundary} = 22\,\%$

Influence of the grain boundary strength. For the evaluation one should keep in mind, that the setup of the fractured specimens in these simulations was identical at the starting point. They all consisted of the same, identical packing of cylinders ranging from 0.1 to 0.5 mm in diameter. The only difference between them is the grain boundary factor $z_{boundary}$ for the grain boundary strength.

However, the evaluation of the fracture pattern reveals, that the crack propagates preferentially along grain boundaries, if they are weakened. For the simulation with a grain boundary factor of 0.6, the percentage of grain boundary breakage is 82 %. This means that the fracturing through grains is more or less an exception. A further interesting finding is, that the weak boundaries seem to abet the outbreak of single grains. This can be seen exemplarily in the upper part of the crack in Figure 4.21a.

In contrast, the crack path does not preferentially follow grain boundaries, if the boundaries do have the same strength as the grains ($z_{boundary} = 1.0$). In this case, the simulation environment treats the specimen like being made of a totally homogeneous material without microstructural influences. Therefore, the percentage of grain boundary breakage drops to 35 %. This value is a direct result of the resolution of the discrete elements. In the used setup 38.67 % of the bondings between the discrete elements belong to grain boundaries. Hence, if the grain boundaries do have the same characteristics as the intragranular bondings, the overall proportion of grain boundary breakage converges towards the proportion of the grain boundary bondings itself.

If the strength of the grain boundaries is further increased, this has only minor influence on the appearance of the crack path. For a grain boundary factor $z_{boundary}$ of 1.4, the percentage of grain boundary breakage decreases further to $p_{boundary} = 22$ %.

However, in the simulations with grain boundary factors of 1.0 and 1.4 a branch-like crack structure is formed in the region of the notch. Detailed analyses of the simulation results, reveal that the reason for this is the touchdown of the indenter in the root of the notch. This happens during the opening of the major crack just before the specimen finally breaks. The same behavior was observed in several of the real fracture tests. The reason for this effect is, that the environment in the root of the notch is subjected to direct normal load, which causes many small, local cracks in the specimen. When using a weak grain boundary structure in the simulation ($z_{boundary} = 0.6$) the specimen breaks before the indenter touches down, which prevents similar shattering in the region of the notch.

Influence of the microstructure. The above presented findings can be seen as direct influence of the microstructure on the fracture behavior. By changing the characteristics of the discrete elements packing from representing a homogeneous material to a structured arrangement of different grains, the breakage behavior is directly affected. In order to imitate the observed preferred intergranular fracture of the real samples, the grain boundary factor $z_{boundary}$ is further adjusted.

Based on the first series of simulations, it is found that $z_{boundary}$ should fall in the range between 0.80 to 0.90. Based on this, a test series with simulations using a finer graded $z_{boundary}$ of 0.825, 0.850, and 0.875 is conducted. The results for the portion of boundary breakage $p_{boundary}$, which belong to these simulations, are listed in Table 4.6. The tabulated results are supplemented by the corresponding arithmetic average AM, the standard deviation SD, and the coefficient of variation CV.

Additionally, Figure 4.22 shows a single specimen of each test series exemplarily. In conclusion, the different factors for the grain boundary strength of 0.825, 0.850, and 0.875 result in a grain boundary breakage of 57.62 % ± 4.52 %, 53.66 % ± 5.01 %, and 50.51 % ± 3.88 %,

Tab. 4.6: Proportion of the length of grain boundary cracks of the total crack length $p_{boundary}$ of the three test series with the finer grained factor for adjusting the grain boundary strength $z_{boundary}$

	$p_{boundary}$ [%]		
No.	$z_{boundary} = 0.825\,\%$	$z_{boundary} = 0.850\,\%$	$z_{boundary} = 0.875\,\%$
1	63.31	50.00	55.00
2	57.33	67.74	58.59
3	55.81	53.51	52.32
4	62.21	54.76	46.24
5	54.05	58.59	54.71
6	55.92	54.75	47.85
7	55.62	53.99	50.62
8	58.27	57.48	46.18
9	52.42	47.95	45.25
10	56.88	47.06	48.86
11	50.17	50.62	47.17
12	57.55	53.56	48.78
13	61.84	51.42	50.22
14	55.09	52.02	51.41
15	67.74	51.49	54.39
AM	57.62	53.66	50.51
SD	4.52	5.01	3.88
CV	7.85	9.33	7.68

respectively. When this is compared to the average value and the standard deviation of the real experiments, which is 55.7 % ± 11.4 %, it can be concluded, that the results for this simulated specimen are clearly in the range of the experimental results. This is seen as proof, that the synthetic microstructure approach can in principle be used for the incorporation of realistic microstructural features in corresponding simulations.

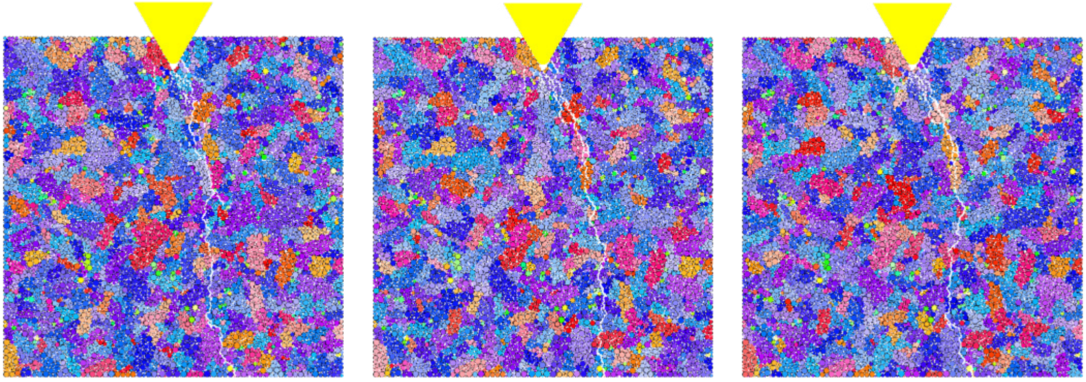
(a) (b) (c)

Fig. 4.22: Broken specimen with different grain boundary factors $z_{boundary}$ and the resulting portion of boundary breakage $p_{boundary}$: (a) $z_{boundary} = 0.825$, $p_{boundary}$ = 57.62 % ± 4.52 %; (b) $z_{boundary} = 0.85$, $p_{boundary}$ = 53.66 % ± 5.01 %; (c) $z_{boundary} = 0.875$, $p_{boundary}$ = 50.51 % ± 3.88 %

Influence of the discrete elements packing. In order to quantify the influence of the packing of the discrete elements, further 15 simulations were done. Therefore, the same synthetic microstructure was mapped to different packings, which were created with the same packing parameters as used for the preceding simulations. Altogether, these packings consist of 12 504 ± 86 discrete elements, which have a porosity of 14.57 % ± 0.05 %. For the DEM configuration, the boundary factor with the best fit to the real experiments ($z_{boundary} = 0.825$) is used.

The evaluation of these simulations reveals, that the variance of the grain boundary breakage due to different packings is as low as the influence of the differences in the microstructure. In detail, the average of the simulated grain boundary breakage is 56.57 % with a standard deviation of 5.07 %. Hence, it is concluded, that the influence of the resolution of discrete elements is small enough for this proof of concept study. For continuative applications, however, it may be necessary to analyze, which discrete element sizes are required for the particular purpose.

With regard to the remaining differences of this analysis, it has however to be considered, that the simulated amount of grain boundary breakage $p_{boundary}$ is the result of simulations with the same simulation setup, varied in one parameter only.

4.2.4 Conclusions on the basic indenter test

First of all, the comparison of the real and the simulated results shows, that this new fracture test is suitable for validating two-dimensional DEM simulations of mineral fracture processes at the grain size level. It is possible to reconstruct the fracture process, of which the primary crack is of particular interest, in greater than previously possible detail. For this, the measured data and high-speed recordings are of special interest. The experimental setup also guarantees that the conditions for the primary cracking are consistent and comparable. In addition, it is a suitable setup for the evaluation of the fracture work, as the primary crack stops within the specimen. This is beneficial as it reduces the potential for errors.

Regarding the intended proof of concept for the applicability of the synthetic microstructure approach, the results are promising. This first experiment shows, that it is possible to successfully utilize a realistic mineral microstructure in a fracture simulation. This includes the original synthesis of the microstructure on the basis of real QMA analysis data, the import of the microstructure into a given DEM environment, and making use of the resulting possibilities. This all is done exemplarily with the granite from Meissen as role model and applied in the scope of the indenter test.

Using that as basis, the grain boundary factor $z_{boundary}$ is used to utilize one feature of simulations at grain size level, exemplarily. Although the used physical model of the granite in the DEM simulation uses abstract parameters and should therefore only be seen as a placeholder for comparable hard rock material, the qualitative fracture behavior of the specimens can be reproduced quite accurately. In summary, the main features of the chosen approach are rated positively. For this reason, it is decided to continue with the second stage of the proof of concept. Within those experiments it is intended to test this approach with a more complex microstructure and a test setup, which is closer to mineral processing reality.

4.3 Extended indenter test

The results of the presented basic indenter test are the basis for the second stage experiments. As explained in Figure 4.4 of Section 4.1.2, the identical test setup is used to test the synthetic microstructure approach with a more complex material but the otherwise same experimental setup. Therefore, this experiment is addressed as extended indenter test in the following section.

4.3.1 Basic considerations for the extended indenter test

The basic considerations for this extended indenter test are in principle the same as for the basic indenter test. In order to allow a good comparability, the exact same setup is used. Hence, the details of the setup are not in the focus again. However, as the basic idea of this test relies on a more complex microstructure, the selection of appropriate test material is explained in detail.

Selection of the test material

The selection of the test material for the extended indenter test is bound to equivalent conditions as for the basic indenter test. Again, it should be a hard rock with a middle to coarse-grained microstructure. Otherwise, for finer grained material, the optical identification of the crack paths during the evaluation of the real fracture test would be hindered. The requirement for a homogeneous and isotropic mineral microstructure is basically valid for this experiment as well. However, as this is somehow contradictory to the intention to test a more complex microstructure, this requirement is subordinated.

The Freiberg deposit and the kb-ore. For the selection of the test material for the extended indenter test, the area around Freiberg is of special interest as it is well known for its lode deposit. In combination with other rich ore deposits in the surrounding area, it can be seen as eponym for the Ore Mountains. Furthermore, the hydrothermal lode deposit of Freiberg is one of the best known and explored ones of the world [182]. It can be distinguished between four main ore formations. Among them is the so called kb-ore. It is named after the abbreviation for its historical German notation "Kiesig-Blendige Bleierzformation". This ore is found in lodes with a typical thickness of 0.1 to 0.8 m. However, these veins can also be as thick as 2 m at some points, while in other places they may be only a few centimeters wide [129].

This specific ore type is characterized by quartz as the main gangue mineral. The main ore components that can be found are pyrite, sphalerite, galena, arsenopyrite, chalcopyrite, and marcasite. The actual composition of these components is very irregular and can differ between two points, which are located just a few centimeters next to each other. Furthermore, a multitude of other gangue and ore minerals are unpredictably spread in smaller quantities in the lodes.

Historically, some of the ore components were important for the silver winning, which is one of the reasons for the long lasting mining activities in the Ore Mountains. In terms of the kb-formation, the valuable silver was mainly found within the galena. However, some of the other ore minerals of the kb-formation like pyrite, arsenopyrite, and chalcopyrite do have also low silver grades. Unfortunately, those were too low for an economic mining or not processable due to metallurgical problems [129].

For the extended indenter test, the kb-ore from Freiberg combines a multitude of advantageous characteristics. Besides its publicity in geological sciences due to its mining history value and its high microstructural variability, it is also well available, since the kb-ore can be obtained directly from the university's own research and teaching mine "Reiche Zeche". Hence, for the presented reasons, the kb-ore from the Freiberg deposit is chosen for the extended indenter test.

Characterization of the kb-ore. The material for the extended indenter test is freshly mined ore from the lode "Wilhelm Stehender". As the material is chosen for the second stage of the proof of concept, attention is payed, that the raw material consists of different portions of quartz in relation to the main ore components (Figure 4.23). This is intended to guaranty a certain variety within the mineral microstructure.

In contrast to the very homogeneous granite from Meissen, no three-dimensional QMA data is available for this material. As the ores from the Freiberg deposit have not been mined anymore in industrial scale since 1969, there was no reason to apply the relatively time-consuming conventional QMA to the different ore types. Furthermore, due to the inhomogeneous structure within the lodes, it would be difficult to gain useful information from the results. It is obvious, that an arbitrary chosen sample would hardly be representative for the typical variety of such a lode.


(a) (b)

Fig. 4.23: Two sample lumps of the kb-Ore: (a) Sample lump with a mixed microstructure containing both gangue and ore minerals - the intended cutting plane is orthogonal to the view in the lump; (b) Sample lump with a high content of ore minerals - the intended cutting plane, which is marked by the white line, is parallel to the view

Nevertheless, based on a classical qualitative mineral characterization and with respect to its genesis, the example material can be classified as brecciated, middle to coarse grained pyrite. The main minerals of the matrix in the samples are quartz, galena, chalcopyrite, and sphalerite with variable portions on the total mass as well as minor amounts of other minerals, which are insignificant for further considerations. In contrast to the compact microstructure of the granite from Meissen, the kb-ore is cracky so that not every lump is appropriate for sample preparation.

For the above mentioned reasons no UCS or Brazilian tests were conducted with the test material, as well. This is because the comparability of these results would not be given due to its inhomogeneity. However, as emerges from the basic indenter test, the classical QMA, the unconfined compressive strength as well as the Brazilian tensile strength would yield only minor benefits for the proof of concept anyway, as they are not usable for the simulation part. Hence, the abandonment of these characterization methods is seen to be disadvantageous but acceptable for the experiment. The actual input parameters for the synthesis will only be generated by the adapted two-dimensional QMA, which will be done anyway.

Setup and procedure of the test

The setup of the extended indenter test is identically to that of the basic indenter test. Hence, for detailed setup information, it is referred to Section 4.2.1. The same applies for the experimental procedure, which also does not differ from the basic indenter test. The explanations for the procedure of the basic indenter test in Section 4.2.1 therefore are also applicable to the extended indenter test.

4.3.2 Realization and evaluation of the real extended indenter test

Because the setup of the extended indenter test is identical to the basic indenter test, the realization is similar as well. However, as the kb-ore is more complex than the homogeneous granite from Meissen, both the specimen preparation as well as the actual sequence of processes during the test are slightly different.

Preparation of the ore specimens

As indicated, the preparation procedure for the kb-ore specimens is the same as for the granite specimens in principle. However, it has to be noticed, that the material is more fragile than the granite. Hence, the preparation and handling is characterized by sometimes unpredictable specimen damages. For this reason, the predefined specimen shape could not be guaranteed for every prepared sample. Some final specimens have broken corners or rough edges. But as long as it can be assumed, that these deviations do not influence the actual test procedure and results, they are tolerated. Major breakouts as well as damages in the region of the notch, or the bottom edge, however, lead to exclusion from further use. This is especially the case for quartz rich samples.

Specimen varieties. Based on the mode of the mineral microstructure, the final specimens can be subclassified into three varieties:

- Pyrite-bearing specimen (py): The coarse grained pyrite is only partly brecciated. With a portion of about 70 to 90 %, it is the major component of the microstructure and it is accompanied by smaller amounts of matrix material.
- Pyrite-bearing specimen with galena (py + ga): The middle to coarse grained pyrite is completely brecciated and occupies approximately 70 % of the microstructure. The quartz and sphalerite matrix is furthermore interspersed with significant amounts of galena.
- Mixed specimen (mix): The microstructure is a mixture between the brecciated pyrite and contiguous, middle to coarse but sometimes also fine grained quartz compounds. Both have reciprocal frequencies of occurrence of 30 to 70 %. Smaller areas are also marked by fine to middle grained galena and sphalerite grains.

However, due to the hydrothermal genesis of the lode system, there is a smooth transition between the different varieties. Hence, it is not possible to encompass all nuances of a specimen with either a qualitative nor a quantitative characterization.

Specimen characteristics. Altogether, a total of 19 specimens were successfully prepared. Although the mineral microstructure shows a certain variability, this number is seen sufficient for the extended indenter test in the scope of the proof of concept, especially, when the idiosyncrasies of the material handling are considered. In summary, five specimens each can be subclassified as pyrite-bearing (py) and pyrite-bearing with galena (py + ga). The remaining eight specimens belong to the mixed group (mix).

The final thickness of the plates is on average 2.71 mm ± 0.28 mm. However, one plate of the mixed group, with a final thickness of approximately 4.08 mm is excluded from this calculation. As all other specimens of this quartz rich sample lump broke earlier during the preparation process, the grinding for this one was stopped before the intended thickness was reached. However, as this specimen is one of a few remaining ones with a notable amount of quartz, it is not excluded. Considering this, all 19 specimens are available in total for the actual test work.

Fluorescent liquid penetrant testing. Following the positive experience of the liquid penetrant testing with fluorescent dye of the granite specimen, the kb-ore specimens are also subjected to this non-destructive surface crack detection technique. In Figure 4.24, pictures of three specimens with different portions of quartz are shown.

The evaluation of this pictures shows, that particularly the quartz rich zones can be analyzed very well with this method, as the quartz is translucent. Therefore, also that dye is activated under the UV light that is not at the surface of the sample, but in flaws or grain boundaries inside the specimen.

In contrast, the ore minerals are characterized by their opacity, which makes it impossible to see the same details as for quartz. Nevertheless, it is possible to satisfactorily determine grain boundaries and flaws in combination with the images taken under visible light. The evaluation of this data confirms the previous impression of the preparation, that the quartz is more cracky than the ore minerals.

Realization of the real fracture tests

After finishing the preparation with the fluorescent dye, the 19 prepared specimens were fractured with the explained test procedure. For illustration, Figure 4.25 shows the test setup exemplary from the back immediately after the specimen is broken. It demonstrates that the used setup and equipment for the extended indenter test is similar to the basic indenter test.

Furthermore, the fracture process can be distinguished into different states as well. Therefore, Figure 4.26 shows exemplarily a sequence of consecutive photos of the test procedure with

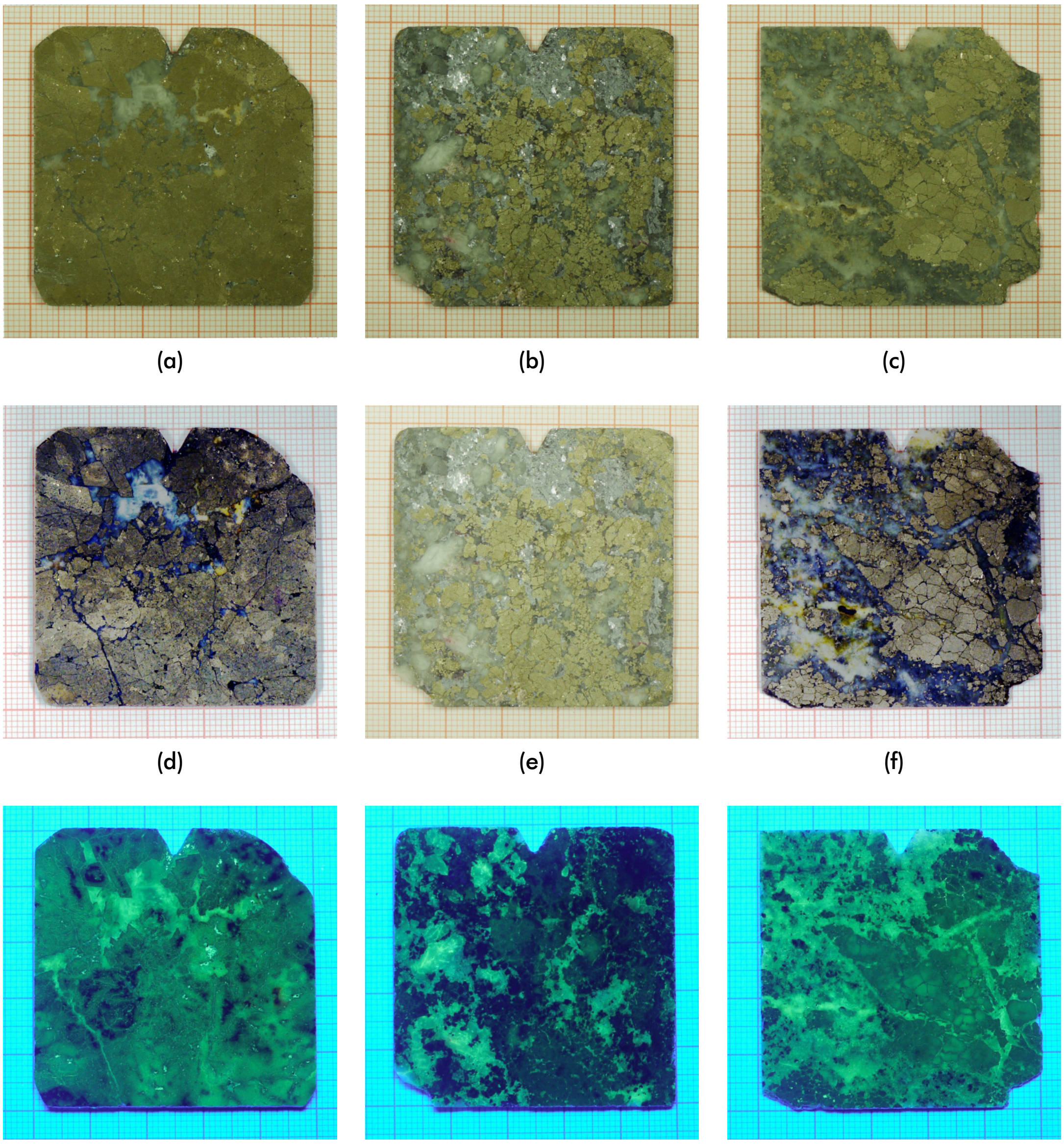

Fig. 4.24: Specimens for the extended indenter test with different ore contents: (a) Pyrite-bearing specimen (py) under normal light; (b) Pyrite-bearing specimen with galena (py + ga) under normal light; (c) Mixed specimen (mix) under normal light; (d) to (f) Photos of the specimens under normal light, optimized with image processing methods for improved recognizability of the microstructure; (g) to (i) Photos of the specimens under UV light, optimized with image processing methods for improved recognizability of the microstructure

a rich ore specimen, which can be compared to the photos of the basic indenter test (Figure 4.11). The photos are taken with the additional digital camera and show the different states of the specimen, which can be examined during the experiment.

The fracture states. The first state is also the pre-failure state at the beginning of the test. It is usually followed by the initial failure event, which is marked by a primary crack and possible subsequent cracks inside the specimen. After further loading and possible further small cracks, the test ends with the finale failure of the specimen.

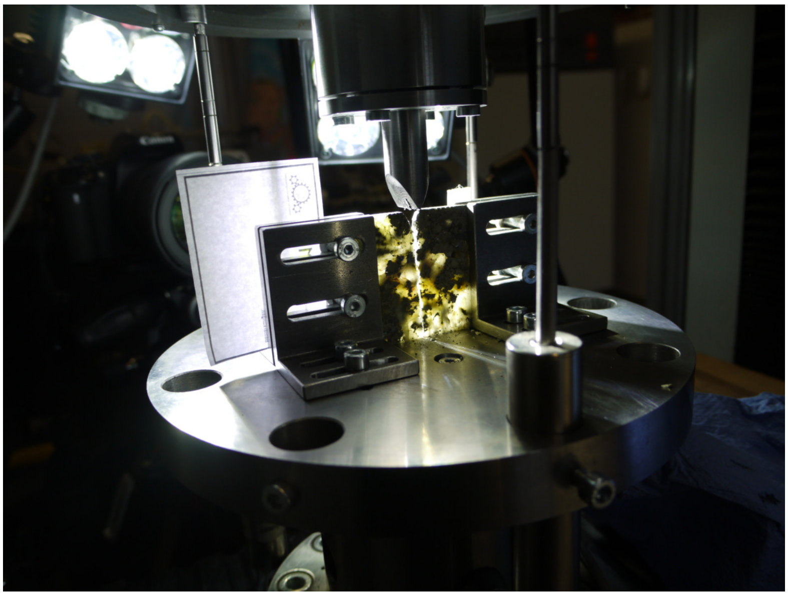

Fig. 4.25: Photo from the rear of the real experimental setup of the extended indenter test. The fracture test is completed as the specimen is already broken and the indenter raised again. The translucent areas are zones with quartz. In the background, the additional digital camera and the switched-on lamps for the high-speed camera are visible. The high-speed camera itself is in the dark behind the lamps and therefore not visible.

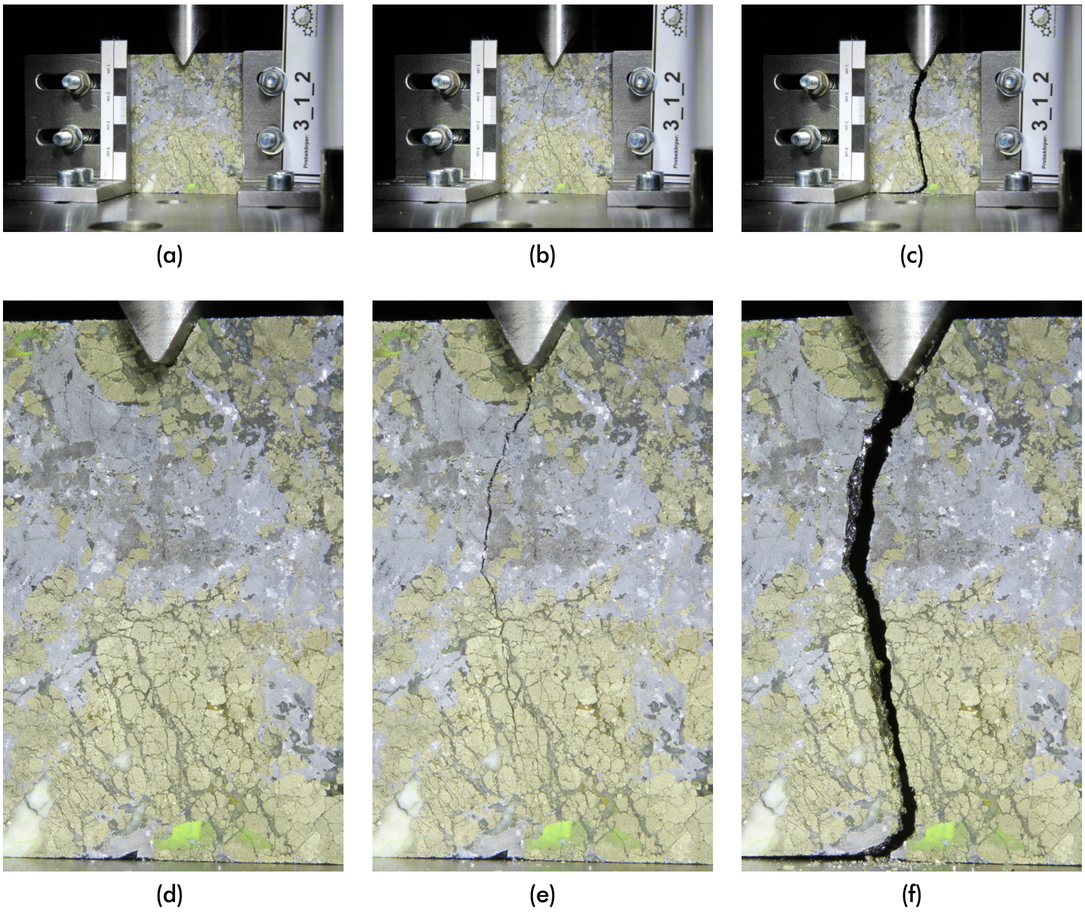

(a) (b) (c)

(d) (e) (f)

Fig. 4.26: Sequences of an extended indenter test: (a) Specimen at the beginning of the test; (b) Specimen after primary and secondary crack; (c) Finally broken specimen; (d) Detailed view on the initial microstructure; (e) Detailed view on the secondary crack; (f) Detailed view on the final fracture

However, in contrast to the basic indenter test with the granite from Meissen, this sequence is not always that distinct. For example, during three fracture tests, no second states were discernible because the initial cracks already propagated through the whole specimens. In addition, it should be noted, that one of the tests was not completed since this particular specimen did not break at all. During this test the load on the specimen reached a critical level for the experimental setup. Hence, in order to prevent damage from the load cell, the test was aborted before any fracture could be measured.

Similarly, one test was aborted after the primary crack, but before the specimen broke finally, as the indenter already touched the ground of the notch. Due to this undesired load on the ground of the notch, the expected final fracture event would not have been usefully evaluable. Hence, this test was also stopped in order to preserve the load cell. Nonetheless, the test is considered to be successful up to this point, so that at least the data for the primary crack is taken into account for the evaluation process.

In summary, 17 of the 19 prepared specimens were successfully tested. Although the primary cracks of three tests fractured the whole specimen, this is seen to be an acceptable result for the more complex and difficult to handle specimens. In addition, the results of the one test that was stopped before the final fracture can also be used to evaluate the primary cracks.

Evaluation of the real fracture tests

The evaluation of the extended indenter test is done with the same focus as the evaluation of the basic indenter test. In order to analyze the influence of the mineral microstructure on the fracture behavior, the broken specimens are evaluated in a first step. Additionally, the high-speed recordings and the force-displacement data are consulted, in order to filter out the primary fracture events.

Procedure for the evaluation of the broken specimens. The evaluation of the overall crack path is of course done with the help of the pictures of the broken specimens under different lighting conditions and with the help of image processing methods. This is illustrated by Figure 4.27, where the crack path is marked with different colors for intergranular and intragranular fracture. This single specimen is of particular interest, as the crack path is split just below the middle of the specimen, which is a rarely observed phenomenon.

As explained for the basic indenter test, it is not possible to use these images for further interpretations of the grain combinations involved. This would require further microscopic analysis since the detection of the actual grains using normal photographs is not reliably possible. However, such a detailed analysis for each specimen is out of the scope of this study.

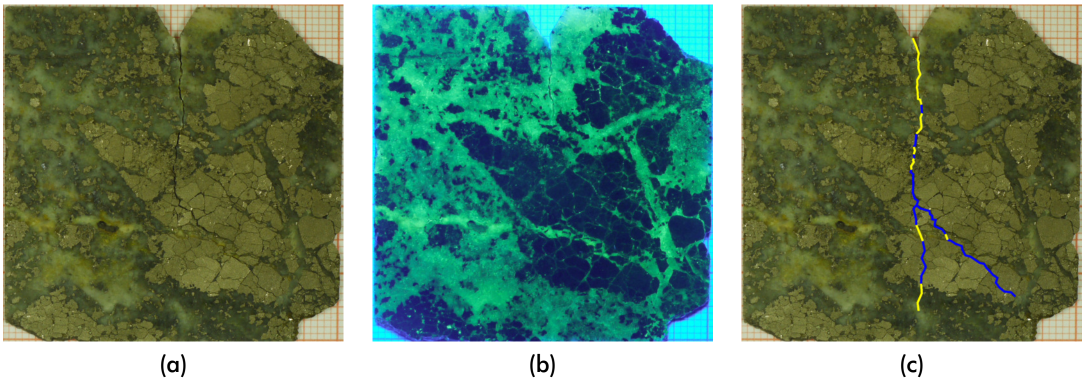

Fig. 4.27: Fractured specimen of the extended indenter test: (a) Normal lighting; (b) UV-lighting - optimized with image processing methods for improved recognizability of the microstructure; (c) Normal lighting with highlighted crack path Blue – Fracture along a grain boundary; Yellow – Fracture through a grain

Hence, equivalent to the basic indenter test, this data is used to determine the fracture surface A_{crack} (Equation 4.1) on the basis of the measured crack length l_{crack} and the specimen thickness $d_{specimen}$.

Procedure for the evaluation of the high-speed recordings. On the whole, the fracture process of the kb-ore, which was monitored with the high speed camera, is comparable to the fracture process of the granite specimens. The main difference is, that the first crack is only marked by a milky veil when it passes through quartz grains. Due to the opacity of the ore minerals, no optical changes are registered when they are subjected to fracture without opening the crack. Hence, image processing methods are even more important for determining the length of the primary cracks, as shown in Figure 4.28. Without it, this process would be relatively error-prone, as the small cracks in the ore material are barely visible.

Procedure for the evaluation of the force-displacement data. As the monitored fracture processes of the extended indenter test are very similar to their pendants of the basic indenter test, it is possible to adopt the evaluation procedure of the force-displacement data one-to-one. For comparison, the measured data of a fracture test with the kb-ore is shown in Figure 4.29, exemplarily. As explained for the basic indenter test, the relatively long offsets on the time scale between the various crack events are due to the test pauses, since these are needed to save the high-speed recordings. Despite this, the similarities to the plots of the basic indenter test are apparent.

Summary of the results. The final results of the evaluated data belonging to the primary crack are summarized in Table 4.7. As explained, one test was stopped before the specimen broke. Hence, the table contains only the summarized results for the 18 fractured specimens. However, the characteristic values are identical to those, which were used for the evaluation of the basic indenter test.

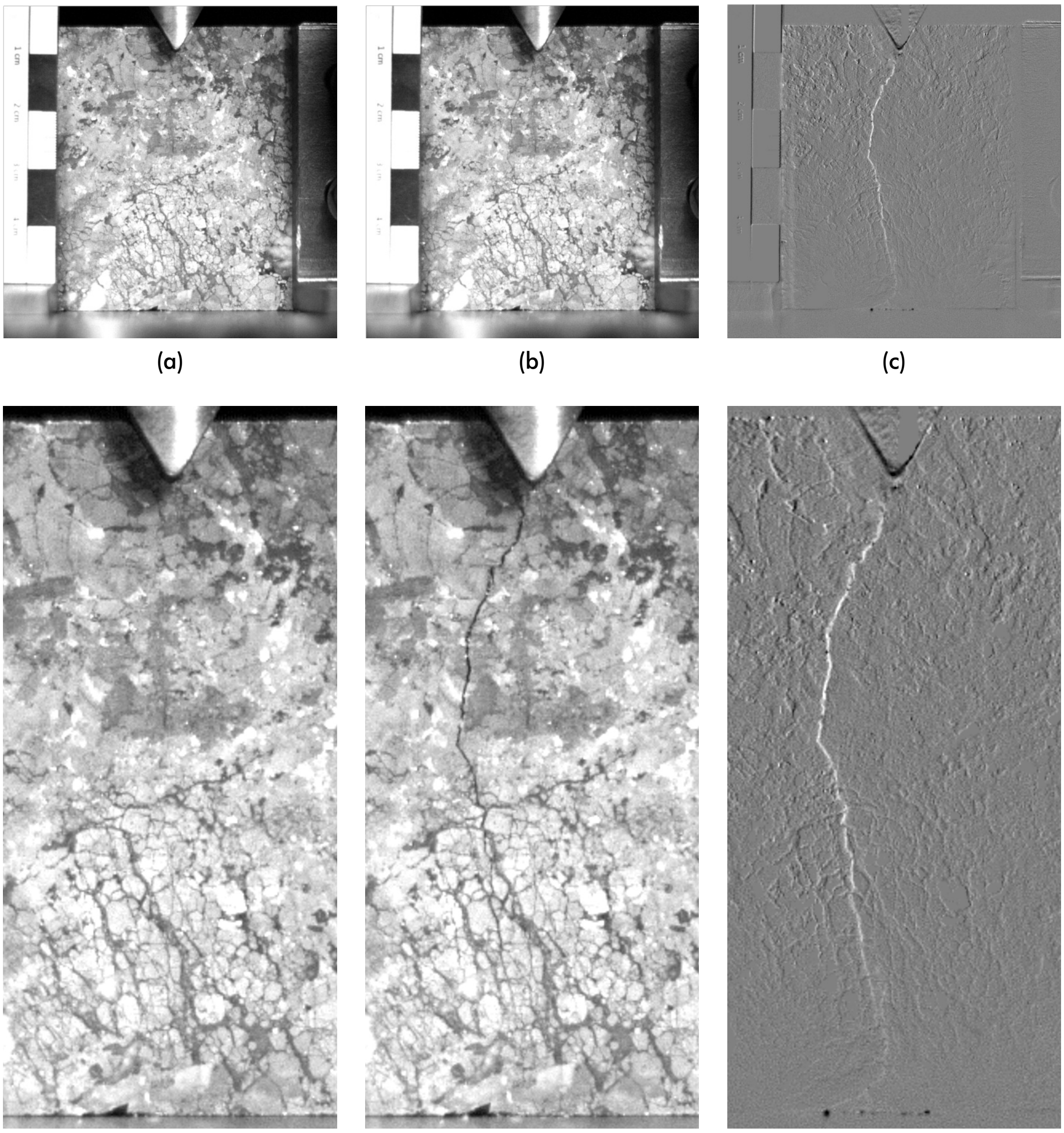

(a) (b) (c)

(d) (e) (f)

Fig. 4.28: High-speed recordings of a kb-ore specimen after the primary crack: (a) Primary crack can be recognized by the small black line near the notch. The milky veil is barely visible in the bottom part; (b) Primary crack is opened; (c) Visualization of path of the primary crack in the high-speed records using image processing methods (d) Detailed view of the primary crack; (e) Detailed view of the opened primary crack; (f) Detailed view of the path of the primary crack

Besides this, in order to allow the evaluation of the influences of the actual ore type, this group of measured parameters is completed by the particular variety of the kb-ore specimen. According to Section 4.3.2, in total five pyrite bearing specimen with galena (py + ga), five pyrite bearing specimen (py), and eight specimens with a mixed microstructure (mix) were tested.

Since, however, it is basically material of the same origin and it is a smooth transition between the different types of microstructure, first the data of all samples are evaluated together. On this basis, it can be summarized, that the results of the extended indenter test are comparable to the results of the basic indenter test.

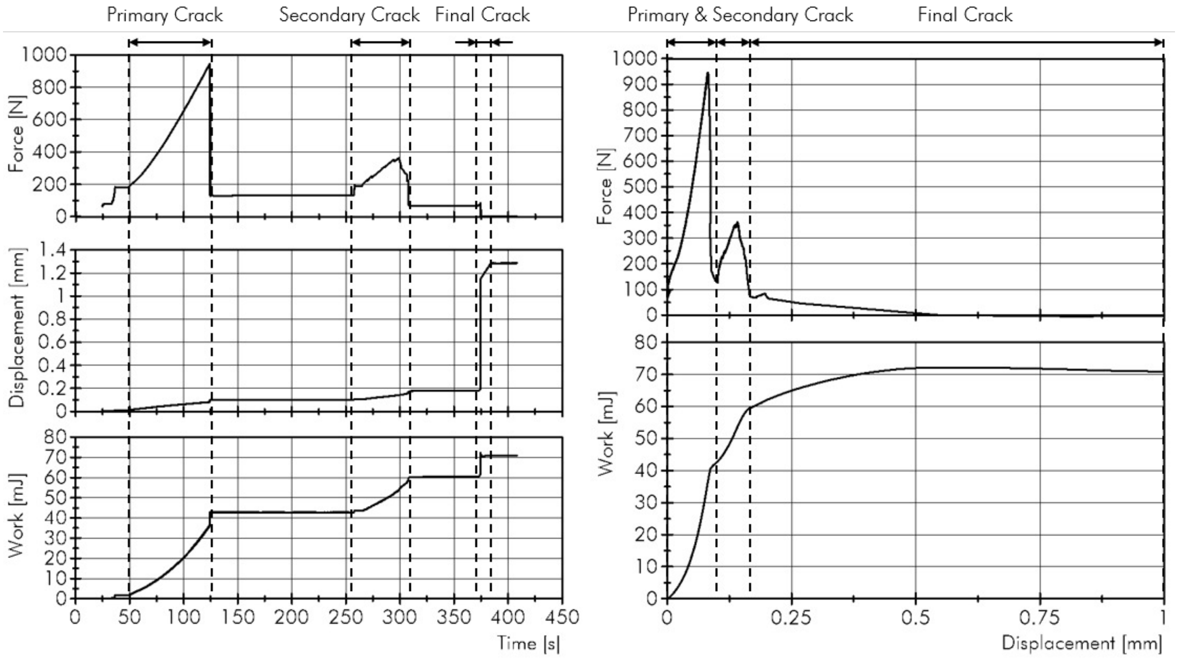

Fig. 4.29: Exemplary plots of the data of an extended indenter test: Force, displacement, and energy consumption as function of the experimental time (left); Force and energy consumption as function of the displacement (right)

However, it seems, that the ore specimens break at higher loads than the granite specimens. That is in so far surprising, as the tested specimens of the kb-ore are thinner and were more fragile in preparation than their granitic counterparts. The higher resistance to breakage is also reflected in the values of the fracture work W_{crack}. Compared to the granite specimens, the primary cracks of the kb-ore specimens require approximately three times as much energy for propagation. Despite this, it is further found, that the portion of grain boundary breakage $p_{boundary}$ is higher as well.

Evaluation of the crack speed. The most significant difference, however, can be seen in the measured time Δt_{crack}, which the primary cracks need to propagate. First, it is referred to the seven tests, where it is not possible to determine the actual duration of the crack propagation. Of these, one test was simply not evaluable, as it was not recorded correctly by mistake. In contrast, the specimens of the remaining six tests, were successfully broken and recorded. However, the primary crack during those was so slow and/or the crack path and its length was hardly to identify, so that a reliable evaluation is not possible. Hence, they have to be suspended from this specific evaluation.

Taking the remaining eleven tests into account, the actual primary cracking of the kb-ore specimens can be summarized as more heterogeneous than the primary cracks of the granite. This is confirmed by the variation of Δt_{crack}. Although some of the evaluable tests are in the same range as the granite samples, there are also specimens, which cracked significantly faster. In case of test No. 16 a time of approximately 0.003 s was measured. This is about 30 times less than for the granite specimen with the shortest duration.

Tab. 4.7: Raw measurement data for the extended indenter test: Shown are the results of all 18 tests with distinct primary crack. They represent the status of the specimens just after propagation and stoppage of the primary crack. Values that are not available are labeled with n.a.

No.	variety	$d_{specimen}$ [mm]	F_{crack} [N]	l_{crack} [mm]	A_{crack} [mm^2]	$p_{boundary}$ [%]	W_{crack} [J]	Δt_{crack} [s]	v_{crack} [mm/s]
1	py + ga	2.9	720.1	45.8	130.6	77.6	53.7	0.011	4259.3
2	py + ga	2.8	789.0	49.5	136.2	46.1	60.4	0.015	3407.4
3	py + ga	2.4	548.1	59.7	144.3	49.6	54.9	n.a.	n.a.
4	py + ga	3.0	982.1	38.7	115.4	51.6	74.5	n.a.	n.a.
5	py + ga	3.0	342.1	50.7	151.3	65.5	22.5	n.a.	n.a.
6	py	2.8	426.9	64.5	178.4	89.6	78.2	n.a.	n.a.
7	py	2.6	422.8	48.1	123.5	77.7	44.7	n.a.	n.a.
8	py	2.6	599.3	58.4	151.9	83.9	109.8	0.038	1534.6
9	py	2.9	723.0	45.1	132.4	79.1	51.9	0.012	3618.0
10	py	2.1	437.4	32.2	66.0	41.5	22.5	n.a.	n.a.
11	mix	2.2	706.7	44.9	98.9	39.5	42.1	0.310	144.9
12	mix	2.7	1217.7	73.3	197.8	70.8	117.8	1.878	39.0
13	mix	2.8	541.7	14.5	40.4	60.7	26.9	n.a.	n.a.
14	mix	2.9	1298.8	57.2	165.7	52.4	84.4	1.281	44.6
15	mix	2.8	466.7	42.4	117.4	49.1	40.7	0.372	113.9
16	mix	2.8	946.3	51.8	142.4	64.3	42.8	0.003	17 830.7
17	mix	3.0	597.3	41.6	124.2	88.8	50.2	0.437	95.4
18	mix	4.1	1540.2	51.4	210.1	36.6	163.0	0.012	4428.3
AM	–	2.8	739.2	48.3	134.8	62.5	63.4	0.397	3228.7
SD	–	0.4	336.6	12.9	41.4	17.5	36.5	0.621	5178.0
CV	–	15.0	45.5	26.7	30.7	27.9	57.7	156.4	160.4

This finding is reflected by the calculated crack speeds v_{crack} as well. These are on average significantly higher and more variable than those of the basic indenter test. Nevertheless, even specimen No. 16, which has the highest crack speed $v_{crack} = 17\,830.7\,\mathrm{mm\,s^{-1}} \cong 17.83\,\mathrm{mm\,s^{-1}}$, broke significantly slower than the calculated maximum separation velocity of $1297\,\mathrm{m\,s^{-1}}$ at the crack tip for α-quartz [208].

Evaluation of correlations. According to the evaluation of the basic indenter test, the most promising combinations of the variables are tested for correlations with Spearman's rank correlation test. The corresponding results are shown in Table 4.8.

Tab. 4.8: Spearman's rank correlation coefficients $\rho_{spearman}$ and the corresponding $p - values$ for specific data pairings of the extended indenter tests

pairing	$F_{crack} \sim d_{specimen}$	$F_{crack} \sim A_{crack}$	$F_{crack} \sim W_{crack}$	$l_{crack} \sim A_{crack}$	$W_{crack} \sim A_{crack}$
$p - value$	0.233	0.142	0.004	0.000	0.001
$\rho_{spearman}$	0.223	0.809	0.654	0.855	0.882

As it is expected, these are the same combinations as for the granite. Based on the presented results, it can be concluded, that the same correlations apply in principle to the extended indenter tests. Although the results of the correlation test between the fracture force F_{crack} and the specimen thickness $d_{specimen}$ are not significant, it is assumed to correlate anyway. Since the thicknesses of the tested kb ore samples are more uniform than those of the granite samples, apparently the effect of the thickness variations on the fracture force is too low for finding correlations.

Furthermore, the same applies for the pairing $F_{crack} \sim A_{crack}$. However, an effect size of $\rho_{spearman} = 0.809$ indicates, that there is also a high correlation. The low p-values and the high effect sizes for the pairings $F_{crack} \sim W_{crack}$, $l_{crack} \sim A_{crack}$, and $W_{crack} \sim A_{crack}$ demonstrate that there are strong correlations as already proven for the basic indenter test.

In addition, these interesting pairings are plotted for visual verification in Figure 4.30. For the sake of completeness, the different microstructure types of the kb-ore are represented with different markers. Based on these plots, it becomes apparent, that it is not possible to reliably distinguish the test results of the three groups. Although there are differences in the mineral microstructure, it is impossible to statistically satisfactorily discriminate the test results based on these 18 experiments. However, this could also be due to the limited data base. For a truly meaningful conclusion on this question, significantly more tests per microstructure type are therefore mandatory.

Besides that, the plots illustrate the above-mentioned findings for the different pairings. In detail it can be seen that the spread of the thickness of the specimens $d_{specimen}$ is too small to prove a correlation to the fracture force F_{crack}. The one test with a thickness of about 4.1 mm does not provide sufficient parameter variation in contrast to the other 17 tests with a narrow thickness distribution between 2.1 mm and 3.0 mm.

The plot of the pairing $F_{crack} \sim A_{crack}$, however, offers an interesting detail. Taking into account only the values of the mixed microstructure (mix) samples, a linear relationship can be assumed since the results are arranged along a diagonal from bottom left to top right of the plot. The values of the specimens with less quartz, however, are more accumulated in the center of the plot.

Howsoever, the data basis is seen to be insufficient to derive reliable characteristics for the particular variations of the kb-ore for this pairing. It cannot be precluded with an adequate statistical certainty that the found tendencies are only a random arrangement due to the small number measuring points. Hence, a further evaluation for the single varieties of the specimens is therefore refrained.

As explained and in contrast to the first two pairings, the results of Spearman's rank correlation test for the other three pairings indicate strong correlations. These findings are supported by

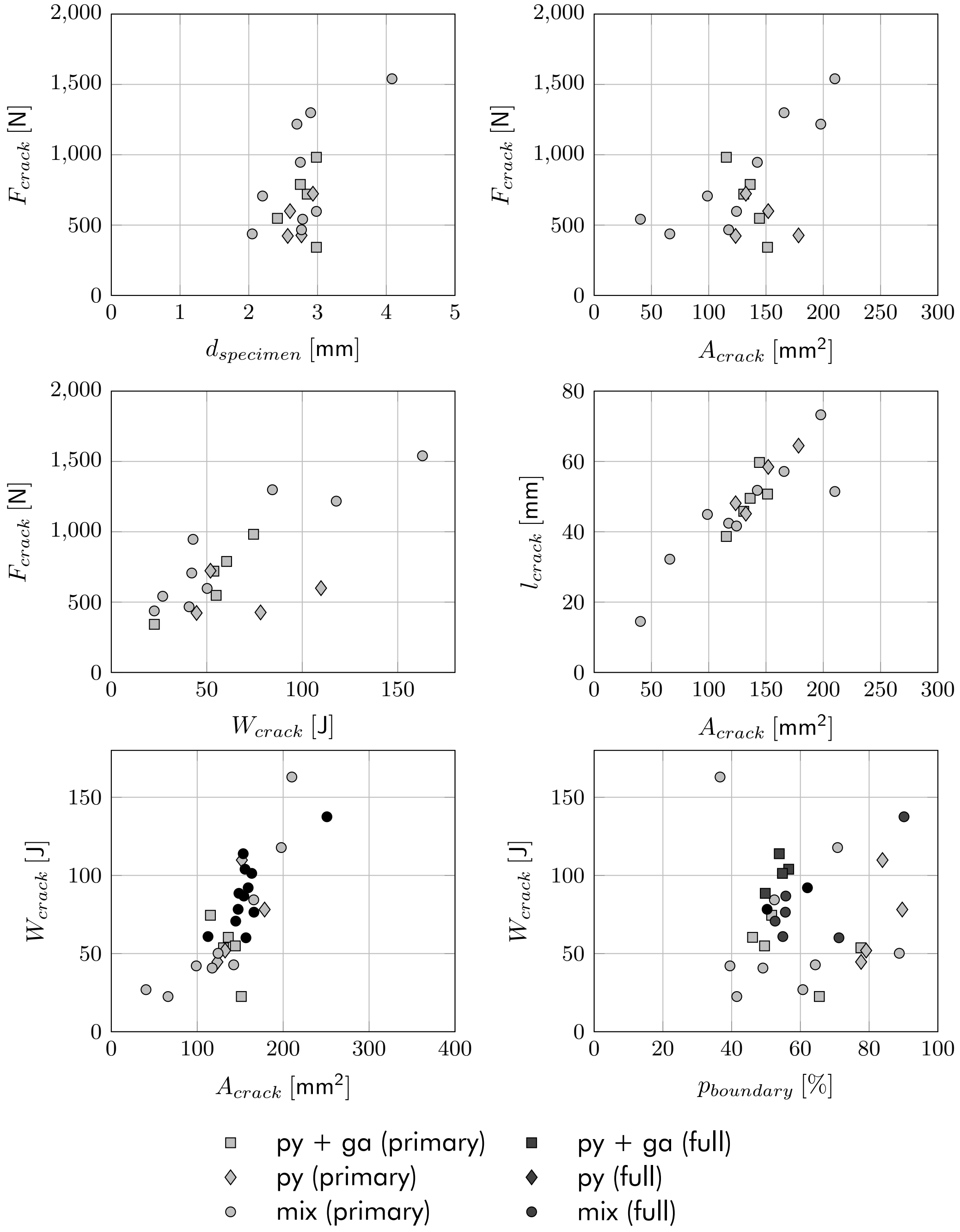

Fig. 4.30: Plots of possible correlations between the measured data

the associated plots as well. Besides the trivial pairing of $l_{crack} \sim A_{crack}$, also the plots of $F_{crack} \sim W_{crack}$ and $W_{crack} \sim A_{crack}$ show significant correlations, if it is not distinguished between the different ore varieties.

Evaluation of the intergranular breakage. However, compared to the results of the basic indenter test, it becomes obvious, that the microstructure of the specimens has a significant influence on the fracture behavior. Although the thickness $d_{specimen}$ of the specimens of the extended indenter test is more uniform, the measured values like fracture force F_{crack} or the fracture work W_{crack} show a higher spread. It seems that the variability and inhomogeneity of the microstructure is a main reason for this effect.

In addition, the plot for the pairing $W_{crack} \sim p_{boundary}$ shows, that there is also no correlation ($p - value = 0.522$, $\rho_{spearman} = -0.009$) ascertainable, as demonstrated for the basic indenter test. However, as explained in the evaluation of the test results of the basic indenter test, the relatively high values of the proportion of the length of grain boundary cracks of the total crack length ($p_{boundary} = 62.5\,\%$) indicate that there is no random breakage, but somehow preferential breakage along the grain boundaries. The thesis of interfacial breakage is therefore supported by the subjective visual evaluation of the crack paths.

For this reason, Figure 4.31 shows exemplarily the magnified image sections of the crack through an ore specimen of the mixed variety (mix). Analogous to the findings for the specimens of the granite, the close-up views show, that significant parts of the crack path are clearly orientated along the grain structure.

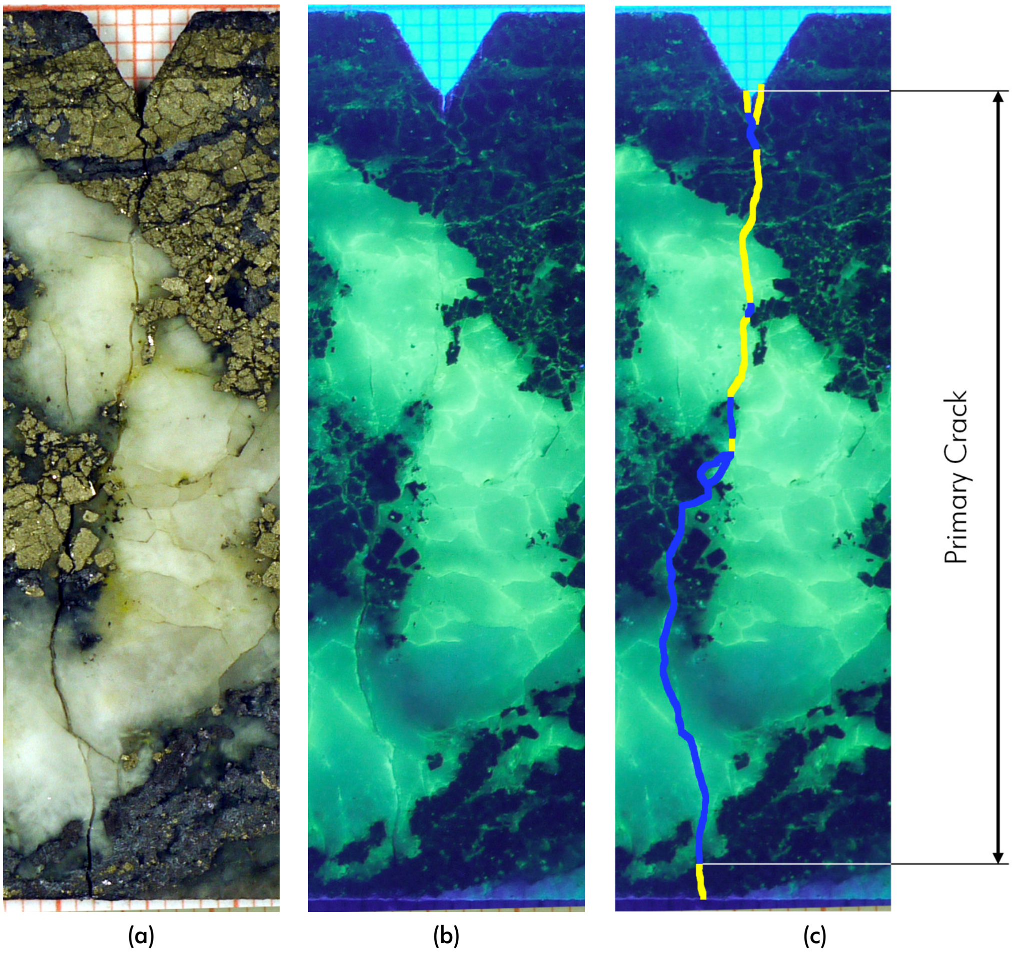

(a) (b) (c)

Fig. 4.31: Exemplary crack path in a kb-ore specimen: (a) Normal lighting; (b) UV-lighting; (c) UV-lighting of the unbroken specimen with highlighted crack path Blue – Fracture along a grain boundary; Yellow – Fracture through a grain

Though, it is not possible to identify boundary types, which are more prone to interfacial breakage with this simple image evaluation method. This, however, does not necessarily mean that all grain boundaries have the same fracture characteristics. It has to be considered, that the used method is not capable to reliably determine all aspects of a mineral microstructure. Based on the photos taken under normal and UV light, it is only possible to estimate whether the crack path and recognizable mineral structures are adjoining each other or not. Hence, for further evaluations more appropriate methods such as polarization microscopy would be necessary.

Nevertheless, considering the focus of these validation experiments, the level of detail of the findings is seen to be sufficient. The extended indenter test and its evaluation are not intended to be an all-encompassing tool for characterizing all fracture characteristics of minerals like interfacial breakage. Instead, it is the aim of this second stage experiment, to allow the synthesis and simulation of a more complex mineral microstructure and use the real experiment as validation reference. Based on the presented results, this goal is seen to be accomplished. Hence, the simulation will be setup and compared with these identified characteristics of the kb-ore. A more detailed analysis might be possible with the help of more elaborative methods, but this is not mandatory for proving the applicability of the synthetic microstructure approach.

4.3.3 Realization and evaluation of the simulated extended indenter test

Similar to the procedure for the first stage experiment, simulating the extended indenter test is done in the YADE simulation environment. Therefore, the kb-ore has to be synthesized. Analogous to the basic indenter test, the realistic synthetic twin is then used to map the microstructure to YADE, where the fracturing of the notched specimens is simulated.

Synthesis the kb-ore from Freiberg

Although the general approach is similar to the procedure for the granite from Meissen, especially the digitalization has to be adapted significantly. This is due to the complex nature of the ore microstructure, which makes the sampling and the sample preparation more difficult. Hence, in order to allow a well-founded evaluation of the synthetic microstructure approach within the scope of the extended indenter setup, the synthesis of the kb-ore from Freiberg is subdivided.

First, it is analyzed how accurate the microstructure of the kb-ore can be synthesized using the synthetic microstructure approach. In the following, the gained information is used to synthesize a microstructure that finally fits to the requirements of the simulation of the extended indenter test in YADE.

Digitalization and analysis of the real microstructure of the kb-ore. As explained in Section 4.3.1, the kb-ore from Freiberg is a relatively inhomogeneous material. For this reason, taking a representative sample for the digitalization is difficult because the maximum possible sample size for the microscopy analysis is too small to representatively contain all varieties of the microstructure. Furthermore, the transmitted light analysis of a thin section only is not sufficient, since the optical characteristics of the ore minerals differ significantly from those of the gangue minerals. Hence, in order to digitize the opaque ore grains, it is therefore necessary to additionally analyze the microstructure by reflected light microscopy. This, however, makes the digitalization process even more laborious.

Due to the limitations presented and in view of the high cost of digitizing such a complex microstructure with two different microscopy techniques, it does not make sense to seek a precise analysis of all microstructure variants. Even if this were achievable with reasonable effort, this would only result in limited added value. The reason for this is that the notched samples for the indenter test are too small to allow representatively mapping of a synthetic microstructure of the kb ore thereon. Hence, every specimen is non-representative per se.

For this reason, it is decided to forgo the representative digitization of all varieties. Instead, a single sample is selected as reference for the digitization, which can be assigned to the group of pyrite-bearing specimen with galena (py + ga). It combines all major minerals and a wide range of grain sizes and is therefore considered an acceptable compromise for the digitizing procedure. Although this implies that the characteristic values of the real sample are not representative for the single tested specimens, it, however, allows to get first of all a detailed overview of the complexity of the microstructure, including all mineral phases.

The resulting final sample section is shown in Figure 4.32. Due to the changed microscopy methods, a resolution of 140 Pixels mm^{-1} is used for the kb-ore. For the digitization, the maps of the microstructure taken under both the reflected light microscope and the transmitted light microscope are used as basis to create the false color map.

As indicated by the legend of Figure 4.32c, the mineral microstructure of this ore sample consists of eight different minerals, which were analyzed with the adapted two-dimensional QMA subsequently. The main results are shown in Table 4.9. Additionally, the roses of intersections and the grain size distributions can be found in Appendix C.2.

It can be seen that the major mineral of the sample is pyrite, which has an areal proportion ϵ_A of approximately 43.19 %. The remaining sample is mainly populated by grains of sphalerite, quartz, carbonate, and mica. As the sample can be classified as belonging to the py + ga

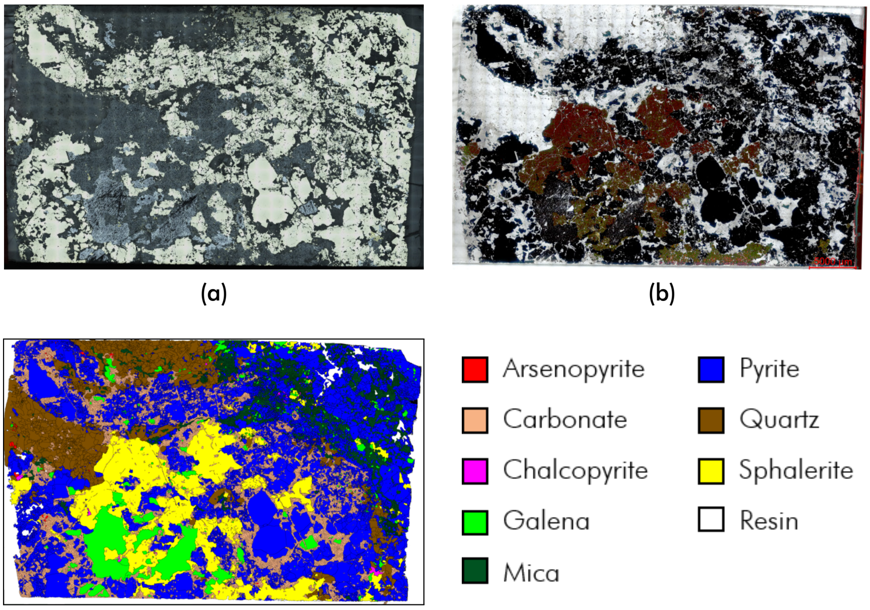
(a)
(b)
(c)

Fig. 4.32: Map of the 35 mm × 21 mm thin section of the kb-ore from Freiberg for the two-dimensional QMA (a) Stitched view under the reflected light microscope with 16-x magnification - contrast and brightness of the colors are post processed for recognizability reasons; (b) Stitched view under the transmitted light microscope with 16-x magnification - contrast and brightness of the colors are post processed for recognizability reasons; (c) Corresponding false color map with legend for the different phases

variety, there is also a significant amount of galena. In contrast, the amounts of chalcopyrite and arsenopyrite are insignificant.

With regard to the grain sizes, it is noted that the majority of the pyrite is finer grained than in the originally tested specimens, which is indicated by its moderate median grain size of 0.55 mm. However, there are at least some bigger pyrite grains in the sample, which results in the relatively high standard deviation σ_{ln} of the grain size of 2.29 mm. This is seen as an effect of the non-representative sampling.

Regardless of this limitation, it is again noted, that the QMA results of phases with low areal portions like arsenopyrite and chalcopyrite may not be overrated. Especially the calculative results of the line analysis like the specific boundary line length C_A or the degree of roughness K_R are prone to bad sampling, which can result in nonsensical characteristic values. This is for example the case for the chalcopyrite, which, according to the QMA results, has a degree of roughness C_α of $-6754.35\,\%$. It is obvious that this value is a computational singularity due to the low phase content since negative roughnesses are not defined.

In contrast, the grain sizes of galena $x_{50,2} = 4.06\,\mathrm{mm}$ and sphalerite $x_{50,2} = 6.82\,\mathrm{mm}$ are matching the expectations of the coarse grained microstructure. It is further noted that quartz, mica, and carbonate are characterized by a relatively high degree of clustering. This can exemplarily be seen Figure 4.32c. The main amount of the quartz grains is aggregated in the two bigger clusters at the top left of the sample. In contrast, the mica and carbonate grains are clustered in smaller clusters, which are more spread.

Generation and analysis of the synthetic microstructure of the kb-ore. According to the proposed procedure, the analysis results are used as input for the synthesis program. The resin found on the original sample is again ignored for the synthesis process. It is assumed that the synthetic rock has no porosity. Due to the size of the grains of the kb-ore a microstructure of 15 000 Pixels × 15 000 Pixels is synthesized. This size is found suitable for creating reproducible synthetic microstructures of the kb-ore with satisfying low coefficients of variation. In combination with the used resolution of 140 Pixels mm^{-1} this equates to a quadratic sample of approximately 107.1 mm edge length.

In Figure 4.33 a detailed section of approximately 10.2 mm × 10.2 mm of the original thin section is shown in comparison with the initially synthesized microstructure. Although the synthetic microstructure has comparable proportions of the different mineral phases and grain sizes, an important limitation of the current synthesis algorithm becomes apparent. As the grain generator is not yet able to explicitly create clusters, there are significant differences between both microstructures. While the quartz, mica and carbonate grains are aggregated in the real microstructure, the same mineral phases are evenly spread through the synthetic section.

This is confirmed by the QMA results listed in Table 4.10 and Appendix C.3. There is a relatively good fit in the major parameters like areal proportion and grain size. However, although the synthesis parameters were optimized, the degrees of clustering of the relevant synthetic phases are significantly lower than those of the real sample.

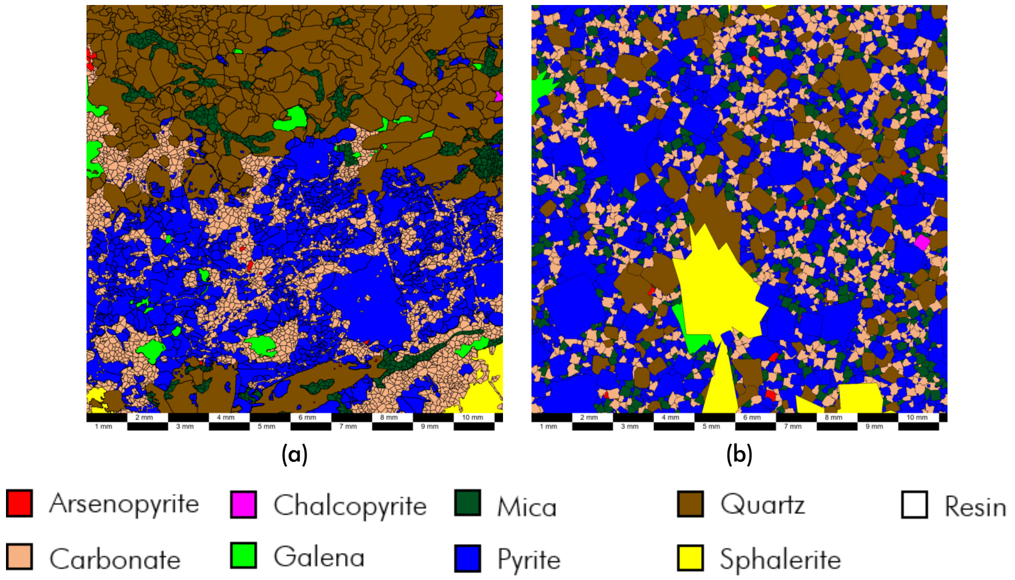
(a) (b)

Fig. 4.33: Detailed false colored sections of the kb-ore from Freiberg: (a) Real thin section with clustered mineral phases; (b) Synthesized equivalent without clusters

Tab. 4.9: Results of the planar QMA for the sample section of the kb-ore from Freiberg

QMA Parameter	Symbol	Unit	Arsenopyrite	Carbonate	Chalcopyrite	Galena	Mica	Pyrite	Quartz	Sphalerite	$\sum$
Areal proportion	ϵ_A	[%]	0.10	13.91	0.16	7.10	6.59	43.19	13.33	15.62	100.00
Median grain size	$x_{50,2}$	[mm]	0.29	0.11	0.56	4.06	0.09	0.55	0.68	6.82	1.71
Standard deviation	σ_{ln}	[mm]	1.15	0.76	1.91	2.22	0.89	2.29	1.43	1.38	1.72
Elongation	El	[-]	1.00	1.13	10.06	1.35	1.36	1.26	1.39	1.42	1.06
Boundary line length	C_A	$[\frac{\text{mm}}{\text{mm}^2}]$	31.17	58.07	44.75	8.26	74.50	19.49	15.35	7.44	25.68
Deg. of roughness	K_R	[%]	29.31	25.19	−6754.35	45.65	28.95	38.95	45.24	76.34	36.79
Deg. of iso. orientation	K_{iso}	[%]	99.99	93.47	0.00	84.16	83.84	87.71	82.74	81.39	96.97
Deg. of lin. orientation	K_{lin}	[%]	0.01	6.53	100.00	15.84	16.16	12.29	17.26	18.61	3.03
Deg. of clustering	C_α	[%]	0.00	67.80	14.55	12.78	74.68	57.51	68.33	19.99	52.38
Deg. of space filling	ϵ_{AF}	[%]	—	—	—	—	—	—	—	—	100.00

Tab. 4.10: Results of the planar QMA for the initially synthesized microstructure

QMA Parameter	Symbol	Unit	Arsenopyrite	Carbonate	Chalcopyrite	Galena	Mica	Pyrite	Quartz	Sphalerite	$\sum$
Areal proportion	ϵ_A	[%]	0.14	14.98	0.23	2.91	7.62	46.54	13.37	14.21	100.00
Median grain size	$x_{50,2}$	[mm]	0.20	0.20	1.41	1.54	0.20	0.56	0.52	6.29	1.32
Standard deviation	σ_{ln}	[mm]	0.64	0.63	1.66	0.98	0.63	2.84	0.95	1.30	1.81
Elongation	El	[-]	1.45	1.05	1.46	1.24	1.04	1.00	1.01	1.13	1.03
Boundary line length	C_A	$[\frac{\text{mm}}{\text{mm}^2}]$	26.30	29.55	6.41	5.39	27.80	16.23	11.02	2.00	16.07
Deg. of roughness	K_R	[%]	8.91	19.98	15.21	41.99	15.93	18.56	17.99	53.27	20.95
Deg. of iso. orientation	K_{iso}	[%]	80.51	97.52	80.09	88.44	97.97	99.84	99.54	93.23	98.26
Deg. of lin. orientation	K_{lin}	[%]	19.49	2.48	19.91	11.56	2.03	0.16	0.46	6.77	1.74
Deg. of clustering	C_α	[%]	5.67	34.40	6.83	10.50	20.30	51.27	17.89	11.89	35.91
Deg. of space filling	ϵ_{AF}	[%]	—	—	—	—	—	—	—	—	100.00

The presented differences of the clustering are a direct result of the shortcomings of the QMA with regard to the characterization of clusters. By now, the degree of clustering C_α is the only parameter of the QMA, which characterizes aggregated grains of the same phase. Unfortunately, this parameter is not sufficient for the synthesis of realistic clusters, as it does not allow any inferences on the cluster sizes.

For example, the degrees of clustering C_α of quartz (67.27 %) and carbonate (68.04 %) in the real sample are nearly equal. Nevertheless, the actual shape and size of the clusters is quite different. As this is not measured by any other QMA parameter, it is by now not possible to create a reliable cluster generator. Hence, there is no explicit clustering implemented in the current version of the synthetic microstructure generator.

Digitalization and analysis of the real microstructure of the kb-ore with clusters. Because of the above mentioned shortcomings, it is decided to adapt the digitizing procedure. In order to allow the synthesis of a kb-ore microstructure with a more realistic dispersion of the mineral phases, especially regarding the clusters, the false color image of the real thin section is adjusted. In detail, the quartz, mica and carbonate clusters, are combined to single grains by eliminating the grain boundaries inside the clusters. By doing so, it is possible to characterize the clusters as contiguous areas with the methods of the QMA.

On this basis, the QMA, which is usually associated with the grain size level, is partly shifted to the level of the clusters. Although this approach compromises the original intention of the QMA, it is seen to be a justifiable restriction. It allows to quantify the clusters without enhancing the QMA or introducing a new approach, as any of the two alternatives would go beyond the scope of this study. It is noted, however, that the results of the QMA of the real thin section with fade-out boundaries inside the clusters are not comparable to any other QMA results, since the determination which boundaries have to be fade-out is not standardized.

The results of this approach can be seen in Figure 4.34a. As explained, in comparison to Figure 4.33a, the boundaries inside the clusters are mostly fade out, while the other properties of the false color image are unchanged. Consequentially, by and large, the corresponding QMA results in Table 4.11 are nearly equal to the results of the original microstructure in Table 4.9. However, due to the missing grain boundaries inside the main clusters, the grain size distribution of quartz, mica and carbonate is increased significantly, while those of the other minerals are identically. This is also comprehensively shown in the plots for the grain size distributions in Appendix C.4.

The differences in the areal proportion ϵ_A of the phases are due to the fade-out process. Because of this, the boundaries inside the clusters, which are originally represented by black pixels, are replaced by pixels in the color of the cluster phase. By doing so, the total amount of boundary pixels in the false color map is reduced while the amount of cluster phase pixels

Tab. 4.11: Results of the planar QMA for the sample section of the kb-ore from Freiberg with fade-out inner cluster boundaries

QMA Parameter	Symbol	Unit	Arsenopyrite	Carbonate	Chalcopyrite	Galena	Mica	Pyrite	Quartz	Sphalerite	$\sum$
Areal proportion	ϵ_A	[%]	0.10	16.48	0.15	6.62	8.30	40.28	13.51	14.57	100.00
Median grain size	$x_{50,2}$	[mm]	0.29	1.48	0.56	4.06	2.83	0.55	12.20	6.82	3.61
Standard deviation	σ_{ln}	[mm]	1.15	2.40	1.91	2.22	2.26	2.29	1.69	1.38	2.09
Elongation	El	[-]	3.58	1.05	10.06	1.34	1.30	1.26	1.45	1.37	1.11
Boundary line length	C_A	$[\frac{mm}{mm^2}]$	32.38	19.33	46.49	8.58	18.71	20.25	5.93	7.73	15.85
Deg. of roughness	K_R	[%]	10.52	68.16	12.10	47.74	72.20	41.24	73.97	77.32	57.68
Deg. of iso. orientation	K_{iso}	[%]	41.80	97.42	16.96	84.66	86.19	87.70	80.46	83.26	94.60
Deg. of lin. orientation	K_{lin}	[%]	58.20	2.58	83.04	15.34	13.81	12.30	19.54	16.74	5.40
Deg. of clustering	C_α	[%]	11.74	18.57	10.39	15.26	20.11	55.98	23.41	17.75	34.06
Deg. of space filling	ϵ_{AF}	[%]	—	—	—	—	—	—	—	—	100.00

Tab. 4.12: Results of the planar QMA for the synthesized microstructure of kb-ore from Freiberg with explicit clusters

QMA Parameter	Symbol	Unit	Arsenopyrite	Carbonate	Chalcopyrite	Galena	Mica	Pyrite	Quartz	Sphalerite	$\sum$
Areal proportion	ϵ_A	[%]	0.11	20.73	0.18	7.29	7.81	43.87	9.78	10.22	100.00
Median grain size	$x_{50,2}$	[mm]	0.15	2.04	1.43	8.04	3.09	0.41	13.56	6.86	3.78
Standard deviation	σ_{ln}	[mm]	0.82	2.75	2.16	2.00	2.58	2.73	1.79	1.87	2.50
Elongation	El	[-]	1.17	1.04	1.14	1.07	1.05	1.02	1.09	1.07	1.02
Boundary line length	C_A	$[\frac{mm}{mm^2}]$	48.04	14.98	20.81	9.18	13.05	31.18	5.50	5.42	19.56
Deg. of roughness	K_R	[%]	25.11	58.69	27.20	72.10	61.84	31.94	73.72	69.24	44.40
Deg. of iso. orientation	K_{iso}	[%]	91.74	98.02	93.26	96.51	97.37	98.97	95.66	96.42	98.86
Deg. of lin. orientation	K_{lin}	[%]	38.27	1.98	6.74	3.49	2.63	1.03	4.34	3.58	1.14
Deg. of clustering	C_α	[%]	14.12	30.22	12.54	21.15	21.80	77.78	22.16	24.76	47.39
Deg. of space filling	ϵ_{AF}	[%]	—	—	—	—	—	—	—	—	100.00

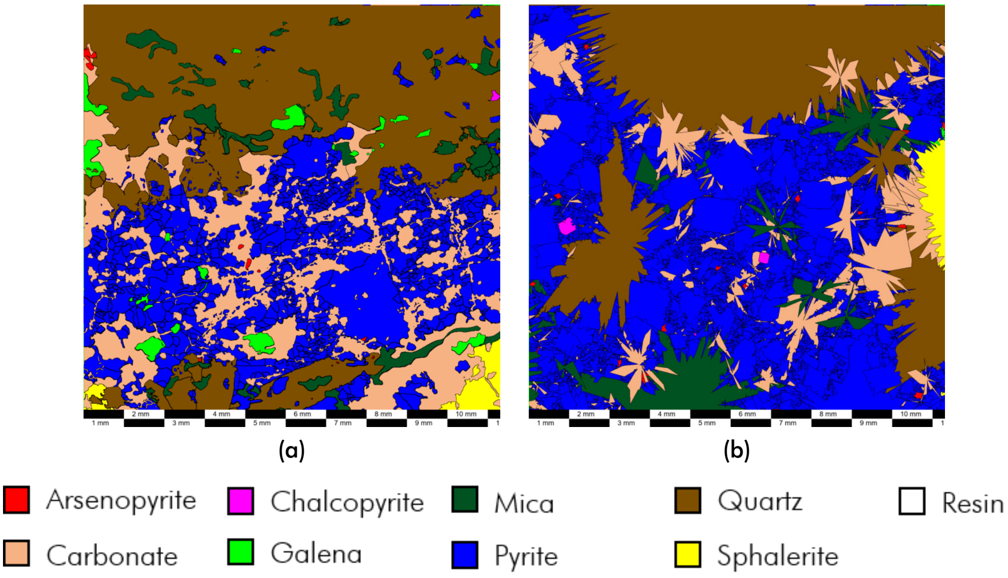

(a) (b)

Fig. 4.34: Adapted detailed false colored sections of the kb-ore from Freiberg: (a) Real thin section with clustered mineral phases; (b) Synthesized equivalent with clusters

is increased. Hence, the areal portion of the cluster phases is slightly increased as well. As a result, although the number of pixels of the other phases is unchanged, their share of the total population decreases, since the proportions of all phases together must always be 100 %.

In addition, the changes in the specific boundary line length of the phases without clusters are also explained by the changes of the areal proportion, since this is an input parameter for the calculation (Equation 3.5) as well. However, as the changes of the areal proportions are relatively small, these affects can be neglected.

Generation and analysis of the synthetic microstructure of the kb-ore with clusters. Based on the digitized map of the thin section with adapted cluster recognition, it is possible to synthesize a microstructure, which includes cluster like grain structures. This is exemplarily shown in Figure 4.34b. While most of the synthesis parameters are kept equal, it is possible to create a synthetic microstructure with an appearance, which is comparable to the real one, by adjusting the grain size parameters of the phases with the main clusters.

Subsequently, in order to ensure a certain confidence level, this microstructure was synthesized 15 times with equal parameters. The chosen size was again 15 000 Pixels × 15 000 Pixels with a resolution of 140 Pixels mm^{-1}. The comparison of the average characteristic values of these synthetic microstructures with clusters in Table 4.12 to the results of the real section synthesized microstructures in Table 4.11 reveals a satisfactorily fit of the data. For comparison, the roses of intersections and grain size distributions of single synthesized microstructure are shown in Appendix C.5.

Hence, the presented synthesis results are seen to be a good proof, that it is possible to synthesize a complex microstructure like the kb-ore from Freiberg with the proposed approach. However, particularly the synthesis of clusters is limited by the applicability of the QMA for this specific task. This circumstance illustrates, that there is still potential for further development.

Adapting the synthesis of the kb-ore to the extended indenter test setup.

The presented final microstructure can technically directly be used for the simulation in YADE. However, in order to allow the comparison with the real extended indenter tests, it is advisable to further adapt the synthesized microstructure to the conditions of the real experiments. As the analyzed section was made of a sample, which belongs the variety of pyrite-bearing specimen with galena (py + ga) it is obvious to choose this variety for the reference simulations.

Adjustments to the synthesis process. Therefore, it is necessary to adjust the synthesis of the proportions of the mineral content to the characteristics of the real py + ga specimens. As explained in the chapter of the specimen characterization in Section 4.3.2, it is not possible to determine the mineral content of the phases of the used real specimens with the accuracy of the QMA, as the classification is based on a visual estimation only. However, due to the well distinguishable appearance of pyrite, it is possible to limit its content in these samples to approximately 70 %, which is a slightly more than in the analyzed thin section. This difference may be due to the explained sampling problem. Nevertheless, this is seen to be a manageable limitation, as there is a smooth transition between the three different varieties anyway.

Furthermore, the grain size distribution of the pyrite has to be adjusted as well. Due to the boundary conditions for the sampling, the analyzed thin section contains a significantly higher content of fine grained pyrite than it is representative for the real pyrite-bearing specimens with galena (py + ga).

Regardless of this, it is advantageous to slightly adjust the grain sizes and the roughness for the synthetic microstructure anyway. Due to the differences in the resolution of the false color maps and the packing of the discrete elements in the DEM environment, especially the details of the filigree structures are prone to get lost during the mapping process. Hence, even though these details can be synthesized with the proposed approach, they do not have an effect on the simulation as they are below the resolution limit of the packing. Because of this, the computational effort for the synthesis of the microstructure can be decreased significantly without affecting the quality of the DEM simulation, by reducing the level of details of the roughness. The same applies for very fine grains, which are below the resolution of the discrete elements. This is especially true for those pyrite grains, which are very fine.

For the above described reasons, the synthesis process is again adjusted in order to guarantee suitable conditions for the comparison between the real and simulated extended indenter test with the kb-ore from Freiberg. Therefore, the following adjustments to the synthesis process are made:

- The pyrite content is increased to approximately 70 %, while the proportions of the other minerals are kept approximately equal among each other.
- The amount of very fine grains of pyrite is decreased.
- The roughness of all phases is reduced.

The final synthesized pyrite-bearing variety with galena for the DEM simulation. Based on these specifications to the synthesis parameters, the final synthetic twin material is generated. In Figure 4.35 a sample section of the final synthetic kb-ore is shown in comparison with the original thin section with the clusters. Based on the evaluation of the QMA results of 15 synthesized samples of 107.1 mm × 107.1 mm, the microstructure can be evaluated. The tabulated average QMA results of Table 4.13 reveal, that the adjustment to the real microstructure was successfully.

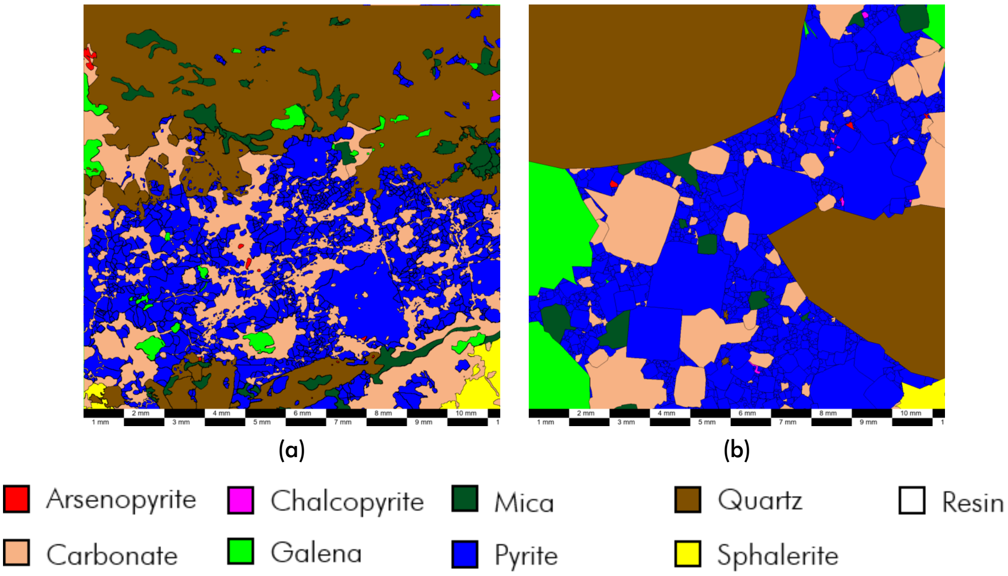
(a)

(b)

Fig. 4.35: Comparison of the adapted real false color map of the kb ore from Freiberg and its final synthetic twin: (a) Real thin section with clustered mineral phases; (b) Final synthetic twin with clusters for the simulation

Thereby, now the pyrite content of the synthetic sample matches the pyrite content of the real pyrite-bearing sample with galena (py + ga). Furthermore, the deviation of the grain sizes of pyrite is decreased as the synthesis of the fine grains is reduced. Consequently, the effect of reduced roughness is reflected by the lower degrees of roughness and specific boundary line lengths. Despite this, the other major parameters of the synthetic twin material still match the real sample section with the clusters in Table 4.11.

The corresponding standard deviations in Table 4.14 confirm, that the synthesis process generates reproducible microstructures with comparable characteristics. Nevertheless, it is noted that the variations increase if a phase is mainly formed by few bigger grains or clusters, like galena or quartz. This, however, is in accordance with the appearance of the real samples of the (py + ga) group.

Further characteristics about the final synthetic twin can be taken from the roses of intersections and distributions of the grain sizes in Appendix C.6. However, as those are the analysis results of a single randomly created synthetic microstructure, small differences to the average QMA results in Table 4.13 are possible.

Setup of the extended indenter test in YADE

Setting up the extended indenter test in YADE is in principle similar to the procedure for the basic indenter test, which is explained in Section 4.2.3. However, due to the adaption of the synthesize process to the characteristics of the clustered phases in the kb-ore, there are a few changes in the parametrization of the DEM model.

Mapping the synthetic microstructure to the simulation environment. The mapping process is comparable to the approach used in the basic indenter test. Therefore, the raw packing is again generated with the GenGeo library with the original specimen contour as outline. Due to the positive experiences with the setup in the basic indenter test, the packing is done with spheres ranging between 0.1 to 0.5 mm as well. Consequentially, the packed spheres are transformed into cylinders, as the extended indenter test is also two-dimensional.

However, as the final real kb-ore specimens are thinner than the used granite specimens of the basic indenter test, the thickness of the simulative specimens of the extended indenter test has to be adjusted. Therefore, the calculative length of the cylinders is set to 2.8 mm, which corresponds to the average thickness of the real kb-ore specimens.

The subsequent mapping procedure is shown in Figure 4.36 exemplarily. Based on the synthetic twin of the kb-ore and the two-dimensional raw packing of discrete elements, the final model of the specimen for the simulation in YADE is created. The individual grains are then represented by compounds of individual elements (cylinders), with diameters in the range of 0.1 to 0.5 mm, but otherwise identical parameters.

Tab. 4.13: Results of the planar QMA for the final synthetic twin of the kb-ore from Freiberg

QMA Parameter	Symbol	Unit	Arsenopyrite	Carbonate	Chalcopyrite	Galena	Mica	Pyrite	Quartz	Sphalerite	$\sum$
Areal portion	ϵ_A	[%]	0.08	6.18	0.07	5.52	1.41	70.95	4.80	11.00	100.00
Median grain size	$x_{50,2}$	[mm]	0.41	1.22	0.80	14.93	1.44	2.91	14.54	9.76	5.31
Standard deviation	σ_{ln}	[mm]	1.46	2.10	1.37	1.34	1.65	2.01	1.07	1.60	1.89
Elongation	El	[-]	1.23	1.04	1.46	1.14	1.08	1.03	1.15	1.09	1.03
Boundary line length	C_A	$[\frac{\text{mm}}{\text{mm}^2}]$	25.13	10.51	17.04	2.50	9.99	6.08	1.97	2.44	5.35
Deg. of roughness	K_R	[%]	38.80	39.76	35.36	48.60	44.19	37.87	42.84	51.13	41.60
Deg. of iso. orientation	K_{iso}	[%]	89.43	97.91	81.96	92.97	95.94	98.37	92.57	95.58	98.21
Deg. of lin. orientation	K_{lin}	[%]	10.57	2.09	18.04	7.03	4.06	1.63	7.43	4.42	1.79
Deg. of clustering	C_α	[%]	8.21	21.70	7.62	9.88	11.76	76.23	9.63	14.27	58.69
Deg. of space filling	ϵ_{AF}	[%]	—	—	—	—	—	—	—	—	100.00

Tab. 4.14: Standard deviations of the planar QMA for the final synthetic twin of the kb-ore from Freiberg

QMA Parameter	Symbol	Unit	Arsenopyrite	Carbonate	Chalcopyrite	Galena	Mica	Pyrite	Quartz	Sphalerite	$\sum$
Areal portion	ϵ_A	[%]	0.02	0.66	0.02	3.15	0.19	3.71	2.67	2.51	0.00
Median grain size	$x_{50,2}$	[mm]	0.17	0.12	0.40	11.64	0.28	0.25	10.74	4.77	1.77
Standard deviation	σ_{ln}	[mm]	0.26	0.42	0.31	0.34	0.32	0.16	0.27	0.39	0.12
Elongation	El	[-]	0.16	0.03	0.37	0.07	0.06	0.01	0.09	0.05	0.02
Boundary line length	C_A	$[\frac{\text{mm}}{\text{mm}^2}]$	3.96	0.45	3.51	0.55	1.02	0.17	0.39	0.28	0.21
Deg. of roughness	K_R	[%]	6.30	2.98	10.97	9.47	3.95	1.93	10.02	3.90	1.88
Deg. of iso. orientation	K_{iso}	[%]	6.65	1.80	12.10	3.37	2.87	0.69	4.28	2.52	0.94
Deg. of lin. orientation	K_{lin}	[%]	6.65	1.80	12.10	3.37	2.87	0.69	4.28	2.52	0.94
Deg. of clustering	C_α	[%]	1.56	0.85	1.99	1.29	0.82	0.54	2.31	2.01	2.69
Deg. of space filling	ϵ_{AF}	[%]	—	—	—	—	—	—	—	—	100.00

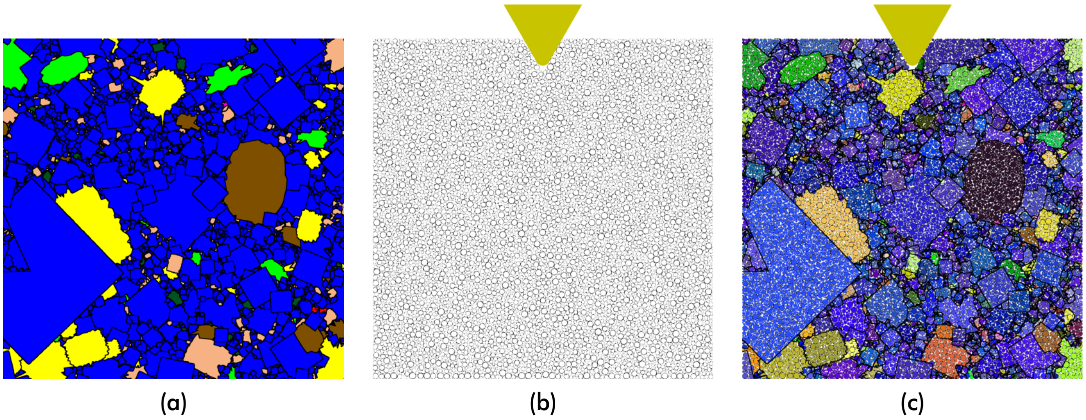

Fig. 4.36: Implementation of the synthetic kb-ore microstructure into the DEM environment: (a) Image of the synthetic kb-ore with the size of the specimen; (b) Raw single-layered dense packing of cylinders with the indenter; (c) Final experimental setup in the DEM environment – For a better demarcation, grains of the same material are painted in variations of the paired base color. Additionally, the grain boundaries are drawn into the picture as well. The ground support is not visible, since it is a plane, which is orthogonal to the view.

Abstract integral parametrization approach for the kb-ore. Due to the similarities, the simulative part of the extended indenter test has to deal with the same problems as already explained for the basic indenter test. Since the micro mechanical properties of the different phases and boundaries are unknown and not reliably measurable, an analytical and realistic parameterization is not possible.

Unfortunately, there is no comparable material from other DEM studies that could serve as a reference. Hence, it is not possible to configure the parametrization based on the results of such equivalent comminution tests and simulations like done in the basic indenter test, where the Lac du Bonnet granite was used. However, as the focus of this study is on the proof of concept of the synthetic microstructure approach, it is not of primary importance to create an absolute realistic mechanical model of the kb-ore inside the DEM environment. Without the possibility to measure the micromechanical properties, this would result in a trial and error based adjustment. The ultimate quality of such an approach depends first and foremost on the diligence and not on the proper understanding of the micromechanics. This, however, is not the purpose of this study and is therefore not followed up.

Hence, it is decided to use an abstract integral parametrization for the simulation of the kb-ore in YADE as well. In order to prove the concept of using realistic microstructures on grain size level in DEM simulations, the influence of the grain boundaries is once again brought into focus. As the actual force-displacement behavior is not predictable anyway, and due to the qualitative similarities in the load behavior of the real specimens, the parametrization of the granite from Meissen is used as a substitute (Figure 4.20). Hence, it is clear, that the resulting load displacement behavior of the simulations will not reproduce the exact forces measured during the real indenter test. However, as discussed earlier, this is not the scope of this study so that the evaluation of the force displacement behavior of the simulated extended fracture test will be neglected like for the basic indenter test.

The enhanced grain boundary factor. Following the basic indenter test, the interfacial breakage is investigated exemplarily. Therefore, the grain boundary factor $z_{boundary}$ is used to strengthen or weaken the bondings between the different grains. Subsequently, it will be analyzed, which grain boundary factor has to be used to get a realistic fracture behavior in the simulation.

However, due to the difficulty with the quartz, carbonate and mica clusters, the grain boundary factor approach has to be enhanced. By now, the clusters are represented by conventional grains in the synthetic twin of the kb-ore. On the level of the false color maps there is now no difference between a pyrite grain and a quartz cluster despite the color. In order to differentiate between both in the final simulation, the grain boundary factor is applied to the intra cluster boundaries as well. This is shown schematically in Figure 4.37.

By doing so, the discrete elements, which form the clusters are treated like single grains. Hence, a fracture through these clusters, is like a pure fracture along grain boundaries. Thus, the clusters are implicitly modeled like a set of single grains in the size range of the resolution of the discrete elements packing. For carbonate and mica this is easily permitted as the median grain sizes $x_{50,2}$ of 0.11 mm and 0.09 mm are significantly below the resolution of the discrete elements. Hence, even if the clusters would have properly by generated as single grains by the synthesis program, the outcome would be equal, as the model quality for these two phases is limited by the resolution of the discrete elements.

The sizes of the original clustered quartz grains ($x_{50,2} = 0.68$ mm), however, are in the size range of the discrete elements. Therefore, it has to be assumed, that the level of abstraction of the enhanced grain boundary approach is slightly too high for the quartz clusters. This is because of some grains, which would have been represented by two or three discrete elements, are not modeled properly due to this abstraction. However, as the proportion of quartz in the final pyrite bearing specimens with galena (py + ga) is relatively low, this is seen to be an acceptable limitation of the model.

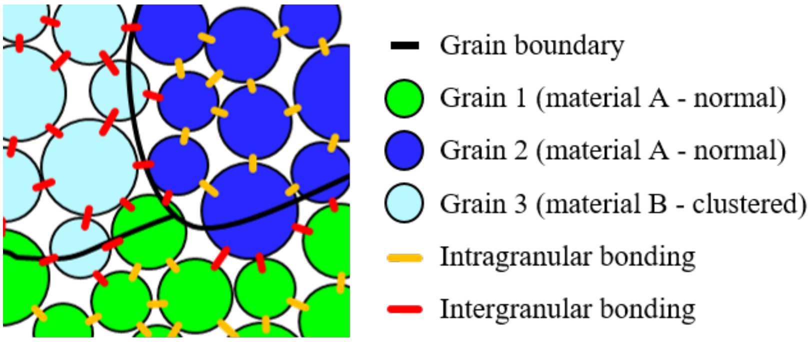

Fig. 4.37: Schematic illustration of the enhanced grain boundary factor approach

Hence, based on this, it is decided to vary the grain boundary strength of the model in order to imitate the real fracture behavior of the kb-ore. Following the basic indenter test, the normal and shear strengths of relevant bondings are multiplied with a grain boundary factor

$z_{boundary}$ in the range of 0.6 to 1.4 in the first step. Subsequently, the grain boundary factor, which results in the best fit of the observed fracture pattern, is used for further simulations to analyze the influence of the microstructure.

The indenter speed. As the boundary conditions for the extended indenter test are the same as for the basic indenter test, weighting up the right load rate in simulation comes to the same result. Hence, the speed of the indenter in the simulation is set to 0.05 m s^{-1}, which is again significantly faster than the speed of the indenter in the real test setup (0.1 mm min^{-1} $\approx$ 0.000 001 7 m s^{-1}), but allows to minimize the computation time by negligible influences on the simulation quality.

Evaluation of the simulated extended indenter test

Similar to the simulations of the granite from Meissen, the simulations of the kb-ore from Freiberg show, that the grain boundary factor $z_{boundary}$ does influence the appearance of the fracture significantly. In order to illustrate this, three example simulations of the same synthetic microstructure but with different grain boundary factors are presented in Figure 4.38.

However, at this point it has to be noted, that the evaluation of the grain boundary breakage has to be slightly enhanced as well. Due to the adaption of the grain boundary factor approach, not only the bondings between the different grains are evaluated as grain boundaries. This has also to be done for the bondings in the quartz, carbonate and mica clusters, as those are affected by the grain boundary factor as well.

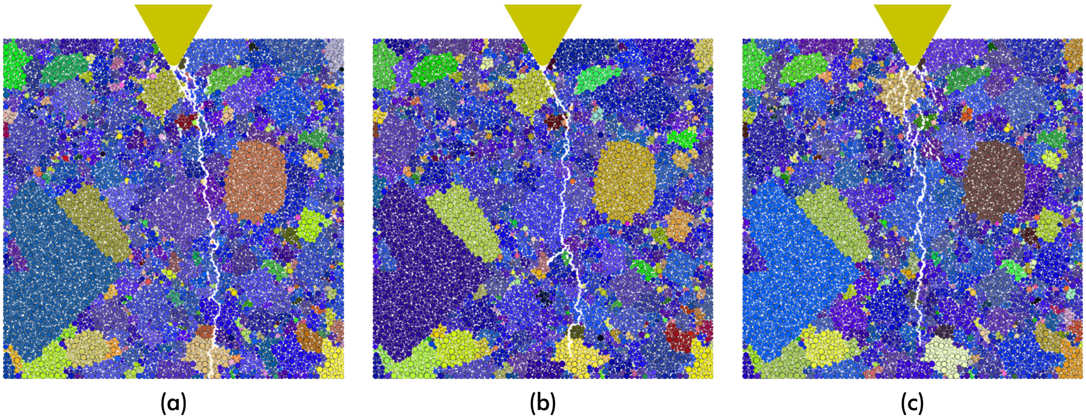
(a) (b) (c)

Fig. 4.38: Broken specimens with different grain boundary factors $z_{boundary}$ and the resulting portion of boundary breakage $p_{boundary}$: (a) $z_{boundary} = 0.6$, $p_{boundary} = 84\,\%$; (b) $z_{boundary} = 1.0$, $p_{boundary} = 50\,\%$; (c) $z_{boundary} = 1.4$, $p_{boundary} = 21\,\%$

Influence of the grain boundary strength. The analysis of the influence of the grain boundary strength on the fracture behavior confirms the findings of the simulations of the basic indenter tests. If the grain and intra cluster boundaries are weakened ($z_{boundary} = 0.6$), the cracks propagate preferentially along the such regions. In the above presented example 84 % of grain boundary breakage is measured. For this value the broken intra cluster boundaries are already considered.

If the grain boundaries have the same strength like the intragranular bondings ($z_{boundary} = 1.0$), a random fracture is observed. As, in this case, the specimen is a physically homogeneous body, the amount of grain boundary breakage drops to 50 % for the shown example. This result might be astonishing in the first instance, as only 29.17 % of the overall bondings are between different grains. However, as explained, also the broken cluster bondings are counted due to the enhanced grain boundary factor approach. If those were ignored, the value of grain boundary breakage drops to 35 %, which is in the range of dispersion for the random breakage of a specimen with approximately 30 % grain boundary bondings.

If the boundaries and the intra cluster bondings are further strengthened, it seems that the cracks are diverted from these regions. Similar to the findings of the basic indenter simulations, the proportion of grain boundary breakage drops further to 22 % for a grain boundary factor of 1.4 in the shown example.

Concluding this, the results confirm, that the grain boundary factor approach is a suitable method to influence the fracture behavior significantly. By altering this single parameter, the fracture can be caused to prefer grain boundaries, to be absolutely random, or to avoid regions with a high amount of boundaries.

Influence of the microstructure. As for the basic indenter test, the above discussed influence of the grain boundary factor can also be interpreted as direct influence of the microstructure on the fracture behavior. It is immanent to the grain boundary factor approach, that changing the characteristics of the discrete elements packing from representing a homogeneous material to a structured arrangement of different grains has a direct influence on the breakage behavior.

In order to prove that it is possible to imitate the breakage behavior of the kb-ore with the synthetic microstructure approach, the grain boundary factor is further adjusted. Therefore, the amount of grain boundary breakage of the real indenter experiments with the kb-ore is used as reference. For all 18 successfully tested specimens, an arithmetic mean AM of 62.5 % ± 17.5 % can be determined. If the focus is set on the five pyrite bearing specimens with galena (py + ga), which are used as reference for the simulation, this characteristic value is about 58.1 % ± 13.1 %.

Based on the evaluation of the preliminary simulations, it is supposed that the grain boundary factor for the simulation of the py + ga specimens of the kb-ore should also range between

0.80 to 0.90, like for the granite from Meissen. Therefore, a test series with simulations using a finer graded $z_{boundary}$ of 0.825, 0.850, and 0.875 is conducted. The results for the proportion of boundary breakage $p_{boundary}$, which belong to these simulations, are listed in Table 4.6.

Tab. 4.15: Proportion of the length of grain boundary cracks of the total crack length $p_{boundary}$ of the three test series with the finer grained factor for adjusting the grain boundary strength $z_{boundary}$

No.	$p_{boundary}$ [%] $z_{boundary} = 0.825\,\%$	 $z_{boundary} = 0.850\,\%$	 $z_{boundary} = 0.875\,\%$
1	59.39	55.38	53.13
2	64.37	54.72	59.24
3	59.83	57.28	53.15
4	69.34	62.50	67.11
5	59.41	55.84	52.31
6	41.08	43.88	40.88
7	70.64	69.23	64.88
8	59.82	53.11	45.15
9	50.25	55.70	58.06
10	76.13	71.84	72.31
11	65.50	67.00	60.82
12	52.76	55.04	50.00
13	65.14	65.29	75.41
14	44.83	47.69	45.02
15	40.11	43.81	37.78
AM	58.57	57.22	55.68
SD	10.82	8.58	11.17
CV	18.47	15.00	20.06

Additionally, Figure 4.39 shows a single kb-ore specimen after simulating the indenter test with the three different grain boundary factors exemplarily. In summary, it is found, that the used parameter set is clearly in the range, where the breakage behavior of the py + ga specimens can successfully be simulated with the chosen approach. For the 15 simulations with $z_{boundary} = 0.825$, an arithmetic mean AM of 58.57 % and a standard deviation of 10.82 % are measured for the proportion of the grain boundary breakage $p_{boundary}$. This is comparable to the results of the real indenter tests of the py + ga specimens (58.1 % $\pm$ 13.1 %), which is seen as proof for the chosen approaches.

Influence of the discrete elements packing Additionally, the influence of the packings of the discrete elements on the simulation is analyzed for the extended indenter tests. Although for the previous test series always the same packing was used, this might be interesting for further analyzes. For this the equal microstructure was mapped to 15 different packings, which were generated with equal packing parameters. For the grain boundary factor a value of 0.825 % was used.

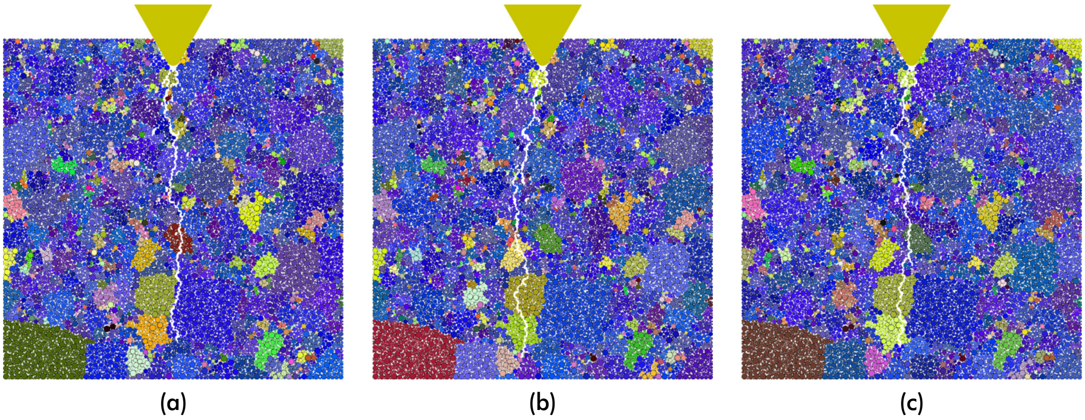

Fig. 4.39: Broken kb-ore specimen with different grain boundary factors $z_{boundary}$ and the resulting portion of boundary breakage $p_{boundary}$: (a) $z_{boundary} = 0.825$, $p_{boundary} = 58.57\,\% \pm 10.82\,\%$; (b) $z_{boundary} = 0.85$, $p_{boundary} = 57.21\,\% \pm 8.58\,\%$; (c) $z_{boundary} = 0.875$, $p_{boundary} = 55.68\,\% \pm 11.17\,\%$

This results in a slightly higher deviation of the boundary breakage than in the corresponding test series of the basic indenter test (Section 4.2.3). With the synthesized kb-ore a standard deviation SD of 7.64 % was measured while the arithmetic average AM of the boundary breakage $p_{boundary}$ was 56.62 %. Nevertheless, this is still seen to be small enough so that the assessments of the applicability of the synthetic microstructure approach should not be compromised even if the packings would be variated.

4.3.4 Conclusions on the extended indenter test

First of all, the comparison of the real and simulated extended indenter tests confirms the findings of the basic indenter tests, that the concept for the synthetic microstructure approach is applicable for fracture simulations at grain size level. It is shown, that it is possible to analyze a complex microstructure like the kb-ore with the adapted QMA and use random synthetic twins of this microstructure for simulative purposes. Based on this, it is confirmed that the indenter test setup can successfully be used to evaluate and validate the fracture behavior of minerals at grain size level.

However, for this, certain limitations have to be considered. Besides the known restriction to two-dimensional problems and middle- to coarse grained microstructures, it becomes problematic, if the microstructures are so inhomogeneous, that the specimen size of 50 mm × 50 mm becomes insufficient small for proper sampling. Furthermore, microstructures with clusters pose a significant limitation of the current approach. Although the methods of the QMA characterize clusters, they are insufficient for further microstructure synthesis approaches as the size and shape of the clusters are not evaluated at the moment.

Nonetheless, this limitation can be bypassed by adapting the QMA, so that it recognizes the whole clusters instead of the single grains inside the clusters. Although this was only intended to be a kludge, in order to allow to proceed with the proof of concept study, it might be an interesting approach to subdivide the general QMA into a grain specific QMA and a QMA, which explicitly analyzes all areas where grains of the same phase form contiguous areas like clusters. Based on this, it would be possible to derive all the typical information, which are used to describe the microstructure on the grain level also on the cluster level. Hence, besides the cluster sizes, the more sophisticated parameters like the cluster orientation or cluster shape could be evaluated as well without spending too much effort on developing a totally new approach. This, however, is seen to be a challenge for further research, since the comprehensively further development and assessment of this method would clearly be outside the scope of the presented study.

Howsoever, based on this interim solution, it is shown, that the more complex synthetic microstructure, including the clusters, can be mapped to a given DEM environment, such as YADE. Subsequently, it is also possible to simulate the fracture behavior of these specimen with special consideration of the influence of the grain boundaries. For this, the boundary factor approach is used again. This, however, has to be enhanced, so that the areas, which represent clusters are interpreted as a set of individual grains. Subsequently, the factor is applied to these intra cluster bondings as well.

It is found that this approach is acceptable as long as the size of the grains that form the clusters originally is lower or equal than the resolution of the discrete elements packing. In this case any geometric details of the single grains are lost anyway during the mapping process to the "coarse" packing, so that the modeling error is kept within a limit.

In conclusion, the presented results of the extended indenter tests are seen to be a confirmation for the synthetic microstructure approach with a more complex microstructure. Therefore, it is decided to continue with the next experiment of the second stage of this study, which transfers the approach to a more realistic comminution task.

4.4 Particle bed test

In contrast to the two indenter tests, the last test transfers the synthetic microstructure approach to an experimental setup, which is closer to real-world comminution applications. Therefore, it is intended to evaluate the benefits and applicability of this approach exemplarily within the scope of a particle bed comminution in a piston die press.

4.4.1 Basic considerations for the particle bed test

The principle for this test is shown in Figure 4.40. Analogously to both indenter tests, this particle bed test is designed as comparative study.

The first part is the real particle bed comminution test, which consists of the preparation of the particles, setting up the particle bed inside the piston die press, and finally the particle bed comminution.

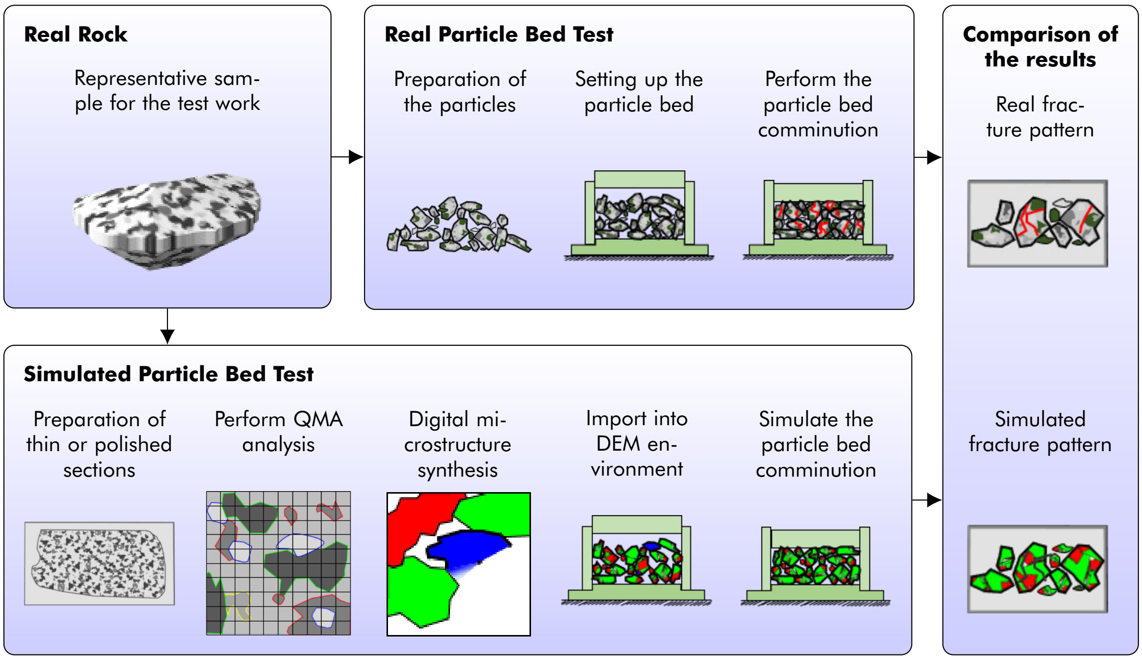

Fig. 4.40: Schema for the particle bed test

The second part is the simulative test. For this, the first steps are similar to those of the simulations of the indenter experiments. To make the simulation of particle bed comminution with realistic synthetic mineral microstructure possible, the test material has to be evaluated previously. The thin section, which is required for this, is made of a representative rock sample. Following, the microstructure is analyzed with the help of the adapted QMA. The results are then used as reference for synthesizing a two-dimensional, realistic digital twin, which is mapped to single particles inside the DEM environment. Based on this, the piston die press setup is adopted into the DEM environment and the particle bed comminution is simulated.

However, due to the modalities of particle bed comminution, it is not possible to carry out the real comminution test two-dimensionally. Hence, the evaluation capabilities of this experiment are more restricted than those of the two indenter experiments, as the influence of the differences in the dimensionality are hard to quantify.

Nevertheless, the basis for this final step is the comparison of the fracture behaviors. For this purpose, the comminuted particle bed is embedded in resin after the test. The so fixed particle bed structure is used to evaluate the fracture pattern of the real particles, which is compared with the directly accessible fracture pattern of the simulated particle bed. Due to the mentioned differences in the dimensionality of both tests, it will be difficult to do the comparison on a quantitative basis, so that the conclusions are forced to be of a more qualitative nature.

Selection of the test material

According to the specifications of Section 4.1.2, this second stage experiment shall be done with a relatively simple mineral microstructure. By doing so, it is possible to keep the link to the results and conclusions of the basic indenter test. This allows to comparatively evaluate the influence of the more complex test setup.

Because of the practical advantages and the positive experiences, which were made with the granite from Meissen in the basic indenter test, it is decided to use this material for this second stage validation test as well. The homogeneity and isotropy of the fabric of this material prevents any influences of the characteristics of mineral microstructure on spatial properties of the particle bed.

That is in so far important, as the formation of the particle bed filling is characterized by random processes. Therefore, it is important to avoid any kind of segregation of particles with somehow different characteristics and ensure a certain level of homogeneity. Otherwise, it would be impossible to use this test setup as validation experiment in this early stage, since such possible segregation effects could overlay the effects of the mineral microstructure of the single particles on the fracture pattern.

Hence, as it is the same material like in the basic indenter test, the material characteristics are not repeated at this point. These can directly be taken from the corresponding paragraphs in Section 4.2.1.

Setup of the particle bed test

The setup for the particle bed test is shown in Figure 4.41 in principle. For this purpose, a piston die press of the type KV.135.02, manufactured by the RUCKS Maschinenbau GmbH, is available. This press has a capacity of approximately 4000 kN and can be used with different tool configurations, which are suitable for particle bed experiments. The actually used diameter of the piston is 160 mm. The inner diameter of the pot, where the particles are filled in, is slightly oversized so that the piston can be moved without jamming. All parts of the press, which are in contact with the material are made of steel. For measuring purposes, the piston die press is equipped with force and displacement sensors, which allow to monitor the force-displacement behavior of the particle bed during the test. In contrast to the both indenter tests, it is not possible to capture the fracturing of the particles with a high-speed camera, as the process chamber if fully enclosed by the cylindrical pot.

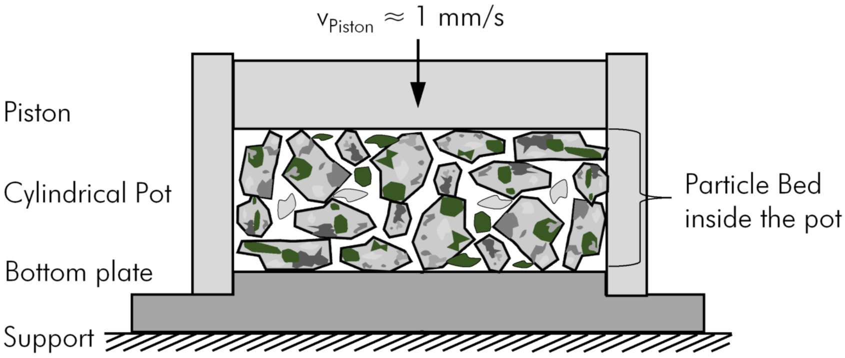

Fig. 4.41: Experimental setup of the particle bed test in a schematic sectional view. The particles are placed inside a cylindrical pot, which in turn is situated on a bottom plate. The round piston stresses the particles with approximately 1 mm s^{-1}.

The test procedure

Since the particle bed tests are done in the scope of the validation process for proving the applicability of synthetic mineral microstructures for comminution simulations, the actual procedure and evaluation is quite different from typical piston die comminution experiments. The focus is set less on the measurement of quantitative experimental parameters, such as the specific comminution work or the product particle size distribution in dependence of different side conditions. It is rather important to assess the comminution product in such a manner, that a comparison with a two-dimensional simulation is possible.

In order to allow such a comparison, a special procedure for fixing the comminution product after the crushing is used [95]. As explained in Figure 4.42, the compacted crushing product is carefully encased with a cylinder with an inner diameter of 120 mm and grouted with resin. The resin specimen produced in this way, contains the fixed particle bed in the structure it had just after it was crushed. In this fixed condition, the particle bed can be handled and further processed without changing the original arrangement of the comminution product. For the comparison with a simulation, it is therefore cut into slices so that the actual arrangement inside the particle bed can be accessed.

However, in contrast to the indenter tests, it is hardly possible to evaluate the results based on simple photographs of the slices. Due to the complex structure and irregular shape of the particles, this requires a more sophisticated analysis, than it is used for the indenter tests. For

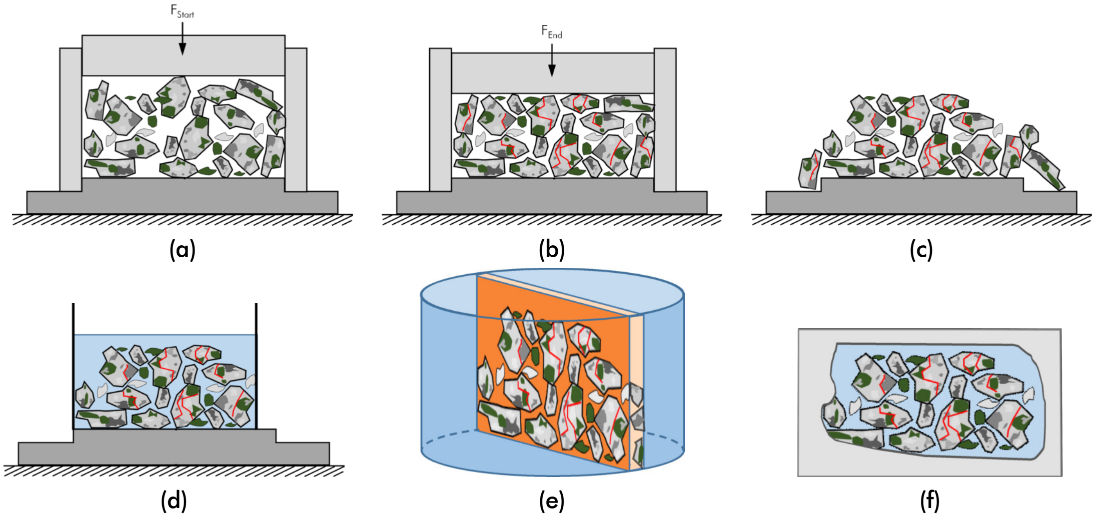

Fig. 4.42: Schema of the experimental procedure and subsequent specimen preparation of the real particle bed test: (a) Particle bed comminution is just started. The piston starts to compress the particles; (b) Particle bed comminution is stopped at the final load F_{end}. Fractured particles are indicated by their red crack paths; (c) After releasing the load, the pot is lifted and removed, so that the particle bed can freely be reached for further handling. Due to the compaction, the particle bed stays largely intact, although it is no more supported by the pot wall; (d) The loose particles at the outer side of the briquette like press product are cautiously removed and the inner part is encased with a cylinder. The cylinder is positioned so that as much of the intact center of the press product as possible is enclosed. This, however, can also be a bit eccentric, depending on the condition of the briquette. Following, the gap between the cylinder edge and the bottom plate is sealed and the inner part of the particle bed is carefully grouted with resin; (e) After the curing of the resin, the so fixed specimen with the inner part of the particle bed is removed and cut into slices. The slice of the center, which is marked orange, is used to prepare a thin section; (f) The thin section of the center is used to analyze the fracture pattern

this reason, it is decided to use polarization microscopy, as it is possible to reliably distinguish particles, grains, and cracks with this method. Therefore, thin sections from the center slices of the fixed specimens are prepared.

4.4.2 Realization and evaluation of the real particle bed test

The realization and evaluation of the particle bed test is significantly different from the procedures for both indenter tests. Hence, besides the preparation of the particles and the actual comminution test, the evaluation procedure is emphasized in the following, as it requires an adapted approach.

Preparation of the particles

For the particles, which were used for this test, a suitable particle size range has to be chosen. Therefore, specific side conditions in relation with the microstructure of the granite from Meissen have to be considered.

Side conditions for the particle fraction. On the one side, the particles have to be sufficiently small, so that the wall effects of single particles are negligible. On the other side, they have to be coarse enough, so that even the smaller particles consist of a sufficient amount of individual grains. If too small particles are used, one has to keep in mind, that the influence of the mineral microstructure on the fracture behavior will be reduced at a certain point, as the diversity of grains inside the particles decreases.

Hence, based on these considerations and the results of preliminary tests, the particle size range of 8 to 12.5 mm is chosen for the tests. Assuming an average minimal particle size of approximately 8 mm this should guarantee, that even the smallest granite particles consist of at least ten different grains, if the median grain size of 1.97 mm of the granite is considered (Table 4.1). The final fraction, which is shown in Figure 4.43, is then prepared by screening of material ranging in size from 8 to 16 mm, which was directly obtained from the quarry.

Fig. 4.43: Raw particles of the granite from Meissen in the size fraction 8 to 12.5 mm

Evaluation of the wall effects. Based on the maximum particle size of the chosen fraction, the amount of material, and the dimensions of the pot, it is subsequently possible to evaluate the wall effects. It is therefore assumed, that approximately 1500 g shall be used for the later particle bed comminution tests. If this material is evenly distributed in the pot, this results in an initial particle bed height of 50 to 55 mm, depending on the actual orientation of the top layer of the particles and the chosen reference point of measurement.

To assess whether the wall effects of such a filling are sufficiently small compared to all other effects, the approach of SCHWECHTEN [181] is used. In detail the maximum particle size of the particle filling $d_{p,max}$, the height of the particle filling h_0 and the diameter of the pot d_{pot} are therefore considered with the following conditions:

$$\frac{h_0}{d_{p,max}} > 4 \tag{4.6}$$

$$\frac{d_{pot}}{d_{p,max}} > 10 \tag{4.7}$$

$$\frac{d_{pot}}{h_0} > 3 \tag{4.8}$$

Inserting the parameters of the particle bed and the pot results in:

$$\frac{h_0}{d_{p,max}} = \frac{50\,\text{mm}, ..., 55\,\text{mm}}{12.5\,\text{mm}} = 4, ..., 4.4 \tag{4.9}$$

$$\frac{d_{pot}}{d_{p,max}} = \frac{160\,\text{mm}}{12.5\,\text{mm}} = 12.8 \tag{4.10}$$

$$\frac{d_{p,max}}{h_0} = \frac{12.5\,\text{mm}}{50\,\text{mm}, ..., 55\,\text{mm}} = 3.2, ..., 2.9 \tag{4.11}$$

The results show, that the used setup can be classified as only just an ideal particle bed with negligible wall friction effects. However, as those definitions are based on assessments of comparative studies, which are not analytically justifiable, the results should not be seen as exact limit values. Applying the proposed conditions of other authors like AZIZ and SCHÖNERT [6] may result in other, slightly differing limits. In addition, one has to keep in mind that the focus is on the evaluation of the fracture pattern of the center of the particle bed filling, where the wall effects play only a minor role anyway. For this reason, the quality of the proposed particle filling is considered to be sufficient for this task.

Realization of the real particle bed test

For the understanding of the procedure of the particle test, it is important to understand, that it is not necessary to do multiple retries with identical parameters, as it is normally done. The reason therefore is, that the intended particle bed tests do not result in single, measurable values, like the maximum load or the energy absorption, as it is otherwise common practice. In such cases, it is mandatory to do multiple tests in order to evaluate the variance between such single integral measurements.

In contrast, the focus of this study is set on the evaluation of the fracture pattern, which can be seen as result of individually measurable cracks. Fortunately, these are accessible by analyzing the prepared sections. Furthermore, and in contrast to the fractured, notched specimens of the preceding stage tests, a fixed specimen of the particle bed test contains already numerous cracks and fissures. Hence, the statistical reproducibility for the fracture pattern is already achieved through analyzing a sufficient large part of a single fixed particle bed.

Furthermore, as already being stated, there is no parameter field, which has to be analyzed like in a typical mineral processing study of a comminution process. The only side condition is, that the tests must allow the comparison to the simulation, in order to validate its outcome. Against this background and considering the work expense for the product preparation and microstructural analysis with polarized microscopy, it is decided to do three tests with different settings.

The test parameters. The first test is actually only an imaginary comminution test, as it is done without any load. In order to generate a reliable reference point for the comparison of the three-dimensional real test and its two-dimensional counterpart, it is decided to fix the particle bed, before it is stressed. Based on this sample, it is later possible to compare the initial state of the real particle bed with the initial state of the simulated particle bed.

For the second test, it is decided to max out the capability of the piston die press, in order to achieve a comminution product with the maximum possible amount of fracture. This means, that the particle bed is loaded with approximately 150 MPa. Contrary, the remaining test is done with a significant lower load of approximately 20 MPa. The reason for this approach is, that it is intended to achieve a comminution product, which is already fractured but has still a significant amount of bigger particles. These in turn, are probably easier to analyze.

According to these specifications, two particle bed tests with actual comminution are done with the presented setup. The comminution product of both tests is shown in Figure 4.44. It can be seen that the states of the particle beds are quite different. The briquette of the test with the lower load contains significantly coarser fragments. Although the particle bed in the peripheral zone has partly collapsed without the support of the pot wall, the area at the center is relatively stable. In comparison, the stability of the particle bed, which was stressed with the maximum load, is much higher, so that even the zone at the edge stays intact without any external support. However, the high amount of very small debris at the bottom of the edge indicates, that the degree of comminution is significantly higher.

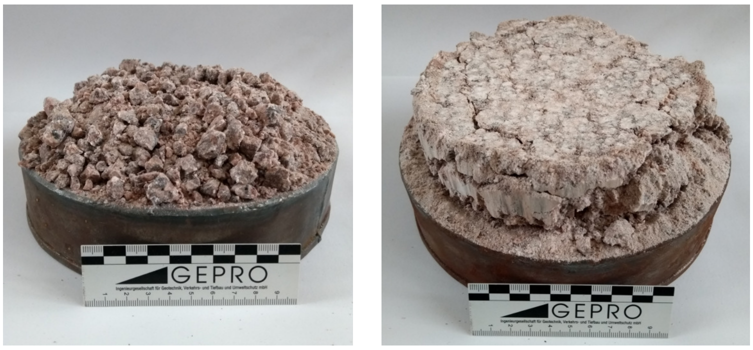

(a) (b)

Fig. 4.44: Granite particles after their comminution in the piston die press. The particles are already extracted from the pot and are ready for the preparation with the resin: (a) Particle bed after stressing with approximately 20 MPa; (b) Particle bed after stressing with approximately 150 MPa

The specimen preparation. Subsequently, according to the procedure in Figure 4.42, the shown briquettes were fixed with resin. The same was done as well with the particle bed of the imaginary test without load. However, as there no real comminution happened also no real briquette was formed, which could be shown here. Instead, the initial particle bed was directly grouted with the resin.

Figure 4.45 shows the resulting fixed specimens after cutting them into plates. The section of the initial particle bed suggests, that the particles are floating in the resin as they do not touch each other. Indeed, this is only an illusion. The particles are arranged in a way, where each particle is in contact with the other surrounding particles. However, as this is a spatial arrangement, these, in their number limited contact points, are spatially distributed as well. The probability that a random cut through such a particle bed, as shown in Figure 4.45a, intersects such a coordination point is limited. Hence, it seems that the particles are not in contact because their coordination points are in different spatial depths then that of the actual slice.

This is different in the cuts through the comminuted particle beds. It can be seen, that the particles are touching each other in these two sections. The reason for this is, that both sections are filled with uncountable more, smaller particles. Those, in turn, are supporting each other with a significant larger amount of coordination points as well. As this happens in an even smaller volume, the probability of cutting through such contact points is much higher.

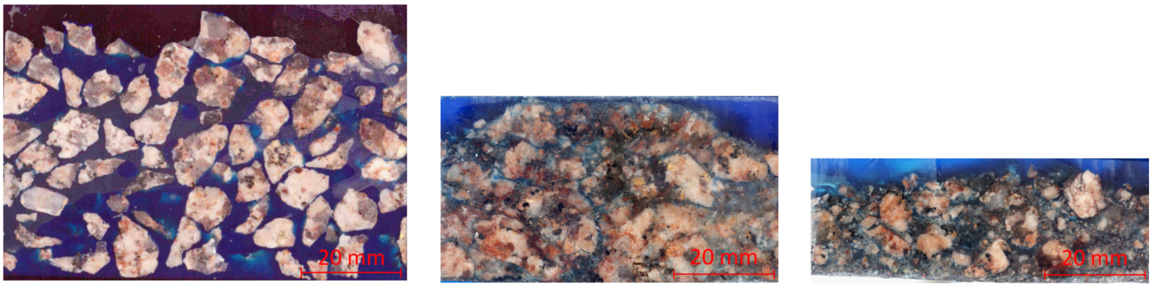

(a) (b) (c)

Fig. 4.45: Specimens with embedded particle beds: (a) Raw packing; (b) Particle bed after stressing with approximately 20 MPa; (c) Particle bed after stressing with approximately 150 MPa

Evaluation of the real particle bed test

The evaluation of the fracture pattern is mainly based on the analysis of the thin sections of the three specimens with the different fixed particle beds. The limiting parameter is the difference in the dimensionality between the real and the simulative particle bed test. Hence, further-reaching evaluations of force-displacement data or absorbed energy cannot be used for the validation, as they directly depend on the dimensionality.

Hence, the focus is entirely set on the fracture pattern and it is decided to forgo a detailed analysis of the typical parameters like the specific comminution work. However, for the interested reader, it is referred to the study of SCHÖNFELD [174], which was done in parallel. Its focus is set on the analysis of the fracture work for particle bed comminution and the resulting product particle size distribution. Conveniently, the same material and same piston die press was used with similar settings in the mentioned study for one of the test series.

General evaluation of the thin sections. In order to be able to assess the fracture pattern, the thin sections have to be digitalized firstly. Unfortunately, the thin sections of the particle bed tests are significantly bigger than normal thin sections. Hence, it is not practicable to create digital maps, of the whole sections. The main reason for this limitation can be seen in the missing automation of the available polarization microscope. Due to this, the sections have to be photographed and stitched manually. Furthermore, the length and width of the thin sections are too big for the adjusting device of the microscope slide. Hence, the specimens have to be adjusted by hand as well.

For this reasons, the general evaluation of the results is done directly at the microscope and cannot be shown here because of the presented limitations. Based on this, it is decided to digitize only parts of the thin section, which seem to show a representative section and contain multiple grains. The results of this process, which are the basis for the detailed analysis, are shown in Figure 4.46.

The digitized map of the initial packing (Figure 4.46a) covers multiple intact grains of different sizes. As already explained, it can be seen, that the grains do not touch each other, as the contact points are in other spatial depths. Despite this, the detailed analysis of the single grains shows, that the mineral microstructure of the grains is free of cracks and fissures, as it is expected from the fresh particles. These findings confirm to the overall characteristics of the thin section, which were evaluated at the microscope directly.

The corresponding maps of the particle beds after being comminuted with approximately 20 MPa and 150 MPa are different. In both, many fragments from the crushing process are visible. Thereby, larger particles, which can even belong to the size range of the feed particles, are surrounded by numerous smaller fragments. This result is conforming to the typical character of the product particle size distributions of particle bed tests. Due to the typical stressing behavior inside particle bed, the size distribution of product particles tends to have a relatively high spread. The reason for this result can be found in the intrinsic characteristics of particle bed comminution, which explained in short as follows.

Interpretation of the general fracture pattern. Starting from a somehow coarse feed particle filling, the particle bed is stressed by an external tool like the piston. The majority of the particles, however, is only in contact with surrounding particles, which transfer the load from the piston through other particles to the support. In this setup, all particles are exposed to different loads, depending on their positions, orientations and arrangements of their contact points. If all other major processes of particle bed comminution, like deaeration, elastic and plastic deformation, friction effects, attrition on particle surfaces, and compaction are ignored for a moment, it is possible to concentrate on the fracture and rearrangement processes. These two are most relevant for those broad distributions.

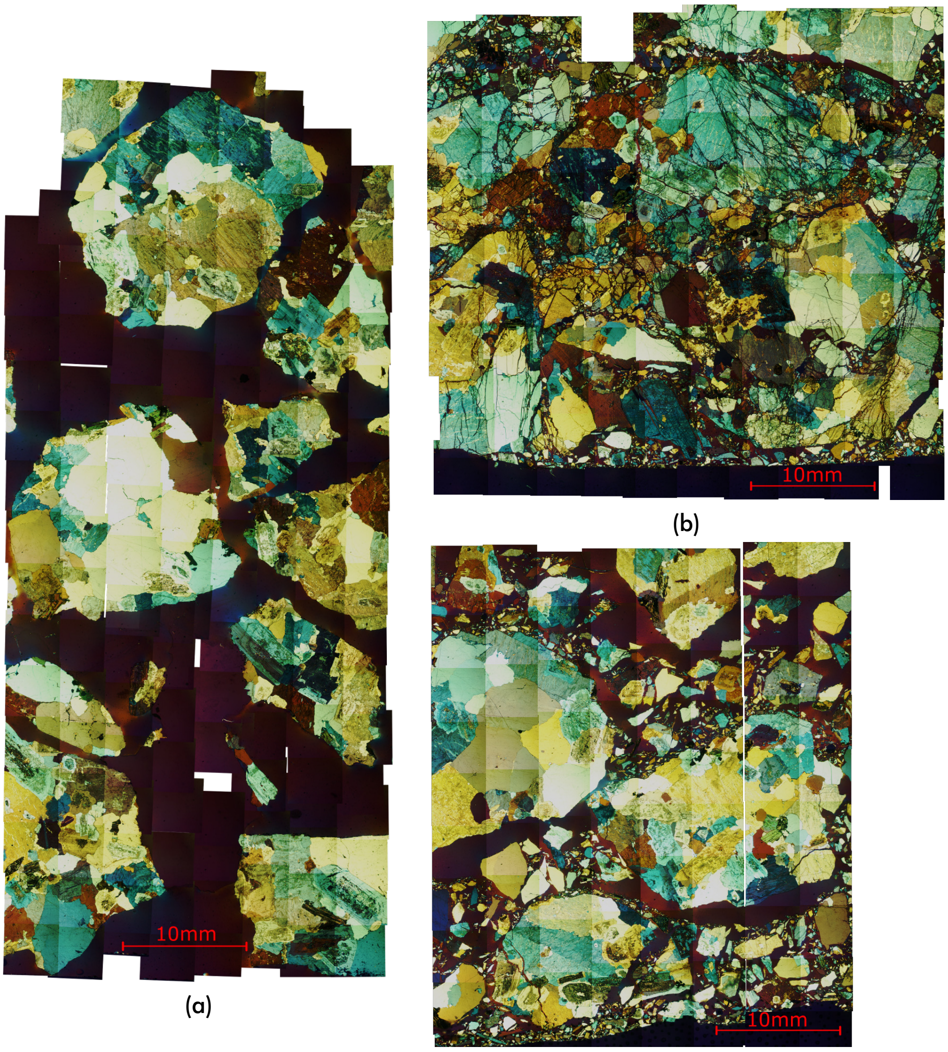

(a) (b) (c)

Fig. 4.46: Digitized thin sections of the particle bed tests. The shown maps are stitched views from photos taken with the polarized microscope with 16-x magnification. Blank areas are relicts from the manual photographing and stitching process. (a) Section of the raw packing; (b) Section of the particle bed of the test with approximately 20 MPa; (c) Section of the particle bed of the test with approximately 150 MPa

The combination of different loading conditions and the different shapes and sizes of the numerous particles results in a very broad distribution of the inner stresses on the particles. Some particles, which have unfavorable positions inside the particle bed, are intensively loaded and crushed, while other particles in a more favorable position are loaded less or even not at all. This diversity is characteristic for the particle bed comminution and is even increased by the influence of the fragments of prior crushed particles.

Those fragments are of course subjected to the same conditions like the larger particles. However, due to their smaller size, they can rearrange and fill up the voids between the larger particles. By doing so, the number of contact points of the larger particles increases rapidly, as they get in touch with numerous smaller fragments. This, however, increases the resistance of the remaining larger particles against fracturing as the increasing load is distributed more evenly throughout the particles.

In a more advanced state of the particle bed comminution, this effect can be compared with an isostatic state of stress, which results in very little fracturing of the remaining, favorable positioned, larger particles, even if the load is further increased. In the result of these processes, there are very small fragments and relatively large particles side by side in the comminution products as can be seen in Figures 4.46b and 4.46c

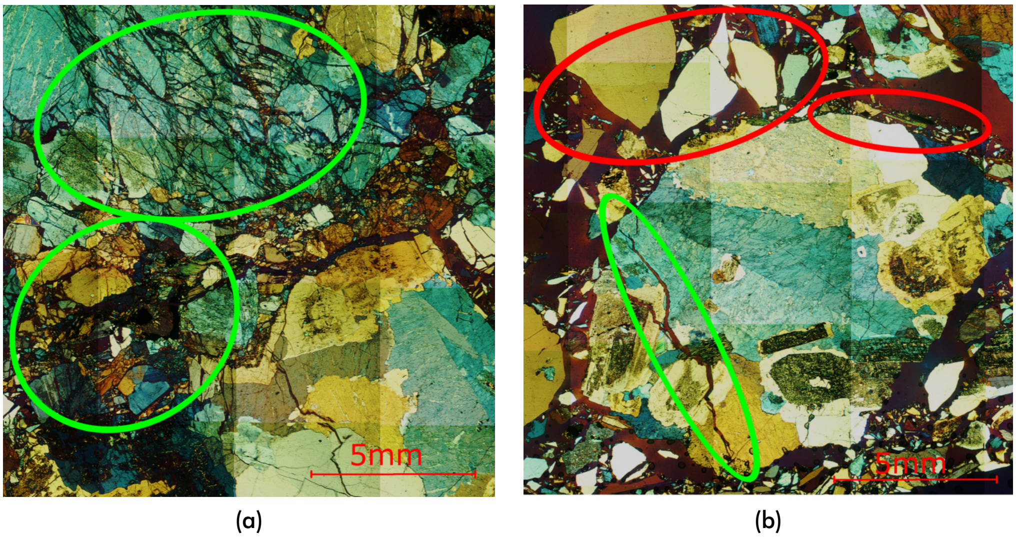

(a) (b)

Fig. 4.47: Enlarged views of the thin sections of the comminuted particle beds with marked areas that are exemplary for the specimens: (b) View of the structure of the test with 20 MPa load. Successfully embedded crack structures at the top and successfully fixed fragments at the bottom are marked green (a) View of the structure of the test with 150 MPa load. Successfully embedded crack at the bottom is marked green. Irregularly fixed and sedimented fragments at the top left and right are marked red;

Damages of the particle bed structure. Despite this, a closer look at the fixed particle beds of the comminution products reveals also significant differences between them. Therefore, enlarged image sections of the thin sections of Figure 4.46 are presented in Figure 4.47. The enlarged section of the test with 20 MPa load shows, that the particle bed has mostly stayed in the structure, it had directly after ending the comminution process. A good indicator for this is, that the majority of fragments and crack structures are intact and appear to be a puzzle of the former parent particles.

In contrast, it is not possible to identify the fragments, originally belonging together, within the specimen of the test with 150 MPa load. In this case the structure of the particle bed was changed during the grouting with the resin. As the example shows, there are only small areas with fragments and cracks that are successfully fixed. Hence, it is decided to discard this test from the further evaluation, as a reliable characterization of its fracture pattern is not possible.

Detailed evaluation of the 20 MPa **specimen.** For the presented reason, only the specimen of the particle bed test with approximately 20 MPa is used for the detailed analysis of the fracture pattern. As even the digitalized part of this section contains too many fragments and cracks for a manual analysis of the entire sample, it is decided to analyze only a part of it. In order to minimize the human influence on this sampling, a raster of 5 by 4 subsections is used for this purpose as shown in Figure 4.48.

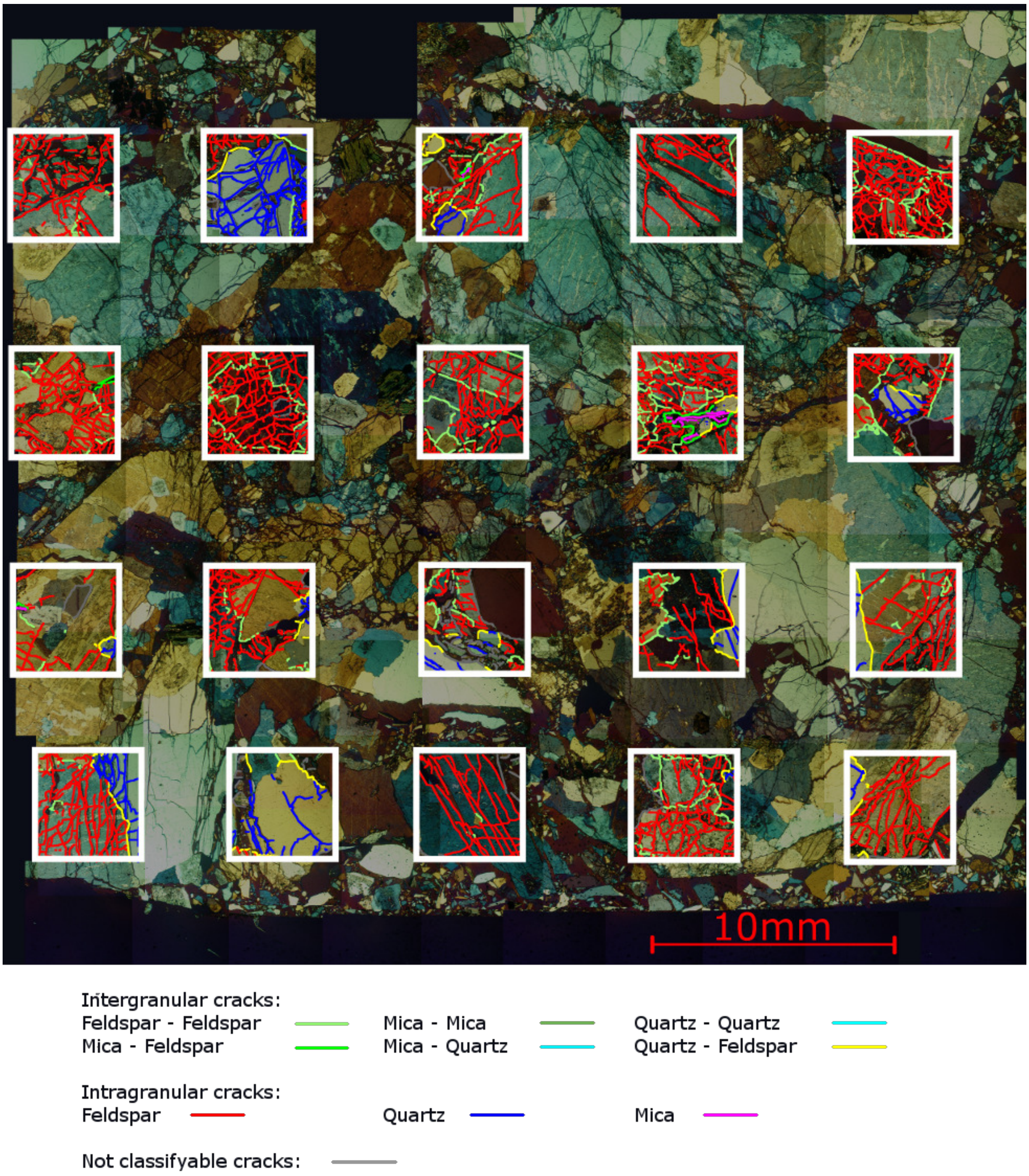

Fig. 4.48: Section of the particle bed of the test with approximately 20 MPa with the analysis raster. Cracks are marked by different colors according to the involved mineral phases. In the presented view, the different colors and smaller crack structures may be reproduced incorrectly due to effects from down scaling and transforming to the plot size and format. Hence, fracture structures that are smaller than 1 mm are ignored for clarity reasons in this view from the outset.

Based on this analysis, the fracture pattern in the particle bed is quantitatively broken down into the different crack types. Therefore, Table 4.16 shows the corresponding measured proportions of the different cracks. Besides this, the table also presents the results, if crack structures smaller than approximately 1 mm are ignored. The measurements reveal a significant change of the fracture pattern of the granite, if it is compared to the results of the basic indenter test. There is a significant drop in the intergranular breakage from 55.7 % for fractures in the basic indenter to 12.5 % for particle bed comminution.

Tab. 4.16: Proportions of the different crack types in the particle bed of the test with 20 MPa load.

	proportion [%]	
crack type	all	> 1 mm
Intergranular cracks	**12.50**	**16.96**
Feldspar - Feldspar	9.05	12.27
Mica - Mica	0.00	0.00
Quartz - Quartz	0.00	0.00
Mica - Feldspar	0.66	0.92
Mica - Quartz	0.00	0.00
Quartz - Feldspar	2.55	3.52
Intragranular cracks	**87.50**	**83.04**
Feldspar	77.68	72.85
Quartz	8.93	9.64
Mica	0.88	0.54

The detailed analysis of the crack types shows, that a majority of the cracks occur in feldspar grains. This can be put down to the high amount of feldspar in the granite (approximately 70 % according to Table 4.1 in Section 4.2.1). Assuming, that the particle bed comminution of the granite causes a more random breakage than the indenter test, the proportions of the breakage should converge to the content of the corresponding phases, which is a nearby explanation for the results.

Intragranular shattering. However, a closer look at the fracture pattern reveals, that a significant amount of the intragranular breakage is measured in areas, where the grains are literally shattered to small debris under the load of the die. A good example for this effect is exemplarily shown in Figure 4.49a. Technically, this is an enlarged view of the highlighted area of the upper part of Figure 4.47a, since the crack structure successfully embedded in this picture is actually such a broken feldspar. Due to the filigree structure, this becomes clearly recognizable, if it is zoomed in.

Furthermore, the proportions between measured intragranular breakage in the particle bed specimen and the content of the mineral phases in the granite seem to be shifted. Although, the general ranking order of the mineral phases by content is correct, the intergranular breakage of feldspar seems to be overrepresented and especially the quartz underrepresented. Even though, it cannot be excluded, that there is a bias in the results due to deviations in the mineral content between this part of the analyzed section and the QMA results, there is another characteristic, which has to be considered for the general evaluation of the fracture pattern.

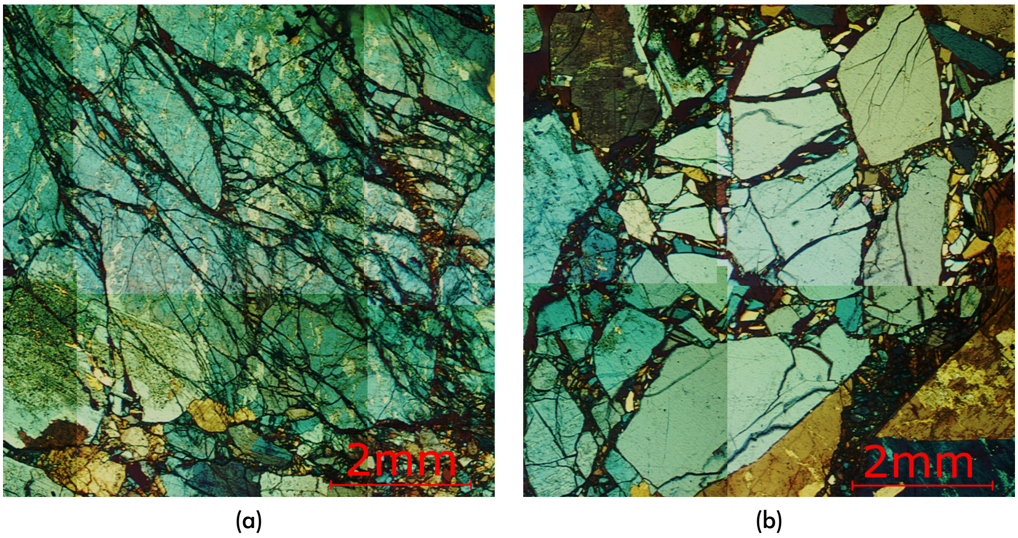

(a) (b)

Fig. 4.49: Areas with shattered minerals after the particle bed comminution: (a) Fragments of fine shattered feldspar; (b) Fragments of coarser shattered quartz. The quartz fragments are in the center of the image and can be identified by their less textured and more bright bluish appearance

It appears, that the shattering effect in the other phases than feldspar is less pronounced. This is especially for quartz noticeable. There are also areas dominated by quartz debris, but the fragments appear to be larger and less crushed, than in areas with shattered feldspar. Two exemplary sections that document these characteristics in comparison are shown in Figure 4.49b. This finding is supported by the significantly reduced amount of measurable intragranular feldspar cracks, if structures smaller than approximately 1 mm are ignored.

If it is assumed, that these differences in the shattering are due to a higher resistance to fracture of quartz compared to feldspar, this would logically cause a lower amount of intragranular quartz cracks. Although this somehow corresponds to the common thinking of quartz having a higher strength than feldspar, the results presented here are not considered to be sufficient for a final assessment of these characteristics since the data base is relatively small.

Of course, it would be beneficial for the modeling of comminution processes at grain size level, if the differences in strength could be correctly quantified. However, it should be noted at this point, that this is not so easy. Unfortunately, many influencing parameters like strength, hardness, toughness, brittleness, and cleavability as well as their correlations are insufficiently understood. In addition, they are not or only partially measurable with the available conventional approaches at the grain size scale. Hence, proving and quantifying such differences in the mineral resistance against fracture requires more substantial efforts in both the theoretical understanding and the actual measuring of the relevant physical parameters. This, however, is not the scope of this study and is therefore not further regarded.

Intergranular fracture. Irrespective of the characteristics of the intragranular fracture pattern, there is also a comparatively small but still significant intergranular fracture of 12.50 % and 16.96 %, respectively, if the cracks smaller than approximately 1 mm are filtered out. This implies that at least some of the grain boundaries are preferably chosen by the cracks to propagate. If the existence of the grain boundaries would have no effect on fracture behavior, the crack propagation would be random. In this case the proportion of intergranular fracture would converge to zero.

This can be explained by the difference between the limited set of possible crack paths along grain boundaries and the infinite set of possible crack paths through grains. Considering the two-dimensional case as example, the grain boundaries and cracks can be seen as slightly contoured lines. According to the fractal geometry, their dimensions are assumed to be a bit higher than one. Grains, however, are in this case faces with contoured outlines. Those have a fractal dimension just below two. For a problem with little contoured objects, the dimensions of the grain boundaries and cracks are approximately one and the dimension of the grains is approximately two. Such a simple microstructure is schematically shown in Figure 4.50. For clarity reason, the boundaries of the grains are simplified drawn with black straight lines.

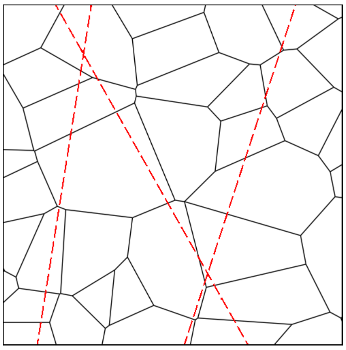

Fig. 4.50: Schema of random cracks in a two-dimensional microstructure. Grain boundaries are simplified drawn with black straight lines. Random straight cracks are drawn with dashed red lines.

It can generally be noted, that the probability for a random crack to propagate exactly orientated along an object of the same dimension like a grain boundary is negligible compared to the probability to propagate through an object of a higher dimension like a grain. This effect is all the more important, as the space for crack propagation is fully filled with grains. This relationship is illustrated by the three red, straight cracks in Figure 4.50, which were randomly drawn in the microstructure. In no case do they fall exactly on a grain boundary. Even if the straight cracks would be replaced by more sophisticated structures like polygonal lines with random orientations of the segments, this would not change the overall outcome.

Considering this, it is clear, that the measured amount of intergranular cracks is an unambiguous indicator for the existent tendency of the cracks to not propagate completely randomly. Moreover, it indicates that the cracks at least partly orientate along grain boundaries, if the spatial proximity and the state of stress allow it.

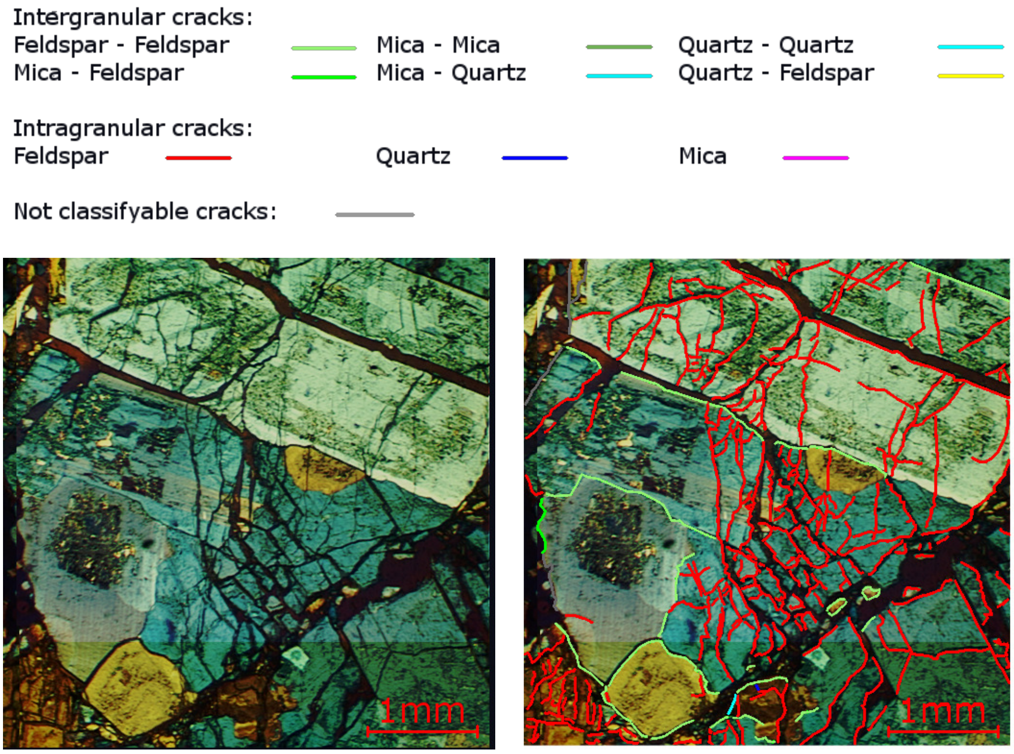

(a) (b)

Fig. 4.51: Area with clearly recognizable grain boundary fracture: (a) Original view of the fractured microstructure; (b) View with highlighted cracks.

This effect can be seen exemplary in Figure 4.51b, where the stressing inside the particle bed induced the breakup of significant parts of the microstructure along grain boundaries. Interestingly, right next to the intergranular cracks is an area dominated by intragranular shattering, which shows that both different effects are not mutually exclusive.

The presented results, especially the measurable intergranular fracture, are seen to be a good basis for the validation of the appropriateness of the synthetic microstructure approach in a more realistic comminution setup. Because of the fact, that even the single thin section of the test with 20 MPa contains numerous evaluable cracks, it is seen to be no drawback, that the second test with approximately 150 MPa cannot be used for a detailed comparison.

4.4.3 Realization and evaluation of the simulated particle bed test

Considering the evaluation results of the real particle bed tests, it is decided to focus on the simulation of the particle bed test with approximately 20 MPa load, as this promises the best comparability. Furthermore, because of the positive results with the simulation procedure of the granite from Meissen during the basic indenter test, it is obvious to transfer the particle bed setup with basically the same procedure to YADE. Therefore, the synthesis of the granite can directly be taken from the basic indenter test (Section 4.2.3) and is not explained again in detail. In order to keep the link and the comparability to the models of the simulated basic indenter test, the same parametrization will be used. Moreover, it makes sense to reconsider the influence of the grain boundary strength on the fracture behavior as subject of investigation again, as this feature can be directly compared with the real results.

Principle of the particle modeling

In order to allow a realistic simulation of the particle bed test in YADE, the modeling of the particles is crucial. Against the background of the validation of the synthetic microstructure approach for comminution simulations, such model particles have to meet two major conditions. The first one is, that it has to be possible to map a synthetic microstructure to a breakable particle. This is already known from the indenter test. However, in this more realistic environment of particle bed comminution, also the particle shape has to be considered. Hence, the second condition is, that the shape of the simulated particles has to be equivalent to the shape of the real particles in order to allow a reliable simulation.

In general, there are different approaches applicable for modeling the shape of the particles. As explained in Section 2.1.1, it is possible to model the particles from single primitives, to use polygonal objects, or composite particles. Referring to a two-dimensional simulation, single primitives could be circles or ellipsis, for example. However, these allow only very crude approximations of shapes. Polygonal discrete elements seem to be more suitable for this task, as it is possible to create arbitrary shapes with this approach. Unfortunately, both polygonal particles and primitives are unbreakable in YADE. Furthermore, they cannot be used in connection with synthetic microstructures, since they are treated as single homogeneous elements. Breakable particles in YADE can only be realized with fragile composite particles, as they were used in the indenter test simulations.

The basic coupled mapping procedure. Hence, the polygon approach and the fragile composite particle approach have to be linked for the particle bed test. The idea is, to use a coupled mapping procedure. A basic example of such a procedure is shown in Figure 4.52. The most important characteristic is, that besides the synthetic microstructure, also the particle shape has to be mapped onto a given packing of bonded discrete elements inside YADE. By doing so, it is possible to make use of the polygon approach for mapping the particle shape in combination with the composite particle approach, to ensure the breakability.

In the result, this basic coupled procedure allows to map both, the mineral microstructure and the particle shape. Unfortunately, it has a critical disadvantage as well as it is based on deleting discrete elements, which are outside of the mapped polygon. Hence, the resulting particle, which is made of numerous coupled discrete elements, has a relatively rough outline. Furthermore, this outline also differs from the original pattern as shown in Figure 4.52f. This

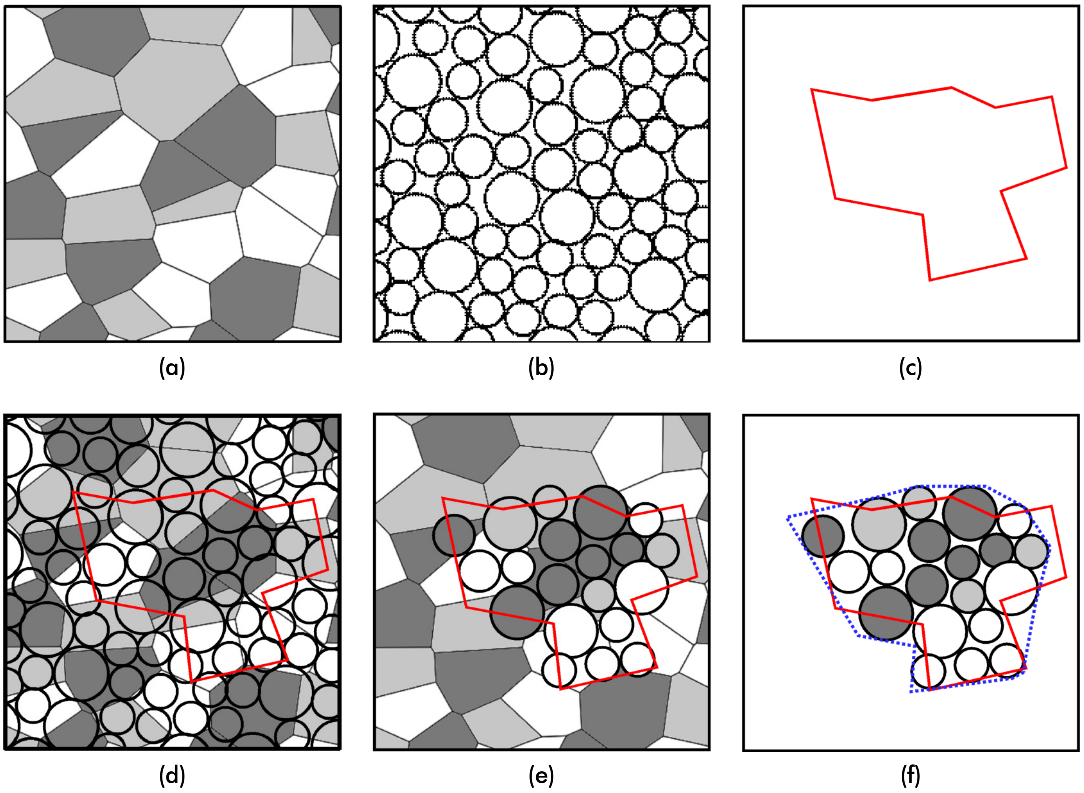

Fig. 4.52: Schema of the basic mapping procedure to create particles with realistic shape and microstructure in YADE: (a) Initial synthetic microstructure; (b) Initial packing of bonded discrete elements; (c) Initial polygon of the particle shape; (d) Initial packing superimposed with the synthetic microstructure and the polygon; (e) Packing after deletion of the elements outside of the polygon; (f) Final coupled particle with realistic microstructure - The resulting outline (blue, dotted) is relatively rough and differs significantly from the original pattern (red, straight)

circumstance is independent of the applied decision rule, which is used to decide whether an element is inside or outside.

This unintended roughness is directly proportional to the sizes of the used discrete elements. Hence, in order to create particles with smooth outlines, which in addition fit well with the original pattern, relatively small discrete elements have to be used. This, however, is impractical considering the increasing computational effort for the simulation.

The improved coupled mapping procedure. This problem can be reduced, if the approach is adapted. Therefore, the mapping process has to be improved. Instead of cropping the discrete element packing to the shape of a polygon, it is possible to pack the elements directly into the outlining polygon. By doing so, a higher shape accuracy can be achieved. The resulting adapted procedure is shown schematically in Figure 4.53.

The particle drawing approach. Besides the presented coupled mapping process, it is also conceivable to synthesize the particles in an approach, which is comparable to the presented drawing process for grains. Considering this, it should be possible to create synthetic

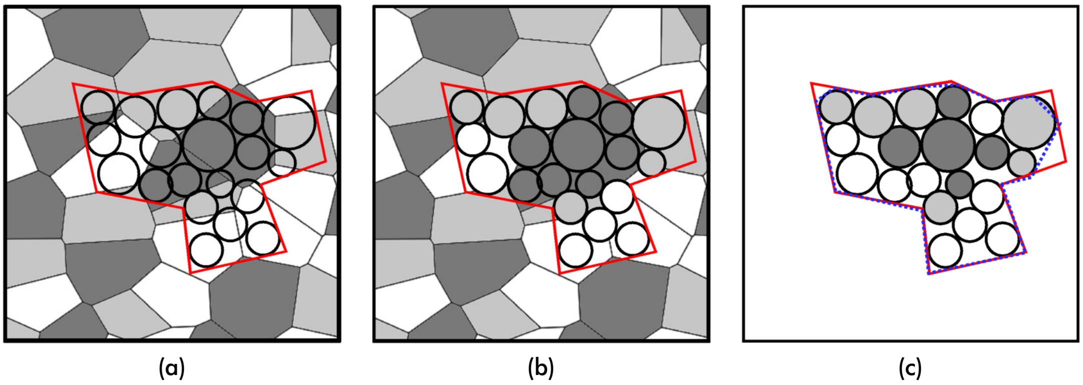

Fig. 4.53: Schema of the improved approach to create particles with realistic shape and microstructure in YADE: (a) The initial packing of the bonded particles is created directly inside the polygon; (b) The initial microstructure is mapped to the packing; (c) Final coupled particle with realistic microstructure - The resulting outline (blue, dotted) is less rough and fits the original pattern (red, straight)

particles at the computer, which have comparable characteristics to their real counterparts, based on a quantitative characterization of the granulometry and shape of a given set of particles. For this purpose, the presented grain generation algorithms are seen to be an appropriate basis. However, this would go beyond the scope of this validation study and is therefore not implemented. Instead, the setup of the simulation is based on the coupled mapping procedure, as it has comprehensible and reproducible results, without the need of a further proof-of-principle.

Realization of the particle modeling

As explained in the preceding section, the particle shape is an important characteristic, which is incorporated by the improved mapping process. Hence, in order to make real use of such a complex approach, it is mandatory to use realistic particle shapes as pattern for the polygons.

Determining realistic particle shapes. For this task, Imaging Particle Analysis (IPA) of the original particle fraction is seen to be a suitable basis. For this, a representative sample of the material is analyzed using a HAVER CPA 4-2. This machine uses dynamic imaging particle analysis for measuring the size and shape characteristics of bulk goods in the size range of approximately 34 µm to 90 mm [70]. According to the principle of this analysis method, it is possible to analyze the shadow images of the single particles [71]. Due to the two-dimensional measuring principle, these silhouettes are already planar approximations of the spatial contoured particles. Hence, this images are seen to be a suitable basis for deriving the particle shape for the two-dimensional simulation.

Mapping the discrete elements. The corresponding procedure for utilizing the measuring results from the IPA is shown exemplary for one particle in Figure 4.54. At the beginning, the single shadow images have to be exported from the HAVER CPA software. Subsequently, the actual bitmap silhouettes in those images are cropped and traced to paths using image processing methods. The resulting Bézier splines are then reduced to simple polygonal paths. The vertices, in turn, are used as input for the packing process, which is done with the `PolygonWithLines2D` function of the GenGeo library [60]. For reasons of comparability, the same packing parameters like for the basic indenter test are chosen, so that the final packing consists of discrete elements with diameters ranging between 0.1 mm to 0.5 mm. Additionally, a packing with significantly coarser discrete elements ranging between 1 mm and 5 mm is created, for comparative simulations with reduced computation duration.

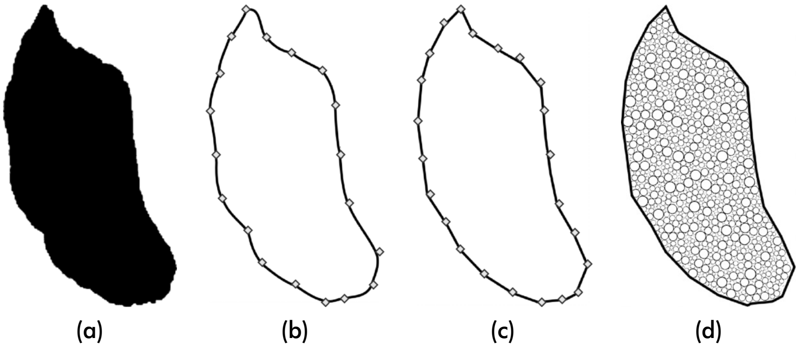

Fig. 4.54: Procedure of creating a packing of discrete elements inside an outlining polygon of a shadow image of a real particle: (a) Shadow image of a real particle exported from the HAVER CPA; (b) Outlining Bézier spline generated with image processing methods; (c) Polygonalized outline; (d) Final packing of discrete elements in the range of 0.1 mm to 0.5 mm generated with the `PolygonWithLines2D` function of the GenGeo library inside the polygonal outline

Because of software restrictions, it is not possible to automate or script this procedure. Hence, it is impractical to create packings for all of the approximately 670 analyzed particles in the range of 8 to 16 mm, as this would require extensive manual work. For this reason, a random subset of 67 shadow images was selected that represent the patterns for the improved mapping process.

Mapping the microstructure. In the next step, a synthetic microstructure of the granite has to be generated. As it is the same material like in the basic indenter test, the synthesis parameters are identical as well. In order to achieve sufficient variation in the synthetic microstructure of the final particles, an adequate pattern microstructure has to be synthesized first. Based on the results of the synthesis for the basic indenter test in Section 4.2.3, it is decided to use also a synthesis size of 10 000 Pixels × 10 000 Pixels, which equates to a quadratic section with approximately 87.7 mm edge length.

The comparison between the initial silhouette of a given particle (Figure 4.54a) and the final packed discrete elements for the simulation (Figure 4.55d) shows, that this approach is satisfactory with regard to the accuracy of the particle shape.

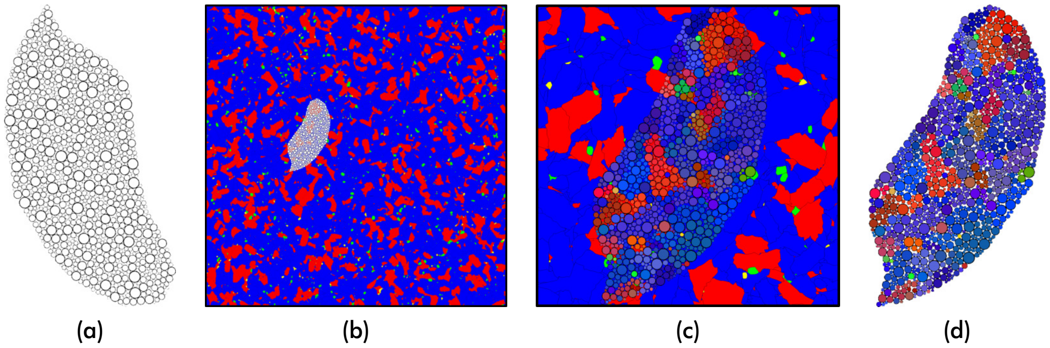

Fig. 4.55: Procedure of mapping a microstructure onto a packing inside a polygonal particle: (a) Initial packing of discrete elements (0.1 to 0.5 mm) in the shape of a realistic particle; (b) Random superimposition of the microstructure and the initial packing; (c) Actual mapping of the microstructure information onto the individual discrete elements of the packing; (d) Final particle with realistic shape and microstructure

Admittedly, a further improvement is possible, if more accurate polygonal approximations of the outline are used. This, however, makes only sense, if the size of the discrete elements is also decreased. Otherwise, the more filigree outline cannot be approximated by the discrete elements as they would be too coarse. Nevertheless, due to the scope of this validation experiment, a further reduction of the sizes of the discrete elements is not intended, as it would result in impractical computation efforts.

Implementation in YADE. Based on this microstructural modeling approach, it is decided to set up the particle bed test in YADE as well. It is then possible to analyze the influence of the grain boundary strength on the fracture pattern and the amount of intergranular fracture $p_{boundary}$ in particular and compare it to the results of the real test and the results of the basic indenter test, which was done with the same material. For this reason, again different grain boundary factors $z_{boundary}$ are applied to weaken and strengthen the cohesion between the different grains, while the other physical parameters are unchanged.

Setup for the simulation of the whole particle bed test in YADE

In order to make the simulative setup comparable to the real one, it is evident to use the same dimensions. However, as the YADE simulation is two-dimensional, the pot is set up as rigid group of planar, open-top facets with a width of 160 mm and a height of 100 mm, which represent a planar central section of the originally spatial real setup. The corresponding piston is a movable facet that fits exactly into the top-opening of the facets of the pot. Based on this, it is possible to perform a two-dimensional simulation in which the composite particles with realistic microstructures are comminuted in particle bed mode in a planar piston die setup.

Procedure for simulating the whole particle bed system. At the beginning of such a simulation, a random sample of particles with the synthetic microstructure is placed and sedimented inside the pot. This is shown in Figure 4.56. In comparison to the real counterpart and with regard to the initial particle bed height, it is found suitable to initiate five layers of particles. After sedimentation, they form a particle bed height of 63 mm on average, which is seen to be a good fit to the approximately 50 to 55 mm of the real test.

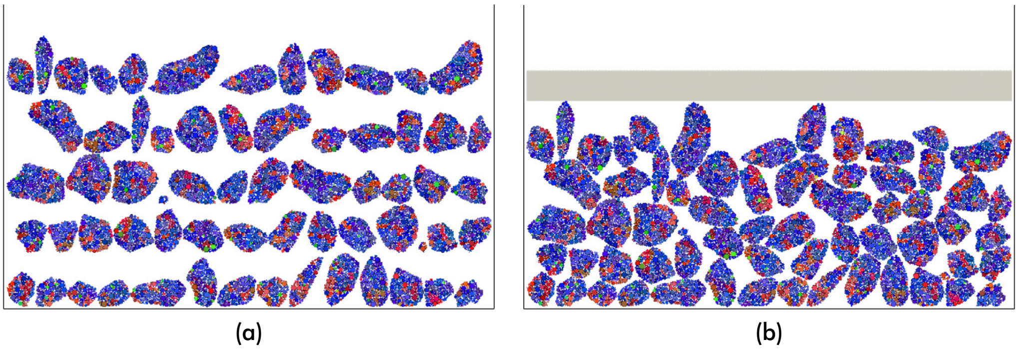
(a) (b)

Fig. 4.56: Setup of the whole particle bed test in YADE: (a) Initially loaded particles; (b) Particles after sedimentation - The piston is set to its start position just above the top particle

The remaining differences of the particle bed height are due to the differences in measuring. While the manually measured height of the real particle bed describes the distance between the support and the average height of the top layer, the automatically calculated height of the simulated particle bed describes the distance between the support and the highest point of the packing. If the same is done for the fixed sample of the raw particle bed (Figure 4.45a), this results in a height of approximately 60 mm. Hence, as the resulting differences are considerably small, the simulative setup is seen to be satisfactorily.

Unfortunately, the resulting setup is comparatively large in terms of the computational effort, which is needed to simulate it. If a size range for the packing generation of 0.1 mm to 0.5 mm is used, this results in a total amount of approximately 40 000 discrete elements, which have to be simulated. Although, this is basically a manageable task for YADE, it results in impractically high simulation durations of several weeks for a single test. The main reason for this is, that the used model parametrization inside YADE is focused on a reliable approximation of the real physics instead of being optimized for high computation speeds (compare for Figure 4.20 in Section 4.2.3). Hence, it is decided to use the coarser packing with discrete elements of 1 mm and 5 mm for simulating the comminution of the entire particle bed. Although, the resulting resolution for the microstructure of the granite is quite coarse, this allows to simulate the entire particle bed comminution test within the range of single days.

Finding a suitable speed for the piston. Considering this, the coarse packed particles are loaded and sedimented first. Subsequently, then actual test can be started. Therefore, the piston is moved with a speed of $0.06\,\mathrm{m\,s^{-1}} = 60\,\mathrm{mm\,s^{-1}}$. Although this is significantly faster than in the real test, which is done with a speed of approximately $1\,\mathrm{mm\,s^{-1}}$, it is mandatory in order to decrease the time needed for the simulation, which is even then in the range of approximately 10 days. As the same speed-independent physical model like for the basic indenter test is used, no negative model characteristics have to be considered.

Besides the physical model stability, the main limitation for this approach for speeding up the simulation is the difference in the relative speed between the piston and particle fragments after fracture events. Compared to reality, the fragments have less time to re-sediment after a particle breakage, until the piston has moved further down and stresses the next particles. However, this is relevant only at the beginning of the particle bed comminution. If the comminution progresses, the voids between the larger particles are rapidly filled with smaller fragments and debris. Hence, the movement behavior of the fragments has only minor influence during the later part of the test, where most particles will be broken. In order to allow practical computation times, this limitation in model accuracy is seen as an acceptable trade-off and was proved in preliminary simulations.

Finding a suitable condition for stopping the simulation. In order to make the simulation comparable to the one successful real experiment with approximately 20 MPa load, some further considerations have to be done. Because of the differences in dimensionality and the known simplifications in the physical model, it is not possible to use a load-controlled simulation. The calculated load on the particles in the simulation depends on too many model parameters, which are not validated, so that the result cannot reliably be converted to an equivalent three-dimensional load, or vice versa. For this reason, it is decided to use the relative stroke h_{rel} as comparative value. It is calculated as fraction of the final stroke h of the piston at the end of the test and initial packing height h_0 (Equation 4.12). This value is approximately 42 % for the test with 20 MPa.

$$h_{rel} = \frac{h}{h_0} \tag{4.12}$$

In the result, it is decided to run the simulative particle bed simulations for 0.05 s. During this time the piston moves 30 mm. Based on a particle packing height of 63 mm at the beginning, this results in the final height of 33 mm for the compressed particle bed. Consequently, this equals to a relative stroke of 44 %, which is comparable to the real counterpart. The remaining small differences, however, should not be overrated. Due to the differences in the dimensionality, the comparison can only be done on a vague basis anyway.

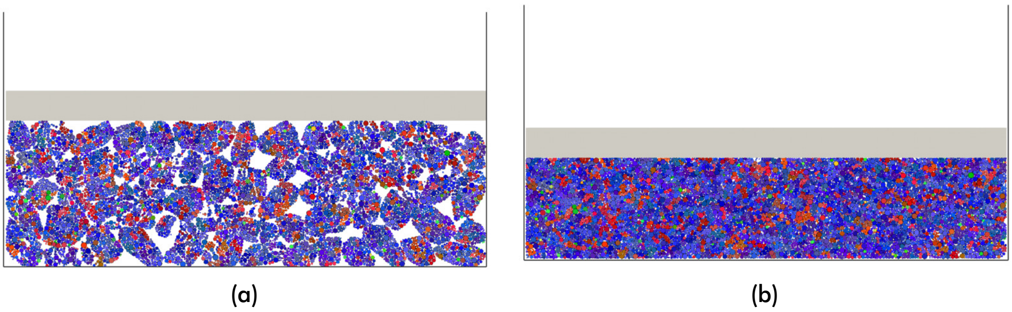

Fig. 4.57: Stopping the simulation of the whole particle bed test: (a) Particles during the particle bed comminution; (b) Particle bed after stopping the test at a relative stroke of 44 %

Setup for the simulation of a detailed section particle bed test in YADE

Due to the discrete element resolution limitations, it is decided to set up another simulation, which will only represent a vertical section of the particle bed. By reducing the total amount of particles, it is possible to increase the resolution of the discrete elements to the original range of 0.1 mm to 0.5 mm, while retaining acceptable computation times.

Particle bed with periodic boundaries. For doing so, a specialty of the YADE engine is used. Instead of a simulation with conventional boundary conditions, this test is done with a periodic boundary. In such a setup there are no walls at the sides, which would represent the pot, but periodic boundaries. Those allow the particles to leave the simulation at the one side and simultaneously enter it again at the other side, without being physically affected. Actually, those beamed particles behave as if there is no boundary at all. Hence, from their perspective, they are located in an infinite large periodic two-dimensional space, which is only bordered by the bottom plate of the pot and the above piston.

In consequence this artifice allows to simulate the particle bed with a significantly less amount of particles by retaining the particle bed character. Furthermore, no wall effects do occur at all. The limiting factor is only the particle size. In order to keep the simulations free from physical singularities, it has to be guaranteed, that no particle can be in contact with itself through such a periodic boundary.

Therefore, it is decided to simulate a section of 40 mm width, which represents a quarter of the original setup. As it is a vertical section, it is also filled with five layers of particles. This ensures that normally two to four particles are initiated in each layer and guarantees that the single particles are small enough for a stable simulation. Despite these differences, the actual procedure for generating the particles is still the same as described for the conventional simulation for the whole particle bed test. The only change is, that the discrete elements for the packings are smaller, which allows a better resolution of the microstructure.

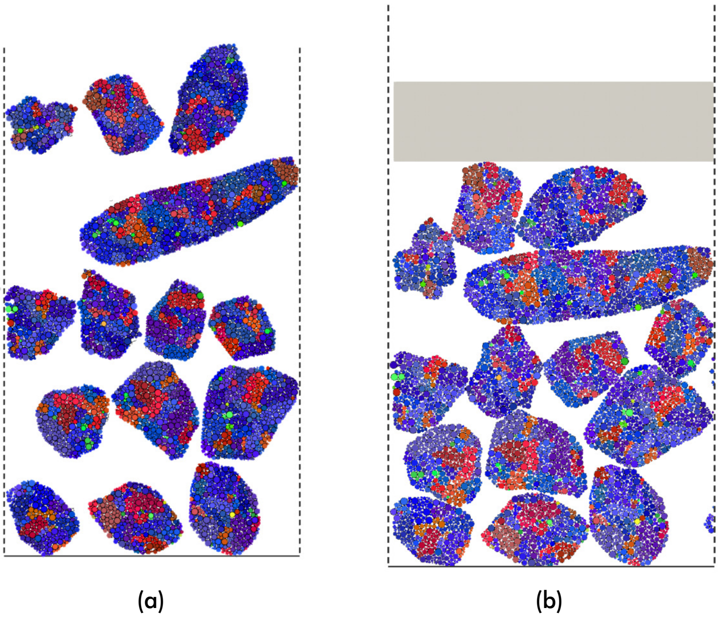
(a) (b)

Fig. 4.58: Setup of the detailed section of the particle bed test in YADE. The periodic boundaries are indicated by the dashed vertical lines: (a) Initially loaded particles; (b) Particles after sedimentation - The piston is set to its start position just above the top particle

The resulting setup is shown exemplarily in Figure 4.58. For reasons of clarity, the periodic boundaries are indicated by the dashed vertical lines although they do not affect the particle motions. However, due to the ordered, dense initial packing, the particles do only slightly cross the periodic boundaries during sedimentations. Nevertheless, a hint for the unhindered movement can be seen in the lower right part, where a small edge of the lower left particle has moved through the boundary.

This is all the more apparent in later stages of the test, where the fragments can move through these periodic boundaries as shown in Figure 4.59a. Despite of this, the significantly better resolution of the discrete elements becomes apparent if it is compared to the simulation of the whole particle bed system (Figure 4.56).

Finding a suitable speed and stopping condition for the simulation. The speed of the piston is set to the value of $0.5\,\mathrm{m\,s^{-1}}$, which is again significantly faster than for the real test and the simulation of the whole particle bed setup. However, as the used models are not time dependent, this helps limit the simulation time for these more detailed simulations to single days.

As the vertical arrangement of the particles is similar to the setup of the whole particle bed test, the simulation ending is determined by the relative stroke as well. Based on the initial packing height of 55.8 mm, the simulation is run for 0.047 s, which results in a final particle bed height of 32.3 mm. This is equivalent to a relative stroke of 42.1 %, which is clearly in the range of the real experiment. This final situation is exemplarily shown in Figure 4.59b.

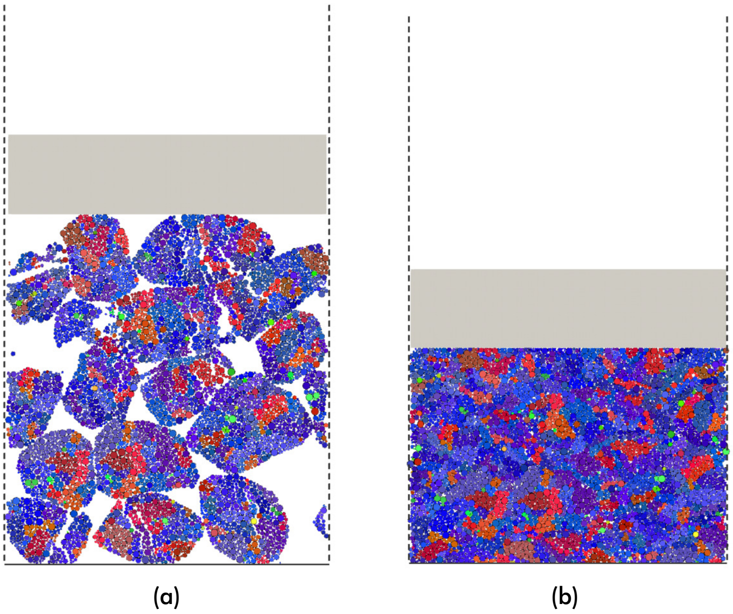

Fig. 4.59: Particle bed simulation in YADE with periodic boundaries: (a) Particles during the particle bed comminution; (b) Particle bed after stopping the test at a relative stroke of 42.1 %

Evaluation of the particle bed simulations

With progression of the particle bed compression through the piston, the single particles and cracks become harder to distinguish as can be seen in Figures 4.57b and 4.59b. Hence, for the visual evaluation of the fracture pattern of the simulations, it is useful to analyze the particle bed at an early stage of the particle bed comminution. In this state, the broken bondings and the influence of the microstructure are clearly visible.

For reasons of clarity, this is shown exemplarily at image sections from an early stage of both simulation setups. In Figure 4.60 a large particle and its environment is shown for the simulations of the whole particle bed, with grain boundary factors $z_{boundary}$ of 0.6, 1.0, and 1.4.

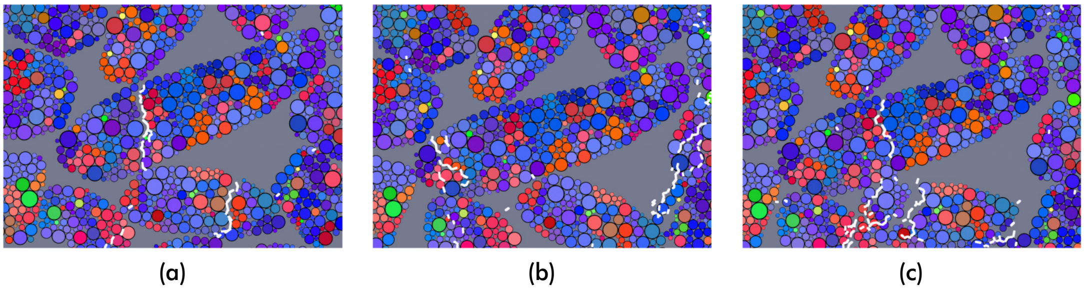

Fig. 4.60: Image sections of the simulation of the whole particle bed for different grain boundary factors $z_{boundary}$. For reasons of clarity, the background is colored gray and broken bondings are colored withe. Furthermore, the grain boundaries are not drawn separately, since the grains are already colored in variations of the base colors: (a) $z_{boundary} = 0.6$; (b) $z_{boundary} = 1.0$; (c) $z_{boundary} = 1.4$

The images were taken just after the large particle cracked. Due to the different simulative progresses, this happened at slightly different points of time. In order to increase the contrast, the background is colored gray, while the broken bondings of the cracks are illustrated by white lines. It is noted, that due to the particle movements after the fracture events, some lines indicating the cracks may seem to be misaligned slightly. This, however, is only a problem of plotting the data of different time steps where the distinct bondings broke. It does not diminish the correctness or the significance the shown characteristics.

The images in Figure 4.61 show a comparable situation in the more detailed setup with the periodic boundaries. In order to ease the comparison, a particle of the same large shape is set into the focus, just after it cracked.

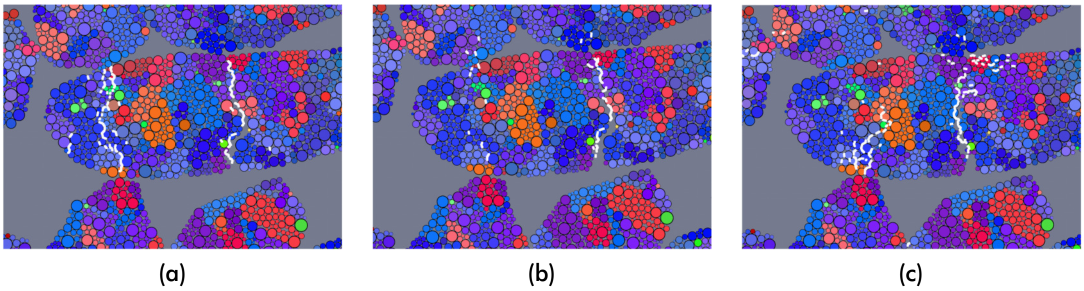
(a) (b) (c)

Fig. 4.61: Image sections of the more detailed particle bed simulation for different grain boundary factors $z_{boundary}$. For reasons of clarity, the background is colored gray and broken bondings are colored withe. Furthermore, the grain boundaries are not drawn separately, since the grains are already colored in variations of the base colors: (a) $z_{boundary} = 0.6$; (b) $z_{boundary} = 1.0$; (c) $z_{boundary} = 1.4$

Influence of the grain boundary factor. The visual evaluation of both simulation types shows, that the microstructure that is represented on the physical level of the simulation by the weakened or strengthened boundaries has major influence on the fracture pattern. The cracks do also preferentially propagate along such weakened structures in particle beds, if possible. This can be seen exemplarily in the image sections of the cracked large particle with a grain boundary factor $z_{boundary} = 0.6$ in Figures 4.60a and 4.61a.

This is not the case if particles with homogeneous physical properties are cracked ($z_{boundary} = 1.0$). As can be seen in Figures 4.60b and 4.61b, the fractures are more random in this case. The example in Figure 4.61c even suggests, that the cracks avoid to propagate along grain boundaries if those are strengthened ($z_{boundary} = 1.4$).

Those qualitative findings are supported by the quantitative evaluation of the data of all broken boundaries. In order to allow a comparison to the real tests, the data of the simulation endings, as shown in Figures 4.57b and 4.59b, is used to analyze the fracture pattern. For this reason, Table 4.17 shows the proportion of grain boundary breakage $p_{boundary}$, which represents the intergranular fracture in dependence of the different grain boundary factors $z_{boundary}$.

Tab. 4.17: Proportions of intergranular fracture after finishing the particle bed simulations

$z_{boundary}$ [–]	$p_{boundary}$ [%] whole particle bed	 detailed section
0.4	64.37	46.83
0.6	65.05	43.36
0.8	62.86	40.37
1.0	60.65	36.60
1.2	58.94	34.73
1.4	56.82	31.77
1.6	49.08	31.09

These quantitative results clearly prove the findings of the visual analysis of the fracture pattern. Based on this data, it becomes clear that the grain boundary factor $z_{boundary}$ has also a significant influence on the fracture pattern in such particle bed simulations.

As can be seen, lowering the grain boundary strength ($z_{boundary} < 1.0$) increases the proportion of intergranular fracture ($z_{boundary} \uparrow$). In contrast, if homogeneous material with no physical differences between inter- and intragranular bondings is simulated ($z_{boundary} = 1.0$), $p_{boundary}$ converges to the proportion of intergranular bondings of the initial packing. This are 61.53 % for the simulation of the whole particle bed and 37.70 % for the more detailed simulation with the periodic boundaries. In turn, if the grain boundaries are strengthened ($z_{boundary} > 1.0$), also the proportion of grain boundary fracture decreases ($z_{boundary} \downarrow$).

Influence of the resolution of the discrete elements. Despite the influence of the grain boundary strength on the fracture pattern, there is also an effect of the resolution of the discrete elements recognizable. Comparing the differences between both simulation setups in Table 4.17 reveals, that the more detailed simulation has always a lower proportion of grain boundary breakage after finishing the comminution. The reason for this is the smaller discrete elements, which form the grains and particles. Because the synthetic mineral microstructure used for the mapping process is the same for both simulation setups, the proportion of initial intergranular bonds decreases when smaller discrete elements are used for the package.

As the comparison of the large particles in Figures 4.60 and 4.61 shows, the approximate size of the grains is similar. Nevertheless, the grains are formed by about four times more discrete elements in the more detailed simulation. Hence, the number of total bondings forming the single grains increases approximately by a factor of four as well. As the grain sizes of the synthetic microstructure remain constant, the amount of intergranular bondings is increased to a lesser extent than the amount of intragranular bondings. Hence, increasing the resolution of the discrete elements results in a drop of the proportion of the initial intergranular bondings.

Consequentially, further increasing the resolution of the discrete packings would result in more realistic simulations. If the size of the elements converges to zero, this would correspond to the theoretical considerations for random cuts through microstructures, as explained by Figure 4.50. Thus, the amount of grain boundaries in a random section through a microstructure is infinitesimal compared to the amount of cut grains.

Hence, the used resolutions are seen to be the main reason why the amount of grain boundary breakage for both particle bed simulation setups is significantly higher than the result of the corresponding real particle bed test with approximately 20 MPa. It can be assumed that the discrete element size is still not sufficient to simulate the real fracture pattern ($p_{boundary} =$ 16.96 %) with the required level of detail, even if the very filigree shattered crack structures of the real sample are ignored ($p_{boundary} =$ 12.50 %).

Assuming that the results of the basic indenter test are applicable to the particle bed setup, a grain boundary factor of $z_{boundary} = 0.825$ should provide realistic results. However, as can be seen from the results of the simulations with $z_{boundary} = 0.8$ in Table 4.17, both setups tend to have too high proportions of the grain boundary breakage in this parameter range.

The influence of the moment of the analysis. By further analyzing the simulation data it becomes apparent, that the moment of the observation or analysis of the process is another important parameter, which has to be considered if the fracture pattern of the particle bed is in the focus. In order to illustrate this, the data of both the periodic boundary simulations and the simulation of the entire particle bed are used as reference.

For this purpose, in Figure 4.62 the proportions of grain boundary breakage $p_{boundary}$ are plotted as functions of the relative strokes h_{rel} for different grain boundary factors $z_{boundary}$. The proportion of the non-limiting cracks p_{grain} is also plotted in each diagram, since these is the complement set to $p_{boundary}$.

In detail the data for the simulations with the grain boundary factors 0.6, 1.0, and 1.4 is presented for the both simulation types. As the speed of the piston is constant during the simulations, there is a linear interrelation between the relative stroke h_{rel} and the simulation time. In the result, analyzing the simulations at different simulation times is equivalent to analyze them at different relative strokes.

First of all, the already explained influences of the resolution of the discrete elements and grain boundary factor can be seen in these plots as well. For example, the overall proportion of grain boundary breakage of the simulation of the whole particle bed is higher than in the simulation of the detailed particle bed section.

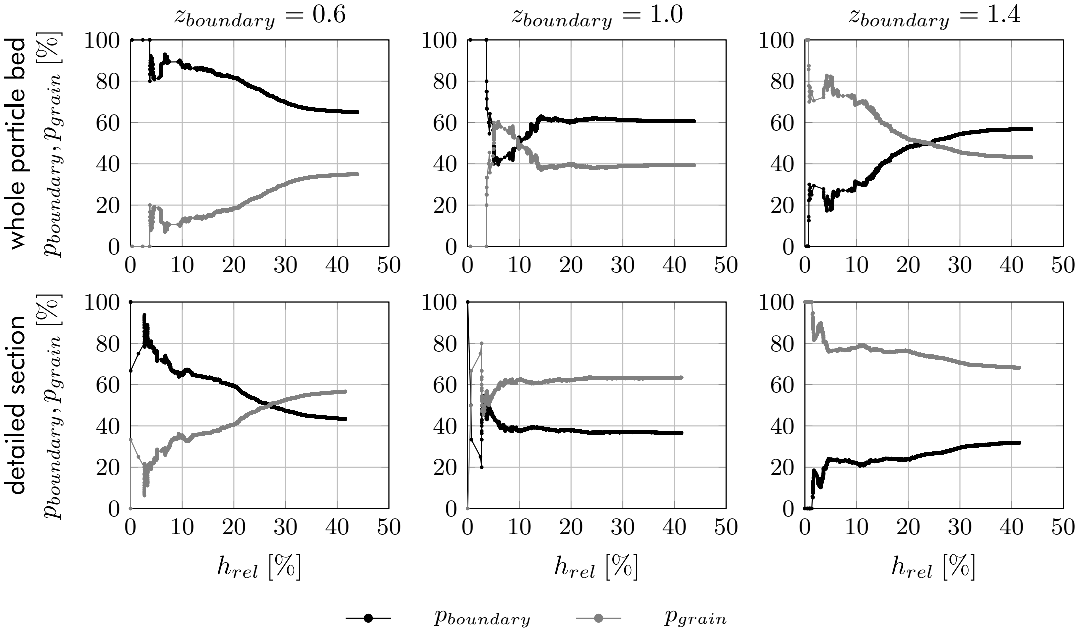

Fig. 4.62: Plots of time-depending fracture characteristics of the different particle bed simulations with different grain boundary factors.

Concerning the grain boundary factor, it can be seen that the simulations with weakened grain boundaries ($z_{boundary} = 0.6$) have generally a higher proportion of grain boundary breakage. However, as can be seen by the different plots in Figure 4.62 there is a significant influence of the relative stroke h_{rel} on the breakage characteristics. This shall exemplarily be explained for the results of the more detailed simulation.

First of all, the focus is set on the plot where no grain boundaries are existent on the physical level of the simulation ($z_{boundary} = 1.0$). This can be seen as reference, since it is interpreted as a simulation of homogeneous material. It can be seen, that the proportions of the intergranular and intragranular cracks line up at relative constant levels after a short period at the beginning. Subsequently, there are no significant changes in the fracture patterns.

This stabilization period can be seen in the plots with physically relevant grain boundaries ($z_{boundary} \neq 1.0$) as well. However, in contrast to the simulation with homogeneous material, there is no constancy of the fracture characteristics after the initial period.

Using the example of the weakened grain boundaries ($z_{boundary} = 0.6$), the curves are interpreted in such a way that the grain boundaries break more easily than the other bondings. Therefore, the proportion of intergranular breakage is still relatively high. However, since there is only a limited amount of grain boundary bondings existent in the simulation, their proportion on the breakage decreases as the simulation progresses. It is supposed that it converges to the overall proportion of grain boundary bondings in the system as the comminution continues until all bondings are broken.

The contrary characteristics can be seen if the grain boundaries are strengthened ($z_{boundary} = 1.4$). After the stabilization period, the amount of grain boundary breakage is lower than its proportion on the overall bondings. Nonetheless, due to the changes in the particle bed and due to the decreasing amount of existing breakable non-boundary bondings, its proportion increases steadily. Again, it is supposed that it would also converge to its overall proportion on the initial bondings, if the comminution simulation would be continued.

With regard to this time dependent behavior, it is concluded that a comparison between two particle bed simulations should always be done at comparable comminution conditions. Otherwise it should be noted that the fracture characteristics can change during comminution. Furthermore, this effect should always be seen in relation to the chosen resolution of the discrete elements and the resulting amount of breakable initial bondings. The presented results indicate that the overall appearance of the curves for different resolutions can vary significantly.

4.4.4 Conclusions on the particle bed test

Based on the results, it can be concluded, that the intended proof of concept for the synthetic microstructure was provided in the context of a more realistic mineral processing environment. It is shown, that it is in principle possible to transfer a realistic synthetic microstructure to a particle filling, which is later crushed in a DEM simulation with YADE in particle bed mode. However, the comparison of the simulation and the real experiment also demonstrates the limitations of the chosen test setup.

First of all, there are discrepancies in the particle bed characteristics of the real and the simulated experiment. Due to the restriction to two-dimensional microstructures, it is not possible to create a three-dimensional simulation, which fits exactly to the real spatial particle bed experiment. Hence, it is only possible, to compare both on a quantitative level to a limited extend. For this reason, the evaluation is focused on the analysis of the qualitative appearance of the fracture pattern.

Despite this, it is shown that the resolution of the discrete elements is crucial for a detailed comparison. With the two different simulation setups it is possible to simulate preferential breakage along grain boundaries as their strengths are reduced using the grain boundary factor $z_{boundary}$. Nevertheless, due to the resolution restrictions, it is for example not possible to simulate the shattering of grains without doubt. For doing so, the scale of the discrete elements has to be further decreased, which, however, increases the computation effort.

Howsoever, it should also be noted that it was not the intention of this second stage experiment to present an exact simulation of an arbitrary realistic comminution example, but to prove the principal applicability of the synthetic microstructure approach. The reader should be aware of the fact that both limitations can be overcome if necessary. The resolution of the discrete elements could simply be further increased without any more changes. Admittedly, in this case, one should keep in mind the computational effort for such an approach.

In order to match the dimensionality of the simulated and the real experiment, the synthetic microstructure approach has to be transferred to the third dimension. This is not done yet but clearly in the focus of the further research.

5 Conclusions and directions for future development

The objective of this study was to find a method to allow the use of realistic mineral microstructures in Discrete Element Method (DEM) simulations, on the basis of the Quantitative Microstructural Analysis (QMA). In particular, simulations of comminution applications were in the focus. Based on a comprehensive review of the current state of DEM simulations in mineral processing, it was found that there are no comparable approaches publicized in the literature yet. Hence, it was decided to restrict this initially study to the two-dimensional case, since the basic functionality of this approach must first be proven in a proof of concept study. For this, the restriction to the two-dimensional case facilitates the comparability and analyzability of the results, as two-dimensional data is more tangible and better to handle.

Based on these specifications, the QMA is adjusted to the needs of such a two-dimensional approach firstly. The results of this adapted QMA are then used as input parameters for a newly developed synthesis program, which can generate two-dimensional realistic microstructures. Both the adapted QMA and the synthesis algorithms are implemented in combination in a GUI-based python program. This means that all of the steps required to create a realistic two-dimensional microstructure can be performed in a single application. For this purpose, false-color images of real microstructures are used as input, and after doing the automated analysis and computer-assisted synthesis, false-color images of the realistic synthetic microstructure are exported for further use.

Subsequently, the applicability of this synthetic microstructure approach in general and the usability of these realistic two-dimensional twins of given real microstructures in particular, are analyzed in a two-staged proof of concept study using comparative experiments. For this purpose, a new indenter fracture test was developed, which allows to analyze the fracture behavior of real microstructures in a quasi-two-dimensional setup.

In the first stage of the study, the relatively isotropic, homogeneous, and middle to coarse grained granite from Meissen was used as test material. In this so-called basic indenter test, the fracture behavior of this material was compared in real experiment with the fracture simulation of the same test setup in the DEM environment YADE. Accordingly, for the simulation, the synthesized realistic twin microstructure of the granite was used as basis.

Considering that, a new approach for mapping microstructures to DEM environments was developed and successfully applied to these comparative experiments. Furthermore, in order to make real use of such a realistic microstructure inside the DEM environment, the grain boundary factor approach was introduced to YADE as well. In addition, it has been further developed so that the bondings between the different grains can be given particular characteristics. Based on this, it is in principle possible to model the microstructure with phase- or even grain-specific micromechanical properties.

This, however, would go beyond the scope of the proof of concept for the synthetic microstructure approach, as the parametrization of the micromechanical parameters at grain size level is still a challenge. Hence, the setup of the simulated granite microstructure was restricted to a more general, but comprehensible homogeneous material model. This can be seen as placeholder for future improvements in the analysis and parametrization of those micromechanical parameters.

Since first-stage investigations were consistently positive, the synthetic microstructure approach was subsequently tested with more complex side conditions in the second stage of the validation process. Within the first experiment of this second stage, it was therefore analyzed whether and how the synthetic microstructure approach can be applied to a more complex mineral material like the kb-ore from Freiberg. In contrast, in the second experiment, the synthetic microstructure approach was used in a particle bed experiment, which is a far more realistic application in mineral processing than the indenter test.

General conclusions for the synthetic microstructure approach. As the evaluation of the second stage is also positive, this is considered a confirmation for applicability of the synthetic microstructure approach. The shown examples prove that such realistic twins can be used as basis for sophisticated models and simulations of mineral processing applications at grain size level. The proposed approach can therefore be seen as an advantageous tool for improving the level of detail in DEM simulations.

Furthermore, the following general conclusions can be made, based on the present results:

- It is possible to synthesize a realistic two-dimensional microstructure on the basis of the QMA results of a given real mineral microstructure.
- The synthetic two-dimensional microstructure, in shape of a false-color image, can be imported to a DEM environment like YADE.
- Based on the imported false-color image, it is possible to map the microstructure onto a packing of discrete elements. The differences in the micromechanics between grains

and grain boundaries are imitated via the grain boundary approach in a Bonded Particle Model (BPM) in this process.

- The resulting model of the microstructure inside the DEM environment can be used to simulate fracture behavior and associated effects of randomly created, realistic microstructures at the grain size level, which, in this form is a novel for mineral processing applications.

Current limitations of synthetic microstructure approach. In summary it can be stated, that one of the main limitations of DEM in comminution science, the lack of microstructural realism inside the simulations, can be overcome with the synthetic microstructure approach. However, the experiments in the proof of concept study also revealed some interesting limitations, which have to be considered:

- Although the QMA has proven to be a powerful and appropriate analysis tool, further development is needed to allow more precise analysis of clusters inside mineral microstructures.

- Due to the limitation of the QMA in the analysis of clusters, their synthesis and mapping onto DEM simulations is only indirectly possible.

- The new level of detail of simulations, where the resolution limit is now below the grain sizes, requires proper micromechanical parametrization of the underlying models that characterize the bonding and interaction behavior of the discrete elements.

- Determining or measuring these micromechanical parameters is currently only possible to a very limited extent. This is because the understanding as well as the measuring and testing technology for this kind of micromechanics of mineral grains and their interfaces are still in their infancy.

Starting points for future developments. The conclusions presented provide also interesting starting points for future developments, which are outlined below:

- In order make full use of the synthetic microstructure approach, it is necessary to enhance it to the third dimension. For this purpose, the presented two-dimensional approach can be used as blueprint. The first step is seen to be the extension of the synthesis algorithms to create spatial objects, which should be a logical and straight forward task. For the analysis and evaluation of the synthesized spatial microstructures, one could resort to the original, three-dimensional QMA.

- The further development of the QMA, especially regarding the proper analysis of clusters, is seen to be an important point to further improve the qualities of this tool. This is furthermore considered a key step to simplify the synthesis of microstructures with clusters, which would greatly enhance the capabilities of this approach.

- As the computer assisted QMA is based on false-color images of the real microstructure, the automated generation of these on the basis of real thin or polished sections would be an important improvement as well. The manual false-color image creation, which was used in this study, is very time consuming and slows down the otherwise relatively fast synthesis process. For this task it is considered essential to use automated light microscopy that can autonomously scan thin or polished sections with different settings. In addition to polarization microscopy, other methods such as spectral analysis could also be used. Based on such a set of combined, multi-layered microstructure images, it should be possible to enhance the existing basic edge detecting algorithms and to create a program, which significantly assists the user in creating the false-color images.

- Although it can be seen as a trivial matter of course, the actual import of a synthesized microstructure to a given simulation environment is a critical step for the applicability of this approach. Without the ability to do this, the synthesized microstructures will be of little further use. Therefore, it has to be figured out how this can be adopted to the various other simulation environments. For this, the proposed procedure of mapping the microstructures on a given set of discrete elements in YADE, can be used as blueprint.

- Furthermore, in order to use the synthetic microstructure approach sensibly, the prerequisites for a reliable simulation at grain size must be created. This includes the measuring of the micromechanical properties and the correct parametrization inside the DEM models for the mineral phases. In addition, it is necessary to figure out how such a simulation can be speed up. For this, it is conceivable to use techniques like timestep scaling [81] or density scaling [191] for example. To do this, however, it must be ensured that the correctness of the simulation physics remains guaranteed. Besides that, it is also possible to use more computation efficient approaches like GPU based DEM for the simulation of fracture events at grain size level. Finding the best approach to allow physical correct simulations at grain size level with affordable computational effort is clearly a starting point for future developments.

Further possible fields of application. In addition, in the context of this conclusion, the presented synthetic microstructure approach shall finally be briefly reviewed in a more general context. As already stated, the presented results are seen to be proof that synthetic microstructures, which are synthesized with the help of the QMA, can successfully be used to provide realistic, mineralogical input parameters for the modeling of mineral microstructures in DEM. Moreover, it is also presented how this approach can be used to create and make use of such more detailed models at grain size level, by selective strengthening or weakening of selected bonds.

However, it should be noted that there is no intrinsic limitation, which restricts this approach to this specific application. Based on this train of thought, one can find other interesting applications in which synthetic microstructures could be used as well. Some promising ideas are highlighted exemplarily in the following. However, as mineral processing is a very wide area, this is done without the claim to completeness.

- The synthetic microstructures can basically be imported in any other simulation environment. Although the majority of the comminution simulations of minerals are currently conducted with the various types of DEM, also FEM approaches could make use of this additional parameters, in principle.

- The simulation of grain fracture of minerals can directly be used to enhance our understanding of selective comminution. With the proposed method, it should be possible to simulate the material characteristics, which if they are exploited by an appropriate combination of suitable comminution and separation processes are the basis for efficient selective comminution processing. Conversely, if the material characteristics and the micromechanical relations that make up the potential for the selective comminution are well-known and understood, such simulations can be used to find the best process characteristics to exploit this potential.

- Besides the focus on comminution tasks, one always should keep in mind, that the crushing and grinding of minerals is not done as an end in itself. In many cases its purpose is to either increase the specific surface of the particles or to liberate the valuable minerals to permit separation and further processing into concentrates. An important point for the latter case is the mineral liberation, which is often a mandatory requirement for the efficient production of valuables concentrates. Hence, much scientific effort is spent on this crucial point. However, at present, the corresponding models typically use rather abstract representations for the mineral microstructures. Further improvements are therefore considered possible, if realistic synthetic microstructures are used in this field of research as well.

- The introduction explained that the term mineral microstructure refers not only to natural rock, but also to other materials such as artificial stone, concrete or ceramics, which consist of minerals and mineraloid matter. Hence, although this study focused on mineral processing, it is obvious that the presented approach could also be used in principle for related fields of research. This can clearly be an application field for further projects.

Final comments on the presented synthesis approach. Finally, the proposed synthesis approach shall be evaluated in the context of the already existing simulation tools for mineral process design and optimization. By doing so, one has to admit that there is always the reasonable doubt, that the presented approach and the corresponding simulation is too complex and to computationally intensive for applied process and plant design and therefore has little or no influence on the real engineering. This criticism might be legitimate from the perspective of a project engineer who actually designs plants.

However, as outlined at the beginning, it is a matter of fact that various different computer-based modeling and simulation tools are already used for the very different tasks in the plant design and optimizing process. None of these, however, can simulate or model all processes at the greatest possible level of detail. In contrast, the used software of this toolbox represents a broad range, covering various size scales. This range goes from modeling the deposit on a geological scale, to modeling the design of the processing plant and individual processing machines, down to the scale of macro and micro processes. In combination, this can be seen as a multi-scale modeling and simulation approach, where each tool is optimized for a specific group of tasks.

The same could be possible in the future for DEM simulations. So it is conceivable, that existing plant process models, which are already used for plant design, are extended. For example, these systems, which typically use population balance approaches, could be equipped with interfaces that allow to embed subordinated simulations of particular single processes. Hence, the characteristic process parameters of the primary crushing process, which might take place in a jaw crusher, could be taken from such a lower level simulation. This sub-simulation in turn might be a DEM simulation that uses a Particle Replacement Model for fast, time-efficient simulation of the entire crushing process. This, however, does not care about the previous or subsequent processing of the material. The global input parameters, relevant to the simulation of the crusher, such as the mass flow and size distribution of the feed material, are then provided by the superordinate plant model.

In turn, intrinsic fracture parameters, like the breakage function or the degree of mineral liberation could be taken from another sub-simulation. For this, a Bonded Particle Models approach could be used to simulate the load and fracture behavior of single particles at grain size level. Based on the described logic of multi-scale approaches, the resulting process characteristics, for example concerning selective comminution or mineral liberation, could subsequently be used as input parameters for the superordinate simulation level and thus included in the general process design. Hence, the present study contributes to this approach by offering the possibility to use synthetic realistic minerals in order to perform proper fracture simulation at the grain size level for example.

6 References

[1] ABE, STEFFEN; DAVID PLACE, and PETER MORA. "A Parallel Implementation of the Lattice Solid Model for the Simulation of Rock Mechanics and Earthquake Dynamics". In: *Pure and Applied Geophysics* 161.11 (December 2004), pp. 2265–2277.

[2] ALDER, B. J. and T. E. WAINWRIGHT. "Phase Transition for a Hard Sphere System". In: *The Journal of Chemical Physics* 27.5 (1957), pp. 1208–1209. eprint: `http://dx.doi.org/10.1063/1.1743957`.

[3] ALLEN, M. P.; D. FRENKEL, and J. TALBOT. "Molecular dynamics simulation using hard particles". In: *Computer Physics Reports* 9.6 (1989), pp. 301–353.

[4] AMSTUTZ, G. C. and H. GIGER. "Stereological methods applied to mineralogy, petrology, mineral deposits and ceramics". In: *Journal of Microscopy* 95.1 (February 1972), pp. 145–164.

[5] ASBJÖRNSSON, GAUTI; ERIK HULTHÉN, and MAGNUS EVERTSSON. "Modelling and simulation of dynamic crushing plant behavior with MATLAB/Simulink". In: *Minerals Engineering* 43-44 (2013). SI: Comminution, pp. 112–120.

[6] AZIZ, J.-A. and K. SCHÖNERT. "Einzelkornzerkleinerung und Gutbettbeanspruchung von Zementklinker-Fraktionen". In: *Zement Kalk Gips* 33 (1980), pp. 213–218.

[7] BAILEY, C. et al. "What Can Go Wrong in Comminution Circuit Design?" In: *Proceedings of the Tenth Mill Operator's Conference* (October 12, 2009). Adelaide, 2009.

[8] BARRATT, DAEREK and ALEX DOLL. "Testwork Programs that Deliver Multiple Data Sets of Comminution Parameters for Use in Mine Planning and Project Engineering". In: *Proceedings of the Procemin 2008: V International Mineral Processing Seminar*. Procemin 2008 (October 22, 2008). Santiago, Chile, 2008.

[9] BARRIE, CRAIG D.; ALAN P. BOYLE, and DAVID J. PRIOR. "An analysis of the microstructures developed in experimentally deformed polycrystalline pyrite and minor sulphide phases using electron backscatter diffraction". In: *Journal of Structural Geology* 29.9 (2007), pp. 1494–1511.

[10] BARRIOS, GABRIEL K. P. and LUÍS MARCELO TAVARES. "A preliminary model of high pressure roll grinding using the discrete element method and multi-body dynamics coupling". In: *International Journal of Mineral Processing* 156 (2016). In Honor of Professor Heinrich Schubert on his 90th birthday, pp. 32–42.

[11] Baxter, G. William and R. P. Behringer. "Cellular automata models of granular flow". In: *Physical Review A* 42 (2 July 1990), pp. 1017–1020.

[12] Becker, Stephan et al. "Crack-seal microstructure evolution in bi-mineralic quartz-chlorite veins in shales and siltstones from the RWTH-1 well, Aachen, Germany". In: *Journal of Structural Geology* 33.4 (2016), pp. 676–689.

[13] Bessonov, Nikolai and Vitaly Volpert. "Deformable Cell Model of Tissue Growth". In: *Computation* 5.4 (2017).

[14] Bewick, R. P.; P. K. Kaiser, and W. F. Bawden. "DEM Simulation of Direct Shear: 2. Grain Boundary and Mineral Grain Strength Component Influence on Shear Rupture". In: *Rock Mechanics and Rock Engineering* 47 (2014), pp. 1673–1692.

[15] Bibak, Z. et al. "Investigation of Liner Shape Effects on Load Movement in Tumbling Mills by Discrete Element Method (DEM) - The Sarcheshmeh Copper Complex and Gol-E-Gohar Iron Ore Company SAG Mill Cases". In: *Proceedings of the XXVIII International Mineral Processing Congress*. 2016.

[16] Blaschke, R. "Spezifische Oberflächen und Grenzflächen der Mineralphasen als Gefügeparameter". In: *Fortschritte der Mineralogie* 47 (1970), pp. 197–241.

[17] Bons, P. D. "Development of crystal morphology during unitaxial growth in a progressively widening vein: I. The numerical model". In: *Journal of Structural Geology* 23.6 (2001), pp. 865–872.

[18] Brochot, S. et al. "Modeling and Simulations of Comminution Circuits with USIM PAC". In: *Advances in Comminution*. Ed. by Kawatra, S. Komar. Society for Mining, Metallurgy and Exploration, Inc., 2006. Chap. Part 5: Instrumentation, Modeling, and Simulation, pp. 481–493.

[19] Brochot, Stéphane et al. "USIM PAC 3.0: New Features for a Global Approach in Mineral Processing Design". In: *Proceedings of the APCOM 2002- Applications of Computers and Operations Research in the Minerals Industry*. 2002.

[20] Burtsev, S. V. and Ye. P. Kuzmin. "An efficient flood-filling algorithm". In: *Computers & Graphics* 17.5 (1993), pp. 549–561.

[21] Camp, Philip J. and Michael P. Allen. "Hard ellipsoid rod-plate mixtures: Onsager theory and computer simulations". In: *Physica A: Statistical Mechanics and its Applications* 229.3 (1996), pp. 410–427.

[22] Caram and Hong. "Random-walk approach to granular flows." eng. In: *Physical review letters* 67 (7 August 1991), pp. 828–831.

[23] Carnell, Rob. *lhs: Latin Hypercube Samples*. R package version 1.0.1. 2019.

[24] Cho, N.; C. D. Martin, and D. C. Sego. "A clumped particle model for rock". In: *International Journal of Rock Mechanics and Mining Sciences* 44.7 (October 2007), pp. 997–1010.

[25] Clark, Alex. *Pillow (PIL Fork) Documentation Release 5.2.0*. September 2018.

[26] CLEARY, P. W. “Recent Advances in DEM Modelling of Tumbling Mills”. In: *Minerals Engineering* 14.10 (2001), pp. 1295–1319.

[27] CLEARY, PAUL W. “Axial transport in dry ball mills”. In: *Applied Mathematical Modelling* 30.11 (2006). Selected papers from the Third International Conference on CFD in the Minerals and Process Industries, pp. 1343–1355.

[28] CLEARY, PAUL W. “DEM simulation of industrial particle flows: case studies of dragline excavators, mixing in tumblers and centrifugal mills”. In: *Powder Technology* 109.1 (2000), pp. 83–104.

[29] CLEARY, PAUL W. and PHIL OWEN. “Development of models relating charge shape and power draw to SAG mill operating parameters and their use in devising mill operating strategies to account for liner wear”. In: *Minerals Engineering* 117 (2018), pp. 42–62.

[30] CLEARY, PAUL W.; MATT SINNOTT, and ROB MORRISON. “Analysis of stirred mill performance using DEM simulation: Part 2 – Coherent flow structures, liner stress and wear, mixing and transport”. In: *Minerals Engineering* 19.15 (2006), pp. 1551–1572.

[31] CLEARY, PAUL W.; MATT SINNOTT, and ROB MORRISON. “Prediction of slurry transport in SAG mills using SPH fluid flow in a dynamic DEM based porous media”. In: *Minerals Engineering* 19.15 (2006), pp. 1517–1527.

[32] CLEARY, PAUL W. and MATTHEW D. SINNOTT. “Simulation of particle flows and breakage in crushers using DEM: Part 1 – Compression crushers”. In: *Minerals Engineering* 74 (2015), pp. 178–197.

[33] CLEARY, PAUL W. et al. “Smooth particle hydrodynamics: status and future potential”. In: *Progress in Computational Fluid Dynamics,* 7.2/3/4 (2007), pp. 70–90.

[34] COHEN, JACOB. “A Power Primer”. In: *Psychological Bulletin* 112.1 (1992), pp. 155–159.

[35] COHEN, JACOB. *Statistical Power Analysis for the Behavioral Sciences*. 2nd ed. Lawrence Erlbaum Associates, 1988.

[36] CUNDALL, P. A. “A computer model for simulating progressive, large-scale movements in blocky rock systems”. In: *Proc. Symp. Int. Rock Mech.* Vol. 2. 8. Nancy, 1971.

[37] CUNDALL, P. A. “Formulation of a Three-dimensional and Distinct Element Model - Part I. A Scheme to Detect and Represent Contacts in a System Composed of Many Polyhedral Blocks”. In: *International Journal of Rock Mechanics and Mining Sciences and Geomechanics Abstracts* 25 (1988), pp. 107–116.

[38] CUNDALL, P. A. and O. D. L. STRACK. “A discrete numerical model for granular assemblies”. In: *Géotechnique* 29.1 (1979), pp. 47–65.

[39] DANIEL, M.; G. LANE, and E. MCLEAN. "Efficiency, economics, energy and emissions – Emerging criteria for comminution circuit decision making". In: *Proceedings of XXV International Mineral Processing Congress* (October 6, 2010). Brisbane, Australia, 2010.

[40] DEHOFF, ROBERT T. *Quantitative microscopy*. Repr. Herndon, Va.: TechBooks, 1968. 422 pp.

[41] DELANEY, G. W. et al. "DEM modelling of non-spherical particle breakage and flow in an industrial scale cone crusher". In: *Minerals Engineering* (2015), pp. 112–122.

[42] DELANEY, GARY W. et al. "Novel application of DEM to modelling comminution processes". In: *IOP Conf. Series: Materials Science and Engineering 10*. 2010.

[43] DEM SOLUTIONS LTD. *EDEM*. Comp. software.

[44] DEVILLARD, PIERRE. "Scaling behaviour in size segregation ("Brazil Nuts")". In: *J. Phys. France* 51.5 (1990), pp. 369–373.

[45] DJORDJEVIC, N.; F. N. SHI, and R. D. MORRISON. "Applying discrete element modelling to vertical and horizontal shaft impact crushers". In: *Minerals Engineering* 16.10 (October 2003), pp. 983–991.

[46] DOLL, ALEX and DEREK BARRATT. "Grinding: Why So Many Tests?" In: *Proceedings of the 43rd Annual Meeting of the Canadian Mineral Processors*. Ottawa, 2001.

[47] DŽIUGYS, ALGIS and BERNHARD PETERS. "An approach to simulate the motion of spherical and non-spherical fuel particles in combustion chambers". In: *Granular Matter* 3.4 (December 2001), pp. 231–266.

[48] ERKAN, YAVUZ. "Ein Versuch zur quantitativen Erfassung der Festigkeitseigenschaften und zur quantitativen Charakterisierung der Granite". In: *Neues Jahrbuch fuer Mineralogie, Abhandlungen* 113.1 (1970), pp. 91–109.

[49] *Esys-Particle*. https://launchpad.net/esys-particle/. Comp. software.

[50] EXNER, HANS ECKART and HANS PAUL HOUGARDY. *Quantitative image analysis of microstructures: A practical guide to techniques, instrumentation and assessment of materials*. Oberursel: DGM Informationsgesellschaft, 1988. 235 pp.

[51] FANDRICH, ROLF et al. "Modern SEM-based mineral liberation analysis". In: *International Journal of Mineral Processing* 84 (2007), pp. 310–320.

[52] FAVIER, J. F. et al. "Shape representation of axi-symmetrical, non-spherical particles in discrete element simulation using multi-element model particles". In: *Engineering Computations* 16.4 (1999), pp. 467–480. eprint: `https://doi.org/10.1108/02644409910271894`.

[53] FLEISSNER, F. *Pasimodo v1.9.33, software package and template file*. Inpartik & ITM University of Stuttgart, comp. software. Tübingen, 2012.

[54] FOLGNER, T. and O. POPOV. “Charakterisierung der Festgesteine durch Anwendung der quantitativen Gefügeanalyse”. In: *Scientific Reports on Resource Issues*. Ed. by DREBENSTEDT, CARSTEN. Vol. 2. International University of Resources. 2010, pp. 33–49.

[55] FRAIGE, FERAS Y.; PAUL A. LANGSTON, and GEORGE Z. CHEN. “Distinct element modelling of cubic particle packing and flow”. In: *Powder Technology* 186.3 (2008), pp. 224–240.

[56] FRIES, L. et al. “DEM-CFD modeling of a fluidized bed spray granulator”. In: *Chemical Engineering Science* 66.11 (2011), pp. 2340–2355.

[57] FUERSTENAU, D. W. and A. Z. M. ABOUZEID. “The energy efficiency of ball milling in comminution”. In: *International Journal of Mineral Processing* 67 (2002), pp. 161–185.

[58] GASNIER, J.-B. et al. “3D Morphological modeling of a polycrystaline microstructure with non-convex, anisotropic grains”. In: *Proceedings of 14th International Congress for Stereology and Image Analysis*. Liege, 2015.

[59] GENÇ, Ö. “Optimization of an industrial scale open circuit three-compartment cement grinding ball mill with the aid of simulation”. In: *International Journal of Mineral Processing* 154 (2016), pp. 1–9.

[60] *GenGeo*. http://launchpad.net/esys-particle/gengeo. Comp. software.

[61] GLADKY, ANTON. “Numerische Untersuchung der Beanspruchung in Gutbettwalzenmühlen mit idealisierten Materialien”. German. Tag der Verleihung: Freiberg, den 13. Februar 2019. PhD thesis. Freiberg, 2019.

[62] GOVENDER, NICOLIN; DANIEL N. WILKE, and SCHALK KOK. “Blaze-DEMGPU: Modular high performance DEM framework for the GPU architecture”. In: *SoftwareX* 5 (2016), pp. 62–66.

[63] GOVENDER, NICOLIN; DANIEL N. WILKE, and SCHALK KOK. “Collision detection of convex polyhedra on the NVIDIA GPU architecture for the discrete element method”. In: *Applied Mathematics and Computation* 267 (2015). The Fourth European Seminar on Computing (ESCO 2014), pp. 810–829.

[64] GOVENDER, NICOLIN et al. “A study of shape non-uniformity and poly-dispersity in hopper discharge of spherical and polyhedral particle systems using the Blaze-DEM GPU code”. In: *Applied Mathematics and Computation* 319 (2018). Recent Advances in Computing, pp. 318–336.

[65] GOVENDER, NICOLIN et al. “Discrete element simulation of mill charge in 3D using the BLAZE-DEM GPU framework”. In: *Minerals Engineering* 79 (2015), pp. 152–168.

[66] GOVENDER, NICOLIN et al. “Hopper flow of irregularly shaped particles (non-convex polyhedra): GPU-based DEM simulation and experimental validation”. In: *Chemical Engineering Science* 188 (2018), pp. 34–51.

[67] GROH, U. et al. "Damage simulation of brittle heterogeneous materials at the grain size level". In: *Theoretical and Applied Fracture Mechanics* 55 (2011), pp. 31–38.

[68] GUO, NING and JIDONG ZHAO. "A coupled FEM/DEM approach for hierarchical multiscale modelling of granular media". In: *International Journal for Numerical Methods in Engineering* 99.11 (2014), pp. 789–818.

[69] GURLAND, J. "The Measurement of Grain Contiguity in two-Phase Alloys". In: *Transactions of the Metallurgical Society of AIME* (1958), pp. 452–453.

[70] *HAVER CPA 4-2 - Operating Instructions*. Version 1.2. Haver & Boecker. 2012.

[71] *Haver CpaServ - Manual*. Version 2.0.2. Haver & Boecker. June 29, 2016.

[72] HAZZARD, JAMES F. and R. PAUL YOUNG. "Micromechanical modeling of cracking and failure in brittle rocks". In: *Journal of Geophysical Research* 105.B7 (July 2000), pp. 16683–16697.

[73] HEINICKE, FELIX; HARALD GÜNTHER, and OLEG POPOV. "Mathematical-Petrographic Rock Characterization as Support for HPGR Sizing". In: *Proceedings of the SAG Conference*. Vancouver, 2015.

[74] HILDYARD, REBECCA C. et al. "Electron Backscatter Diffraction (EBSD) Analysis of Bassanite Transformation Textures and Crystal Structure Produced from Experimentally Deformed and Dehydrated Gypsum". In: *Journal of Petrology* 52.5 (2011), pp. 839–856.

[75] HILGERS, C. et al. "Development of crystal morphology during unitaxial growth in a progressively widening vein: II. Numerical simulations of the evolution of antitaxial fibrous veins". In: *Journal of Structural Geology* 23.6 (2001), pp. 873–885.

[76] HLUNGWANI, O. et al. "Further validation of DEM modeling of milling: effects of liner profile and mill speed". In: *Minerals Engineering* 16.10 (2003), pp. 993–998.

[77] HOGUE, CAROLINE and DAVID NEWLAND. "Efficient computer simulation of moving granular particles". In: *Powder Technology* 78.1 (1994), pp. 51–66.

[78] HOOMANS, B. P. B. et al. "Discrete particle simulation of bubble and slug formation in a two-dimensional gas-fluidised bed: A hard-sphere approach". In: *Chemical Engineering Science* 51.1 (1996), pp. 99–118.

[79] HOSSEININIA, EHSAN SEYEDI. "Discrete element modeling of inherently anisotropic granular assemblies with polygonal particles". In: *Particuology* 10.5 (2012), pp. 542–552.

[80] HUANG, YRJÖ JUN et al. "An Introduction to Discrete Element Method: A Meso-scale Mechanism Analysis of Granular Flow". In: *Journal of Dispersion Science and Technology* 36.10 (2015), pp. 1370–1377. eprint: `https://doi.org/10.1080/01932691.2014.984304`.

[81] ITASCA CONSULTING GROUP INC. *PFC — Particle Flow Code, Ver. 5.0*. Itasca. Comp. software. Minneapolis, 2014.

[82] IVARS, DIEGO MAS. “Bonded particle model for jointed rock mass”. PhD thesis. Royal Institute of Technology, Stockholm, 2010.

[83] IVARS, DIEGO MAS et al. “The Smooth-Joint Contact Model”. In: *8th. World Congress on Computational Mechanics / 5th. European Congress on Computational Methods in Applied Sciences and Engineering*. 2008.

[84] IVARS, DIEGO MAS et al. “The synthetic rock mass approach for jointed rock mass modelling”. In: *International Journal of Rock Mechanics and Mining Sciences* 48.2 (February 2011), pp. 219–244.

[85] JAJCEVIC, DALIBOR et al. “Large-scale CFD-DEM simulations of fluidized granular systems”. In: *Chemical Engineering Science* 98 (2013), pp. 298–310.

[86] JAYASUNDARA, C. T. et al. “Discrete particle simulation of particle flow in IsaMill-Effect of grinding medium properties”. English. In: *Chemical Engineering Journal* 135.1-2 (2008), pp. 103–112.

[87] JAYASUNDARA, C. T. et al. “Discrete particle simulation of particle flow in the IsaMill process”. English. In: *Industrial and Engineering Chemistry Research* 45.18 (2006), pp. 6349–6359.

[88] JAYASUNDARA, C. T. et al. “Effect of slurry properties on particle motion in IsaMills”. English. In: *Minerals Engineering* 22.11 (2009), pp. 886–892.

[89] JAYASUNDARA, C. T. et al. “Effects of disc rotation speed and media loading on particle flow and grinding performance in a horizontal stirred mill”. English. In: *International Journal of Mineral Processing* 96.1-4 (2010), pp. 27–35.

[90] JAYASUNDARA, C. T. et al. “Prediction of the disc wear in a model IsaMill and its effect on the flow of grinding media”. English. In: *Minerals Engineering* 24.14 (2011), pp. 1586–1594.

[91] JIMÉNEZ-HERRERA, NARCÉS; GABRIEL K. P. BARRIOS, and LUÍS MARCELO TAVARES. “Comparison of breakage models in DEM in simulating impact on particle beds”. In: *Advanced Powder Technology* 29.3 (2018), pp. 692–706.

[92] JONES, M. P. and J. L. SHAW. “Automatic measurement and stereological assessment of mineral data for use in mineral technology”. In: *Proceedings of the Xth International Minerals Processing Congress*. 1973, pp. 737–756.

[93] KHOSHNAM, FATEMEH et al. “Development of a Dynamic Population Balance Plant Simulator for Mineral Processing Circuits”. In: *International Journal of Mining and Geo-Engineering* 49.1 (June 2015), pp. 143–153.

[94] KING, RONALD PETER and CLÃÍUDIO LUIZ SCHNEIDER. *Modeling and Simulation of Mineral Processing Systems*. 2nd ed. Englewood, Colo.: Society for Mining Metallurgy and Exploration, 2012. 480 pp.

[95] KIRSCH, DENNY. “Untersuchungen zur Selbstähnlichkeit bei der Einzelpartikeldruckzerkleinerung”. MA thesis. Technische Universität Bergakademie Freiberg, 2016.

[96] KLICHOWICZ, MICHAEL and HOLGER LIEBERWIRTH. “Modeling of Realistic Mineral Microstructures as Key Factor for Comminution Simulations”. In: *Proceedings of the XXVIII International Mineral Processing Congress*. 2016.

[97] KLOSS, CHRISTOPH et al. “Models, algorithms and validation for opensource DEM and CFD-DEM”. In: *Progress in Computational Fluid Dynamics, an International Journal* 12.2-3 (2012), pp. 140–152. eprint: `https://www.inderscienceonline.com/doi/pdf/10.1504/PCFD.2012.047457`.

[98] KORNILOVSKY, A. N.; D. R. KINGDON, and A. A. HARMS. “On the dynamics of fuel pellets in suspension”. In: *Annals of Nuclear Energy* 23.3 (1996), pp. 171–182.

[99] KUMARAN, V. “Velocity distribution function for a dilute granular material in shear flow”. In: *Journal of Fluid Mechanics* 340 (1997), pp. 319–341.

[100] KÜPPERS, HORST. “The initial course of crack velocity in glass plates”. In: *International Journal of Fracture Mechanics* 3.1 (March 1967), pp. 13–17.

[101] KURZYDŁOWSKI, KRZYSZTOF JAN and BRIAN RALPH. *The Quantitative description of the microstructure of materials*. CRC Press, 1995. 418 pp.

[102] LANGE, STEPHAN and ROBIN HILLMANN. “Automatic detection of grain boundaries and mineral phases in thin sections of minerals”. Project Thesis. TU Bergakademie Freiberg, 2017.

[103] LAZAR, EMANUEL A. et al. “A more accurate three-dimensional grain growth algorithm”. In: *Acta Materialia* 59 (2011), pp. 6837–6847.

[104] LEEDER, OTTO and HANS-JOACHIM BLANKENBURG. *Polarisationsmikroskopie: Mit 16 Tabellen*. First. Leipzig: Dt. Verl. für Grundstoffindustrie, 1989. 102 pp.

[105] LI, XU-DONG. “Visualized simulation and modularized architecture of microstructures for composite materials”. In: *Composite Interfaces* 12.3-4 (2005), pp. 291–309.

[106] LI, HAIJIE et al. “Dynamic modeling and simulation of a SAG mill-pebble crusher circuit by controlling crusher operational parameters”. In: *Minerals Engineering* 127 (2018), pp. 98–104.

[107] LI, JUN; HEINZ KONIETZKY, and THOMAS FRÜHWIRT. “Voronoi-Based DEM Simulation Approach for Sandstone Considering Grain Structure and Pore Size”. In: *Rock Mechanics and Rock Engineering* 50.10 (October 2017), pp. 2749–2761.

[108] LIN, C. L. and J. D. MILLER. “Cone beam X-ray microtomography for three-dimensional liberation analysis in the 21st century”. In: *International Journal of Mineral Processing* 47 (1996), pp. 61–73.

[109] LIN, X. and T.-T. NG. “A three-dimensional discrete element model using arrays of ellipsoids”. In: *Géotechnique* 47.2 (1997), pp. 319–329. eprint: `https://doi.org/10.1680/geot.1997.47.2.319`.

[110] LIN, XIAOSHAN and TANG-TAT NG. “Contact detection algorithms for three-dimensional ellipsoids in discrete element modelling”. In: *International Journal for Numerical and Analytical Methods in Geomechanics* 19.9 (1995), pp. 653–659.

[111] LUBACHEVSKY, BORIS D. “How to Simulate Billiards and Similar Systems”. In: *Journal of Computational Physics* 94.2 (May 1991), pp. 255–283.

[112] LUBACHEVSKY, BORIS D.; VLADIMIR PRIVMAN, and SUBHAS C. ROY. “Casting Pearls Ballistically: Efficient Massively Parallel Simulation of Particle Deposition”. In: *Journal of Computational Physics* 126.1 (1996), pp. 152–164.

[113] LUDING, S. et al. “Simulations of Dense Granular Flow: Dynamic Arches and Spin Organization”. In: *J. Phys. I France* 6.6 (1996), pp. 823–836.

[114] LUDING, STEFAN. “Introduction to discrete element methods”. In: *European Journal of Environmental and Civil Engineering* 12.7-8 (2008), pp. 785–826. eprint: `https://doi.org/10.1080/19648189.2008.9693050`.

[115] LUDING, STEFAN and SEAN MCNAMARA. “How to handle the inelastic collapse of a dissipative hard-sphere gas with the TC model”. In: *Granular Matter* 1.3 (December 1998), pp. 113–128.

[116] LUNGFIEL, ANDRÉ. “Ermittlung von Belastungsgrößen mittels der Diskrete-Elemente-Methode für die Auslegung von Sturzmühlen”. PhD thesis. Technischen Universität Bergakademie Freiberg, 2002.

[117] MARÍN, MAURICIO. “Event-driven hard-particle molecular dynamics using bulk-synchronous parallelism”. In: *Computer Physics Communications* 102.1 (1997), pp. 81–96.

[118] MARTIN, DEREK. “The effect of cohesion loss and stress path on brittle rock strength”. In: *Canadian Geotechnical Journal* 34.5 (1997), pp. 698–725.

[119] MAYANK, K. et al. “Coupled DEM-CFD Model to Predict the Tumbling Mill Dynamics”. In: *Procedia IUTAM* 15 (2015). IUTAM Symposium on Multiphase Flows with Phase Change: Challenges and Opportunities, pp. 139–149.

[120] MCNAMARA and YOUNG. “Inelastic collapse in two dimensions”. eng. In: *Physical review. E, Statistical physics, plasmas, fluids, and related interdisciplinary topics* 50 (1 July 1994), R28–R31.

[121] MEGURO, KIMIRO and MOTOHIKO HAKUNO. “Fracture Analysis of Concrete Structures by the Modified Distinct Element Method”. In: *Structural Engineering / Earthquake Engineering* (1989), pp. 113–124.

[122] MILLER, J. D. and C. L. LIN. “Three-dimensional analysis of particulates in mineral processing systems by cone beam X-ray microtomography”. In: *Minerals & Metallurgical Processing* 21.3 (2004), pp. 113–124.

[123] MILLER, S. and S. LUDING. “Cluster growth in two- and three-dimensional granular gases”. In: *Physical Review* 69.3 (March 2004), p. 031305. eprint: `cond-mat/0304637`.

[124] MILLER, STEAFAN. "Clusterbildung in granularen Gasen". PhD thesis. Universität Stuttgart, 2004.

[125] MIRGHASEMI, A. A.; L. ROTHENBURG, and E. L. MATYAS. "Numerical simulations of assemblies of two-dimensional polygon-shaped particles and effects of confining pressure on shear strength". In: *Soils and Foundations* 37.3 (1997), pp. 43–52.

[126] MONAGHAN, J. J. "Smoothed particle hydrodynamics". In: *Ann. Rev. Astron. Astrophys.* 30 (1992), pp. 543–574.

[127] MOORE, G. E. "Cramming more components onto integrated circuits". In: *IEEE Solid-State Circuits Society Newsletter* 11.3 (September 1965). Reprinted from Electronics, pp. 33–35.

[128] MORRISON, ROB D.; PAUL W. CLEARY, and MATTHEW D. SINNOTT. "Using DEM to compare the energy efficiency of pilot scale ball and tower mills". In: *Minerals Engineering* 22.7 (2009). Special issue: Comminution, pp. 665–672.

[129] MÜLLER, HERMANN. *Die Erzgänge des Freiberger Bergrevieres.* German. Erläuterungen zur geologischen Specialkarte des Königreichs Sachsen. Leipzig: Engelmann, 1901.

[130] NASSAUER, BENJAMIN. "Entwicklung einer 3D Diskrete Elemente Methode mit polyederförmigen Partikeln zur Simulation der fluidgekoppelten Prozesse beim Drahtsägen". German. PhD thesis. Freiberg: Zugl.: Freiberg (Sachsen), Techn. Univ. Bergakad., Diss., 2015, 2015.

[131] NAUDÉ, GRETHE et al. "The use of X-ray computed tomography in the characterisation of coal and associated char reductants". In: *Minerals Engineering* 52 (2013), pp. 143–154.

[132] NIKONOW, W. and D. RAMMLMAIR. "Automated mineralogy based on micro-energy-dispersive X-ray fluorescence microscopy (μ-EDXRF) applied to plutonic rock thin sections in comparison to a mineral liberation analyzer". In: *Geoscientific Instrumentation, Methods and Data Systems* 6.2 (2017), pp. 429–437.

[133] NIKONOW, WILHELM and DIETER RAMMLMAIR. "Risk and benefit of diffraction in Energy Dispersive X-ray fluorescence mapping". In: *Spectrochimica Acta Part B: Atomic Spectroscopy* 125 (November 2016), pp. 120–126.

[134] NORGATE, TERRY and SHARIF JAHANSHAHI. "Reducing the greenhouse gas footprint of primary metal production: Where should the focus be?" In: *Minerals Engineering* 24.14 (2011), pp. 1563–1570.

[135] *Darstellung von Korn(Teilchen-)größenverteilungen - Logarithmisches Normalverteilungsnetz*. Norm. March 1974.

[136] *Prüfverfahren für Naturstein – Bestimmung der einachsigen Druckfestigkeit; Deutsche Fassung EN 1926:2006*. Norm. 2007.

[137] *Darstellung der Ergebnisse von Partikelgrößenanalysen – Teil 2: Berechnung von mittleren Partikelgrößen/-durchmessern und Momenten aus Partikelgrößenverteilungen (ISO 9276-2:2001)*. Norm. February 2006.

[138] OHSER, J. and U. LORZ. "Quantitative Gefügeanalyse - Theoretische Grundlagen und Anwendung". In: *Freiberger Forschungshefte*. Ed. by TU BERGAKADEMIE FREIBERG, DER REKTOR der. Vol. B 276. Deutscher Verlag für Grundstoffindustrie GmbH, 1994.

[139] OWEN, PHIL and PAUL W. CLEARY. "The relationship between charge shape characteristics and fill level and lifter height for a SAG mill". In: *Minerals Engineering* 83 (2015), pp. 19–32.

[140] *Paris Agreement*. United Nations Treaty Collection, Chapter XXVII 7. d. December 12, 2015.

[141] PATZELT, WALTER J. *Polarisationsmikroskopie: Grundlagen, Instrumente, Anwendungen*. 2nd ed. Wetzlar: Leitz, 1985. 102 pp.

[142] PEÑA, A. A.; R. GARCÍA-ROJO, and H. J. HERRMANN. "Influence of particle shape on sheared dense granular media". In: *Granular Matter* 9.3 (June 2007), pp. 279–291.

[143] PERRAM, J. W. et al. "Monte Carlo simulation of hard spheroids". In: *Chemical Physics Letters* 105.3 (1984), pp. 277–280.

[144] PERRAM, JOHN W. and M. S. WERTHEIM. "Statistical mechanics of hard ellipsoids. I. Overlap algorithm and the contact function". In: *Journal of Computational Physics* 58.3 (1985), pp. 409–416.

[145] PODLOZHNYUK, ALEXANDER; STEFAN PIRKER, and CHRISTOPH KLOSS. "Efficient implementation of superquadric particles in Discrete Element Method within an open-source framework". In: *Computational Particle Mechanics* 4.1 (January 2017), pp. 101–118.

[146] POPOV, OLEG. "Beitrag zur mathematisch-petrographischen Gefügecharakterisierung für die Beurteilung der Festgesteine hinsichtlich ihrer Aufbereitung und ihrer Produkteigenschaften". PhD thesis. Technischen Universität Bergakademie Freiberg, July 2007.

[147] POPOV, OLEG; HOLGER LIEBERWIRTH, and THOMAS FOLGNER. "Properties and system parameters - Quantitative characterization of rock to predict the influence of the rock on relevant product properties and system parameters - Part 1: Application of quantitative microstructural analysis". In: *AT Mineral Processing* 55 (July 2014), pp. 76–88.

[148] POPOV, OLEG; HOLGER LIEBERWIRTH, and THOMAS FOLGNER. "Properties and system parameters - Quantitative characterization of rock to predict the influence of the rock on relevant product properties and system parameters - Part 2: Selected examples". In: *AT Mineral Processing* 55 (October 2014), pp. 54–63.

[149] POTYONDY, D. O. and P. A. CUNDALL. "A bonded-particle model for rock". In: *International Journal of Rock Mechanics and Mining Sciences* 41.8 (December 2004), pp. 1329–1364.

[150] POTYONDY, D. O.; P. A. CUNDALL, and C. A. LEE. "Modelling rock using bonded assemblies of circular particles". In: *Rock Mechanics: Tools and techniques*. 2nd North American Rock Mechanics Symposium: NARMS '96 (June 19, 1996). Ed. by AUBERTIN, M.; F. HASSANI, and H. MITRI. Vol. 2. ISRM. Rotterdam: A.A. Balkema, 1996, pp. 1937–1944.

[151] POWELL, M. S. "The effect of liner design on the motion of the outer grinding elements in a rotary mill". In: *International Journal of Mineral Processing* 31.3 (1991), pp. 163–193.

[152] POWELL, M. S. and L. A. VERMEULEN. "The influence of liner design on the rate of production of fines in a rotary mill". In: *Minerals Engineering* 7.2 (1994), pp. 169–183.

[153] POWELL, MALCOLM S. "A study of charge motion in rotary mills, with particular reference to the grinding action". PhD thesis. University of Cape Town, 1993.

[154] POWELL, MALCOLM S. "The effect of liner design upon charge motion in a rotary mill". MA thesis. University of Cape Town, 1988.

[155] POWELL, MALCOM S. "The design of rotary-mill liners and their and backing materials". In: *Journal of the South African Institute of Mining and Metallurgy* 91.2 (1991), pp. 63–75.

[156] *Produktdatenblatt TIEDE®AP-11 / AP-21 Fluoreszierende Eindringmittel*. Magnaflux GmbH, 2011.

[157] QUIST, JOHANNES. "Cone Crusher Modelling and Simulation. Development of a virtual rock crushing environment based on the discrete element method with industrial scale experiments for validation". Master of Science Thesis. Chalmers University of Technology, 2012.

[158] R CORE TEAM. *R: A Language and Environment for Statistical Computing*. R Foundation for Statistical Computing. Vienna, Austria, 2017.

[159] RAABE, DIERK. "Introduction of a scalable three-dimensional cellular automaton with a probabilistic switching rule for the discrete mesoscale simulation of recrystallization phenomena". In: *Philosophical Magazine A* 79.10 (1999).

[160] RADJAÏ, FARHANG. *Discrete-element modeling of granular materials*. Formerly CIP Uk. - Includes bibliographical references and index. Oxford: ISTE, 2011. 425 pp.

[161] RANDLE, VALERIE. "Electron backscatter diffraction: Strategies for reliable data acquisition and processing". In: *Materials Characterization* 60.9 (2009), pp. 913–922.

[162] RAPAPORT, D. C. "The event scheduling problem in molecular dynamic simulation". In: *Journal of Computational Physics* 34.2 (1980), pp. 184–201.

[163] RICHARDS, JOHN ALAN and XIUPING JIA. *Remote sensing digital image analysis: an introduction*. English. 3rd ed. Berlin; Heidelberg u.a.: Springer, 1999.

[164] ROBINSON, MARTIN; MARCO RAMAIOLI, and STEFAN LUDING. "Fluid-particle flow simulations using two-way-coupled mesoscale SPH-DEM and validation". In: *International Journal of Multiphase Flow* 59 (2014), pp. 121–134.

[165] ROSATO et al. "Why the Brazil nuts are on top: Size segregation of particulate matter by shaking". eng. In: *Physical review letters* 58 (10 March 1987), pp. 1038–1040.

[166] ROSSUM, GUIDO van. *The Python Language Reference Release 3.4.2*. October 2014.

[167] RUMPF, H. and F. EBERT. "Darstellung von Kornverteilungen und Berechnung der spezifischen Oberfläche". In: *Chemie Ingenieur Technik* 36 (5 1964), pp. 523–537.

[168] SADD, MARTIN H.; QIMING TAI, and ARUN SHUKLA. "Contact law effects on wave propagation in particulate materials using distinct element modeling". In: *International Journal of Non-Linear Mechanics* 28.2 (1993), pp. 251–265.

[169] SAEIDI, FATEMEH. "New Approach for Characterising a Breakage Event as a Multistage Process". PhD thesis. The University of Queensland, 2016.

[170] SALTYKOV, S. A. *Stereometrische Metallographie*. Ed. by ECKSTEIN, HANS-JOACHIM. Trans. by RICHLING, W. and H. L. STEYER. First. VEB Deutscher Verlag für Grundstoffindustrie, 1974.

[171] SCHÄFER, BENJAMIN CARRIÓN; STEVEN F. QUIGLEY, and ANDREW H. C. CHAN. "Acceleration of the Discrete Element Method (DEM) on a reconfigurable coprocessor". In: *Computers & Structures* 82.20 (2004), pp. 1707–1718.

[172] SCHNEIDER, BENJAMIN J. "Polygonale diskrete Elemente zur Modellierung heterogener Materialien". PhD thesis. Universität Stuttgart, 2012.

[173] SCHOLTÈS, LUC and FRÉDÉRIC-VICTOR DONZÉ. "A DEM model for soft and hard rocks: Role of grain interlocking on strength". In: *Journal of the Mechanics and Physics of Solids* 61 (2013), pp. 352–369.

[174] SCHÖNFELD, PATRICK. "Untersuchungen zur Selbstähnlichkeit bei der Gutbettzerkleinerung". MA thesis. TU Bergakademie Freiberg, 2018.

[175] SCHRADER, LISA. "Untersuchung numerischer Zerkleinerungsmodelle anhand der Simulation eines Backenbrechers". MA thesis. TU Bergakademie Freiberg, 2014.

[176] SCHREIBER, SABINE. "Beitrag zur quantitativen Gesteinscharakterisierung zur Beurteilung von Gesteinen hinsichtlich ihrer Festigkeit". PhD thesis. Technische Universität Bergakademie Freiberg, 2018.

[177] SCHUBERT, HEINRICH. *Aufbereitung fester mineralischer Rohstoffe*. Vol. I. VEB Deutscher Verlag für Grundstoffindustrie, Leipzig, 1988.

[178] Schwarz, S. and J. Richardson. “Modelling and simulation of mineral processing circuits using JKSimMet and JKSimFloat”. In: *Proceedings of the SME Annual Meeting & Exhibit (SME 2013) and CMA 115th National Western Mining Conference* (February 22, 2013). Denver, CO, United States, 2013.

[179] Schwarz, S.; W. J. Whiten, and M. C. Harris. “JKSimFloat V6: improving flotation circuit performance and understanding”. In: *Proceedings of the XXIII International Mineral Processing Congress*. Istanbul, Turkey, September 2006, pp. 1717–1722.

[180] Schwarz, Sarah and Dan Alexander. “Optimisation of flotation circuits through simulation using JKSimFloat”. In: *Proceedings of the 33rd International Symposium on the Application of Computers and Operations Research in the Minerals Industry (APACOM)* (April 24, 2007). Santiago, Chile: Gecamin Ltd, 2007, pp. 461–466.

[181] Schwechten, Dieter. “Trocken- und Naßmahlung spröder Materialien in der Gutbett-Walzenmühle”. PhD thesis. TU Clausthal, 1987.

[182] Sebastian, Ulrich. *Die Geologie des Erzgebirges*. German. Berlin; Heidelberg: Springer Spektrum, 2013.

[183] Shi, Chong et al. “Discrete element cluster modeling of complex mesoscopic particles for use with the particle flow code method”. In: *Granular Matter* 17.3 (June 2015), pp. 377–387.

[184] *Sicherheitsdatenblatt Tiede®AP-11*. Version 4. ITW Tiede NDT GmbH, April 12, 2011.

[185] Siebertz, Karl; David van Bebber, and Thomas Hochkirchen. *Statistische Versuchsplanung*. Springer Heidelberg Dordrecht London New York, 2010.

[186] Sinnott, M. D.; P. W. Cleary, and R. D. Morrison. “Combined DEM and SPH simulation of overflow ball mill discharge and trommel flow”. In: *Minerals Engineering* 108 (2017), pp. 93–108.

[187] Sinnott, Matt; Paul W. Cleary, and Rob Morrison. “Analysis of stirred mill performance using DEM simulation: Part 1 – Media motion, energy consumption and collisional environment”. In: *Minerals Engineering* 19.15 (2006), pp. 1537–1550.

[188] Sinnott, Matt; Paul W. Cleary, and Rob D. Morrison. “Slurry flow in a tower mill”. In: *Minerals Engineering* 24.2 (2011), pp. 152–159.

[189] Sinnott, Matthew D. and Paul W. Cleary. “Simulation of particle flows and breakage in crushers using DEM: Part 2 – Impact crushers”. In: *Minerals Engineering* 74 (2015), pp. 163–177.

[190] Sinnott, Matthew D.; Paul W. Cleary, and Rob D. Morrison. “Is media shape important for grinding performance in stirred mills?” In: *Minerals Engineering* 24.2 (2011), pp. 138–151.

[191] Smilauer, Vaclav et al. *The Yade Project*. 2nd ed. 2015.

[192] Šmilauer, Václav. "Cohesive Particle Model using the Discrete Element Method on the Yade Platform". HAL Id: tel-00502402. PhD thesis. Université de Grenoble; Czech Technical University in Prague, 2010.

[193] Söderman, P. et al. "Modelling the new LKAB and Kiruna concentrator with and USIM PAC". In: *International Journal of Mineral Processing* 44-45 (1996), pp. 223–235.

[194] Soltanbeigi, Behzad et al. "Comparison of multi-sphere and superquadric particle representation for modelling shearing and flow characteristics of granular assemblies". In: *EPJ Web Conf.* 140 (2017), p. 06015.

[195] Soltanbeigi, Behzad et al. "DEM study of mechanical characteristics of multi-spherical and superquadric particles at micro and macro scales". In: *Powder Technology* 329 (2018), pp. 288–303.

[196] Starkey, J. H. "A critical review of grinding design procedures for the 21st century". In: *Proceedings of the Comminution '01*. March 2001.

[197] Starkey, John; Sami Hindstrom, and George Nadasdy. "SAGDesign Testing - What is it and why it works". In: *Proceedings SAG*. Vol. IV. Vancouver: Department of Mining and Engineering University of British Columbia, 2006, pp. 240–254.

[198] Stiess, Matthias. *Mechanische Verfahrenstechnik-Partikeltechnologie 1*. 3rd ed. Springer-Verlag, 2009.

[199] Stránský, J. and M. Jirásek. "Open-Source FEM-DEM Coupling". In: *Proceedings of the 18th International Conference of Engineering Mechanics*. May 14, 2012, pp. 1237–1251.

[200] Tan, Xin; Heinz Konietzky, and Wei Chen. "Numerical Simulation of Heterogeneous Rock Using Discrete Element Model Based on Digital Image Processing". In: *Rock Mechanics and Rock Engineering* 49.12 (December 2016), pp. 4957–4964.

[201] Tan, Yuanqiang; Dongmin Yang, and Yong Sheng. "Discrete element method (DEM) modeling of fracture and damage in the machining process of polycrystalline SiC". In: *Journal of the European Ceramic Society* 29 (2009), pp. 1029–1037.

[202] Tano, Kent T. et al. "The Use of Process Simulation Methodology in Process Design Where Time and Performance Are Critical". In: *Advances in Comminution*. Ed. by Kawatra, S. Komar. Society for Mining, Metallurgy and Exploration, Inc., 2006. Chap. Part 5: Instrumentation, Modeling, and Simulation, pp. 495–511.

[203] Tavares, Luiz and Homero Delboni. "Modelling and Simulation of the Santa Rita Mine Milling Circuit". In: *Rem: Rev. Esc. Minas* 69.2 (April 2016).

[204] Teuscher, E. O. "Methodisches zur quantitativen Strukturgliederung körniger Gesteine". In: *Zeitschrift für Kristallographie, Mineralogie und Petrographie* 44.5 (September 1933), pp. 410–421.

[205] THYSE, E. L. et al. “3D insights into nickel converter matte phases: Direct observations via TEM and FIB SEM tomography”. In: *Minerals Engineering* 52 (2013), pp. 2–7.

[206] TICHÝ, RICHARD. “Beitrag zur numerischen Untersuchung der Bewegungs- und Beanspruchungsprofilen in einer Kugelmühle unter Verwendung von physikalisch begründeten Stoßparametern”. PhD thesis. Technischen Universität Bergakademie Freiberg, 2010.

[207] TING, JOHN M. et al. “An ellipse-based discrete element model for granular materials”. In: *International Journal for Numerical and Analytical Methods in Geomechanics* 17 (1993).

[208] TROMANS, DESMOND. “Crack Propagation in Brittle Materials: Relevance to Minerals Comminution”. In: *International Journal of Recent Research and Applied Studies* (2 November 2012), pp. 406–427.

[209] TSUJI, TAKUYA; KEIZO YABUMOTO, and TOSHITSUGU TANAKA. “Spontaneous structures in three-dimensional bubbling gas-fluidized bed by parallel DEM-CFD coupling simulation”. In: *Powder Technology* 184.2 (2008), pp. 132–140.

[210] UNLAND, GEORG and VICTOR RAAZ. “Formale Charakterisierung der Gesteine - ein Beitrag aus Sicht des Maschinenbaus”. In: *Zeitschrift für Geologische Wissenschaften* 26.3/4 (1998), pp. 315–328.

[211] VARAS, A. E. CARLOS; E. A. J. F. PETERS, and J. A. M. KUIPERS. “CFD-DEM simulations and experimental validation of clustering phenomena and riser hydrodynamics”. In: *Chemical Engineering Science* 169 (2017), pp. 246–258.

[212] VIDELA, A. R. and C. L. LINAND J. D. MILLER. “3D characterization of individual multiphase particles in packed particle beds by X-ray microtomography (XMT)”. In: *International Journal of Mineral Processing* 84 (2007), pp. 321–326.

[213] VIDELA, ALVARO; CHEN-LUH LIN, and JAN D. MILLER. “Watershed Functions Applied to a 3D Image Segmentation Problem for the Analysis of Packed Particle Beds”. In: *Particle & Particle Systems Characterization* 23 (2006), pp. 237–245.

[214] VIRTANEN, PAULI et al. *SciPy 1.0 – Fundamental Algorithms for Scientific Computing in Python*. 2019. arXiv: `1907.10121 [cs.MS]`.

[215] WALES, DAVID J. and JONATHAN P. K. DOYE. “Global Optimization by Basin-Hopping and the Lowest Energy Structures of Lennard-Jones Clusters Containing up to 110 Atoms”. In: *The Journal of Physical Chemistry A* 101.28 (1997), pp. 5111–5116. eprint: `https://doi.org/10.1021/jp970984n`.

[216] WANG, YUANNIAN and FULVIO TONON. “Modeling Lac du Bonnet granite using a discrete element model”. In: *International Journal of Rock Mechanics and Mining Sciences* 46 (2009), pp. 1124–1135.

[217] WANG, Z. L.; H. KONIETZKY, and R. F. SHEN. “Coupled finite element and discrete element method for underground blast in faulted rock masses”. In: *Soil Dynamics and Earthquake Engineering* 29.6 (2009), pp. 939–945.

[218] WEATHERLEY, D. K. et al. “Scaling Benchmark of ESyS-Particle for Elastic Wave Propagation Simulations”. In: *2010 IEEE Sixth International Conference on e-Science*. December 2010, pp. 277–283.

[219] WEERASEKARA, N. S.; L. X. LIU, and M. S. POWELL. “Estimating energy in grinding using DEM modelling”. In: *Minerals Engineering* 85 (2016), pp. 23–33.

[220] WEERASEKARA, N. S. et al. “The contribution of DEM to the science of comminution”. In: *Powder Technology* 248 (November 2013), pp. 3–24.

[221] WILLIAMS, JOH R. and ALEX P. PENTLAND. “Superquadrics and modal dynamics for discrete elements in interactive design”. In: *Engineering Computations* 9.2 (1992), pp. 115–127. eprint: `https://doi.org/10.1108/eb023852`.

[222] WIMMENAUER, WOLFHARD. *Petrographie der magmatischen und metamorphen Gesteine*. First. Stuttgart: Enke, 1985. 382 pp.

[223] XU, LEI; KUN LUO, and YONGZHI ZHAO. “Numerical prediction of wear in SAG mills based on DEM simulations”. In: *Powder Technology* 329 (2018), pp. 353–363.

[224] XU, ZEDONG. “Simulation der Zerkleinerung in einem Prallbrecher mittels ROCKY DEM”. MA thesis. TU Bergakademie Freiberg, 2019.

[225] YANG, R. Y. et al. “DEM simulation of the flow of grinding media in IsaMill”. In: *Minerals Engineering* 19.10 (2006). Selected papers from Computational Modelling ’05, Cape Town, South Africa, pp. 984–994.

[226] ZENDER, CHARLIE. “Particle Size Distributions: Theory and Application to Aerosols, Clouds, and Soils”. June 2013.

[227] ZHAO, SHIWEI et al. “Random packing of tetrahedral particles using the polyhedral discrete element method”. In: *Particuology* 23 (2015), pp. 109–117.

[228] ZHENG, CHENGWU and DIERK RAABE. “Interaction between recrystallization and phase transformation during intercritical annealing in a cold-rolled dual-phase steel: A cellular automaton model”. In: *Acta Materialia* 61 (2013), pp. 5504–5517.

[229] ZHENG, Q. J. et al. “A coupled FEM/DEM model for pipe conveyor systems: Analysis of the contact forces on belt”. In: *Powder Technology* 314 (2017). Special Issue on Simulation and Modelling of Particulate Systems, pp. 480–489.

List of Figures

List of Tables

Appendix

A Derivations of new parameters for the adapted QMA

A.1 The indirect ideal grain surface

The indirect ideal grain surface describes the surface of grains, which are shaped like ideal, elliptical microbodies. Furthermore, the actual size distribution of these idealized grains is indirectly considered, since it is assumed that the grain sizes are log-normally distributed. This distribution is approximated by the location parameter $x_{50,2}$ and the scatter parameter σ_{ln}.

To quantify the indirect ideal grain surface, the parameter $C_{A,I,approx}$ is used. It describes the ideal specific boundary line length of the approximated grain size distribution, whereby it is referred to the area of the phase of interest. The derivation of $C_{A,I,approx}$ is based on the derivation of the specific particle surface of RUMPF and EBERT [167], which is also described in [135, 137].

Grain area distribution. The derivation of $C_{A,I,approx}$ is started with some general considerations. For an arbitrary rth power we can define the the q_r and the Q_r distribution:

$$q_r(x) = \frac{x^r \cdot q_0(x)}{M_{r,0}} = \frac{dQ_r}{dx} \tag{A.1}$$

The value $M_{r,0}$ is called the complete rth moment of the q_0 distribution:

$$M_{r,0} = \int_0^\infty x^r \cdot q_0(x)\ dx \tag{A.2}$$

Based on this, some standard moments can be formed. $M_{0,0}$ can be seen as a normalization condition:

$$M_{0,0} = \int_0^\infty q_0(x)\ dx = N_0(\infty) = 1 \tag{A.3}$$

$M_{1,0}$ is the average x, which is proportional to the grain length and circumference:

$$M_{1,0} = \int_0^\infty x \cdot q_0(x)\ dx \tag{A.4}$$

$M_{2,0}$ is the average x^2, which is proportional to the grain area:

$$M_{2,0} = \int_0^\infty x^2 \cdot q_0(x)\ dx \tag{A.5}$$

$M_{3,0}$ is the average x^3, which is proportional to the grain volume:

$$M_{3,0} = \int_0^\infty x^3 \cdot q_0(x)\ dx \tag{A.6}$$

Based on Equation A.2 it is possible to define the complete r$^{\text{th}}$ moment of the q_r distribution $M_{k,r}$:

$$M_{k,r} = \int_0^\infty x^k \cdot q_r(x)\ dx \tag{A.7}$$

Using Equations A.1 and A.7 the following relation between different moments can be found:

$$M_{k,r} = \frac{\int_0^\infty x^{k+r} \cdot q_0(x)\ dx}{M_{r,0}} = \frac{M_{k+r,0}}{M_{r,0}} \tag{A.8}$$

The specific boundary line length of an object is defined as the circumference of the object set in relation to its area. With the means of the moments this can be expressed as:

$$C_{A,I,approx} = \kappa \cdot \frac{M_{1,0}}{M_{2,0}} \tag{A.9}$$

In this equation, κ is used as factor that takes the actual grain shape into account.

Combining Equations A.8 and A.9 results in:

$$C_{A,I,approx} = \kappa \cdot M_{-1,2} \tag{A.10}$$

Since moment of the log-normal distribution q_r is known as:

$$M_{k,r} = x_{50,r}^{k} \cdot e^{k^2 \cdot \frac{\sigma_{ln}}{2}} \tag{A.11}$$

The moment $M_{-1,1}$ can be written as:

$$M_{-1,1} = x_{50,2}^{-1} \cdot e^{(-1)^2 \frac{{\sigma_{ln}}^2}{2}} \tag{A.12}$$

In combination with Equation A.10 this results in Equation A.13. This formula defines the ideal specific boundary line length as function of a log-normal grain size distribution and the grain shape factor κ.

$$C_{A,I,approx} = \kappa \cdot \frac{1}{x_{50,2} \cdot e^{\frac{{\sigma_{ln}}^2}{2}}} \tag{A.13}$$

Grain shape factor κ. In order to allow the calculation of $C_{A,I,approx}$, the factor κ for the grain shape has to be specified. For this, it is again assumed, that the specific boundary line length C_A of an arbitrary planar object is defined as its circumference in relation to its area:

$$C_A = \frac{C}{A} \tag{A.14}$$

The circumference and area of such an object can further be described by its length x in combination with the grain shape factors κ_C and κ_A as shown in Equation A.15:

$$C = \kappa_C \cdot x \qquad\qquad A = \kappa_A \cdot x^2 \tag{A.15}$$

The combination of Equations A.14 and A.15 results in:

$$C_A = \frac{\kappa_C \cdot x}{\kappa_A \cdot x^2} = \frac{\kappa_C}{\kappa_A} \cdot \frac{1}{x} \tag{A.16}$$

In order to specify the shape parameters κ_C and κ_A of this general formula, the circle can be used as reference shape.

$$C_{circle} = \pi \cdot d \qquad\qquad A_{circle} = \frac{\pi \cdot d^2}{4} \tag{A.17}$$

By doing so, the length parameter x can be replaced by the diameter d. According to this, the shape parameters κ_C and κ_A are substituted by the factors π and $\frac{\pi}{4}$ and a second set of shape factors φ_C and φ_A.

$$\kappa_C = \pi \cdot \varphi_C \qquad\qquad \kappa_A = \frac{\pi \cdot \varphi_A}{4} \tag{A.18}$$

In this context, φ_C and φ_A characterize how much the shape of the actual analyzed object corresponds to a circular shape. Hence, for an exact circle this yields:

$$\varphi_{C,circle} = 1 \qquad\qquad \varphi_{A,circle} = 1 \tag{A.19}$$

If Equations A.16 and A.18 are combined, the shape factors φ_C and φ_C can be combined to the general factor φ.

$$\kappa = \frac{\kappa_C}{\kappa_A} = \frac{\pi \cdot \varphi_C}{\frac{\pi \cdot}{4} \cdot \varphi_A} = 4 \cdot \varphi \tag{A.20}$$

According to Equation A.19, it follows for an exact circle:

$$\varphi_{circle} = 1 \tag{A.21}$$

Grain shape factor φ. At this point, the second grain shape parameter φ has to be specified. Therefore, the model for the grain shape has to be considered. According to the general assumptions of the three-dimensional QMA, the grains are considered to be tri-ellipsoids. For the adapted, two-dimensional analysis, the corresponding planar shape is an ellipse with the semi-axes a and b, which can be described by the following equations:

$$C_{ellipse} \approx \pi \left(3\frac{a+b}{2} - \sqrt{ab}\right) \qquad A_{ellipse} = \pi \cdot a \cdot b \tag{A.22}$$

In order to set the model of the elliptical grain in reference to a circle, it is assumed that both have equal areas:

$$A_{ellipse} = A_{circle} \tag{A.23}$$

Furthermore, the definitions for a circle (Equation A.17) can be combined with each other.

$$C_{circle} = \pi \cdot \sqrt{\frac{4 \cdot A_{circle}}{\pi}} = \sqrt{4 \cdot \pi \cdot A_{circle}} \tag{A.24}$$

The combination with Equations A.22 and A.23 yields:

$$C_{circle} = \sqrt{4 \cdot \pi \cdot A_{ellipse}} \tag{A.25}$$

$$C_{circle} = \sqrt{4 \cdot \pi^2 \cdot a \cdot b} = 2 \cdot \pi\sqrt{a \cdot b} \tag{A.26}$$

As the grain shape factor φ describes the relation between the actual grain, which is assumed to be an ellipse, and a circle, the combination of Equations A.22 and A.26 can be used to specify φ:

$$\varphi = \frac{C_{ellipse}}{C_{circle}} = \frac{\pi\left(3\frac{a+b}{2} - \sqrt{ab}\right)}{2 \cdot \pi\sqrt{a \cdot b}} = 3\frac{a+b}{4\sqrt{a \cdot b}} - \frac{1}{2} \tag{A.27}$$

Final formulation of the ideal specific boundary line length. Based on the considerations of the particle area distributions (Equation A.13) and the analysis of the grain shape factors κ and φ (Equations A.20 and A.27) can be combined. This results in the final equation for the ideal specific boundary line length of the approximated grain size distribution $C_{A,I,approx}$.

$$C_{A,I,approx} = 4\left[3\frac{a+b}{4\sqrt{a \cdot b}} - \frac{1}{2}\right] \cdot \frac{1}{x_{50,2}} \cdot e^{\frac{\sigma_{ln}{}^2}{2}} \tag{A.28}$$

A.2 The direct ideal grain surface

The ideal surface of two-dimensional, ideal, elliptical microbodies, can also directly be derived during the analysis, if the single grains are assessable. Since this is the case in for the adapted QMA, it is not necessary to a use an approximated grain size distribution. Instead, the specific boundary line lengths of all grains can be calculated separately and subsequently combined to the directly measured ideal boundary line length $C_{A,I,actual}$.

For this, the equations of the circumference and area of an ellipse are needed again:

$$C_{ellipse} \approx \pi \left(3\frac{a+b}{2} - \sqrt{ab}\right) \qquad A_{ellipse} = \pi \cdot a \cdot b \tag{A.29}$$

Furthermore, the general equation considering the specific boundary line length (Equation A.14) is again needed:

$$C_A = \frac{C}{A} \tag{A.30}$$

Setting the circumference of the ellipse (Equation A.29) into to Equation A.30 yields:

$$C_A = \frac{\pi \left(3\frac{a+b}{2} - \sqrt{a \cdot b}\right)}{A} \tag{A.31}$$

The smaller semi-axis b can be substituted using the equation of the ellipse area (Equation A.29):

$$b = \frac{A}{\pi \cdot a} \tag{A.32}$$

Additionally, it is assumed that all grains have the same elliptical shape. Hence, the parameters a and b can be expressed as the elongation El of this ellipse.

$$El = \frac{a}{b} \tag{A.33}$$

If the Equations A.32 and A.33 are combined, this yields:

$$a = \sqrt{\frac{El \cdot A}{\pi}} \tag{A.34}$$

Plugging Equation A.32 and subsequently Equation A.34 into Equation A.31 allows to calculate the specific boundary line length of a single particle as function of the measured area of the grain A and the elongation El of the approximated elliptical microbody.

$$C_{A,I,single} = \sqrt{\frac{\pi}{A}} \left(\frac{3}{2}\left[\frac{El+1}{\sqrt{El}}\right] - 1\right) \tag{A.35}$$

For calculating the specific boundary line length of all particles of a phase, the circumferences of all n particles have to be set in reference to the summarized area of all particles.

$$C_{A,I,actual} = \sqrt{\frac{\sum_{i=0}^{n} C_i}{\sum_{i=0}^{n} A_i}} \tag{A.36}$$

Hence, if Equation A.36 is used instead of Equation A.30 for the derivation, the actual specific boundary line length of all analyzed grains $C_{A,I,actual}$ can be calculated by the following formula.

$$C_{A,I,actual} = \frac{\sqrt{\sum_{i=0}^{n} A_i \cdot \pi}\left(\frac{3}{2}\left[\frac{El+1}{\sqrt{El}}\right] - 1\right)}{\sum_{i=0}^{n} A_i} \tag{A.37}$$

A.3 The grain intergrowth

The grain growth characterizes how often a specific type of grain boundary occurs in the analyzed system. Hence, the degree of intergrowth $K_{I,(\alpha,\beta)}$ between grains of phase α and grains of phase β is defined as the proportion of the specific boundary line length between the grains of the two phases $C_{A,(\alpha,\beta)}$ and the specific boundary line length of the whole mineral microstructure $C_{A,all}$.

Regardless of this independently valid definition, the relationship can also be derived from the equation for the three-dimensional QMA.

$$K_{I,(\alpha,\beta)} = \frac{S_{V,(\alpha\beta)}}{S_{V,all}} \tag{A.38}$$

The basis are the following general relations [101]:

$$S_V = 2P_L \tag{A.39}$$

$$C_A = \frac{\pi}{2} P_L \tag{A.40}$$

$$P_L = \frac{N_{(\alpha,\beta)} \cdot d}{a_0} \tag{A.41}$$

The combination of Equations A.38 to A.41 yields the following basic equation of the grain intergrowth:

$$S_V = \frac{S_{V,(\alpha\beta)}}{S_{V,all}} = \frac{C_{A,(\alpha,\beta)}}{C_{A,all}} = \frac{P_{L,(\alpha\beta)}}{P_{L,all}} = \frac{N_{(\alpha,\beta)}}{N_{all}} \tag{A.42}$$

As can be seen, the parameters S_V, C_A, P_L, and P_L are interchangeable for the calculation of the grain intergrowth. Hence, for the planar analysis, the specific boundary line lengths $C_{A,(\alpha,\beta)}$ and $C_{A,all}$ can be used for the calculation.

According to Equations A.40 and A.41, $C_{A,(\alpha,\beta)}$ is defined as:

$$C_{A,(\alpha,\beta)} = \frac{\pi \cdot N_{(\alpha,\beta)} \cdot d}{2a_0} \tag{A.43}$$

A.4 The spatial distribution of the grains

The spatial distribution of grain in a planar microstructure can be characterized with the degree of clustering, also called contiguity, as well. For this, the general, three-dimensional model for the calculation of the C_α is the basis:

$$C_\alpha = \frac{2S_{V,(\alpha\alpha)}}{2S_{V,(\alpha\alpha)} + S_{V,(\alpha\beta)}} = \frac{2P_{L,(\alpha\alpha)}}{2P_{L,(\alpha\alpha)} + P_{L,(\alpha\beta)}} \tag{A.44}$$

Using the relationship between C_A and P_L (Equation A.40) one can define:

$$C_\alpha = \frac{2C_{A,(\alpha,\alpha)}}{2C_{A,(\alpha,\alpha)} + C_{A,(\alpha,\beta)}} = \frac{2P_{L,(\alpha\alpha)}}{2P_{L,(\alpha\alpha)} + P_{L,(\alpha\beta)}} \tag{A.45}$$

B Program for microstructural analysis and synthesis

B.1 General program description

In the context of this research project, a program was created that links all functions for microstructure import, handling, synthesis, analysis, and export with each other. The program is written in python [166], whereby specific modules can access other programming languages like the R project [158] if necessary. The final program is built up using a tab structure as shown in Figure B.1 and can be accessed through a GUI that is based on PyQt.

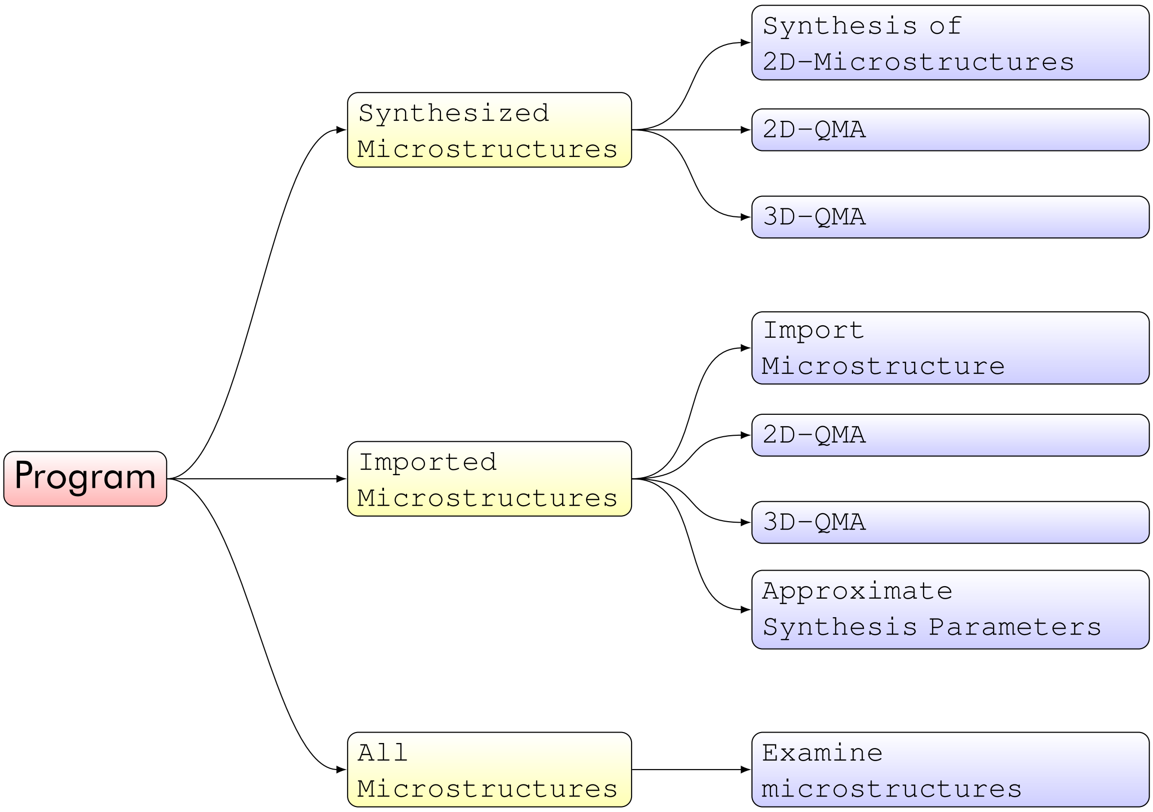

Fig. B.1: The main structure of the program that links all functions for microstructure import, handling, synthesis, analysis, and export with each other

The program is designed as scientific tool that allows the quick analysis and synthesis of microstructures. Hence, it is not comparable to the typical release state of proprietary software. The structure allows quick access to the source code of the functions so that the user or developer can easily implement modifications and improvements. In the consequence, the actual appearance and structure are a result of steady changes leaving some elements as place holders for not yet activated functions. The author is aware of the fact that the user-friendliness of the current state of the program is not fully satisfactory. However, the overall built-up of the program ensures, that all functions that belong together are summarized on the same tabs and it is possible to perform all typical actions with the microstructures without interrupt.

In the first level of the structure it can be chosen between tabs that summarize the functions for the different types of microstructure. From the programming point of view, it is distinguished between imported microstructures and synthesized microstructures. The tabs of the second level combine groups of functions that can be used to work with these two kinds of microstructures.

Imported microstructures are usually based on imported false-color images only. Hence the focus for this group is on importing of the microstructures and performing different types of QMA. Furthermore, there is a tab that can be used to approximate synthesis parameters on the basis of the QMA results of such a microstructure.

In contrast, synthesized microstructures are typically not imported but created by the program. Hence, the first tab for this group of microstructures summarizes all functions, which are needed to control the synthesis process. In accordance with the imported microstructures, there are tabs for the post-process analysis using the QMA methods as well.

Furthermore, the functions, which are used for every type of microstructure are summarized in another tab. This includes especially functions for examining, comparing, and exporting the false-color images of the different microstructures. Although the QMA methods are the same for every type of microstructure, these are assigned directly to the imported and synthesized microstructures for reasons of better clarity. Based on this main structure, the different tabs are shortly explained in the following sections.

B.2 Synthesis tab

Figure B.2 shows the synthesis tab of the GUI. It is possible to synthesize a microstructure for each of the three orthogonal planes of the original three-dimensional QMA. For the purpose of synthesizing two-dimensional microstructures, they can be seen as stand-alone microstructures. In the shown tab, three microstructures, each consisting of four crystalline phases A, B, C, and D were synthesized. The number of phases, however, is not limited by the program. Although the same synthesis parameters were used in the shown example, the synthesized microstructures are different due to the random based nature of the drawing algorithms (Section 3.3).

After the successful synthesis of the microstructure, the user can start the adapted QMA of the two-dimensional microstructures right away, by clicking the corresponding button.

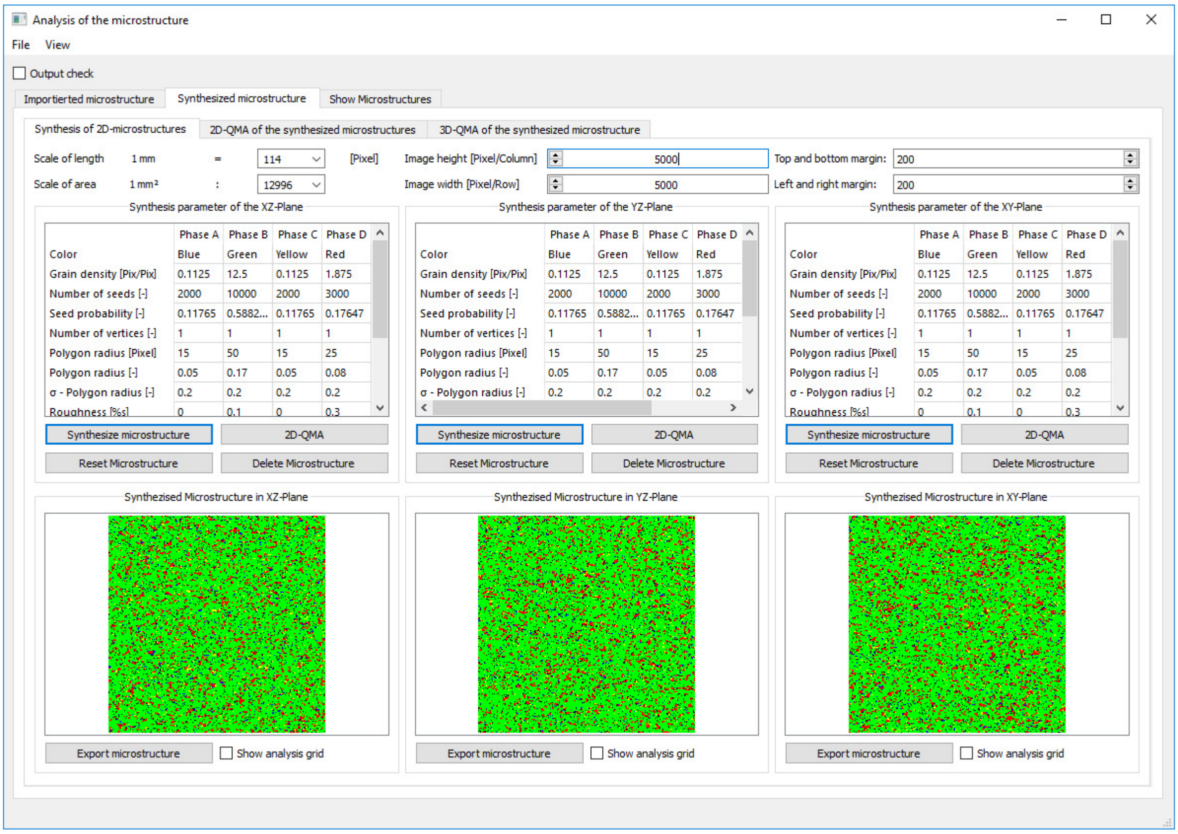

☐ Output check

Scale of length 1 mm = 114 [Pixel]

Scale of area 1 mm² : 12996

Image height [Pixel/Column] 5000

Image width [Pixel/Row] 5000

Top and bottom margin: 200

Left and right margin: 200

Synthesis parameter of the XZ-Plane

	Phase A	Phase B	Phase C	Phase D
Color	Blue	Green	Yellow	Red
Grain density [Pix/Pix]	0.1125	12.5	0.1125	1.875
Number of seeds [-]	2000	10000	2000	3000
Seed probability [-]	0.11765	0.5882...	0.11765	0.17647
Number of vertices [-]	1	1	1	1
Polygon radius [Pixel]	15	50	15	25
Polygon radius [-]	0.05	0.17	0.05	0.08
σ - Polygon radius [-]	0.2	0.2	0.2	0.2
Roughness [%s]	0	0.1	0	0.3

Synthesis parameter of the YZ-Plane

	Phase A	Phase B	Phase C	Phase D
Color	Blue	Green	Yellow	Red
Grain density [Pix/Pix]	0.1125	12.5	0.1125	1.875
Number of seeds [-]	2000	10000	2000	3000
Seed probability [-]	0.11765	0.5882...	0.11765	0.17647
Number of vertices [-]	1	1	1	1
Polygon radius [Pixel]	15	50	15	25
Polygon radius [-]	0.05	0.17	0.05	0.08
σ - Polygon radius [-]	0.2	0.2	0.2	0.2

Synthesis parameter of the XY-Plane

	Phase A	Phase B	Phase C	Phase D
Color	Blue	Green	Yellow	Red
Grain density [Pix/Pix]	0.1125	12.5	0.1125	1.875
Number of seeds [-]	2000	10000	2000	3000
Seed probability [-]	0.11765	0.5882...	0.11765	0.17647
Number of vertices [-]	1	1	1	1
Polygon radius [Pixel]	15	50	15	25
Polygon radius [-]	0.05	0.17	0.05	0.08
σ - Polygon radius [-]	0.2	0.2	0.2	0.2
Roughness [%s]	0	0.1	0	0.3

Fig. B.2: Synthesis tab with three synthesized two-dimensional microstructures and the associated synthesis parameters

B.3 2D-analysis tab

The 2D-analysis tab shows the results of the adopted QMA for the three microstructures. The tab is identical for the imported and synthesized microstructures. Figure B.3 shows exemplarily the results for the synthetic two-dimensional microstructures of Figure B.2. The tab can be further scrolled down to inspect the missing roses of intersections and the plots of the grain size distributions.

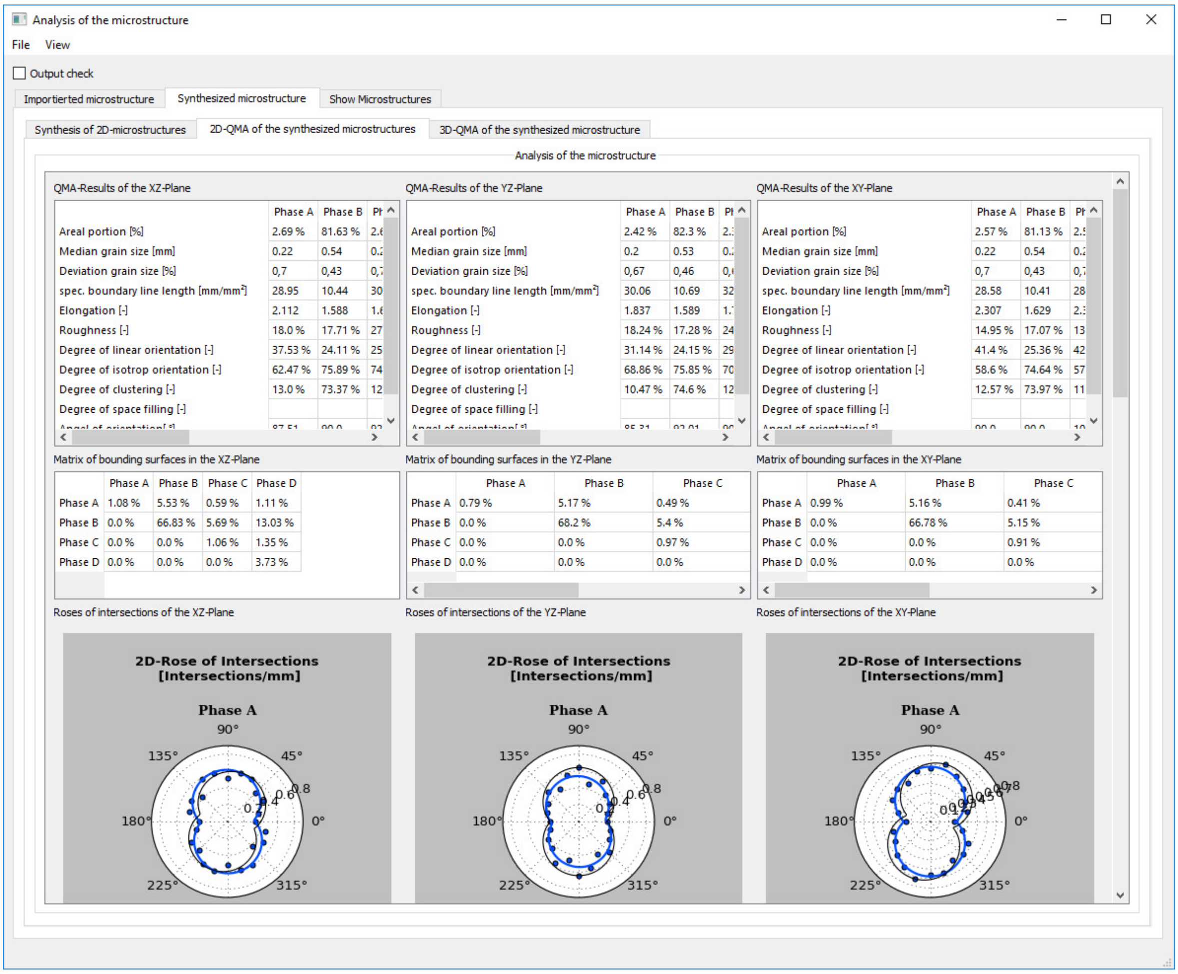

QMA-Results of the XZ-Plane

	Phase A	Phase B	Ph
Areal portion [%]	2.69 %	81.63 %	2.
Median grain size [mm]	0.22	0.54	0.
Deviation grain size [%]	0,7	0,43	0,
spec. boundary line length [mm/mm²]	28.95	10.44	30
Elongation [-]	2.112	1.588	1.
Roughness [-]	18.0 %	17.71 %	27
Degree of linear orientation [-]	37.53 %	24.11 %	25
Degree of isotrop orientation [-]	62.47 %	75.89 %	74
Degree of clustering [-]	13.0 %	73.37 %	12
Degree of space filling [-]			
Angel of orientation[°]	87.51	90.0	92

QMA-Results of the YZ-Plane

	Phase A	Phase B	Ph
Areal portion [%]	2.42 %	82.3 %	2.
Median grain size [mm]	0.2	0.53	0.
Deviation grain size [%]	0,67	0,46	0,
spec. boundary line length [mm/mm²]	30.06	10.69	32
Elongation [-]	1.837	1.589	1.
Roughness [-]	18.24 %	17.28 %	24
Degree of linear orientation [-]	31.14 %	24.15 %	29
Degree of isotrop orientation [-]	68.86 %	75.85 %	70
Degree of clustering [-]	10.47 %	74.6 %	12
Degree of space filling [-]			
Angel of orientation[°]	85.31	92.01	90

QMA-Results of the XY-Plane

	Phase A	Phase B	Ph
Areal portion [%]	2.57 %	81.13 %	2.
Median grain size [mm]	0.22	0.54	0.
Deviation grain size [%]	0,7	0,43	0,
spec. boundary line length [mm/mm²]	28.58	10.41	28
Elongation [-]	2.307	1.629	2.
Roughness [-]	14.95 %	17.07 %	13
Degree of linear orientation [-]	41.4 %	25.36 %	42
Degree of isotrop orientation [-]	58.6 %	74.64 %	57
Degree of clustering [-]	12.57 %	73.97 %	11
Degree of space filling [-]			
Angel of orientation[°]	90.0	90.0	10

Matrix of bounding surfaces in the XZ-Plane

	Phase A	Phase B	Phase C	Phase D
Phase A	1.08 %	5.53 %	0.59 %	1.11 %
Phase B	0.0 %	66.83 %	5.69 %	13.03 %
Phase C	0.0 %	0.0 %	1.06 %	1.35 %
Phase D	0.0 %	0.0 %	0.0 %	3.73 %

Matrix of bounding surfaces in the YZ-Plane

	Phase A	Phase B	Phase C
Phase A	0.79 %	5.17 %	0.49 %
Phase B	0.0 %	68.2 %	5.4 %
Phase C	0.0 %	0.0 %	0.97 %
Phase D	0.0 %	0.0 %	0.0 %

Matrix of bounding surfaces in the XY-Plane

	Phase A	Phase B	Phase C
Phase A	0.99 %	5.16 %	0.41 %
Phase B	0.0 %	66.78 %	5.15 %
Phase C	0.0 %	0.0 %	0.91 %
Phase D	0.0 %	0.0 %	0.0 %

Fig. B.3: Analysis tab with three synthesized two-dimensional microstructures and the associated QMA results

The radii of the two-dimensional roses of intersections n_{iso} and n_{lin} are approximated using basin-hopping. This is a stochastic algorithm for finding the global minimum of a smooth scalar function. This function can have one or more variables. The used form of basin hopping was described by WALES and DOYE [215] and is part of the scipy package [214].

B.4 3D-analysis tab

The 3D-analysis tab can be used to perform an original QMA as proposed by POPOV [146]. Therefore, three microstructures have to be analyzed with the two-dimensional, adopted QMA in the first instance. Regardless of whether the three microstructures are imported or synthesized ones, it is then possible to start a three-dimensional analysis. Therefore, the program assumes that all three microstructures belong to one sample and represent the three orthogonal thin- or polished sections. Hence, the tab is identical for the imported and synthesized microstructures.

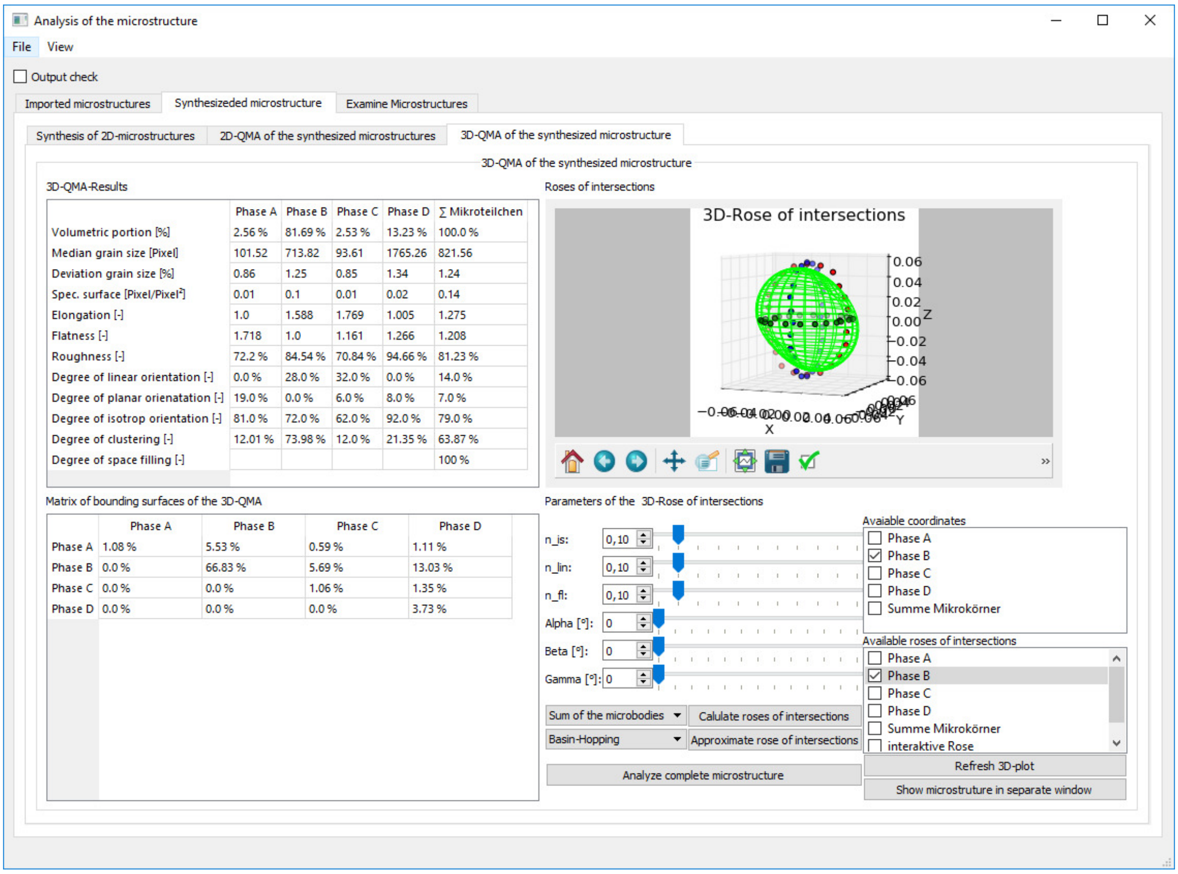

3D-QMA-Results

	Phase A	Phase B	Phase C	Phase D	∑ Mikroteilchen
Volumetric portion [%]	2.56 %	81.69 %	2.53 %	13.23 %	100.0 %
Median grain size [Pixel]	101.52	713.82	93.61	1765.26	821.56
Deviation grain size [%]	0.86	1.25	0.85	1.34	1.24
Spec. surface [Pixel/Pixel²]	0.01	0.1	0.01	0.02	0.14
Elongation [-]	1.0	1.588	1.769	1.005	1.275
Flatness [-]	1.718	1.0	1.161	1.266	1.208
Roughness [-]	72.2 %	84.54 %	70.84 %	94.66 %	81.23 %
Degree of linear orientation [-]	0.0 %	28.0 %	32.0 %	0.0 %	14.0 %
Degree of planar orienatation [-]	19.0 %	0.0 %	6.0 %	8.0 %	7.0 %
Degree of isotrop orientation [-]	81.0 %	72.0 %	62.0 %	92.0 %	79.0 %
Degree of clustering [-]	12.01 %	73.98 %	12.0 %	21.35 %	63.87 %
Degree of space filling [-]					100 %

Matrix of bounding surfaces of the 3D-QMA

	Phase A	Phase B	Phase C	Phase D
Phase A	1.08 %	5.53 %	0.59 %	1.11 %
Phase B	0.0 %	66.83 %	5.69 %	13.03 %
Phase C	0.0 %	0.0 %	1.06 %	1.35 %
Phase D	0.0 %	0.0 %	0.0 %	3.73 %

Parameters of the 3D-Rose of intersections

n_is: 0,10
n_lin: 0,10
n_fl: 0,10
Alpha [°]: 0
Beta [°]: 0
Gamma [°]: 0

Avaiable coordinates
☐ Phase A
☑ Phase B
☐ Phase C
☐ Phase D
☐ Summe Mikrokörner

Available roses of intersections
☐ Phase A
☑ Phase B
☐ Phase C
☐ Phase D
☐ Summe Mikrokörner
☐ interaktive Rose

Fig. B.4: Analysis tab for the 3D-Analysis, which is comparable to the original QMA of three orthogonal thin or polished sections that belong together

In the left part of the tab (Figure B.4) are the tables with the results of the three-dimensional QMA and the corresponding matrix of bounding surfaces. In the right part it is possible to inspect and compare the measured and approximated three-dimensional roses of intersections.

B.5 Import tab

The import tab is used for loading false-color images from the hard drive. Therefore, different convenient functions are available. It is possible to import a set of false-color images that represents the three different planes for a three-dimensional QMA. However, if only two-dimensional microstructures are in the focus, the different planes can be seen as stand-alone microstructures.

The images of the microstructures that have to be imported can be selected using a typical file dialog. If a microstructure is successfully imported, it is further possible to either let the program detect the different phases or specify the microstructural components in the image manually. The different phases can then be named and the right colors can be assigned. If everything is done the user can start the two-dimensional QMA for each false-color image right away.

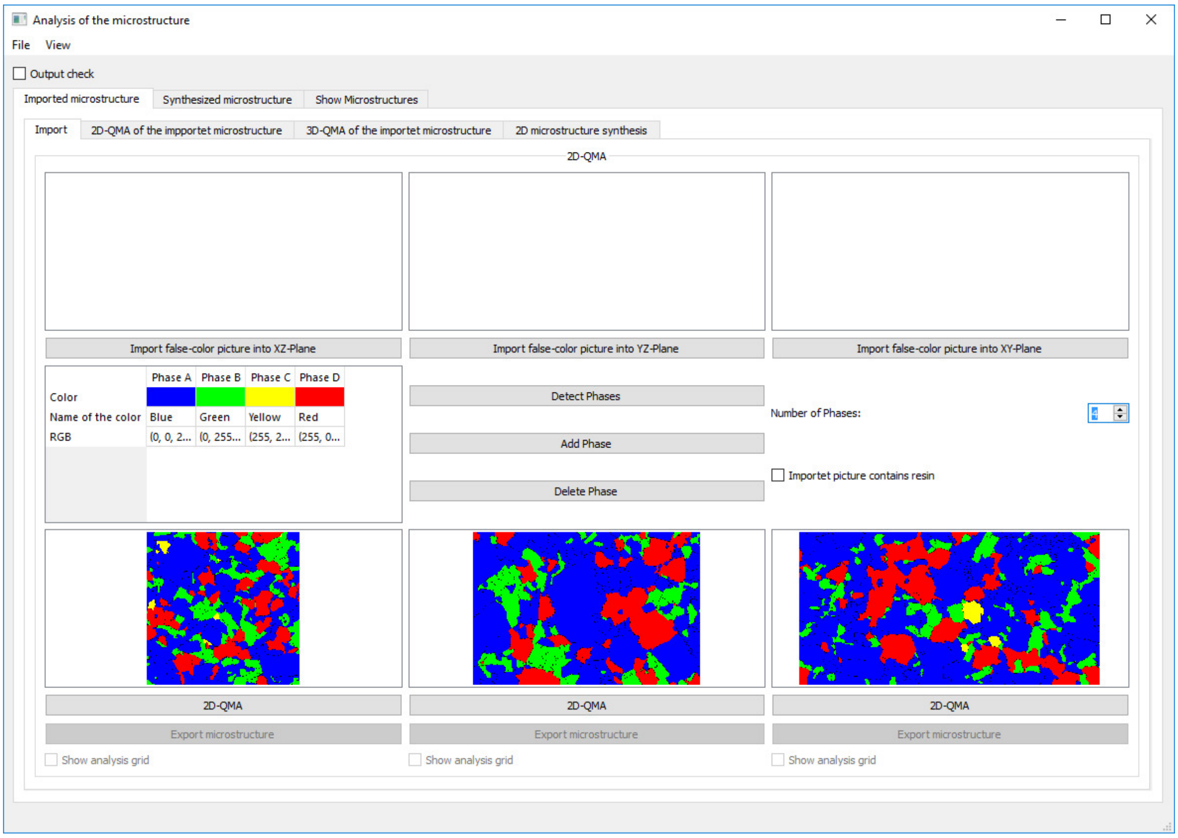

☐ Output check

	Phase A	Phase B	Phase C	Phase D
Color	🟦	🟩	🟨	🟥
Name of the color	Blue	Green	Yellow	Red
RGB	(0, 0, 2...	(0, 255...	(255, 2...	(255, 0...

Number of Phases: 4

☐ Importet picture contains resin

Fig. B.5: Tab for the import of false-color images of microstructures

B.6 Parameter estimation tab

The automated estimation of synthesis parameters can be done in the tab shown in Figure B.6. It is possible to specify the desired microstructural parameters in the table at the top left of the tab and estimate appropriate synthesis parameters, subsequently. The proposed parameters are then displayed in the table underneath.

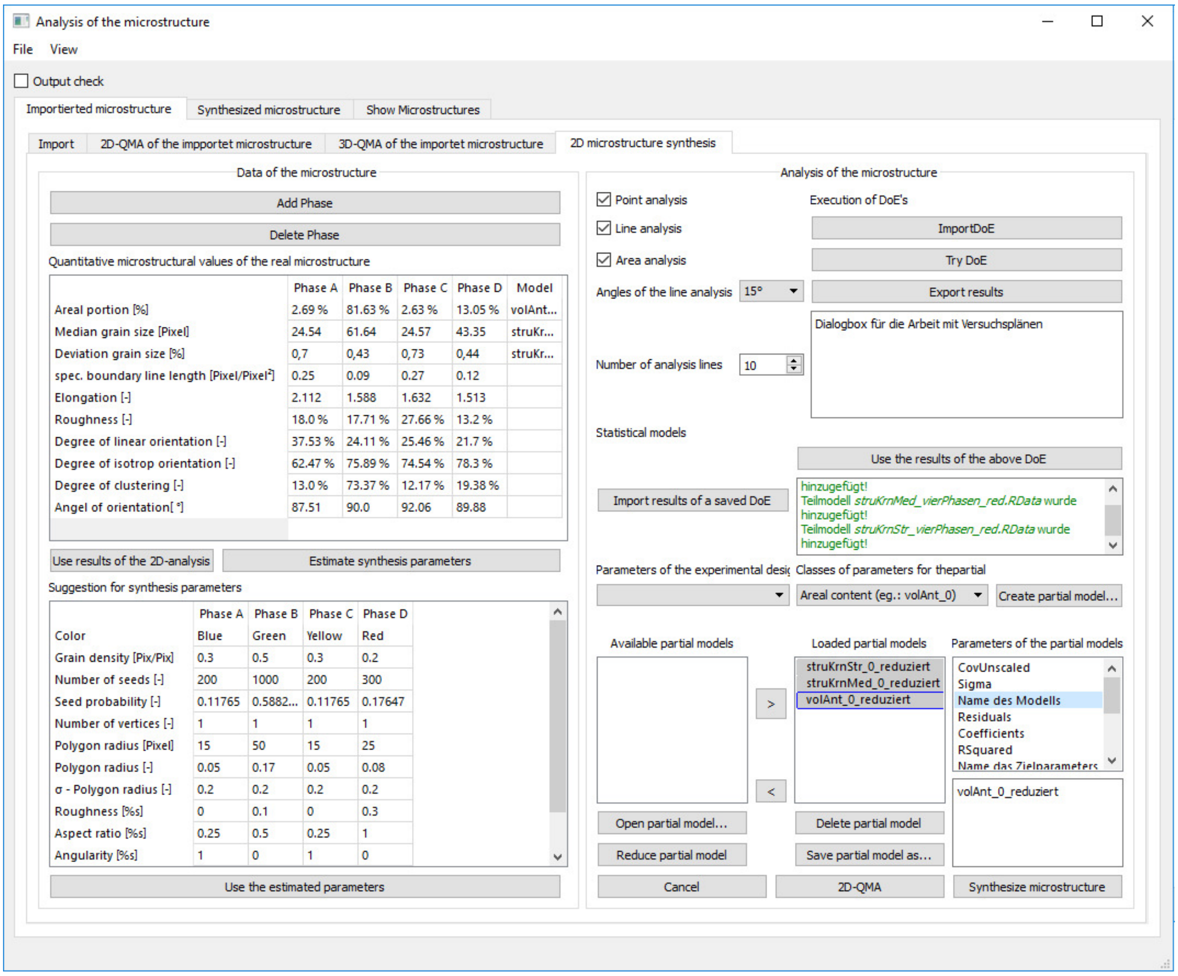

☐ Output check

Quantitative microstructural values of the real microstructure

	Phase A	Phase B	Phase C	Phase D	Model
Areal portion [%]	2.69 %	81.63 %	2.63 %	13.05 %	volAnt...
Median grain size [Pixel]	24.54	61.64	24.57	43.35	struKr...
Deviation grain size [%]	0,7	0,43	0,73	0,44	struKr...
spec. boundary line length [Pixel/Pixel²]	0.25	0.09	0.27	0.12	
Elongation [-]	2.112	1.588	1.632	1.513	
Roughness [-]	18.0 %	17.71 %	27.66 %	13.2 %	
Degree of linear orientation [-]	37.53 %	24.11 %	25.46 %	21.7 %	
Degree of isotrop orientation [-]	62.47 %	75.89 %	74.54 %	78.3 %	
Degree of clustering [-]	13.0 %	73.37 %	12.17 %	19.38 %	
Angel of orientation[°]	87.51	90.0	92.06	89.88	

Suggestion for synthesis parameters

	Phase A	Phase B	Phase C	Phase D
Color	Blue	Green	Yellow	Red
Grain density [Pix/Pix]	0.3	0.5	0.3	0.2
Number of seeds [-]	200	1000	200	300
Seed probability [-]	0.11765	0.5882...	0.11765	0.17647
Number of vertices [-]	1	1	1	1
Polygon radius [Pixel]	15	50	15	25
Polygon radius [-]	0.05	0.17	0.05	0.08
σ - Polygon radius [-]	0.2	0.2	0.2	0.2
Roughness [%s]	0	0.1	0	0.3
Aspect ratio [%s]	0.25	0.5	0.25	1
Angularity [%s]	1	0	1	0

☑ Point analysis
☑ Line analysis
☑ Area analysis
Angles of the line analysis: 15°
Number of analysis lines: 10

Dialogbox für die Arbeit mit Versuchsplänen

hinzugefügt!
Teilmodell *struKrnMed_vierPhasen_red.RData* wurde hinzugefügt!
Teilmodell *struKrnStr_vierPhasen_red.RData* wurde hinzugefügt!

Parameters of the experimental desi
Classes of parameters for thepartial: Areal content (eg.: volAnt_0)

Loaded partial models:
struKrnStr_0_reduziert
struKrnMed_0_reduziert
volAnt_0_reduziert

Parameters of the partial models:
CovUnscaled
Sigma
Name des Modells
Residuals
Coefficients
RSquared
Name das Zielparameters

volAnt_0_reduziert

Fig. B.6: Tab for the estimation of synthesis parameters. In this example three partial models, for the areal portion, the median grain size and for the deviation of the grain size have been loaded.

The estimation process is based on the evaluation of models for the different synthesis parameters. The models itself are created through regression analysis of the synthesis parameters and the QMA results for a given set of synthesized microstructures. According to [185] the combination of synthesis and the analysis of such a microstructure can be considered as a single computer experiment. In order to allow suitable model generation, it reasonable to use special DoEs for such computer experiments.

For this purpose, the software has a connection to the R project [158] and the lhs package [23]. This package uses so-called Latin hypercube sampling, which is particularly suitable for the design of computer experiments. Hence, it is possible to create an appropriate DoE for computer experiments and let the program synthesize and analyze numerous microstructures on this basis. In combination, suitable models for the different synthesis parameters can then be calculate on the basis of the analysis results.

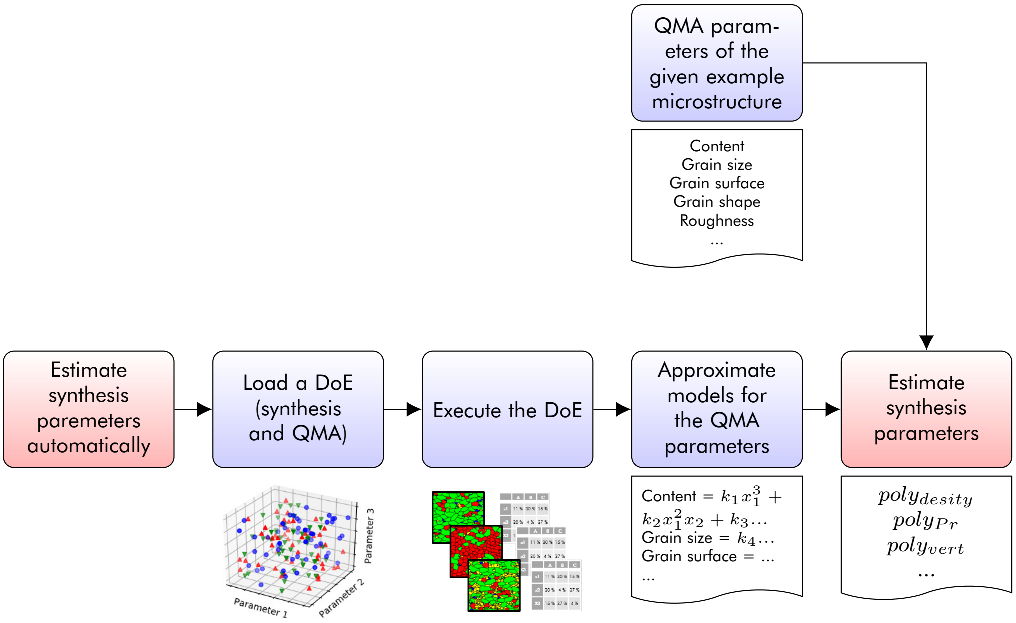

Fig. B.7: Schematically comparison of an enhanced QMA that can analyze real and synthetic mineral microstructures on the basis of false color images

The basic work flow for the estimation is shown in Figure B.7. In order to estimate the parameters automatically, the user has to load an appropriate DoE first. A set of ready-made DoEs is already available inside the program folder. Following, the program has to execute the selected DoE, which implies microstructure synthesis and analysis according to the give synthesis parameters of every knot of the DoE. Afterwards, the program uses again the lhs package of the R project for the model approximation. In combination with the QMA results of the example microstructure, it is then possible to estimate the synthesis parameters. Therefore, the basin-hopping algorithm is used (Appendix B.3).

Afterwards, the estimated parameters can be handled directly to the synthesis tab. In addition, the DoE, the results, and the models can be exported and imported for further use.

B.7 Examination tab

This tab is intended to be used to examine the false-color images of the microstructures. Therefore, the main part of the tab is reserved for the false-color images that can be selected with the radio buttons on the right side. Additionally, it is possible to switch on the length scale and the analysis grid of the line analysis. The view of the false-color image can further be zoomed for better examination of small structures. Finally, the false-color images of the microstructures can be exported for further use.

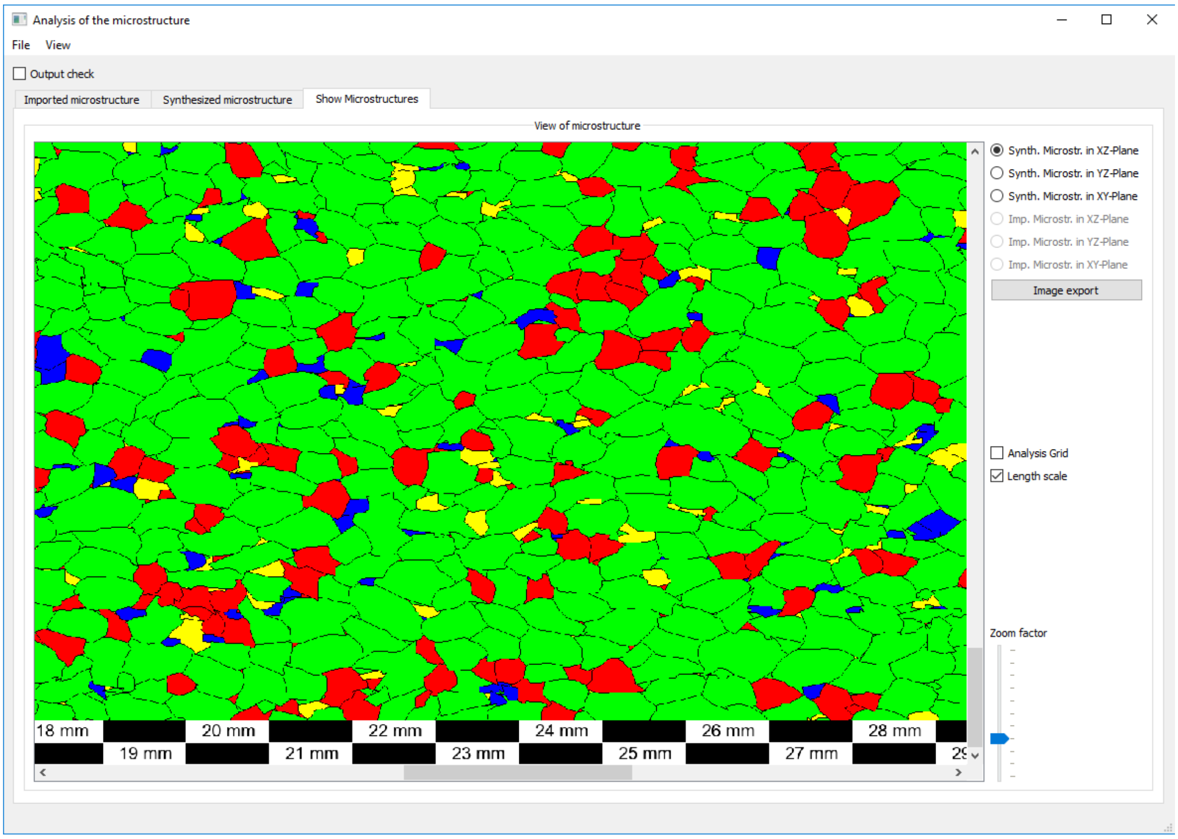

☐ Output check

● Synth. Microstr. in XZ-Plane
○ Synth. Microstr. in YZ-Plane
○ Synth. Microstr. in XY-Plane
○ Imp. Microstr. in XZ-Plane
○ Imp. Microstr. in YZ-Plane
○ Imp. Microstr. in XY-Plane

☐ Analysis Grid
☑ Length scale

Fig. B.8: Tab for inspecting the false-color image of the microstructures

B.8 Additional details of the QMA for the real granite from Meissen

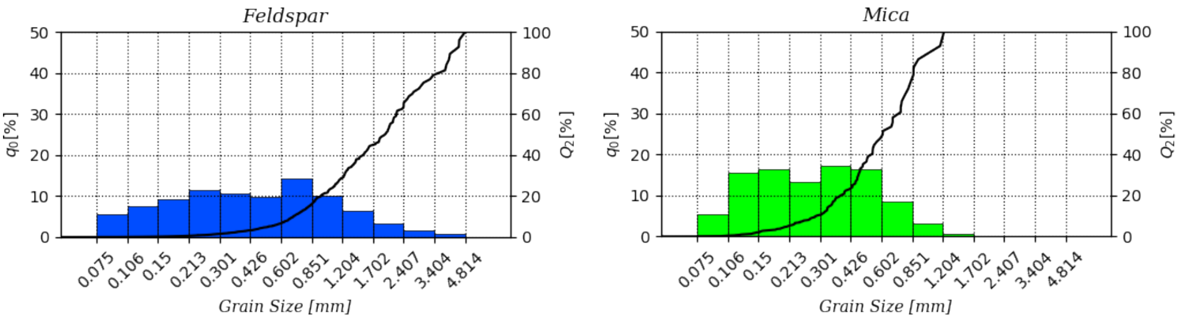

(a) Grain size distribution of Feldspar (b) Grain size distribution of Mica

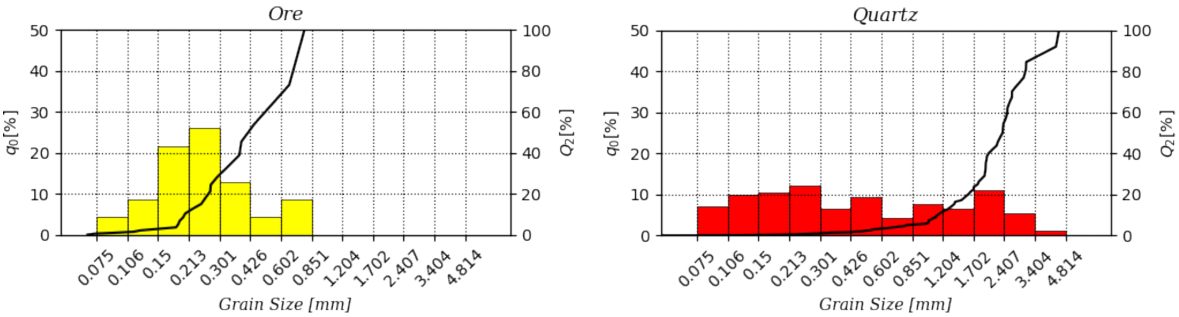

(c) Grain size distribution of Ore (d) Grain size distribution of Quartz

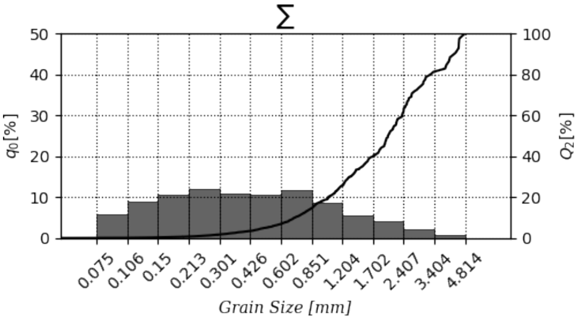

(e) Grain size distribution of the sum of the microbodies

Fig. B.9: Grain size distributions of the granite from Meissen: (a) Feldspar; (b) Mica; (c) Ore; (d) Quartz; (e) Sum of the microbodies

Tab. B.1: Matrix of the bounding surfaces with the degrees of intergrowth of the granite from Meissen

	Feldspar	Mica	Ore	Quartz
Feldspar	64.98	4.47	0.51	14.51
Mica	—	0.61	0.06	1.03
Ore	—	—	0.11	0.21
Quartz	—	—	—	13.51

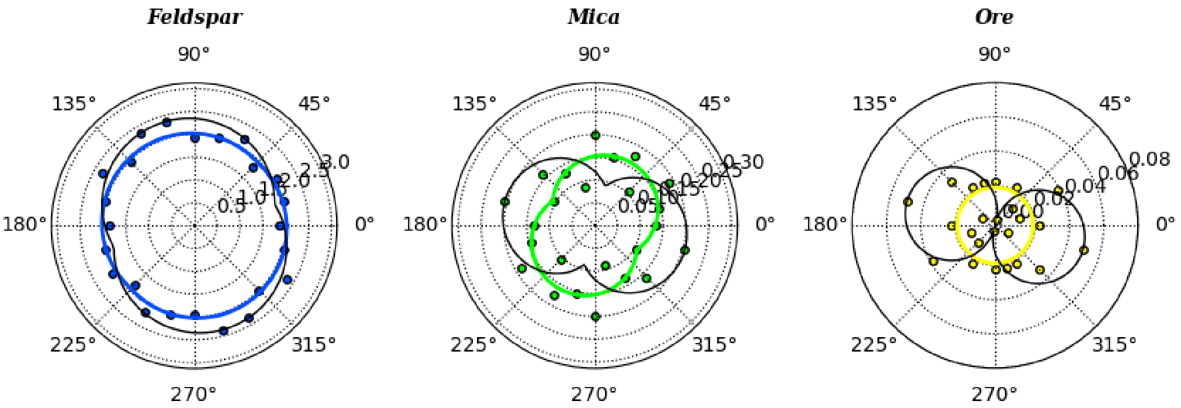

(a) Rose of intersections of Feldspar **(b)** Rose of intersections of Mica **(c)** Rose of intersections of Ore

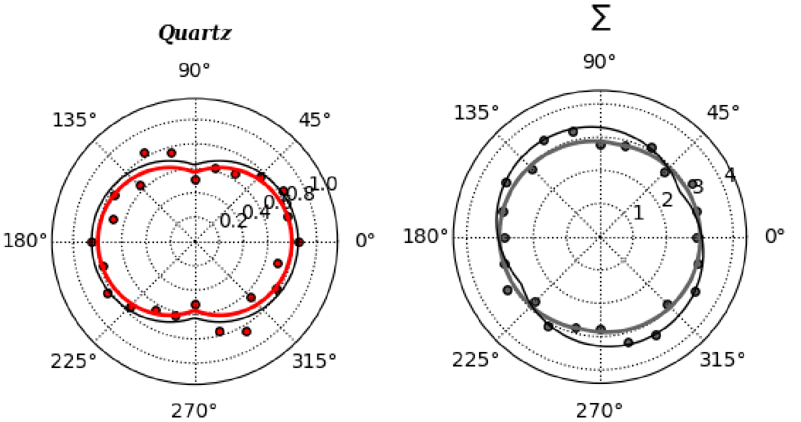

(d) Rose of intersections of Quartz **(e)** Rose of intersections of the sum of the microbodies

Fig. B.10: Two-dimensional roses of intersections of the granite from Meissen Intersections mm^{-1}: (a) Feldspar; (b) Mica; (c) Ore; (d) Quartz; (e) Sum of the microbodies

C Additional QMA details

C.1 The synthetic twin of the granite from Meissen

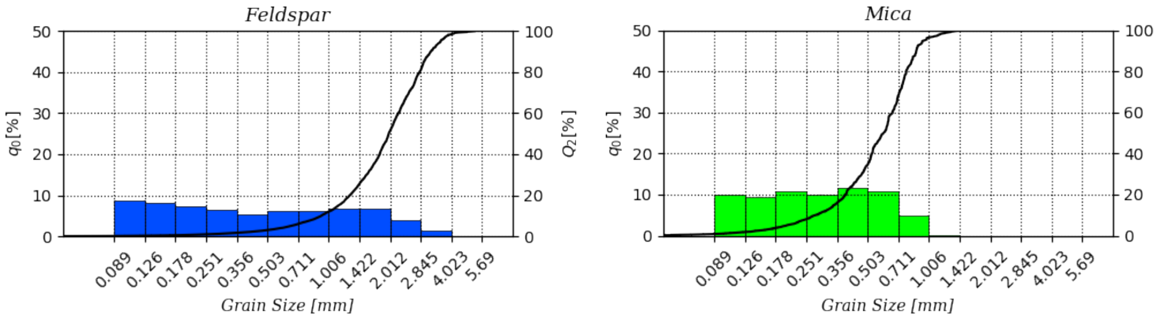

(a) Grain size distribution of Feldspar

(b) Grain size distribution of Mica

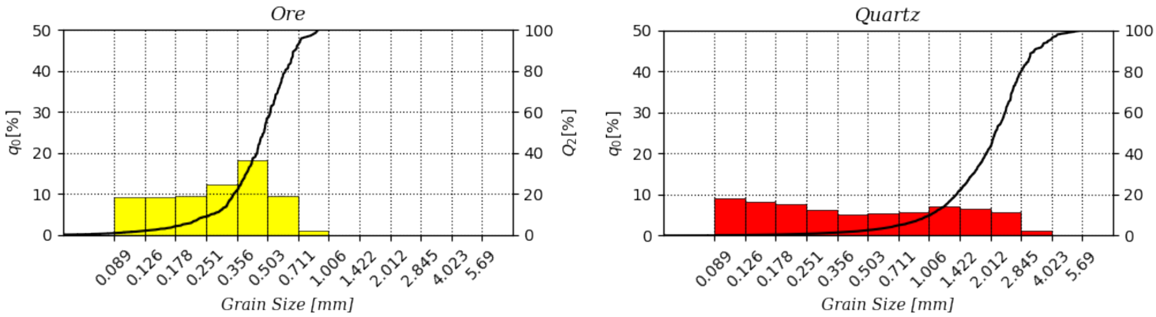

(c) Grain size distribution of Ore

(d) Grain size distribution of Quartz

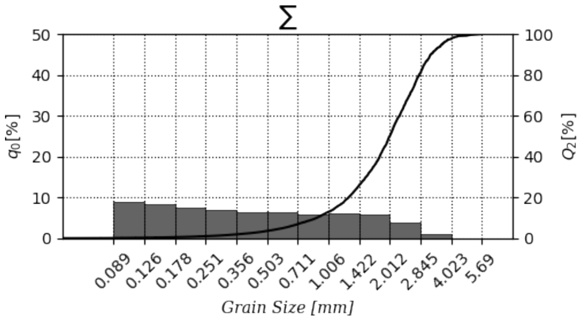

(e) Grain size distribution of the sum of the microbodies

Fig. C.1: Grain size distributions for the synthetic twin of the granite from Meissen

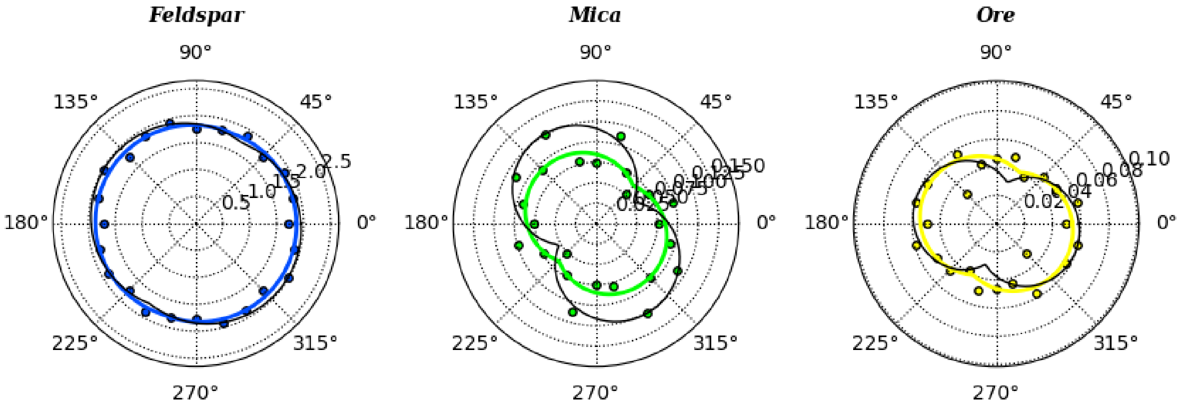

(a) Rose of intersections of Feldspar **(b)** Rose of intersections of Mica **(c)** Rose of intersections of Ore

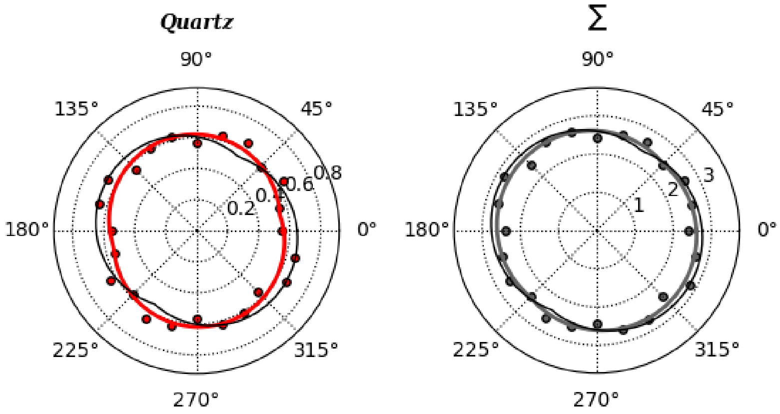

(d) Rose of intersections of Quartz **(e)** Rose of intersections of the sum of the microbodies

Fig. C.2: Two-dimensional roses of intersections for the synthetic twin of the granite from Meissen [Intersections mm^{-1}]

Tab. C.1: Matrix of the bounding surfaces with the degrees of intergrowth for the synthetic twin of the granite from Meissen

	Feldspar	Mica	Ore	Quartz
Feldspar	65.44	2.78	1.48	19.16
Mica	—	0.57	0.09	0.84
Ore	—	—	0.31	0.49
Quartz	—	—	—	8.84

C.2 The real kb-ore from Freiberg

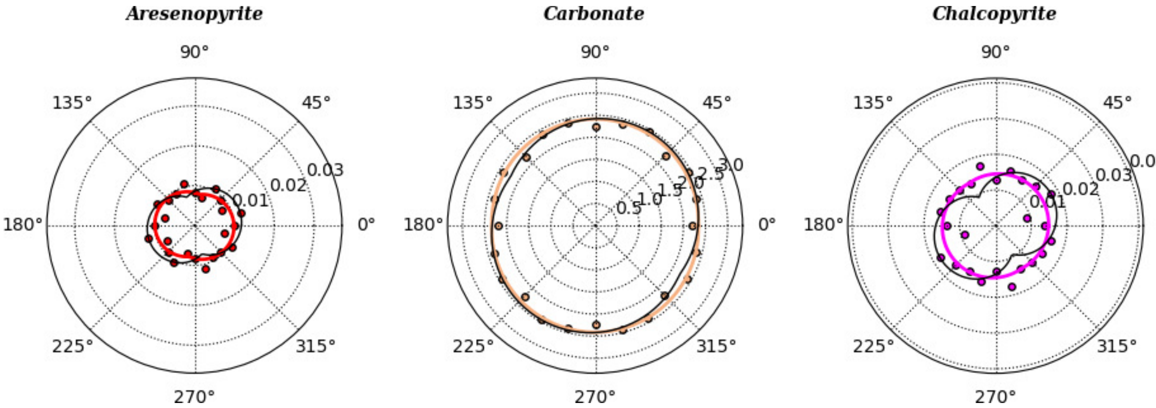

(a) Rose of intersections of Arsenopyrite

(b) Rose of intersections of Carbonate

(c) Rose of intersections of Chalcopyrite

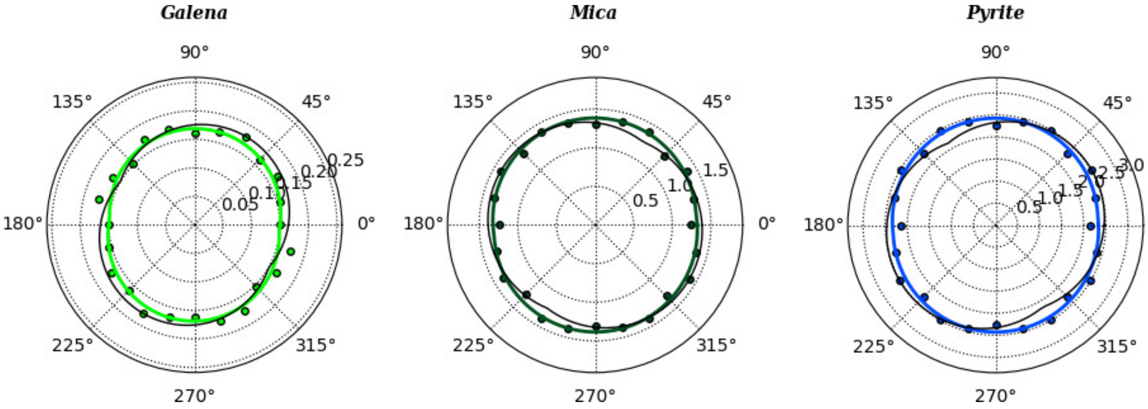

(d) Rose of intersections of Galena

(e) Rose of intersections of Mica

(f) Rose of intersections of Pyrite

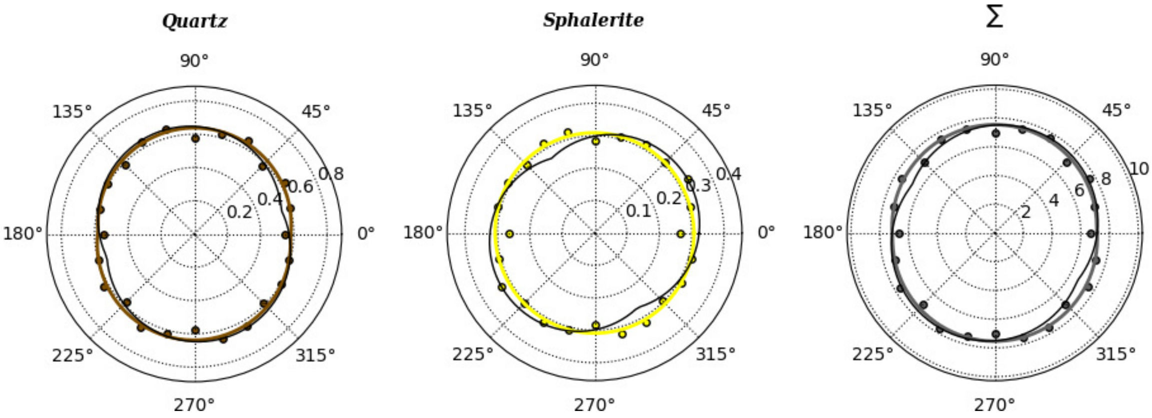

(g) Rose of intersections of Quartz

(h) Rose of intersections of Sphalerite

(i) Rose of intersections of the sum of the microbodies

Fig. C.3: Two-dimensional roses of intersections for real kb-ore from Freiberg [Intersections mm^{-1}]

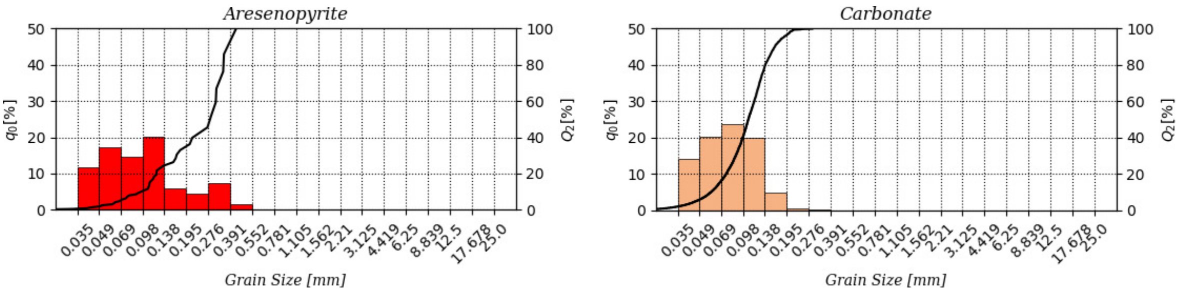

(a) Grain size distribution of Arsenopyrite (b) Grain size distribution of Carbonate

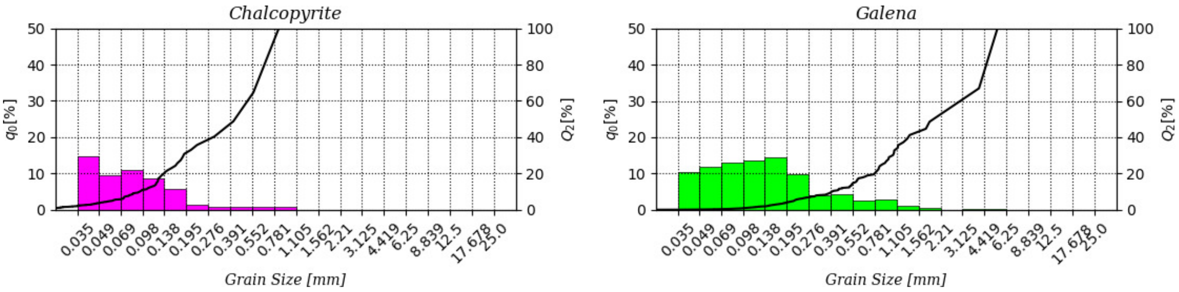

(c) Grain size distribution of Chalcopyrite (d) Grain size distribution of Galena

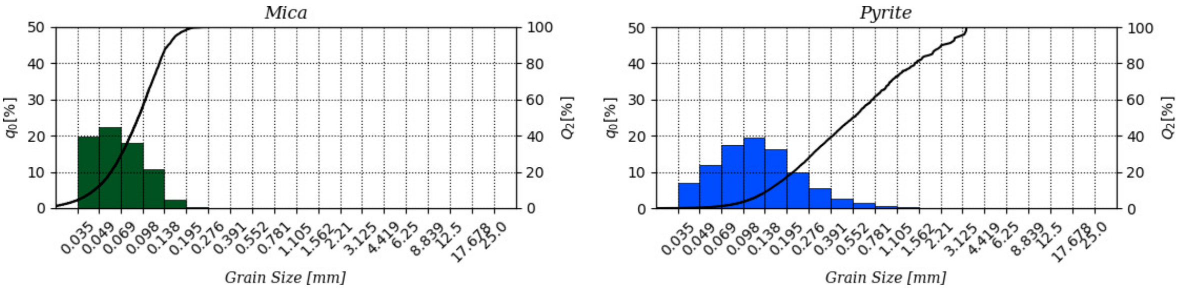

(e) Grain size distribution of Mica (f) Grain size distribution of Pyrite

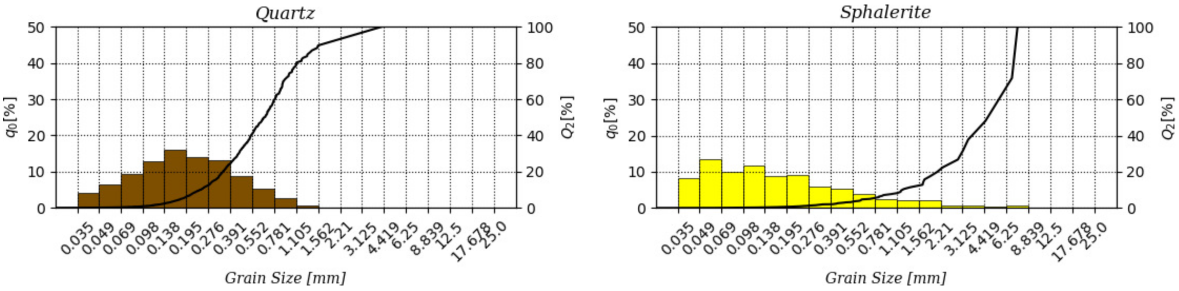

(g) Grain size distribution of Quartz (h) Grain size distribution of Sphalerite

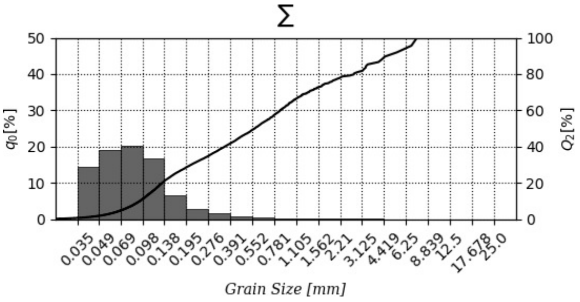

(i) Grain size distribution of the sum of the microbodies

Fig. C.4: Grain size distributions for real kb-ore from Freiberg

C.3 The synthetic twin of the kb-ore from Freiberg

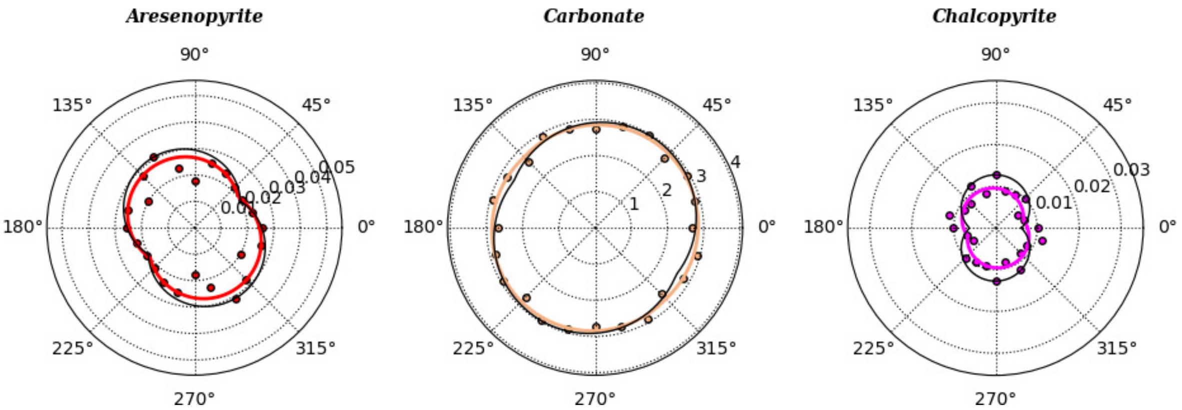

(a) Rose of intersections of Arsenopyrite

(b) Rose of intersections of Carbonate

(c) Rose of intersections of Chalcopyrite

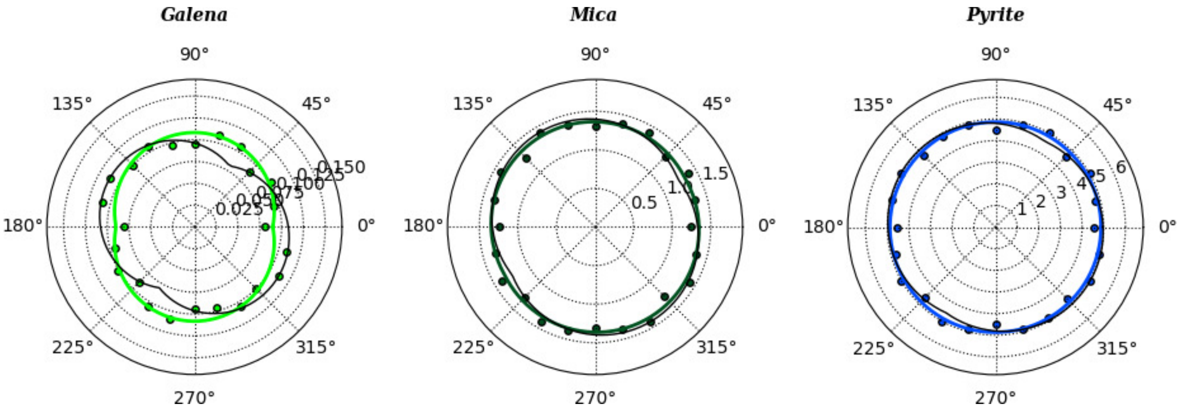

(d) Rose of intersections of Galena

(e) Rose of intersections of Mica

(f) Rose of intersections of Pyrite

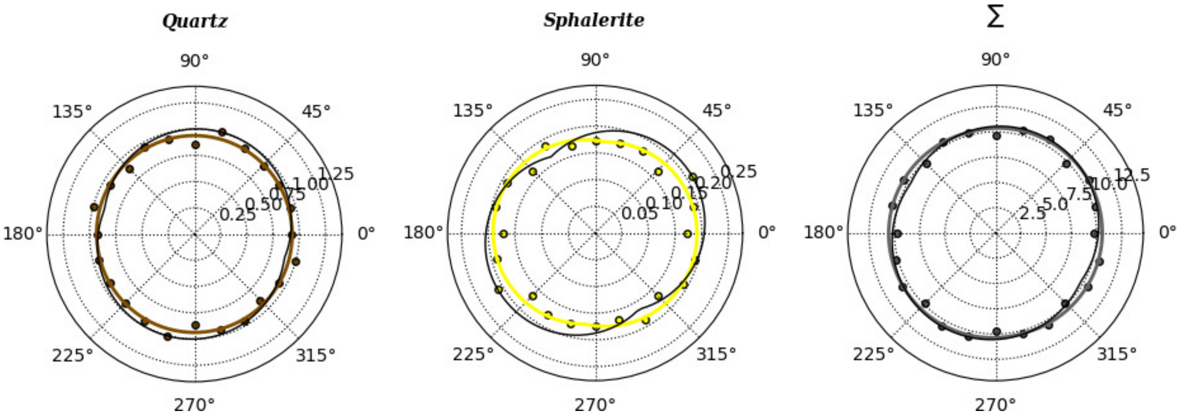

(g) Rose of intersections of Quartz

(h) Rose of intersections of Sphalerite

(i) Rose of intersections of the sum of the microbodies

Fig. C.5: Two-dimensional roses of intersections for the synthetic twin of the kb-ore from Freiberg [Intersections mm^{-1}]

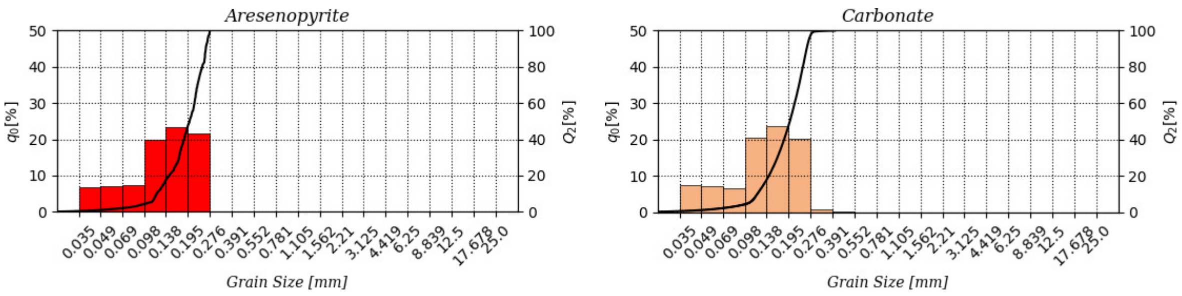

(a) Grain size distribution of Arsenopyrite (b) Grain size distribution of Carbonate

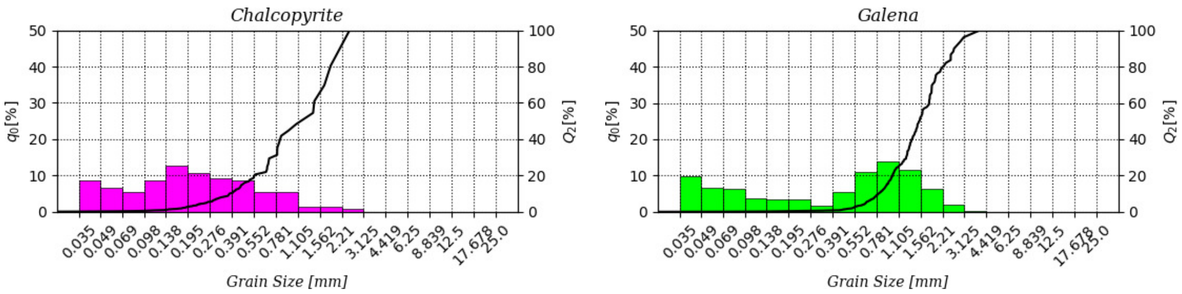

(c) Grain size distribution of Chalcopyrite (d) Grain size distribution of Galena

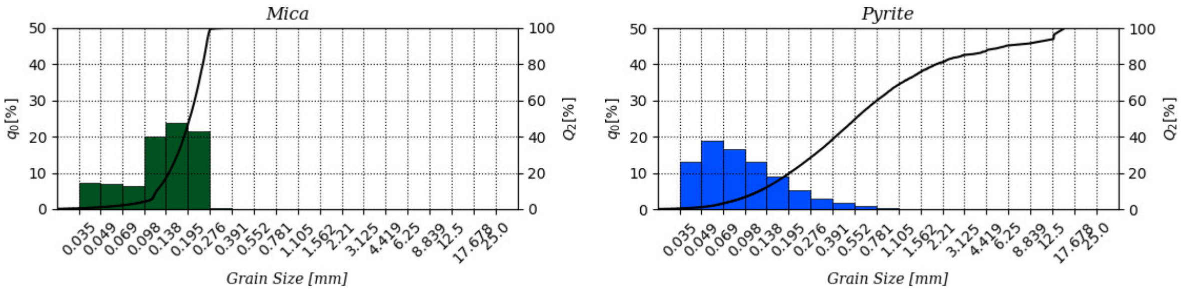

(e) Grain size distribution of Mica (f) Grain size distribution of Pyrite

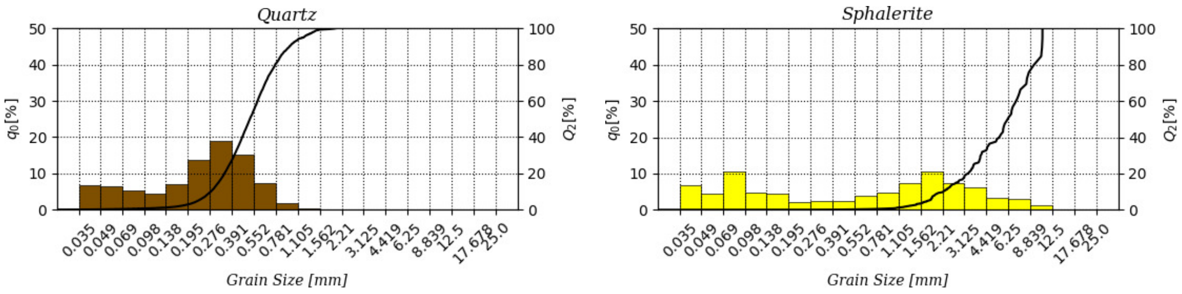

(g) Grain size distribution of Quartz (h) Grain size distribution of Sphalerite

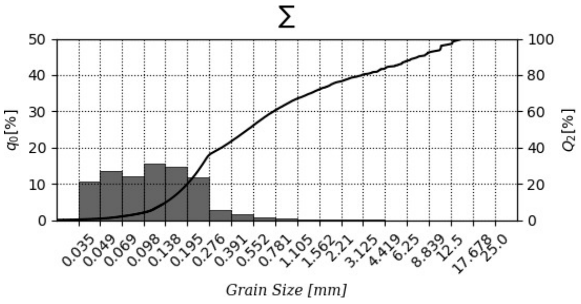

(i) Grain size distribution of the sum of the microbodies

Fig. C.6: Grain size distributions for the synthetic twin of the kb-ore from Freiberg

C.4 The real kb-ore from Freiberg with clusters

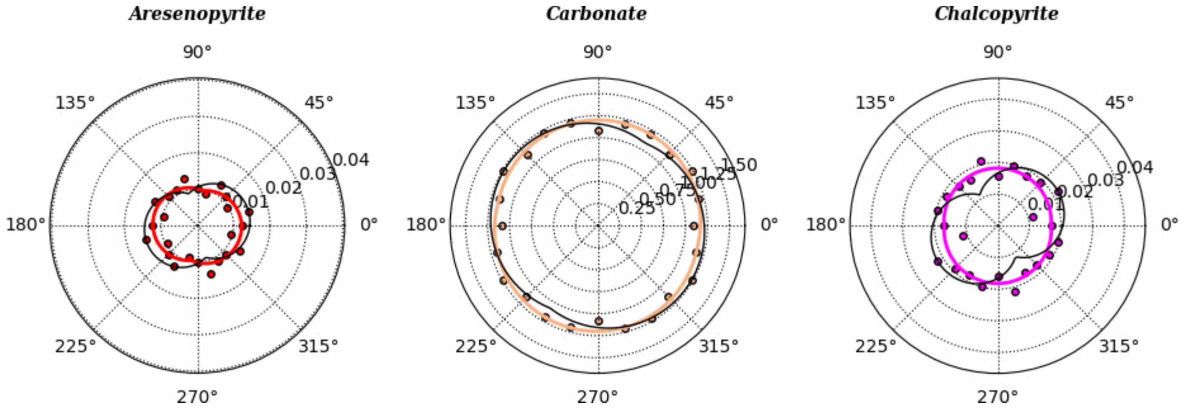

(a) Rose of intersections of Arsenopyrite

(b) Rose of intersections of Carbonate

(c) Rose of intersections of Chalcopyrite

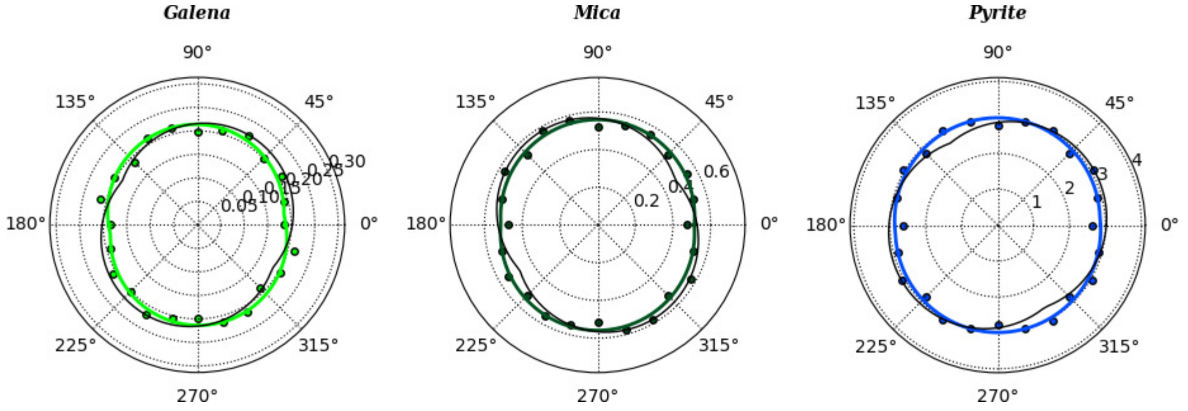

(d) Rose of intersections of Galena

(e) Rose of intersections of Mica

(f) Rose of intersections of Pyrite

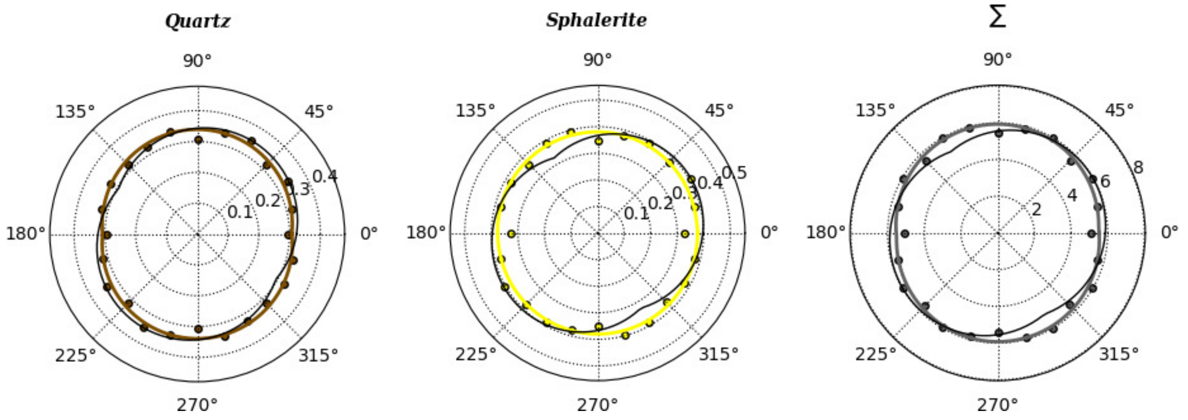

(g) Rose of intersections of Quartz

(h) Rose of intersections of Sphalerite

(i) Rose of intersections of the sum of the microbodies

Fig. C.7: Two-dimensional roses of intersections for the real kb-ore from Freiberg with clusters [Intersections mm^{-1}]

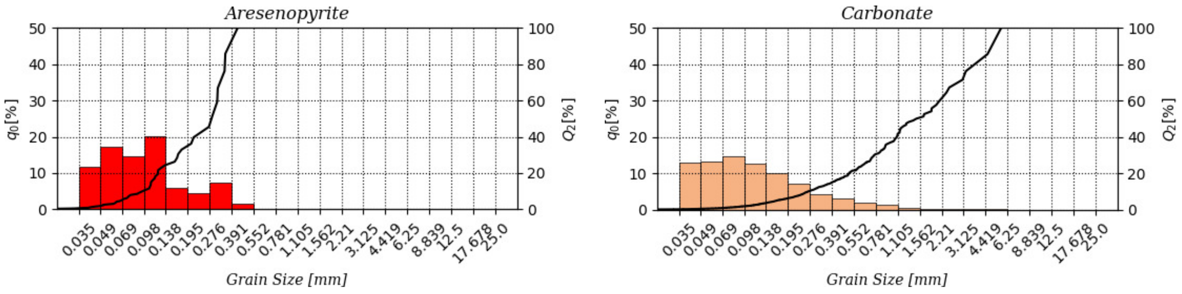

(a) Grain size distribution of Arsenopyrite

(b) Grain size distribution of Carbonate

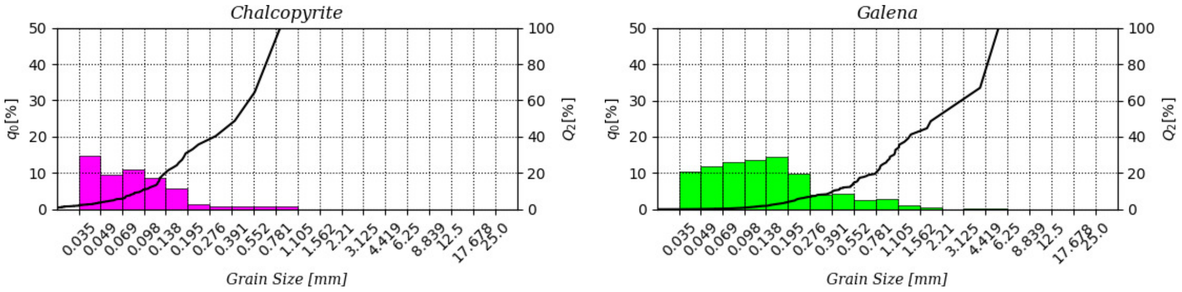

(c) Grain size distribution of Chalcopyrite

(d) Grain size distribution of Galena

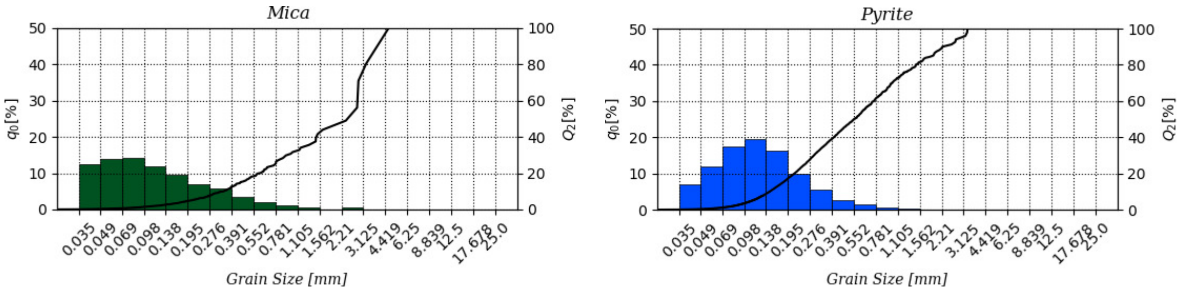

(e) Grain size distribution of Mica

(f) Grain size distribution of Pyrite

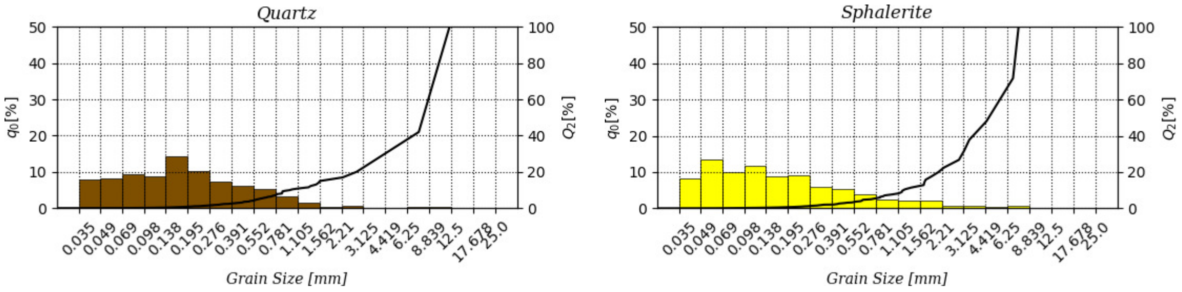

(g) Grain size distribution of Quartz

(h) Grain size distribution of Sphalerite

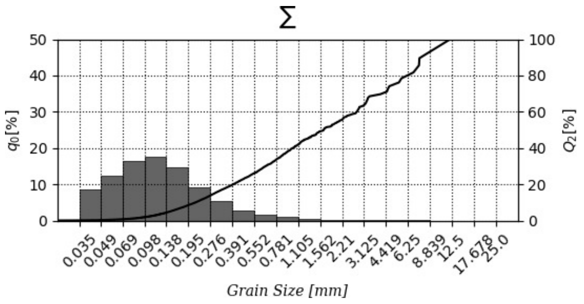

(i) Grain size distribution of the sum of the microbodies

Fig. C.8: Grain size distributions for real kb-ore from Freiberg with clusters

C.5 The synthetic twin of the kb-ore from Freiberg with clusters

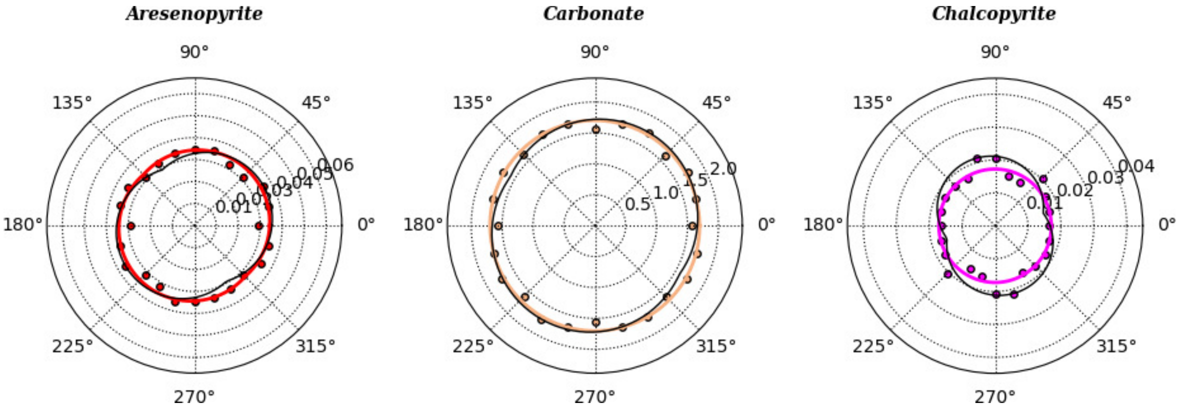

(a) Rose of intersections of Arsenopyrite

(b) Rose of intersections of Carbonate

(c) Rose of intersections of Chalcopyrite

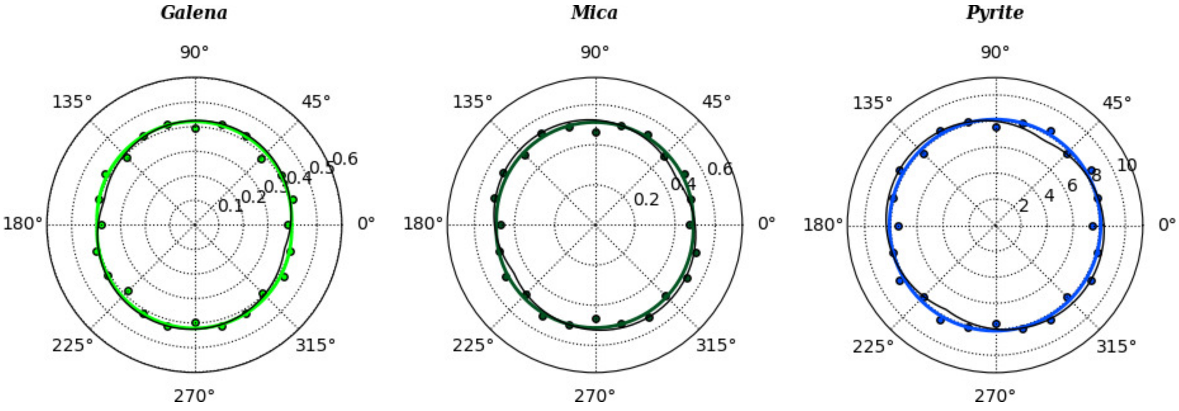

(d) Rose of intersections of Galena

(e) Rose of intersections of Mica

(f) Rose of intersections of Pyrite

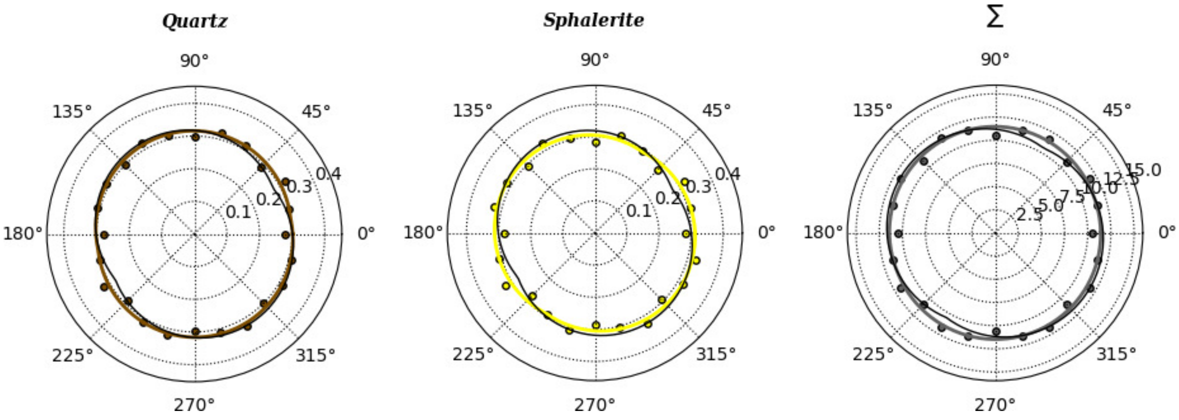

(g) Rose of intersections of Quartz

(h) Rose of intersections of Sphalerite

(i) Rose of intersections of the sum of the microbodies

Fig. C.9: Two-dimensional roses of intersections for the synthetic kb-ore from Freiberg with clusters [Intersections mm^{-1}]

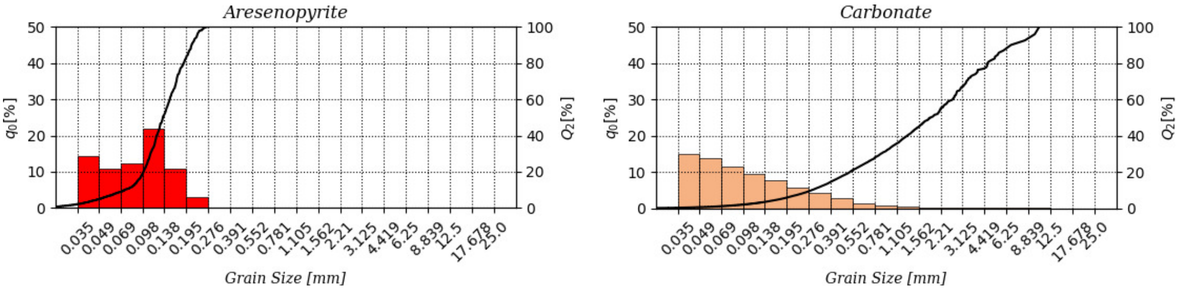

(a) Grain size distribution of Arsenopyrite

(b) Grain size distribution of Carbonate

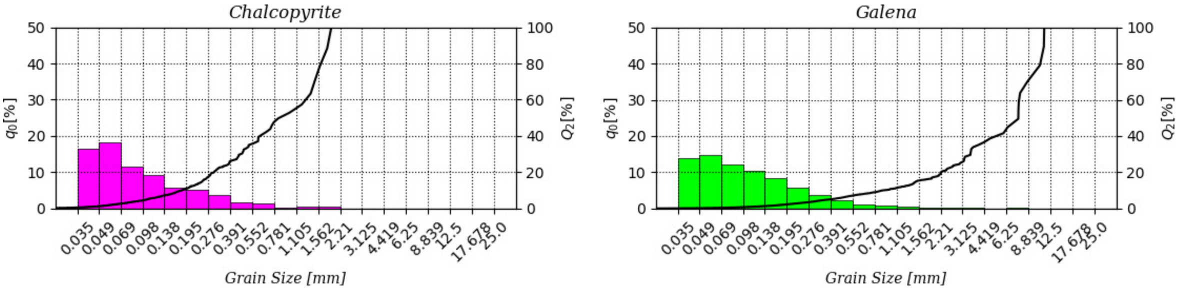

(c) Grain size distribution of Chalcopyrite

(d) Grain size distribution of Galena

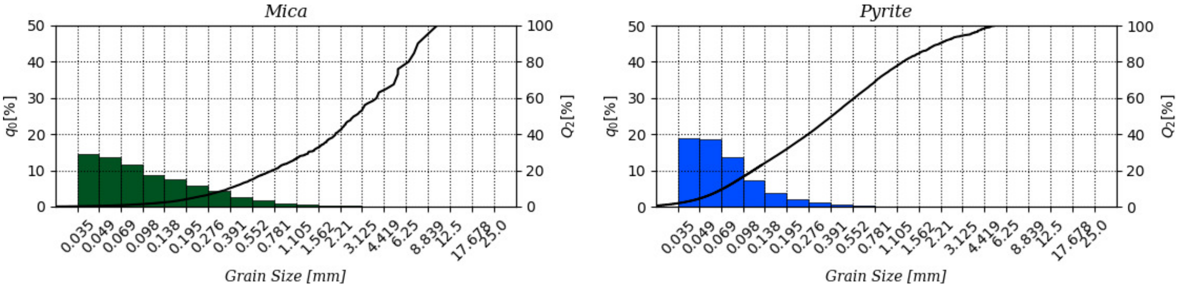

(e) Grain size distribution of Mica

(f) Grain size distribution of Pyrite

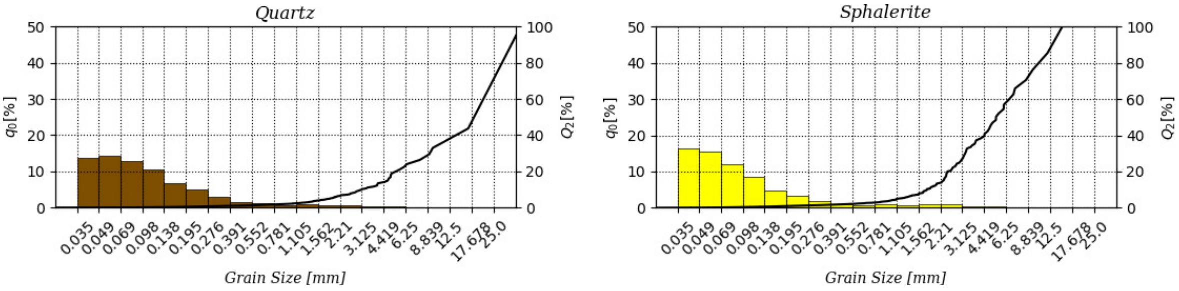

(g) Grain size distribution of Quartz

(h) Grain size distribution of Sphalerite

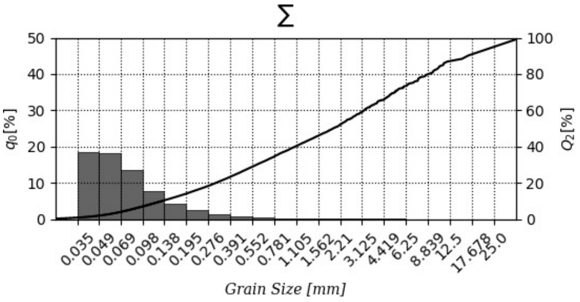

(i) Grain size distribution of the sum of the microbodies

Fig. C.10: Grain size distributions for synthetic kb-ore from Freiberg with clusters

C.6 The final synthetic twin of the kb-ore from Freiberg

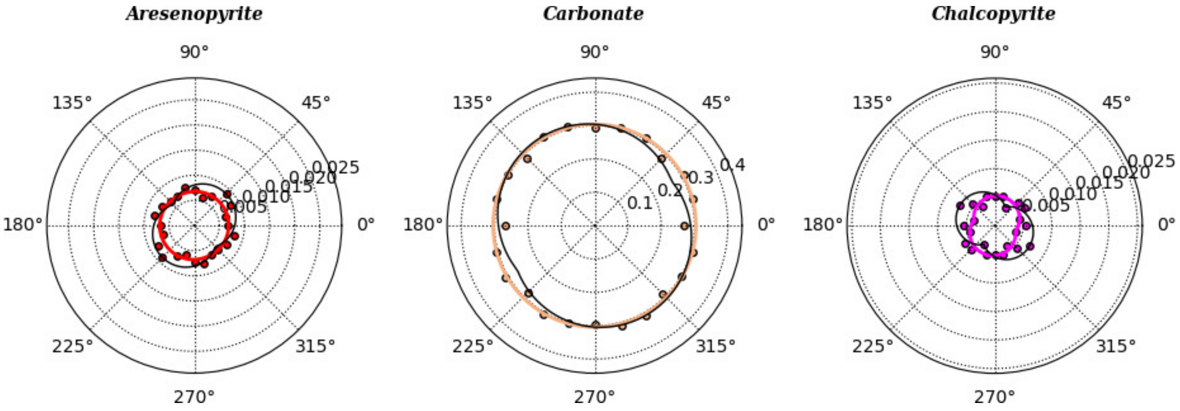

(a) Rose of intersections of Arsenopyrite **(b)** Rose of intersections of Carbonate **(c)** Rose of intersections of Chalcopyrite

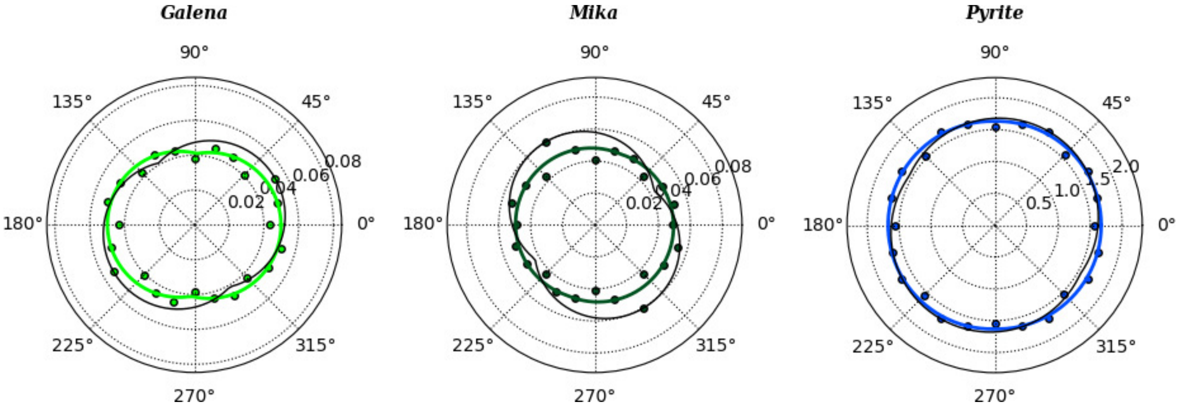

(d) Rose of intersections of Galena **(e)** Rose of intersections of Mica **(f)** Rose of intersections of Pyrite

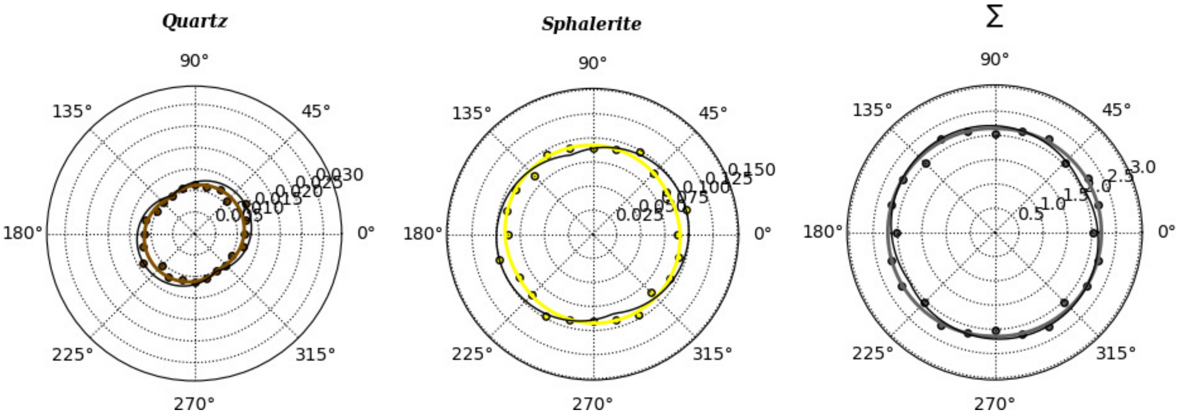

(g) Rose of intersections of Quartz **(h)** Rose of intersections of Sphalerite **(i)** Rose of intersections of the sum of the microbodies

Fig. C.11: Two-dimensional roses of intersections for the final synthetic twin of the kb-ore from Freiberg [Intersections mm^{-1}]

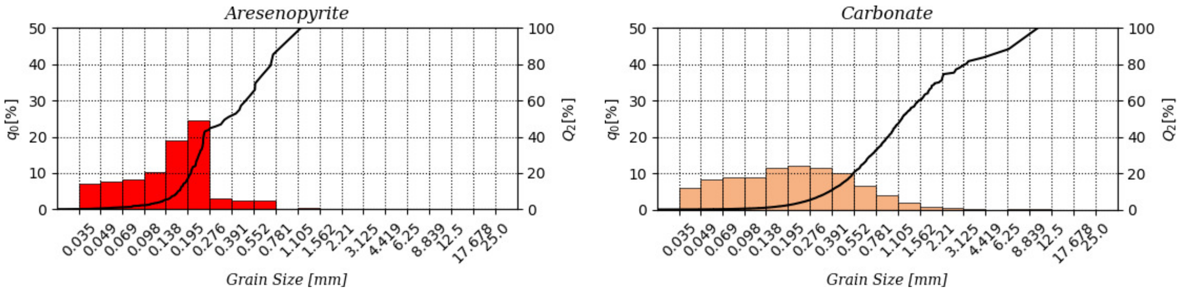

(a) Grain size distribution of Arsenopyrite (b) Grain size distribution of Carbonate

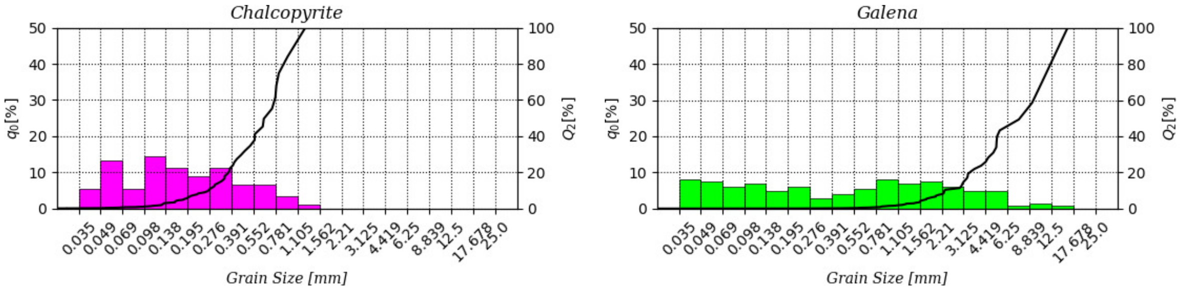

(c) Grain size distribution of Chalcopyrite (d) Grain size distribution of Galena

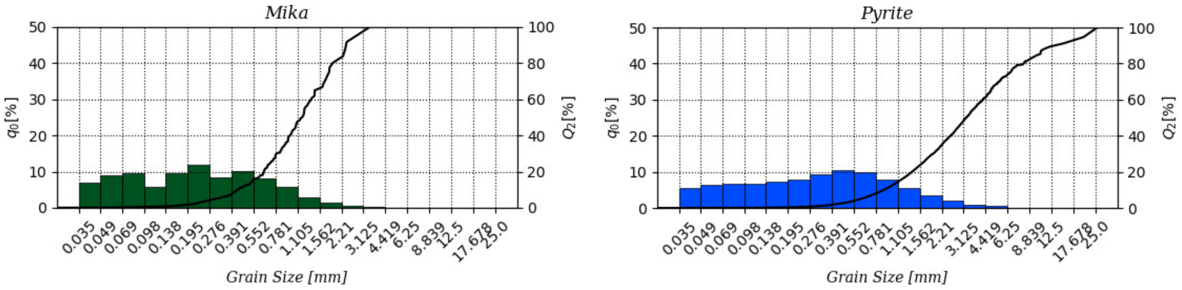

(e) Grain size distribution of Mica (f) Grain size distribution of Pyrite

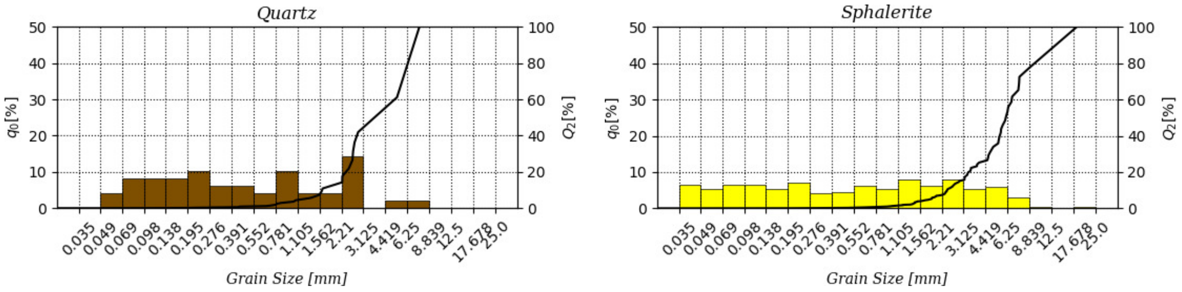

(g) Grain size distribution of Quartz (h) Grain size distribution of Sphalerite

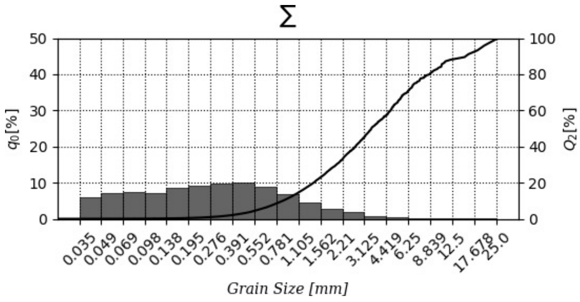

(i) Grain size distribution of the sum of the microbodies

Fig. C.12: Grain size distributions for the final synthetic twin of the kb-ore from Freiberg